LABORATORY MEASUREMENTS AND RESERVOIR MONITORING OF

BITUMEN SAND RESERVOIRS

A DISSERTATION

SUBMITTED TO THE DEPARTMENT OF GEOPHYSICS

AND THE COMMITTEE ON GRADUATE STUDIES

OF STANFORD UNIVERSITY

IN PARTIAL FULFILLMENT OF THE REQUIREMENTS

FOR THE DEGREE

OF DOCTOR OF PHILOSOPHY

Kevin Wolf

July 2010

This dissertation is online at: http://purl.stanford.edu/wj708xw9192

I certify that I have read this dissertation and that, in my opinion, it is fully adequate
in scope and quality as a dissertation for the degree of Doctor of Philosophy.

Gerald Mavko, Primary Adviser

I certify that I have read this dissertation and that, in my opinion, it is fully adequate
in scope and quality as a dissertation for the degree of Doctor of Philosophy.

Anthony Kovscek

I certify that I have read this dissertation and that, in my opinion, it is fully adequate
in scope and quality as a dissertation for the degree of Doctor of Philosophy.

Tiziana Vanorio

Approved for the Stanford University Committee on Graduate Studies.

Patricia J. Gumport, Vice Provost Graduate Education

*This signature page was generated electronically upon submission of this dissertation in
electronic format. An original signed hard copy of the signature page is on file in
University Archives.*

Abstract

This dissertation focuses on the properties of bitumen sand reservoirs and how they change under various temperature and pressure conditions. The key contributions of this dissertation include a new high-temperature, high-pressure ultrasonic pulse transmission system designed specifically with bitumen sands in mind, and a robust dataset of P- and S-wave velocity measurements for several heterogeneous bitumen sand samples. In addition, modeling was performed to determine which rock physics models, if any, are able to predict bitumen sand reservoir properties under various pressure and temperature conditions. Finally, an inversion methodology using P-to-S converted-wave elastic impedance was applied to bitumen sand reservoirs to more accurately track both temperature changes and steam chamber formation in bitumen sand reservoirs undergoing thermal production.

Bitumen sand properties are still poorly understood despite a large push in recent years to measure their properties. Specifically, the change in properties with increasing temperature and pressure is poorly constrained. This is due to the inherent difficulties in measuring soft, highly attenuating bitumen sand samples. To measure and better characterize the properties of bitumen sands I designed and built a novel system which incorporates low impedance piezoelectric transducers. These transducers are optimally

matched in order to obtain large amplitude, clean signals through bitumen sands over a wide temperature and pressure range. This allows both the P- and S-wave velocities of these materials to be better characterized, and the results can be used to calibrate and develop rock physics models applicable to bitumen sand. The lack of a robust rock physics model for these materials is the fundamental hurdle that must be overcome in order to better characterize and monitor the production of bitumen sands reservoirs.

The dissertation uses the dataset collected to lay the groundwork towards the development of a vigorous rock physics model. The data collected is used to ascertain the utility of several widely accepted rock physics models. Though no one single model has been demonstrated to always predict bitumen sand properties correctly, a handful of models show some promise. This work has also demonstrated that several commonly used models are erroneous in their bitumen sand property predictions and should be avoided. Additionally, I investigated the amount of velocity dispersion and attenuation that can be expected for bitumen sands when comparing measurements over a wide range of frequencies. This is of particular importance if we wish to compare measurements made in the laboratory with seismic measurements made in the field.

Seismic characterization and monitoring of bitumen sand reservoirs has been largely inadequate to this point due to the inability to quantitatively evaluate the temperature and presence of steam chambers in the reservoir. This dissertation addresses the problem by employing converted wave seismic data collected at near and far offsets to independently assess both the temperature and steam saturation. This methodology provides the information needed to operate thermal production of these reservoirs in an efficient manner, and provides insight into areas of the reservoir that may yet be untapped.

Acknowledgments

First, I would like to express my gratitude to my advisor, Gary Mavko, not only is he a source of teaching, guidance, and insight - but also nurturer of scientific curiosity and personal growth. Gary"s advising style suits me perfectly in that he will let me stumble my way through things provided I"m on the right path, and I always knew that if I hit a roadblock that his door would always be open. Besides his adeptness in advising, Gary is also a truly warm-hearted person, and was always willing to help out in any way possible – both professionally and personally, and I cannot express my gratitude enough.

I also thank my committee members, Tiziana Vanorio, Tony Kovscek, and Eric Dunham. Tiziana was not only a committee member, but was also beside me (in spirit if not in body) the majority of the time while working in the lab. Thank you for your constant encouragement, helpfulness and ideas. Without your help I know that I probably would have ended up smashing my lab equipment before I ever finished it. Tony was always supportive of my work and provided great insight, as well as the synthetic reservoir simulation that the last 2 chapters of my thesis are largely built upon. Eric was a last minute addition to my committee, but I thank him for his boldness in serving as a committee member for a topic and project that he knew little

of at the time of my asking. I would also like to thank Jerry Harris, who due to scheduling conflicts was not able to serve on the final committee, but provided very valuable insight throughout the duration of my thesis during annual reviews.

Of course I am greatly indebted to the SRB program and its affiliate sponsors for the funding and support I received throughout my time at Stanford. I would also like to thank Fuad Nijim, who not only made sure I was taken care of when issues arose, but also provided a welcome distraction from the mundane. Tapan and Jack are integral parts of SRB, and I am always impressed by their knowledge and willingness to help out, no matter what the problem. Of course SRB is much more than just these poeple, and I would like to thank all the students who I had the pleasure of learning from, being challenged by, and in general having a good time; Kyle, Ezequiel, Anyela, Mauricio, Futoshi, Laura, Ingrid, Kaushik, Tanima, Richa, Ratnas, Ramil, Carmen, Franklin, Piyapa, Danica, Stephanie, Nishank, Fabian, Adam and Kenichi. I hope we continue to cross paths in the future.

Thanks to all the people who kept me entertained over the years in the office. Kristina, Kyle, Youngseuk, Anyela, Ezequiel, Carmen, and Ramil always provided engaging conversation – be it science related or otherwise – and welcome distractions when needed (I still miss 1am hallway tennis…). I am also greatly indebted to everyone at Stanford Muay Thai. Running the club for the last 5 years has allowed me to meet a ton of great people, not to mention give me the opportunity to blow off steam when things in the lab weren"t cooperating. Real friends are the ones who you can punch in the face, and they say "Good one" instead of getting mad. Thanks to all the friends I made during my time here at Stanford – you are too numerous to mention – but you know who you are, and I am truly thankful for everything you"ve done for me during my years at Stanford.

Of course my thanks wouldn"t be complete without mentioning my family. To my mother, Mary, thanks for all you support, encouragement, and love over the years. Without you I would not be the man I am today. To my sister, Michelle, thanks for everything you do for me, even though I rarely give you credit for it. To my father, Karl, you left us too soon, but I know you would be proud of who I am today.

Lastly, my wife, Monica. I can't thank you enough for the love, support, patience and encouragement that you have given me through my years working towards my Ph.D. Without you I would have thrown in the towel long ago, and I am forever indebted to you. Not only have you helped me to accomplish my degree, but you've also given me the greatest gift I've ever received, our baby girl Maiah. Monica, I dedicate this thesis to you with all my love, heart and soul. Thank you.

Contents

List of Tables

List of Figures

xvi

xxii

Chapter 1
Introduction

"Every day you may make progress. Every step may be fruitful. Yet there will stretch out before you an ever-lengthening, ever-ascending, ever-improving path. You know you will never get to the end of the journey. But this, so far from discouraging, only adds to the joy and glory of the climb."
~Sir Winston Churchill

1.1 Motivation and objectives

The depletion of conventional oil supplies, coupled with high energy prices and the need to replenish reserves, has lead to a large increase in research related to heavy oil and bitumen in recent years. Heavy oil reservoirs contain upwards of 6 trillion barrels of oil in place, which is triple the amount of combined world reserves of conventional oil and gas (Curtis *et al.*, 2002). The magnitude of this resource makes it a very attractive target, but to effectively and efficiently produces these reservoirs we need a better fundamental understanding of their properties.

Heavy oil is defined based on the American Petroleum Institute gravity, or API gravity, as a an oil with a gravity between 10° and 22.3° API. Extra-heavy or crude bitumen is below 10° API (Alboudwarej *et al.*, 2006). Although heavy oil and bitumen are classified based on their gravities, often the most important property with regards to producing them is their viscosity. Heavy-oil and bitumen viscosities can range from thousands to tens of millions of centipoises at reservoir temperatures, which makes production of these fluids very challenging. Fortunately, these viscosities are strongly dependent on temperature (Figure 1), which allows many of these reservoirs to be produced by thermal means. Numerous methods have been developed to heat and extract the oil, but for all of them it is vital that we understand the changes occurring in the reservoir to efficiently produce them.
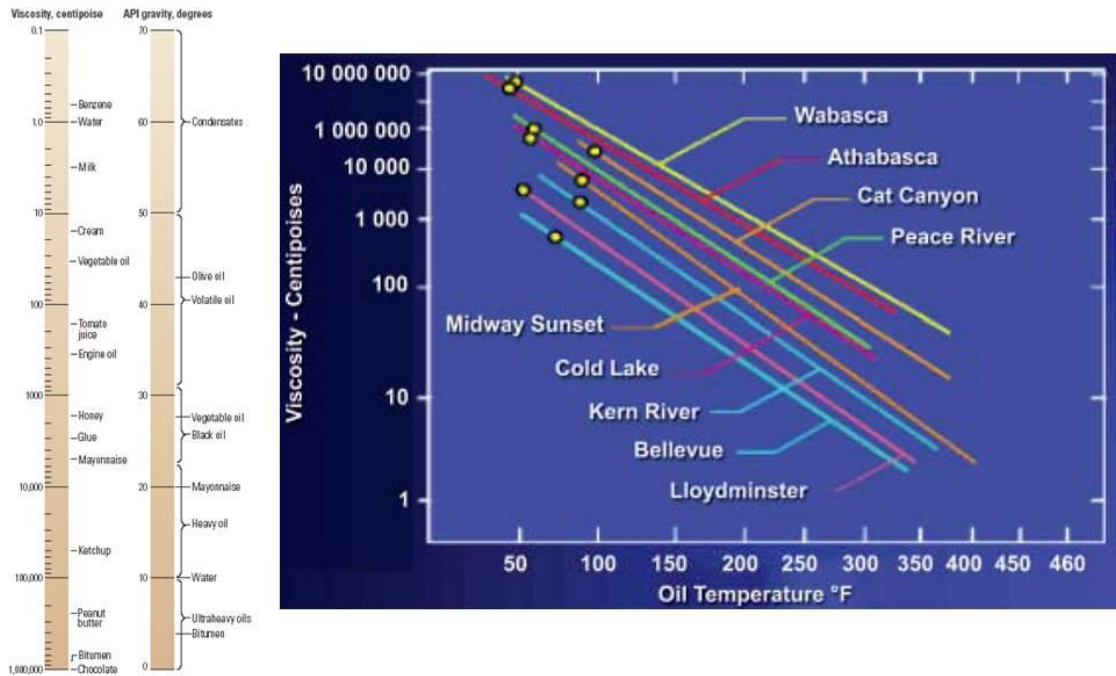
Figure 1.1: Left: viscosity and API gravity for common fluids, including heavy oil and bitumen (from Curtis *et al*, 2002). Right: viscosity–temperature relationships for several heavy-oil fields in Canada, with in-situ reservoir temperatures and viscosities indicated by yellow dots (from Dusseault, 2006).

Most methods currently used to extract heavy oil involve injecting steam into the reservoir to heat and reduce the viscosity of the oil. The generation of steam has many

costs associated with it, such as the burning of natural gas and consumption of water to create steam, as well as CO_2 emissions. To minimize these costs, it is important to monitor how much we are heating the reservoir, and where the steam is distributed in the reservoir. There have been numerous studies addressing these issues (Byerly *et al.*, 2009; Dumtrescu and Lines, 2009; Kendall, 2009; Li *et al.*, 2001; Nakayama *et al.*, 2008; Yuh *et al*, 2009; Eastwood *et al.*, 1994). However, these studies lack a quantitative description of the reservoir conditions. Typically, they rely on either amplitude anomalies, travel-time differences, or a combination of them to make qualitative interpretations of reservoir changes.

I feel that the reason that there has not been a quantitative interpretation of thermal production of heavy-oil reservoirs is because there is not a robust, reliable rock-physics model for interpreting seismic data from these reservoirs in a quantitative manner. To test the applicability of current rock-physics models and develop new ones specifically for heavy-oil reservoirs, we need comprehensive measurements of the properties of both heavy oil and heavy oil mixed with sand.

In recent years, the measurement catalog for heavy oils is growing, and models are being developed to help understand and predict their properties (Han *et al.* 2005; 2006; 2007; 2008a; 2008b; 2009; Batzle *et al.*, 2006; Rojas *et al.*, 2008). However, there are still very limited measurements of heavy-oil sand properties (Nur *et al.*, 1984; Han *et al.*, 2007a; 2007b;, Kato *et al.*, 2008), and few of these report both P- and S-wave velocities for heavy-oil reservoir samples.

This is most likely because measuring heavy oil or bitumen reservoir sample velocities is very challenging. In rock physics, velocity measurements of core plugs are usually made using ultrasonic pulse transmission (King, 1966), whereby an ultrasonic P- or S-wave is sent through a sample of known length, the traveltime of the pulse is recorded, and the velocity is calculated by dividing the length of the sample by the traveltime.

Heavy-oil or bitumen reservoir samples are typically unconsolidated sand held together by the bitumen in the pore space. This makes the samples very soft and

highly attenuating to the waves passing through them. To exacerbate this problem, traditional transducers for velocity measurements are made of steel or aluminum, which provide a very poor impedance match with these samples. This results in much of the signal energy being reflected from the sample instead of passing through it. If the energy of the signal received through the sample is weak, picking the arrival time of the wave is very difficult, and the resulting velocity estimates are unreliable.

This dissertation presents contributions toward resolving many of the problems associated with characterizing and monitoring heavy oil and bitumen sand reservoirs. The first contribution is the design of ultrasonic pulse transmission equipment specialized for use with heavy-oil and bitumen reservoir samples. The second is a dataset collected with the new apparatus, analyzied using several candidate rock-physics models for bitumen sands. The third is an inversion methodology using P-to-S converted wave "elastic" impedance (PSEI) for quantitative seismic monitoring of thermal production in heavy oil reservoirs.

To mitigate the problems associated with measuring bitumen sands in the laboratory, I designed and built a high-temperature, high-pressure ultrasonic pulse-transmission system with low-impedance transducers. This system yields much better signal quality and more accurate velocity estimates than traditional systems. The data I have collected with this system, along with future measurements made with it, will help to determine the applicability of current rock-physics models and guide the development of future models to apply to these materials.

To improve thermal production monitoring of heavy oil reservoirs and move toward quantitative monitoring, I applied PSEI inversion to the problem. This methodology makes it possible to determine the extent of heating in the reservoir, as well as the distribution of steam. This knowledge is invaluable for efficient production of heavy oil by thermal means. It makes it possible to refine the steam injection strategy, optimize well placement and spacing, and locate unswept oil that may justify infill drilling.

Given the varied scope of the work in this thesis, my principle references are also quite varied. The design of the ultrasonic transducers was made possible by using the models originally developed by Krimholtz *et al*. (1970), and then furthered by Desilets *et al*. (1978) and Haller (1998) to aid in the design of broad-band piezoelectric transducers. Many of the rock-physics models that are tested on bitumen and bitumen sands are concisely presented, along with their caveats, in Mavko *et al*. (1998). The derivation of PSEI and the development of an inversion methodology for application to partial gas saturation in reservoirs were given by Gonzalez (2006).

1.2 Chapter description

Chapter 2 outlines the components and design of the new high-temperature and high-pressure ultrasonic pulse-transmission experimental equipment. Particular attention was paid to the design of low-impedance transducers specifically for use with bitumen sands. This was accomplished by modeling the impulse response of various transducer configurations and the signal strength and quality that they would create through a sample of bitumen sand. Problems encountered with the design are also discussed, and the remedies used to resolve them are presented.

Chapter 3 presents the measured ultrasonic properties of several bitumen sands that were measured. Some samples were measured on a preliminary system that provided much insight into the issues associated with making measurements with these challenging materials, and further measurements were made using the newly designed and constructed system at Stanford.

Chapter 4 introduces some initial modeling procedures to match the preliminary laboratory data. Several established models are explored to determine their utility for reproducing the observed properties of bitumen sands, and a new model is proposed that may prove useful once a larger dataset is collected in order to further evaluate its utility.

Chapter 5 presents models for attenuation and dispersion modeling of both bitumen and bitumen-saturated sands. These models attempt to quantify the amount of attenuation and dispersion that can be attributed to the fluid itself, as well as the fluid-

rock interaction. This modeling is of particular importance in relating ultrasonic laboratory-measured data to data collected in the field at seismic frequencies.

Chapter 6 extends earlier work on the "elastic impedance" of incidence-angle-dependent P-to-S converted waves (or PSEI) to the practical case of monitoring and characterizing heavy-oil reservoirs undergoing thermal production. The utility of PSEI for this scenario is first explored, and then two synthetic data cases are presented to show the applicability of the method to these scenarios. The first case is a very simplified view of the assumed properties in a reservoir being produced by steam assisted gravity drainage (SAGD). The second case extracts rock properties from a reservoir simulation of a heterogeneous reservoir undergoing SAGD in order to analyze the utility of PSEI inversion applied to a more realistic reservoir.

Finally, Chapter 7 compares the PSEI inversion result from the last synthetic case with acoustic and elastic impedance inversion results on the same data. The aim of this is to see if the extra costs of acquiring and processing the converted wave data for PSEI analysis are warranted.

Chapter 2

Laboratory equipment design for high-temperature and high-pressure ultrasonic pulse transmission

"Scientific principles and laws do not lie on the surface of nature. They are hidden, and must be wrested from nature by an active and elaborate technique of inquiry."

~ John Dewey

2.1 Abstract

We have designed and built a novel high-temperature and high-pressure ultrasonic pulse-transmission system for measuring acoustic and elastic wave velocities through soft sediments. Our design is specifically intended for use with soft-sand sediments saturated with heavy-oil or bitumen in the pore space. These types of samples are typically very difficult to measure in the lab due to their low impedance and highly attenuating nature.

The main components of the system consist of confining and pore pressure control systems, a heating and cooling system, and a core holder to monitor sample strain and elastic wave traveltimes. Our core holder design incorporates transducers made of a high-temperature plastic, and uses a lead metaniobate crystal to maintain its effectiveness at elevated temperatures. We used extensive modeling to optimize the design of the transducers, ensuring that clean, large-amplitude signals are obtained over a wide temperature range. This makes first arrival picks more accurate, allowing more robust velocity estimates.

2.2 Introduction

Experimental rock physics research has involved a great deal of high- and low-pressure ultrasonic measurements on room-temperature properties of hard rocks such as sandstones, carbonates, and other rock types. The goal of this research has been to establish empirical and theoretical relationships between elastic response and rock properties (mineralogy, porosity, saturation, etc.). Despite the inherent complexities of these hard rocks, they are typically much simpler to study ultrasonically than bitumen sands, for several reasons. Hard rocks have higher impedance and higher quality factor than the soft sediments that typically make up bitumen reservoirs. The relatively low impedance and quality factor of these bitumen sand samples make it more difficult to obtain a large-amplitude P- and S-wave signal through them.

In addition, bitumen sands are generally poorly consolidated and bound together by the bitumen filling the pore space. Bitumen itself can change from a quasi-solid at low temperatures to a fluid at elevated temperatures; as a result, the bulk properties of bitumen sands can vary quite drastically when samples are heated (Han et al, 2006). These variable characteristics make measuring bitumen sand velocities with ultrasonic pulse transmission particularly challenging, and as a result, there is little ultrasonic data on bitumen sands under high-pressure and -temperature conditions.

With these challenges in mind, we constructed a new ultrasonic system specifically designed to handle the challenges presented by high-temperature measurements on soft-sediment samples. The system incorporates a new transducer

design, an advanced heating and cooling system, and many other modifications required for taking measurements at temperatures of up to 200°C and pressures up to 35 MPa. This system allows for the collection of bitumen sand properties under conditions that was previously not possible.

2.3 External System Components

When selecting components for the ultrasonic system, the goal was to maintain the broadest temperature and pressure range possible. The components selected limit the final system to a maximum operating temperature of 200°C and a maximum operating pressure of 35 MPa. Figure 2.1 shows an overview of the entire system, with the external components divided into three primary subsystems: the confining pressure system, the pore pressure system, and the heating and cooling system. These subsystems are described in the following sections. In addition, Table 2.1 lists the system components that were hardest to obtain and lists the manufacturer and model number for the parts used in our ultrasonic system. Of all the components listed in Table 2.1, the three most troublesome to select, and which ultimately limited the temperature and pressure, were the linear variable differential transformers (LVDTs) for sample strain measurement, the pressure vessel feedthroughs, and the piezoelectric crystals.
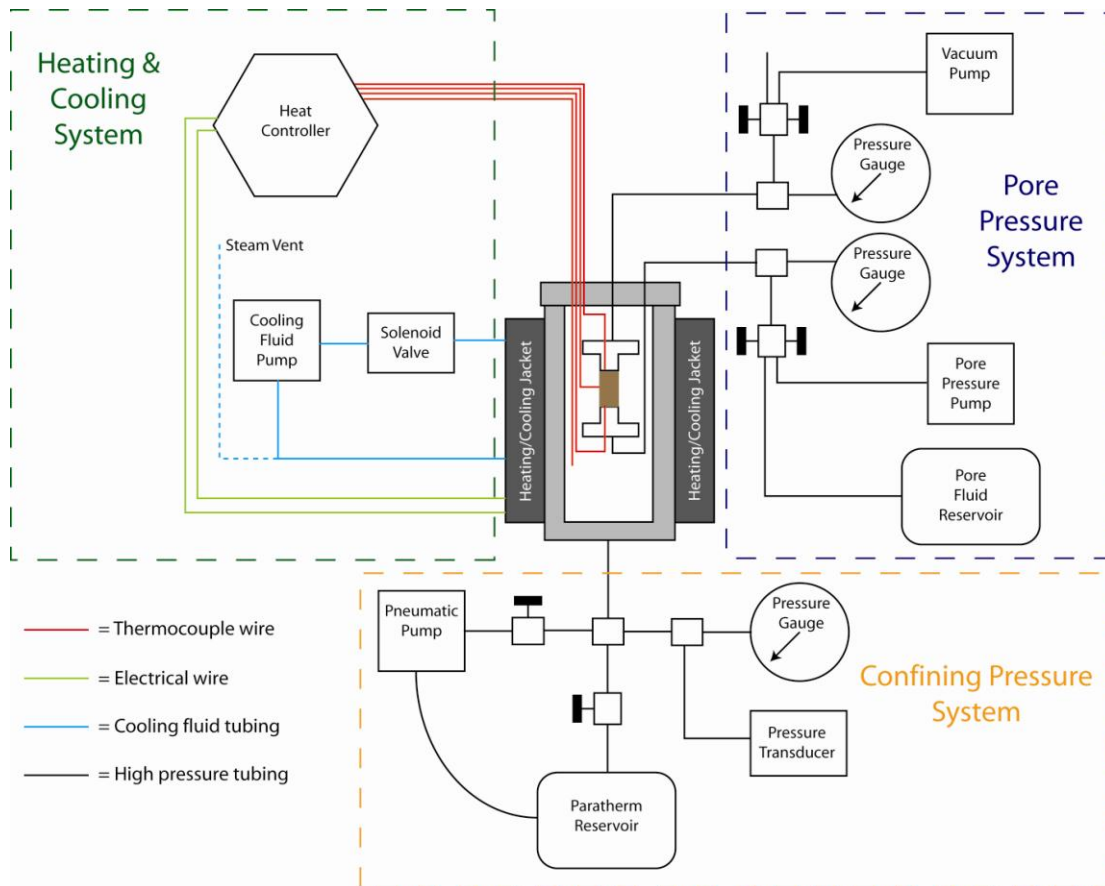
Figure 2.1: High pressure and temperature ultrasonic system schematic. The main components are shown, including the heating and cooling system, the pore pressure system, and the confining pressure system. In the center of the diagram the pressure vessel is shown, with the core holder inside.

Table 2.1: Select components of the ultrasonic pulse transmission system.

Component	Supplier	Model No.	Website
Pressure Vessel	High Pressure Equipment Company	GC-27	http://www.highpressure.com/
Linear Variable Differential Transformer	Measurement Specialties (Schaevitz Sensors)	250 MHR type 1502 with vented case	http://www.meas-spec.com/
End Cap	Drake Plastics	Custom machined Torlon 5030	http://www.drakeplastics.com/
Piezoelectric Crystals	Piezo Kinetics	Custom machined PKI 100	http://www.piezo-kinetics.com/
Pressure Vessel Feedthroughs	Conax Technologies	PL-20-A18-G PL-20(K)-A8-G MHM4-125-A3-G	http://www.conaxbuffalo.com/
End Cap Feedthroughs	Kemlon Products	16-B-01505-11	http://www.kemlon.com/
Heating-Cooling System	Omega Heater Company	Custom aluminum heater/cooler	http://www.omegaheater.com/
Sample Jacket	AAA Acme Rubber Company	Viton tubing, 1.5" ID, 0.25" wall	http://www.acmerubber.com/
Confining Fluid	Paratherm Corporation	Paratherm HE	http://www.paratherm.com/
Vessel Holder	Foundry Service and Supplies Inc.	Glastherm-HT Transite-HT	http://www.foundryservice.com/
Low-Viscosity, High-Temp Epoxy	Epoxies Etc.	Resin 20-3066 Catalyst 185	http://www.epoxies.com/
Conductive, High-Temp Epoxy	Cotronics Corp.	Duralco 120	http://www.cotronics.com/vo/cotr/
High-Temp Lubricant	Jet-Lube	SS-30	http://www.jetlube.com/

2.3.1 Confining Pressure System

The confining pressure inside the pressure vessel is controlled by injecting and removing Paratherm HE heat transfer fluid to exert the desired pressure on the sample jacket. To control the pressure we have used a Quizix QX6000SS pulseless metering pump. The pump is capable of maintaining a constant pressure of up to 41.3 MPa, and has a maximum flow rate of 50 ml/min. The benefit of this pump is that it can maintain pressure by automatically opening and closing solenoid valves to refill or dump fluid from its piston cylinder, without requiring manual valve manipulation. This is very beneficial for maintaining an accurate control of pressure when heating and cooling the vessel, as the Paratherm fluid expands and contracts with temperature changes.

2.3.2 Pore Pressure System

To maintain a given pore pressure, we inject deionized water. As the sample is heated, the fluid inside the sample—particularly the bitumen—will expand. To maintain pore pressure, we again use the Quizix QX6000SS pulseless metering pump to automatically add or remove fluid as required. Also, to help ensure a uniform pressure throughout the sample, pore fluid can be injected into either end, or both ends of the sample using a single pump. This way, if there are any barriers to flow through the core, we are still able to pressurize both sides of the sample. Though highly dependent on the individual sample being tested, the time taken to re-equilibrate pore pressures after changing confining pressure was typically on the order of 15 to 20 minutes.

2.3.3 Heating/Cooling System

The heating and cooling system consists of a two-piece metal jacket mounted on the outside of the pressure vessel, containing both heating elements and cooling fluid tubes. The temperature is controlled via a separate unit which either applies or removes heat from the system as desired. To add heat to the system, the heating coils within the external jacket are switched on. The elements in each half of the jacket are 2000 watts, and are able to increase the temperature of the system quickly. The heat controller has a high-limit switch that automatically shuts down the heating system

should the temperature exceed the rating of the ultrasonic system for any reason. To remove heat from the system, the control unit switches off the heating coils and opens a solenoid valve that allows cold water to circulate through cooling tubes, which are also located inside the external jacket. The cold water is supplied via a separate Neslab pump which keeps the deionized water cooling fluid at a temperature of four degrees Celsius. This cooling system allows measurements to be made at temperatures down to four degrees Celsius.

To attain and maintain a given temperature within the sample while ultrasonic measurements are being made, there are four thermocouples inside the pressure vessel; two extend through the transducer end caps and are in direct contact with the sample, one is attached to the outside of the sample jacket, and one is attached to the metal core holder in the confining fluid. Using these thermocouples as inputs, we can ensure that the sample temperature is monitored and controlled while measurements are made. The temperature controller simply switches between heating and cooling as required to maintain the sample at a constant set temperature to within 0.05°C. The time taken to equilibrate temperatures after changing to a new set-point was typically 5 to 7 hours.

2.4 The Core Holder

The core holder is designed to take 1.5" diameter core plugs of bitumen-saturated sand of lengths from 1 to 2". These core plugs are surrounded by a Viton rubber jacket, which isolates the sample and pore fluid from the external confining fluid. At each end of the sample is a transducer of center frequency 250MHz, which generates the P and S waves that we use to measure the elastic wave velocities in the core.

In addition to the thermocouples previously mentioned, each transducer also has a pore fluid line passing through it that is used to monitor and control the pore pressure (see Fig. 2.2). Besides the transducers, which are further described in section 2.5, the main parts of the core holder are the sample strain monitoring equipment – shown in light blue, and the pore pressure control system – including the black pore-fluid lines and the upper and lower pore-fluid reservoirs.
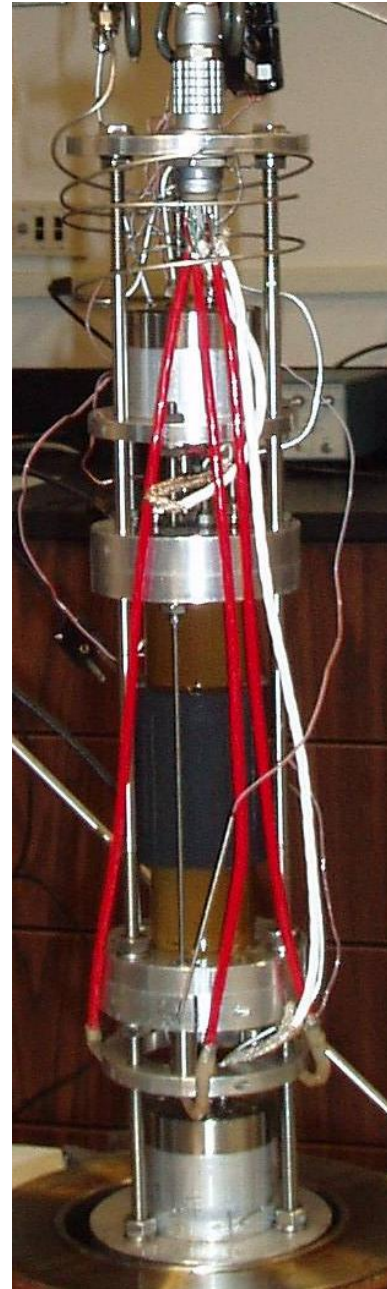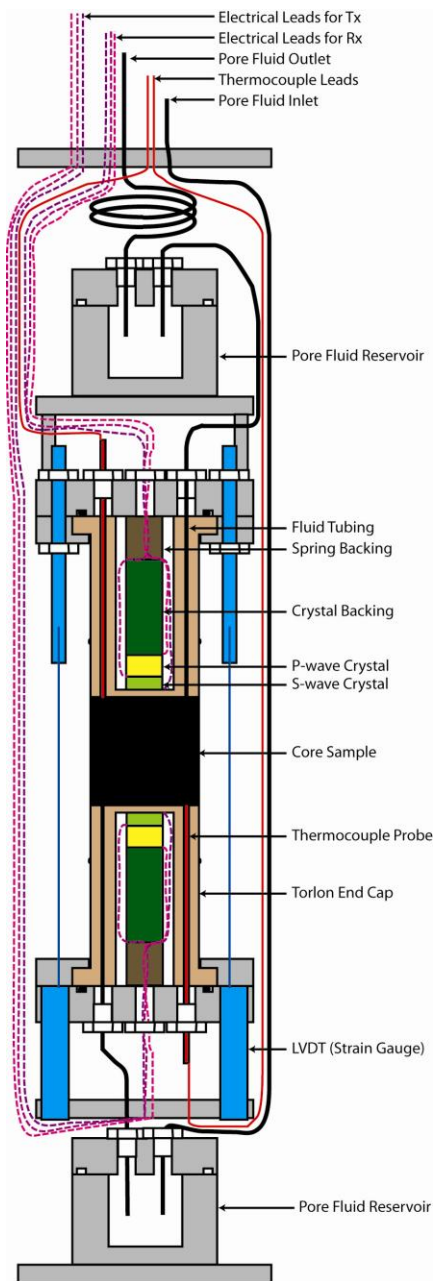
Figure 2.2: Left – schematic of core holder, including cut-away views of the transducers to show the internal components. Right – photo of the core holder. Length of the core holder is 16 inches.

2.4.1 Sample Strain Monitoring

Conventional low-temperature ultrasonic systems in our lab use DC linear potentiometers to monitor longitudinal sample strain. However, we were unable to locate any linear potentiometers that can handle operating temperatures near our requirements. We used LVDTs, which we found can handle much higher operating temperatures. Unfortunately, all DC LVDTs we found were too large to fit into our core holder, so we needed to use an AC model. The AC LVDT, however, introduced an issue with crosstalk between the wires going into the pressure vessel. The LVDTs are powered with a 10 kHz power source, which can induce a signal in the wires carrying our piezoelectric response signal and interfere with our first arrival picking. Fortunately, adequately shielding the wires and properly grounding the shields eliminated the majority of this spurious signal. In addition, the LVDTs can be switched off while recording a wave arrival signal on the oscilloscope, completely eliminating any crosstalk due to the LVDT signal.

The LVDTs provided by Measurement Specialties normally come with sealed cases which cannot withstand elevated pressure. However, we were able to get a version with a vented case which worked quite well at high pressure.

2.4.2 Pore Pressure Control

Within the core holder, we installed two fluid reservoirs that act as a buffer between the core sample and the pore pressure pump located outside of the pressure vessel. The purpose of these reservoirs is to trap any bitumen that is expelled from the core plug. As the bitumen is heated, it expands in volume, and must be removed from the sample to maintain a constant pore pressure. However, if the removed fluid travels outside the pressure vessel and begins to cool, the chances of it clogging the pore pressure lines is very high. To mitigate against this risk, the reservoirs in the core holder trap any bitumen that has been removed from the sample, keeping it heated and preventing it from clogging the pore fluid lines. This ensures that we accurately control the pore pressure within the sample, and not just between the pump and a clog in the pore fluid line.

2.5 High-temperature, Soft-sediment Ultrasonic Transducers

Traditionally, ultrasonic velocity measurements have been made with high-impedance end-caps, with little thought and planning put into the design of the transducers themselves. For the most part, this has not been a major impediment, because the majority of rock-physics measurements have been made on hard rocks, such as sandstones, carbonates, and some hard shales. The properties of these hard rocks are not as variable as unconsolidated sediments, especially unconsolidated sediments that are fixed by bitumen. We have paid particular attention to the design of low-impedance transducers to ensure that we are able to record the best signal possible for loose sediments fixed by bitumen under all operational conditions.

The frequency at which the measurements are made has also been modified from traditional ultrasonic transducers used for consolidated rocks. We use 250 kHz broadband piezoelectric crystals instead of standard 1 MHz crystals; this was found to reduce energy absorption and scattering as the signals pass through soft samples (Zimmer, 2003). Also, by using a frequency of 250 kHz we ensure that we will have at least one wavelength within our samples, which will allow us to obtain robust measurements and avoid edge effects from the samples.

2.5.1 Ultrasonic Transducer Design

Basic transducer design must take into account all vital pieces of a transducer. This includes the piezoelectric crystal (or crystals for generating multiple wave types or polarizations), the backing behind the crystals, the end cap or matching layer between the crystals and the load, and the load that the generated waves will travel through—which in our case is bitumen sand. Figure 2.3 illustrates a general schematic for an ultrasonic transducer with two piezoelectric crystals—one to generate P-waves and one to generate S—waves.

The piezoelectric crystals used in our ultrasonic transducers are made from lead metaniobate. This material was chosen for its high Curie temperature. The high Curie temperature ensures that the crystal will not depolarize when it is heated to high temperatures, which would render the crystal useless. Finding a company that

produces lead metaniobate crystals is not challenging, but finding one that was able to manufacture shear-wave crystals to our specifications was.

The transducer modeling that we performed showed that in order to get large-amplitude signals, the crystal area should be as large as possible. In our case, this amounted to a square crystal of dimensions 0.6" x 0.6" (15.24x15.24mm). The difficulty with this is that none of the companies we contacted could correctly polarize a shear crystal of this size, because of the large voltage required to do so. To overcome this problem, Piezo Kinetics polarized 4 smaller 0.3" square crystals for us, and then glued them into an array, resulting in a single crystal 0.6" square, with the individual components aligned so that the polarizations add together constructively. Creating the P-wave crystal was not a problem, because the polarization direction is across the thickness of the crystal, which is much less than 0.6". The crystal thickness is determined by the frequency desired for the crystal. After completing the polarization of the crystals, each individual crystal then had thin silver electrodes sputtered onto its top and bottom faces to facilitate application of a voltage across the crystals to generate the desired waves. Piezo Kinetics also provided us with pieces of lead metaniobate measuring 0.6" square and 1.389" thick to use as a backing for the active crystal elements. This backing provides a perfect impedance match behind the crystals, which in turn allows for better signals to be generated in our specific case, which will be shown later in this section.
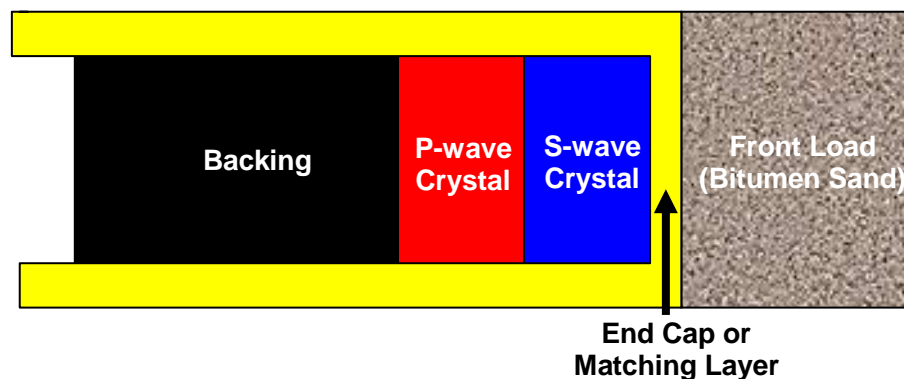
Figure 2.3: Schematic for the generalized transducer modeled. It consists of a crystal backing, two piezoelectric crystals – one to generate P-waves and one to generate S-waves, an end cap or matching layer, and the load at the front of the transducer, which is bitumen sand in this case.

In order to realize the optimum design, a transducer modeling code was written, which utilizes the KLM equivalent circuit, shown in Figure 2.4, (Krimholtz et al, 1970) to simulate the response of the transducer given different transducer and sample properties. This design method has been used extensively in the biomedical industry to model the response of ultrasonic medical transducers (Haller, 1998, Morton, 1999).
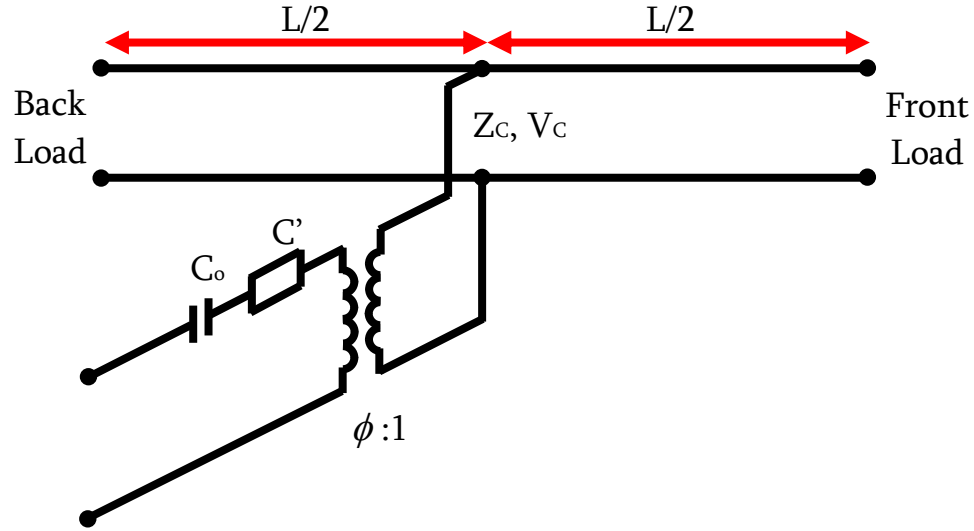
Figure 2.4: KLM equivalent circuit used for transducer modeling. In the diagram, L is the piezoelectric crystal thickness, Z_C is the crystal impedance, V_C is the wave velocity in the crystal, ϕ:1 is the turns ratio of the transformer, and C_o and C are clamped and variable capacitances of the crystal respectively.

The advantage of using the KLM model is that it easily allows for the addition of any number of piezoelectric crystals, matching layers, etc. to be added into the transducer model. This allows modeling of many types of transducers, including those with multiple crystals for making anisotropic measurements. We also use the ABCD matrix representation to represent the individual components and loads in the KLM model. Each component of the KLM model can be represented as a two-port network, which can them be characterized using matrix methods (Ramo et al, 1994). This formulation allows the input and output voltage and current in each component to be related to the others through a 2x2 matrix. Then, to calculate the response of the entire KLM model, the entire chain of 2x2 matrices is multiplied together, which then relates the input voltage and current to the output force and velocity from the transducer. This

matrix representation makes the calculation of the transducer response fast and relatively easy to code. Figure 2.5 shows the ABCD matrix representation of the KLM equivalent circuit used to represent the P-wave transducer that we built. In the figure, V is the matrix representing the power supply to the transducer, $M_{C'}$ and M_C are the matrix representations of the capacitors, M_Φ the transformer, Z_b the impedance of the backing material, M_{bc} the back half of the P-wave crystal being powered, M_{fc} the front half of the P-wave crystal being powered, M_s the shear wave crystal, M_{ml} the matching layer or end cap, and Z_f is the impedance of the front load – bitumen sand in our case.
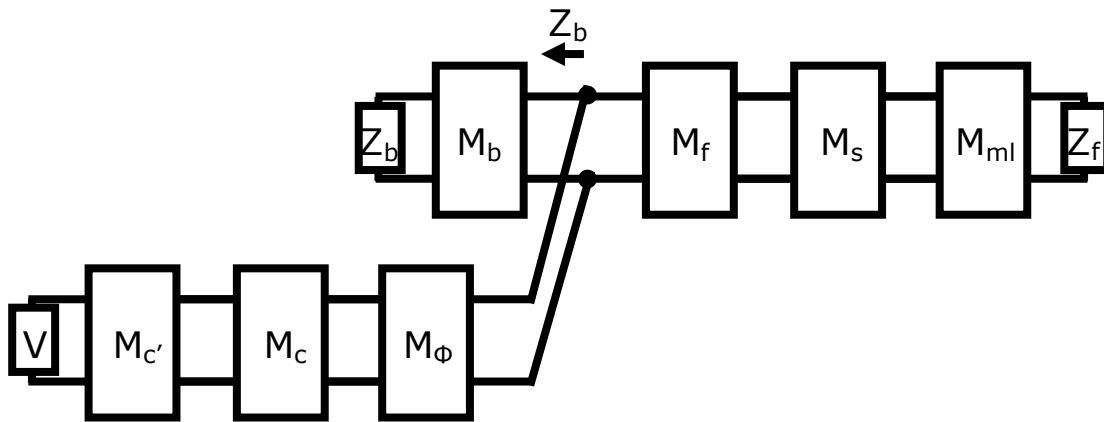
Figure 2.5: ABCD matrix representation of the KLM equivalent circuit used to model the P-wave transducer response.

The responses of the transducer under various configurations and using different components are shown in Figures 2.6 through 2.10. Figure 2.6 shows the effect of varying the surface area of the piezoelectric crystal. The larger the crystal area, the larger the impulse response of the transducer. Therefore, we have tried to maximize the size of the crystal incorporated into the transducer.

The effect of varying the end-cap or matching-layer material is shown in Figures 2.7 and 2.8. Traditional hard-rock transducers utilize stainless steel end caps. For hard rock samples, this does not create a large mismatch in impedance between the transducer and the sample, since the sample itself has a high impedance. However, when dealing with unconsolidated or other soft samples, having a high impedance end cap creates a large impedance contrast between the transducer and the samples, resulting in less energy being transferred to the sample itself. Zimmer (2003)

attempted to overcome these problems for his unconsolidated sand measurements by using a glass-filled polycarbonate end cap. This type of end cap has an impedance more similar to unconsolidated sand than traditional steel end caps. However, this material cannot withstand the elevated temperatures needed for our experiment. We decided to use Torlon for our end caps because it has a low impedance similar to that of unconsolidated sand; in addition, its properties are not drastically affected by increases in temperature. Figure 2.7 shows the impulse response of the transducer at room temperature with two different end cap materials, and Figure 2.8 shows the impulse response of the same end cap materials at elevated temperatures. The traditional steel end cap is shown in blue, and the Torlon end cap is shown in red.
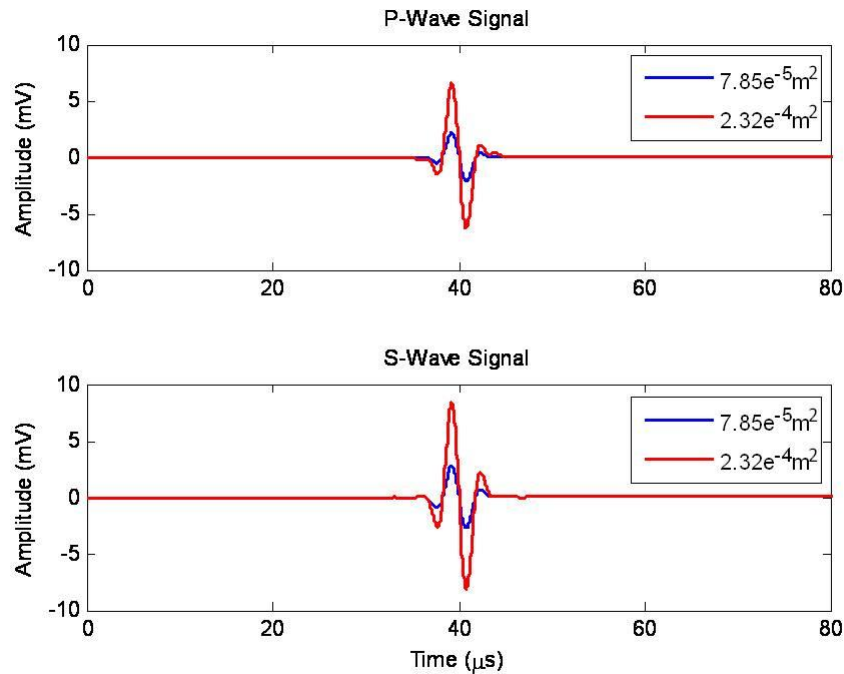
Figure 2.6: The effect of varying the surface area of the piezoelectric crystal in the transducer. The impulse response of a crystal with surface a surface area of $7.85e^{-5}$ m^2 is shown in blue, and the response of a crystal with $2.32e^{-4}$ m^2 is shown in red.
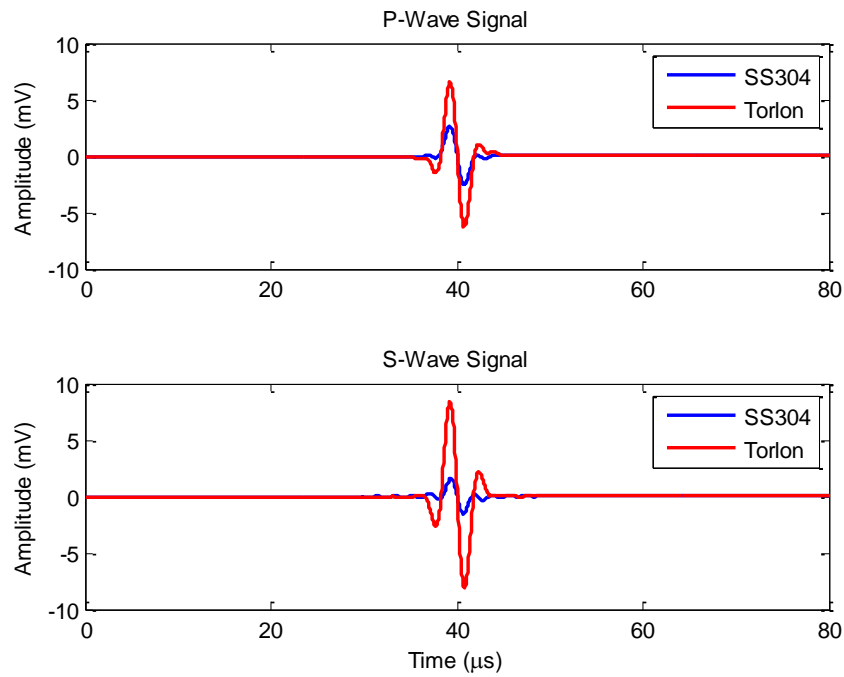
Figure 2.7: The effect of varying end cap material on the response of the transducer at room temperature. The stainless steel end cap is shown in blue, and the Torlon end cap is shown in red.
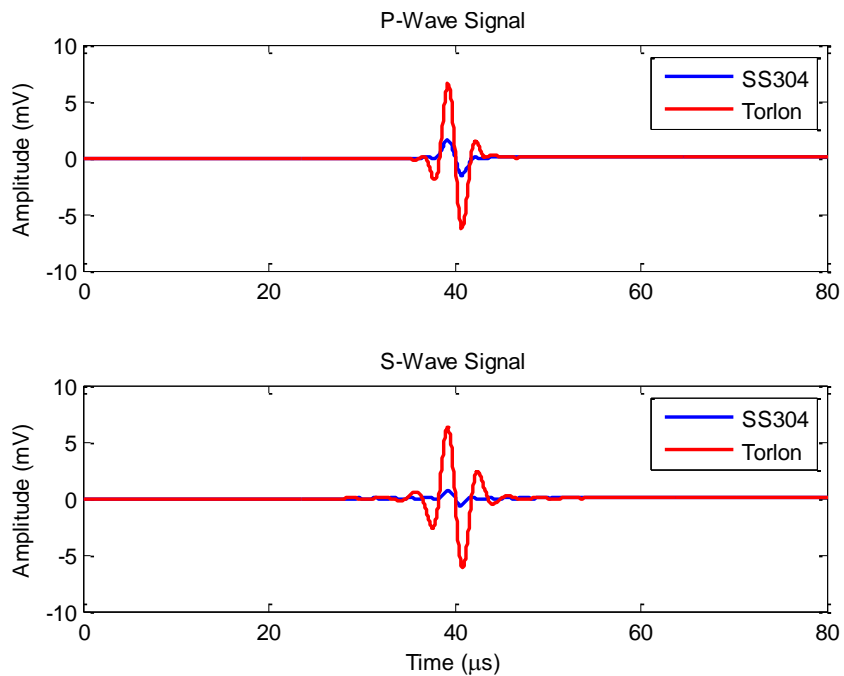
Figure 2.8: The effect of varying end cap material on the response of the transducer at elevated temperature. The stainless steel end cap is shown in blue, and the Torlon end cap is shown in red.

Another important consideration is the thickness of the end cap or matching layer. Ideally, the thickness of the end cap or matching layer should be precisely one quarter of a wavelength thick. This ensures that any reflected energy will constructively interfere and lead to the best possible impulse response of the system at the frequency it is designed to operate at. However, in our case we are trying to generate both compressional- and shear-waves, each having their own associated wavelength. Therefore, a compromise was reached between the two ideal thicknesses for each type of wave. As can be seen in Figure 2.9, a thickness of $2.54e^{-3}$m provides a large amplitude, broadband impulse response for both wave modes. If the thickness is increased or decreased, the impulse response is adversely affected. For increased thickness, shown in blue, the first arrival of the shear-wave is less prominent, and the maximum amplitude is slightly decreased.
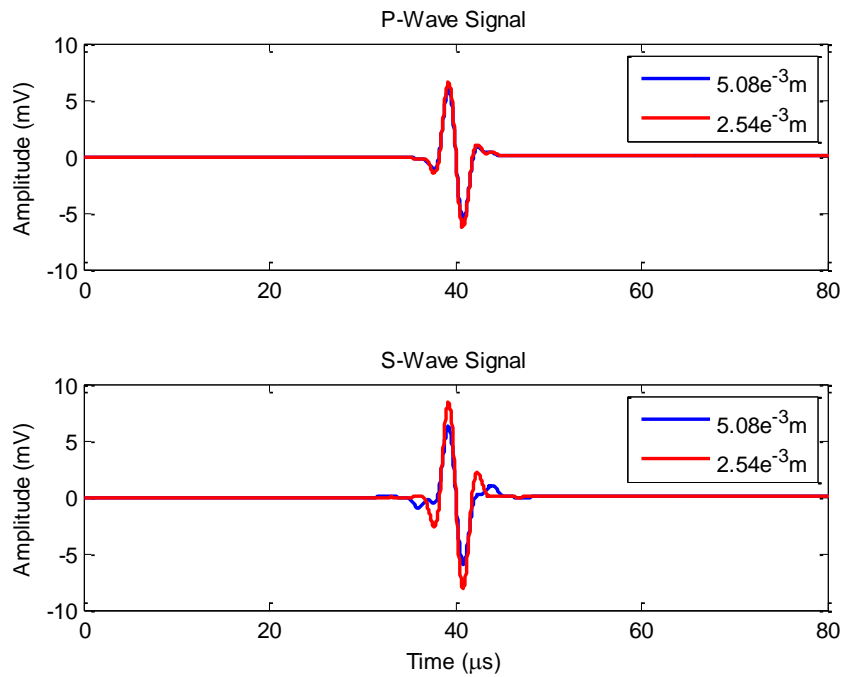
Figure 2.9: The effect of varying Torlon end cap thickness. The impulse response for a thickness of $5.08e^{-3}$ m is shown in blue, and a thickness of $2.54e^{-3}$m is shown in red.

The backing material used in the transducer also has a large affect on the impulse response of the transducer as a whole. Ideally the backing should be a very lossy and

high-impedance material compared to the crystals used to generate the signal. The high impedance will ensure that energy radiated out the back of the crystal is mostly reflected back into the sample. The backing also needs to be very lossy so that any energy that is transmitted into the backing does not reflect off the rear of the backing and adversely affect the signal that is generated. One fairly common procedure for producing high-impedance, lossy backings is to combine tungsten and epoxy in the correct proportions to obtain the desired characteristics. However, this practice poses several difficulties for our system. The first is that the epoxy typically used is not able to withstand elevated temperatures. The second is that we need to match both the P- and S-wave impedances to specific values, which would involve much time-consuming research in order to get the correct ratios and impedances. To overcome these problems we decided to use another approach.

Our approach is to utilize the same piezoelectric material that is used for the crystal as the backing. This way we ensure that the backing has the correct matching impedance for both the P- and S-waves. Figure 2.10 compares the impulse response for three transducers, which are identical except for the backing material employed. It is immediately obvious that the most broadband transducer is the one with the perfectly matched backing of lead metaniobate. It will be easiest to clearly identify the first arrival of this signal given the clear first break on both the P- and S-wave impulse response. It is also apparent that the perfectly matched backing has a lower overall amplitude. This is because the energy leaving the back of the piezoelectric crystal is not reflected back by the backing. Though this is not necessarily desirable, the clean nature of the signal makes up for the loss in amplitude that is suffered.

Also, it is important to keep in mind that the backing is not lossy in any of the three cases presented in Figure 2.10. This means that any energy passed into the backing will reflect off of the rear of the backing and interfere with the desired signal. An easy way to overcome this problem is to ensure that the backing is long enough that the reflected wave will not arrive at the far end of the sample before the first break of the desired signal. Our final design includes this consideration.
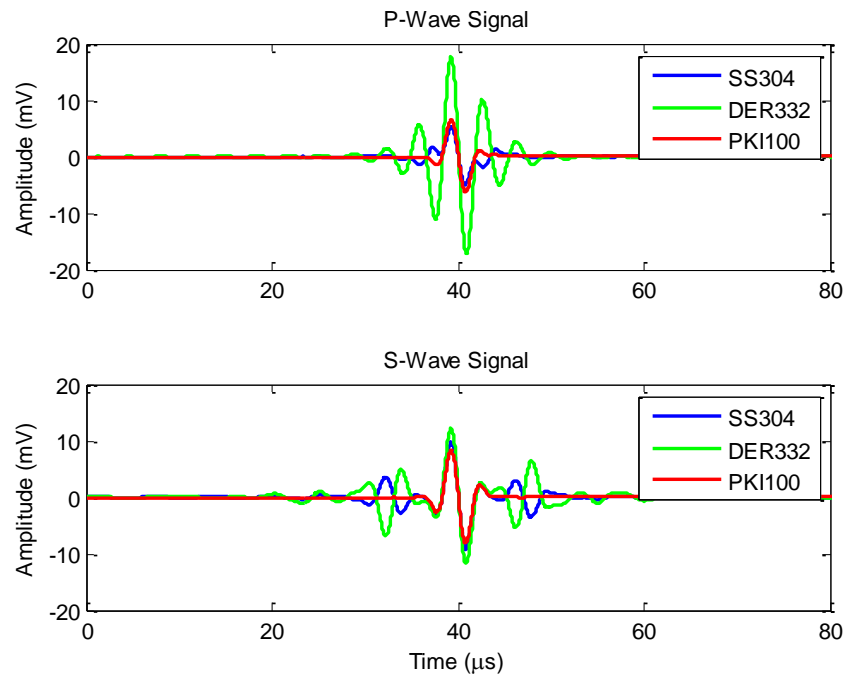
Figure 2.10: The effect of different backing materials on the impulse response of the transducer. The response with a backing of stainless steel is shown in blue, a backing of Dow Epoxy Resin 332 is shown in green, and a lead metaniobate backing is shown in red.

2.5.2 Ultrasonic Transducer Fabrication

The assembly of the transducers was a challenging task, and much care was taken to ensure that the best possible product was produced. Each transducer consisted of a Torlon end cap or matching layer, one S-wave crystal and one P-wave crystal stacked together, copper foil attached to the crystal electrodes to enhance electric coupling and to allow the connection of lead wires, a backing of lead metaniobate, and a silicone rubber spring to compress the entire stack into the end cap. To enhance the mechanical coupling between each element, an extremely thin layer of a rigid, high temperature epoxy was used to bond the elements together (Figure 2.11). The epoxy used was from Epoxies Etc., and consisted of the two-part system of epoxy resin 20-3066 and catalyst 185. This selection was based on the low viscosity of the epoxy before curing, which allows for an extremely thin epoxy layer to be applied, and because of the high temperature resistance and strength of the epoxy after curing.
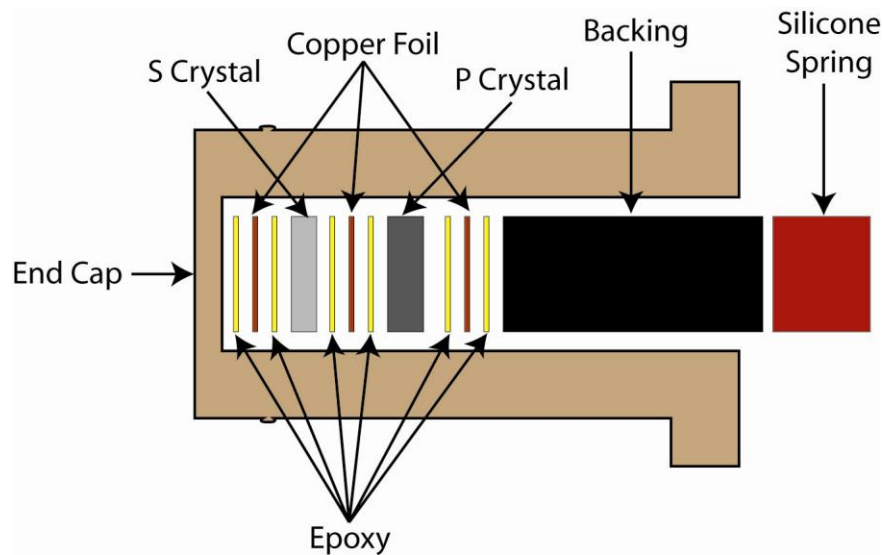
Figure 2.11: The transducer components inside each end cap - note that the drawing is not to scale. The construction method ensures that each epoxy layer at most 1μm thick, and the copper foil is 0.002" thick.

In order to get as thin a layer of epoxy between the components as possible a method similar to that described by Selfridge (1983) was used. In this method, we applied a small amount of epoxy to one of the two pieces to be bonded together, with a small extra amount in the center of the piece. When the pieces being bonded are brought together, the epoxy makes first contact at the center of the two pieces, and pushes outwards, reducing the chances of trapping air bubbles. The pieces are then compressed in a vice with a Teflon base to eliminate sticking, and a rubber spring on the top which is slightly smaller in lateral dimension than the top of the pieces being bonded. This again ensures that when the vice is tightened, the pressure is applied in the central portion of the bond first and pushes outward pushing out any excess epoxy or air bubbles that may have been between the pieces. The entire assembly is then oven cured to the epoxy specifications while still in the vice. This entire process is repeated for each individual epoxy bond in the transducer. By ensuring the thinnest layer of epoxy possible, we avoid any unwanted mechanical interference of the epoxy layer with our generated waves, and also do not adversely affect the electric coupling between the copper foil electrodes and the silver electrodes on the crystals themselves.

To attach the lead wires to the copper foil electrodes, we used a high temperature conductive epoxy, Duralco 120, provided by Cotronics Corp. The high temperature rating and conductivity make the epoxy ideally suited for bonding the lead wires. It was also considered for use to bond the components of the transducers together, but its high viscosity and the large particle size of the silver in it are unsuitable for creating thin bonds between the components of the transducer.

2.6 System Calibration

To ensure that the measurements of samples is correct, the ultrasonic system properties must be fully characterized in the range over which the measurements are going to be made. This includes any changes in the system delay times for P and S waves with temperature and pressure and any variation of the LVDTs output with temperature.

Figure 2.12 shows measurements of the system delay time for both P waves (blue) and S waves (red) over a temperature range from 5 to 190°C. In addition, a best fit line has been plotted for each, which is used to determine the delay time of the system at each given temperature. This delay time can then be subtracted from the measured arrival times to correct for the delay of the system over the entire experimental temperature range.

Of course, there is always a difference between modeled results, and those obtained from real experiments. Figure 2.13 shows the waveforms obtained from pulse transmission experiments using the designed transducers and a one-inch calibration piece of Torlon. There are some marked differences between these results and the modeled waveforms. Many reasons exist for these differences. First off, the modeling included a bitumen layer, which may differ from the actual bitumen tested and have an effect on the obtained results. Secondly, the modeling assumes a simple 1D propagation of waves, whereas with a real transducer we are dealing with 3D propagation. This results in reflected waves from the sides of the transducer components, which lead to the ringing observed after the first initial arrival. The key attribute of Figure 2.13, however, is the first arrival of the P and S waves. We can see

that they are sharp arrivals with large amplitudes, which our modeling has predicted. This shows that even though the modeling may not predict the exact waveforms obtained, it is still a vital step for ensuring a high quality signal under testing conditions.
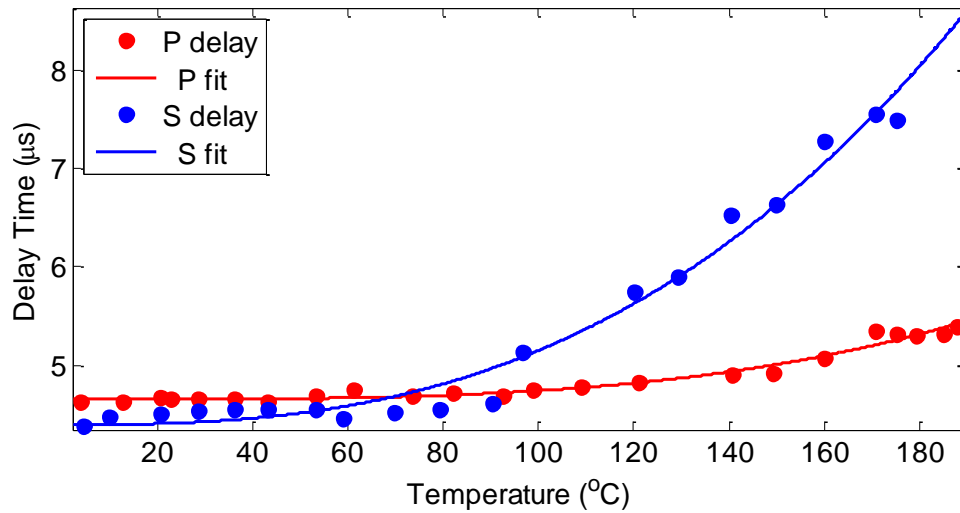
Figure 2.12: Head-to-head calibration of P- and S-wave delay time as a function of temperature.
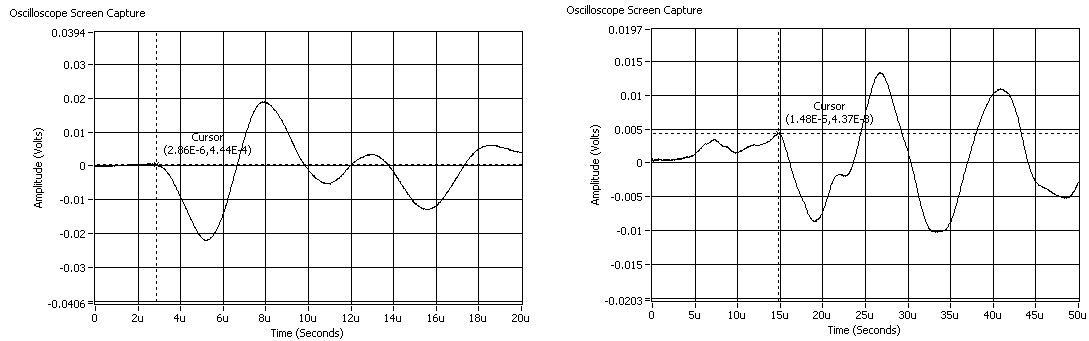
Figure 2.13: P-wave (left) and S-wave (right) signals as obtained through one-inch Torlon calibration piece.

2.7 Ultrasonic Transducer Characteristics

After the ultrasonic transducers were assembled, they were tested head-to-head in order to determine their characteristics. Figure 2.14 shows the P waveform (left) and the associated frequency spectrum (right).
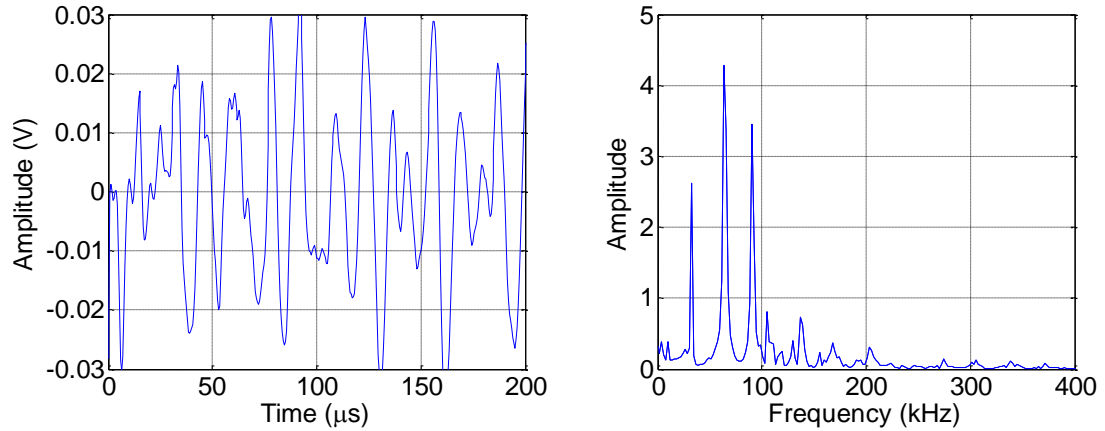
Figure 2.14: Head-to-head P-wave signal (left) and frequency spectrum (right) collected at 1 MPa confining pressure and 20.8°C.

It is commonly observed that the peak signal strength of an assembled transducer is less than that of the individual crystals used in the transducer (Zimmer, 2003); this is true for our transducers as well. Even though the P-wave crystals used operate at a central frequency of 250 kHz, the highest frequency signal received is approximately 90 kHz, with the peak signal strength slightly lower at 65 kHz. Similar results can be seen for the S-wave shown in Figure 2.15. Again, the S-wave crystals used operate at a central frequency of 250 kHz, and the assembled transducer's peak signal strength is approximately 78 kHz. Despite the lower frequency at which the transducers operate, we still maintain a minimum of one wavelength with our samples.

The transducers were also tested using a one-inch-long Torlon sample at 1 MPa confining pressure and room temperature to further determine the transducer characteristics. The sample has a perfect impedance match with the end cap material and should provide further insight into the characteristics of the transducers. Figure 2.16 shows the P-wave received through the Torlon piece, as well as the frequency spectrum. With the Torlon sample between the transducers, the P-wave frequency

spectrum is slightly changed. The same peaks can be seen, but the lower frequency signals are slightly attenuated, and the peak signal is now the one at 90 kHz.
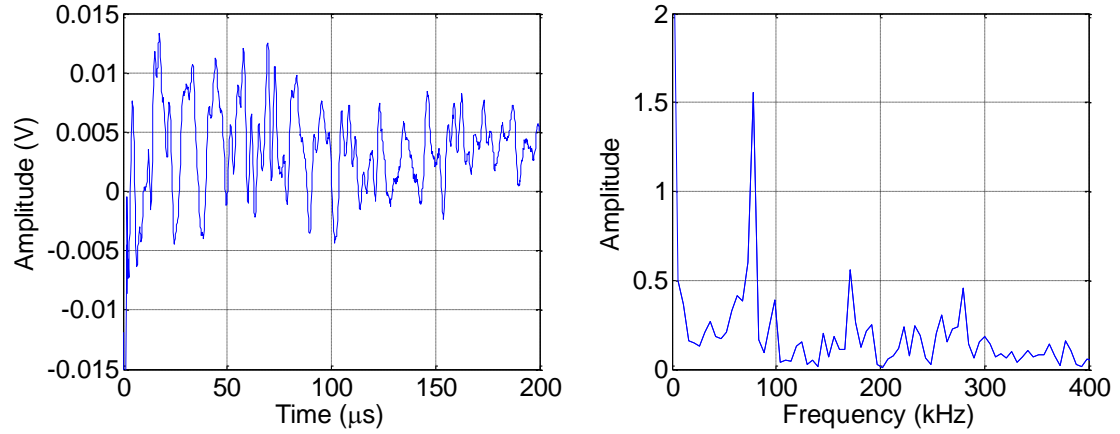
Figure 2.15: Head-to-head S-wave signal (left) and frequency spectrum (right) collected at 1 MPa confining pressure and 20.8°C.
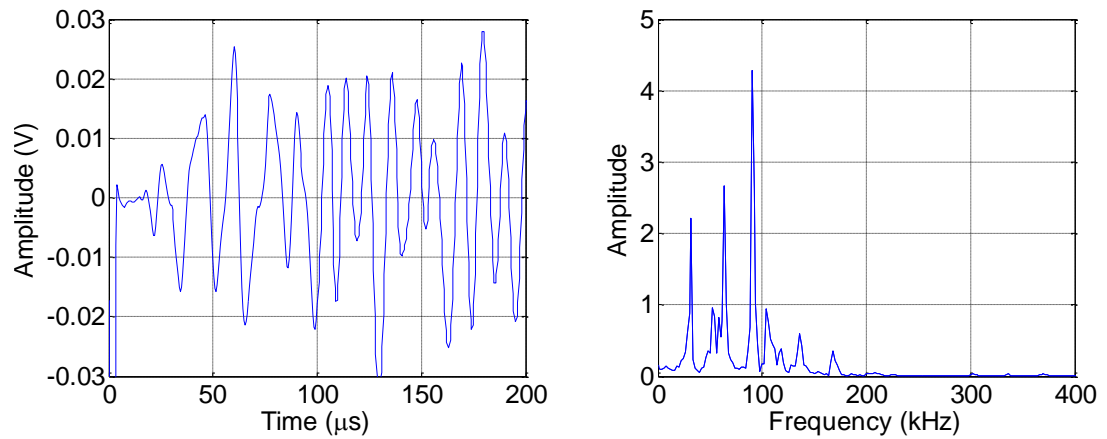
Figure 2.16: Sample P-wave signal and frequency spectra through a one-inch Torlon test piece.

Figure 2.17 shows the S-wave signal and frequency spectra collected at 1 MPa confining pressure and room temperature for the same one-inch Torlon sample. In this case, the peak strength of the signal is further reduced, this time to approximately 65 kHz.
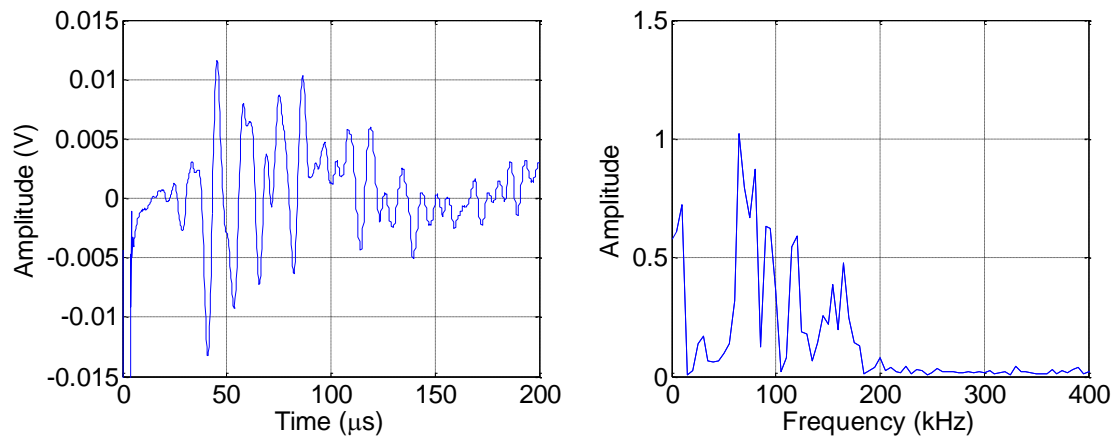
Figure 2.17: Sample S-wave signal and frequency spectra through one inch Torlon test piece.

It should be noted that the attenuation properties of Torlon are not known, and part of the decrease in frequency content of the signals may be due to the one-inch Torlon sample.

2.8 Insights from Experimental Equipment Design

The original design of the transducers and ultrasonic system as outlined previously was found to be lacking in certain respects, and as such was further modified based on the outcome of the first few sets of tests. Figure 2.18 shows a picture of the end of the original transducer design before (left) and after (right) testing.

Figure 2.18: Photograph of original transducer design before (left) and after testing (right). Note that the transducer has collapsed into the hollow back where the crystals are mounted.

From examining the damage observed after running tests with the original transducer design it was apparent that the transducers were not strong enough to withstand the temperatures and pressures they were exposed to. The transducers collapsed where the Torlon was thinnest – where the end cap was hollowed out to allow the crystals to be mounted.

To remedy this problem and make the transducer stronger, the design was modified. Instead of leaving the cavity inside the end cap vacant except for the crystals, a high temperature rigid epoxy was used to backfill the end cap. The epoxy was added so that it completely covered the crystal stack and backing, as shown in Figure 2.19.
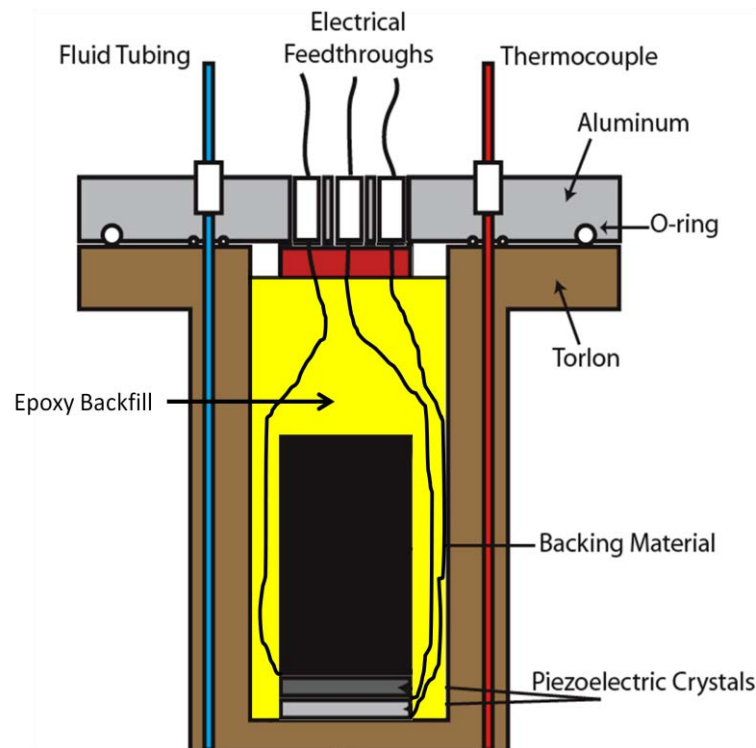
Figure 2.19: Modified transducer design including epoxy backfill inside the transducer to increase transducer strength and resist damage.

Backfilling the cavities of the transducers not only strengthened the transducers, but it also had another unexpected benefit. Once the new transducers were fabricated,

the signals through a one-inch Torlon calibration piece were compared with the signals from the original transducer design (Figure 2.20).
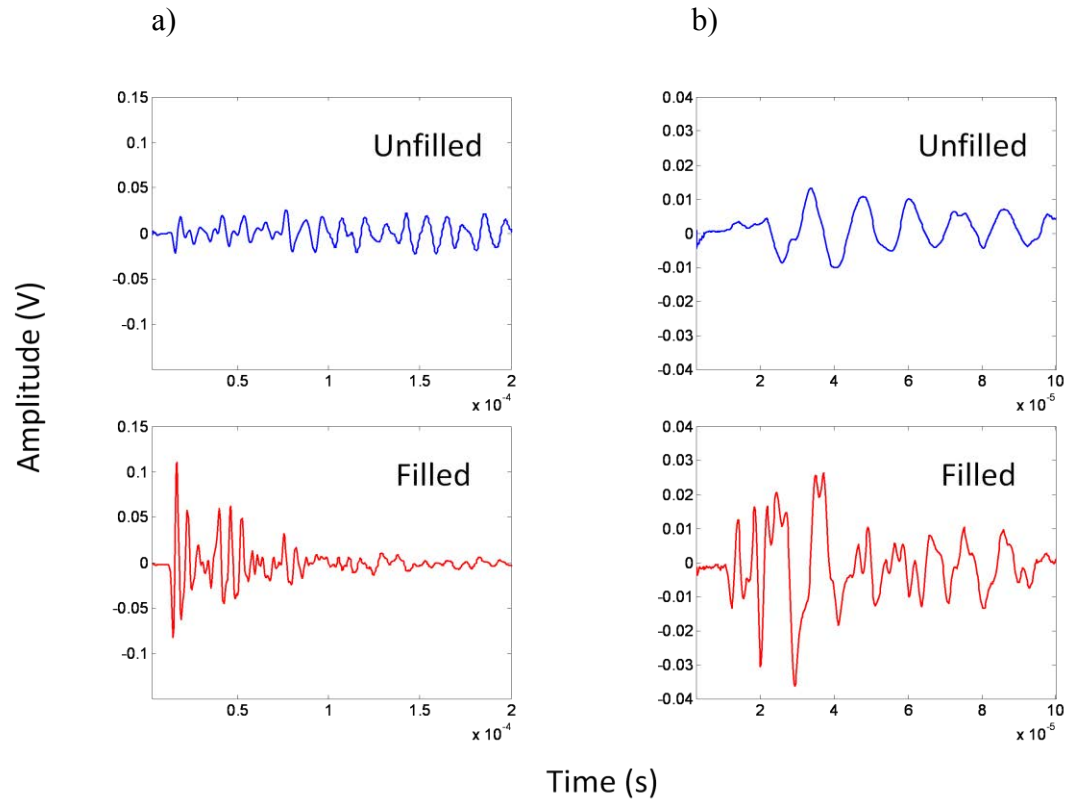
Figure 2.20: Signals through a one-inch Torlon calibration piece with the original transducer design (blue) and with the modified transducer design (red). a) P-waveforms and b) S-waveforms.

By backfilling the transducers the amplitude of the signals received is dramatically increased for both the P- and S-waves. This increased amplitude means that there will be more energy available to transmit through the bitumen sand samples, an increase in the signal to noise ratio of the signals, and more accurate travel-time picks, and in return, more accurate velocity estimates.

Armed with the new, stronger transducer design, we proceeded to test bitumen sands. One sample was successfully tested; however, in testing a second sample, the transducer again suffered damage similar to that suffered by the original transducer design. However, the collapse of the transducer was not as pronounced with the new design (Figure 2.21). It was also noted that there was much more surface damage to the face of the transducer than there was in the first failure. The majority of the

damage to the first transducer was limited to the central collapse of the endcap. In the second transducer, the collapse was not as pronounced, indicating that the strengthening of the transducer was effective. However, despite the increased strength, there were numerous fractures and impressions in the face of the endcap, as can be seen in Figure 2.21. In this case, the damage extended completely to the outside edges of the transducers and was not limited to the central area of the transducer where the crystals are located. This means that even the solid Torlon around the outside edge of the transducer was not strong enough.

Figure 2.21: Photograph of modified transducer design before (left) and after testing (right). Note that numerous fractures and impressions on the face of the transducer after testing. In particular, there is a pronounced fracture running vertically in the picture that is oozing black bitumen.

Given the state of the modified transducer after testing, we originally thought that the design was still not strong enough to withstand the experimental conditions. In order to remedy this, we further strengthened and protected the surface of the endcap, by affixing a steel plate of thickness 1mm to the end of the transducer using an extremely thin layer of high temperature silicone rubber. To ensure a thin layer, a small amount of silicone was applied to the end of the transducer, the endcap was applied, and the silicone was allowed to cure under applied pressure to extrude excess

silicone from between the faces. A photograph of the modified transducer with the steel plate adhered to it is shown in Figure 2.22.
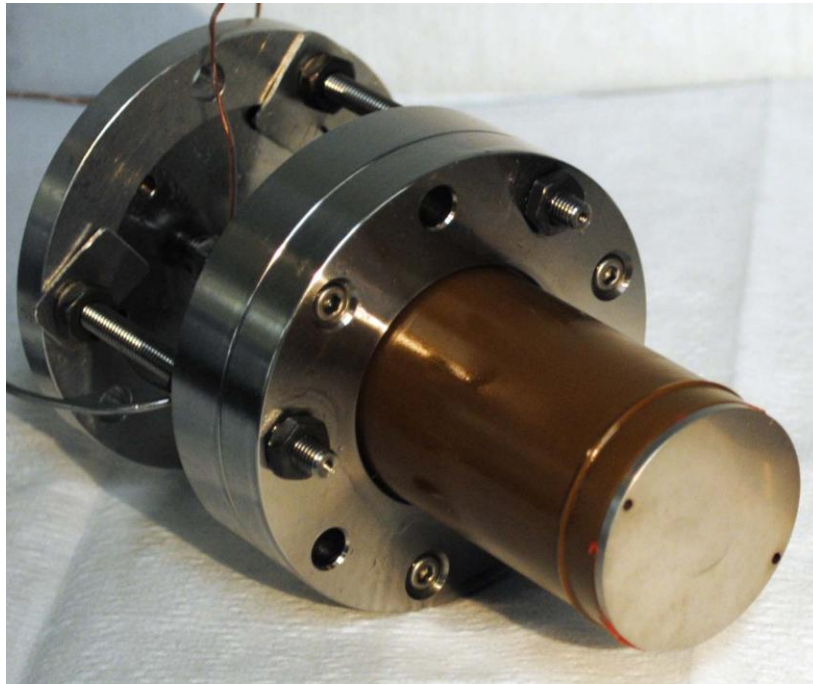
Figure 2.22: Photograph of the modified transducer with the 1mm thick steel plate adhered to the end of the transducer. Also visible is some of the silicone adhesive extruded from between the endcap face and steel plate (orange).

With the steel plate in place, testing continued. However, after a few samples were tested, it became apparent that the amplitude of the signals received through the bitumen sand samples was being adversely affected. The amplitude of the signals received was drastically reduced once the steel plates were added to the ends of the transducers. Figure 2.23 shows the amplitude of P and S waves received for several different samples. Samples S5, S8, S1 and S4 were all tested with the steel plates in place, and the other samples were tested without the steel plates in place. It is immediately apparent that the samples that were tested with the steel plates have much lower amplitude signals than the samples tested without the steel plates. This is especially true for the shear-wave amplitudes. The diminished amplitudes make it much more difficult to accurately pick the first arrivals of the waves from the background noise.

We decided that the added protection offered by the steel plates was not worth the sacrifice in signal quality. In addition, after examining the sample that damaged the epoxy-reinforced transducer, we found that the damage may have been due to heterogeneity within the sample that was being tested.

a)   b)
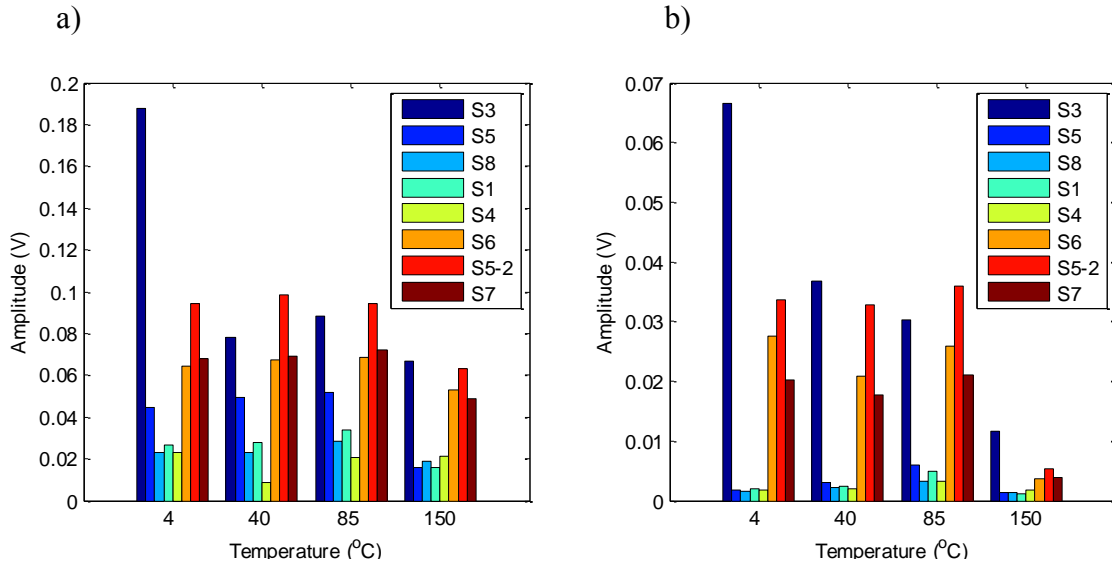
Figure 2.23: Received amplitudes for a) P-waves and b) S-waves for samples tested both with and without steel plates attached to the transducer faces. Samples S5, S8, S1 and S4 were tested with steel plates. Samples S3, S6, S5-2 and S7 were tested without steel plates attached to the transducers.

Upon closer inspection it appears that one face of the sample contained large pyrite clasts that were directly in contact with the transducer face. On the transducer face there are distinct impressions and indentations which correspond to the shape and location of the pyrite clasts on the end of the sample (Figure 2.24), and the large fracture that travels across the transducer face aligns directly with the edge of the largest pyrite piece. We think that if the pyrite had not been present, the transducer would not have been damaged. This is supported by the fact that the transducer that was in contact with the other end of the sample (which did not have any pyrite present) did not suffer any damage. Since the signal quality is vastly superior without the steel plates in place, and the damage is most likely due to the sample that was being tested, it was decided to continue testing without the steel plates in place. However, to

prevent further damage to the transducers, we reduced the maximum experimental temperature to 150°C, and we used fewer steps to cover the same pressure range.
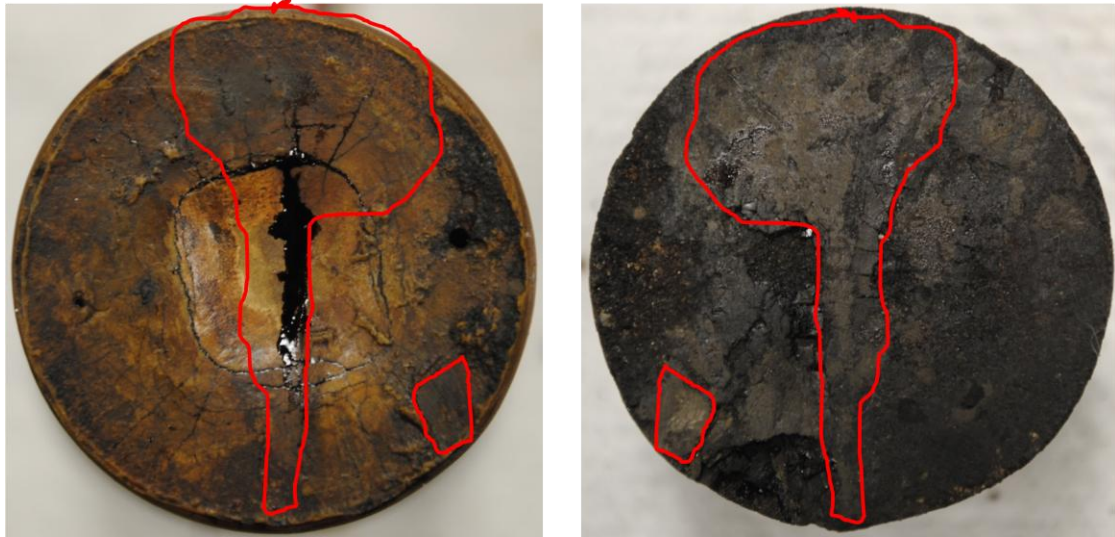
Figure 2.24: Photographs of the Torlon endcap (left) and end of sample S3(right) with pyrite. Note that the pyrite outlined on the sample can be re-aligned with the transducer due to impressions in the Torlon. The main fracture in the end cap aligns with the edge of the pyrite clast.

Fortunately, one sample was large enough that we could cut it into two samples and test one half with transducers with steel plates attached and the other half with the same transducers with the plates removed. This allowed the comparison of signal amplitudes on samples that were very similar—as similar as can be expected for samples of this type—and the differences in observed amplitudes can be attributed to the presence of the steel plate and not to differences between the samples. Also, the modeling performed during the design of the transducers allows for the comparison of signal amplitudes with Torlon and steel transducers, and use that as an analog to compare with the Torlon transducers with and without steel plates.

Figure 2.25 shows the amplitude of the received signals predicted by modeling for both Torlon (in red) transducers and stainless steel (in blue) transducers for both cold and hot conditions. It is clearly evident that the Torlon transducers transfer much more energy through the bitumen sand samples because of the better impedance match, regardless of the temperature. With the steel transducers, the P-wave energy is reduced

by an average of 67%, and the effect is even more pronounced for S-waves, where the energy is reduced by 84%.

a)   b)
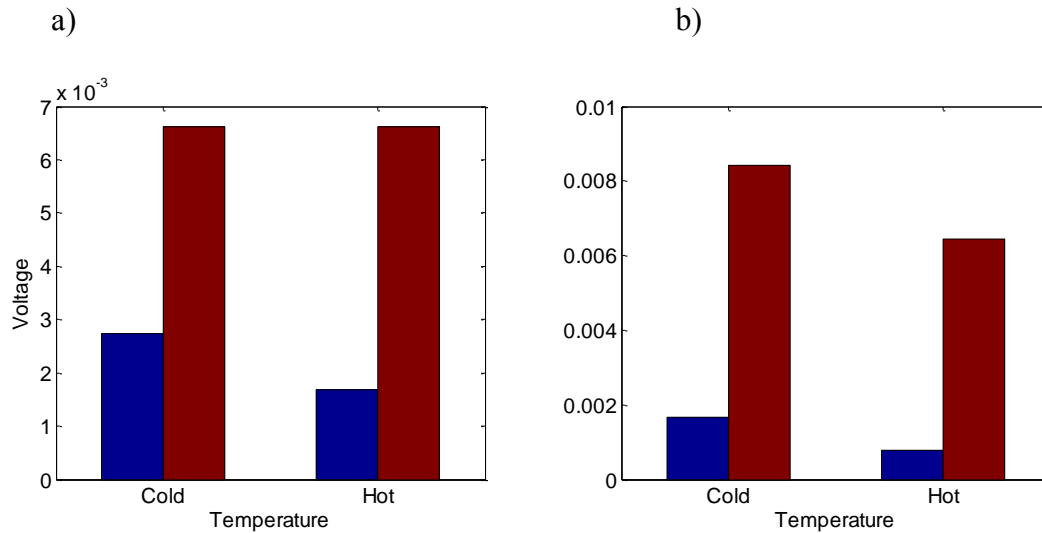
Figure 2.25: Comparison of modeled amplitudes for steel transducers (blue) and Torlon transducers (red). Amplitudes are shown for both a) P-waves and b) S-waves at cold and hot temperatures.

If we compare these results to the measurements made with the two halves of sample S5, we see similar results. Figure 2.26 shows the recorded amplitudes over a wide temperature range spanning from 4 to 150°C. As the modeling predicts, we see a dramatic decrease in the energy received when using the steel plates as compared to the better matched Torlon end caps alone. In fact, the average energy loss for S-waves is even greater than the modeling predicts. On average, the P-wave energy is reduced by 58%, and the S-wave energy is reduced by 90%. These values are in fairly good agreement with the modeling results.

It is true that some of the energy differences may be due to differences between the two samples tested; however, given that they were immediately adjacent to one another before being cut apart, they should be fairly similar in nature. This shows that the modeling and design of the transducers was likely not in vain, and has resulted in substantially more energy being transmitted through the samples because of the use of impedance matched transducers.

a)   b)
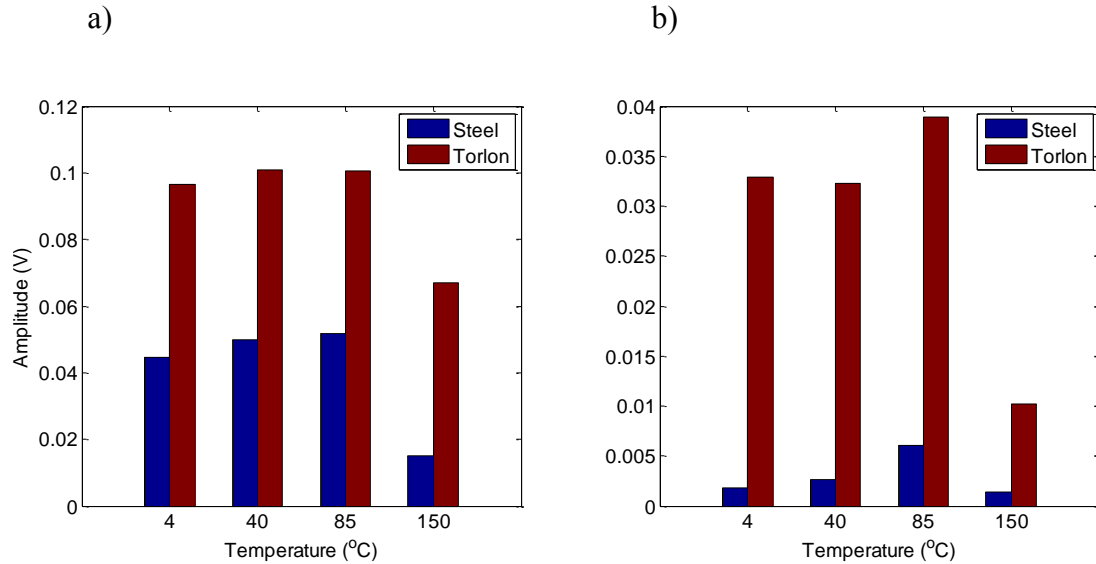
Figure 2.26: Measured (a) P-wave amplitudes, and (b) S-wave amplitudes measured for two halves of sample S5. Note the large reduction in amplitudes received when using steel plates on the transducers instead of the Torlon alone.

The amount of energy received provides good insight into the effect of the impedance match on the signals, but even more enlightening is examining the received signals themselves. Figure 2.27 shows the recorded P-waveforms (upper row) and S-waveforms (lower row) for temperatures of 4, 40, 85 and 150°C (increasing left to right). In order to obtain accurate velocity estimates it is imperative that the first arrival of the waveforms can be identified. For P-waves, despite the differences in amplitude, it is still possible to identify the first arrival of the P-waves both with and without the steel plates attached to the ends of the transducers. However, for S-waves this is not the case. Unfortunately it is impossible to record S-waveforms without some early arriving converted P-wave energy interfering with the first arrival of the S-waves. This is why it is vitally important that the energy of the shear wave arrivals is as high as possible. When looking at the S-wave arrivals with the steel plates in place (Figure 2.27, lower row, blue waveforms) it is extremely difficult to identify the shear wave in general, let alone the first arrival of the wave. In contrast, for the Torlon endcaps (red waveforms) the shear wave is easily identifiable, and the first arrival can be picked with confidence.
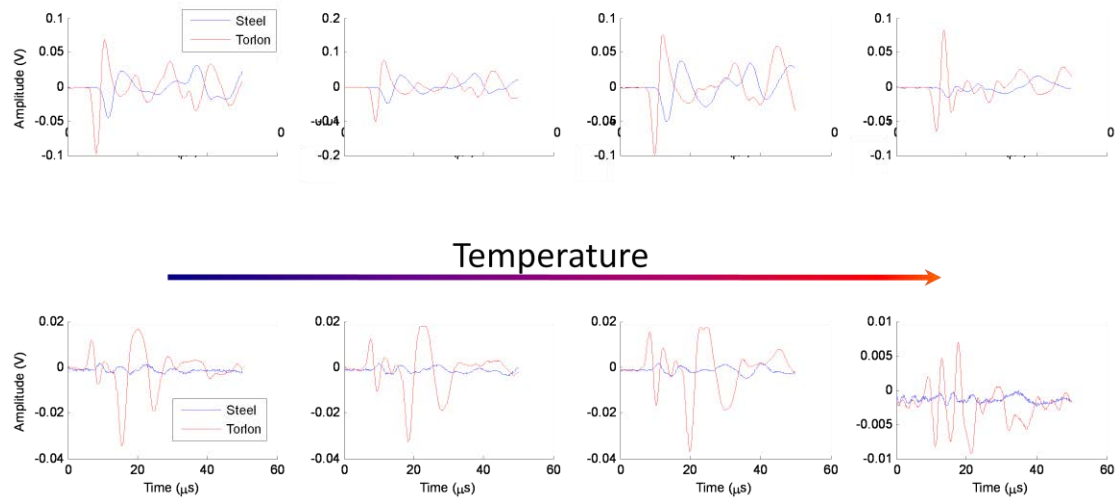
Figure 2.27: Comparison of waveforms recorded for two halves of sample S5 recorded with steel plates on the transducers (blue) and without (red). The upper row shows the P-waveforms and the lower row shows the S-waveforms. Temperatures increases from left to right from 4°C, 40°C, 85°C to 150°C.

It cannot be stressed enough that the robustness of any velocity estimates from pulse transmission experiments such as these is dependent upon accurate first arrival picks. By impedance-matching the transducers, we ensure that maximum energy can be transmitted through the samples, and by backfilling the transducer cavities with epoxy we again increased the amplitude of signals, which will result in more robust velocity estimates.

2.9 Discussion and Conclusions

The design and fabrication of a high-temperature and high-pressure ultrasonic pulse transmission apparatus is not straightforward. The main difficulties are in finding the appropriate compromise between components and performance that will allow the measurements of interest to be made. The high-temperature and high-pressure ultrasonic system we have designed and built has overcome many problems encountered with this type of system. By utilizing LVDTs for our strain measurements, and custom-designed lead metaniobate piezoelectric crystals for mechanical pulse generation, by selecting appropriate feedthroughs into the pressure vessel, and by avoiding wire cross-talk as much as possible, we have achieved the best compromise between temperature and pressure ratings. The resulting system is capable of

generating P-wave and S-wave signals with peak signal strengths at 90 and 78 kHz respectively, at temperatures up to 200°C and pressures up to 35 MPa.

As is evident from the preceding discussion, much thought and planning has gone into building the most effective piezoelectric transducers possible for carrying out ultrasonic pulse transmission experiments on bitumen sands at high temperatures. This planning, though time-consuming, ensures that we obtain the cleanest and largest possible signal through our samples, which will result in accurate first arrival picking and robust velocity estimates.

With this system, we can make measurements on soft sediments, such as bitumen sands, at temperatures and pressures that were not previously possible. With this dataset it will be possible to develop, test and calibrate rock-physics models for use with bitumen sands. These models will allow for better characterization and production monitoring of bitumen and heavy oil reservoirs.

Chapter 3

Ultrasonic properties of bitumen-saturated sands as a function of temperature and pressure

—An experiment is a question which science poses to Nature, and a measurement is the recording of Nature's answer."

~Max Planck

3.1 Abstract

Measurements for sand saturated with bitumen and heavy oil are needed in order to develop reliable, robust rock-physics models. In recent years, studies have started to be published on the properties of these reservoir materials and how the properties change under various conditions, including some preliminary studies that we conducted using equipment at the Colorado School of Mines. The limitations of the equipment used for these preliminary measurements and the need for a reliable dataset

of bitumen sand properties inspired us to try to develop a system at Stanford that can better measure the properties of these materials. Therefore, we designed and built a high-temperature and high-pressure ultrasonic pulse-transmission system that could measure the properties of bitumen and heavy-oil sands using methods and conditions not previously possible. Our system incorporates low-impedance end-caps, that better match the impedance of the samples, yielding more reliable signals and velocity estimates.

In this chapter, we present the results from both the preliminary measurements and the measurements made on the newly designed system at Stanford. The results show an expected trend in P-wave velocity with temperature change where the velocities decrease with increasing temperature up to the upper temperature limit of the experiment. However, there are unexpected results regarding the S-wave velocities. The S-wave velocities were expected to initially drop with temperature increase, and then stabilize as the temperature became higher than approximately sixty to eighty degrees Celsius. However, our experiments show that the S-wave velocity continues to drop as the temperature rises above these temperatures. This phenomenon is not well understood at this time; however it may be due to an extremely heavy fraction of the bitumen having a very high glass point, such that it continues to act as cement between grains at high temperatures. Another possible explanation is that the frame of the sample is being altered in some way as the sample continues to be heated.

3.2 Introduction

Bitumen and heavy-oil reservoirs make up a substantial fraction of worldwide petroleum reserves. Recently, there has been great interest in measuring the properties of heavy oils and heavy-oil sands in the lab as a function of temperature, in order to better understand seismic responses during thermal productions methods (Han et al. 2007; Han, Yao, and Zhao 2007; Han, Liu, and Michael Batzle 2006; Michael Batzle, Hofmann, and Han 2006; Behura et al. 2007). These measurements are a good start towards describing heavy-oil and bitumen sand behavior, but more research is still needed. In particular there is a dearth of shear wave velocity measurements which are

crucial for overcoming the ambiguities in the inversion for rock properties derived from P-wave data alone. To this end, we have designed and built an ultrasonic pulse-transmission apparatus that can acquire signals over a wider temperature range than the previously reported results. In addition, a significant improvement in our system is that we utilize impedance-matched end-caps ,which improve the recorded signal quality and result in more accurate velocity estimates.

3.3 Preliminary Measurements

Our preliminary measurements consisted of measuring a sample of bitumen without sand in it, as well as two core samples from a unconsolidated bitumen sand reservoir. The temperature range of the experiments was from -20°C to 60°C, and the pressure ranged from 2.07 to 8.27MPa. The purpose was to understand how the properties of the bitumen and bitumen-sand mixture change with varying temperature and pressure, and to learn more about the challenges involved in performing pulse-transmission experiments to determine P and S wave velocities in bitumen sand.

3.3.1 Bitumen Measurements

A pure bitumen sample was not available for testing; however, a direct sample of a well-head emulsion was available. After centrifuging the emulsion for 2 hours at 5000 RPM and approximately 70°C to remove the water, a suitable sample was obtained, from which we estimate the remaining water to comprise about 10% of the sample by visual means.

The bitumen sample was jacketed between 2 aluminum transducers, with a thermocouple mounted on the outside of the sample jacket to monitor temperature. The whole assembly was placed in a freezer at -21°C. It was then wrapped in insulation to allow for a slow, uniform temperature increase throughout the sample during heating (Figure 3.1). Compressional- and shear-wave measurements were taken approximately every 5 degrees. At each measurement the length of the sample was measured by a linear potentiometer in an attempt to monitor the thermal expansion of the sample.

Figure 3.2 shows the compressional-wave velocity as a function of temperature. The most noticeable features of the plot are the two distinct domains where the velocity changes at different rates. This is interpreted to be due to the presence of water in the bitumen sample. At low temperatures ($<0^{o}$C), when the water is frozen, velocity has a higher dependence on temperature. After the water melts, the observed temperature dependence is due to the changing properties of the bitumen, such as modulus, density and viscosity. The reason that the change in slope is not observed at 0°C is due to the sample not thawing uniformly, and because the temperature reading is from within the sample jacket, and not directly from the sample.
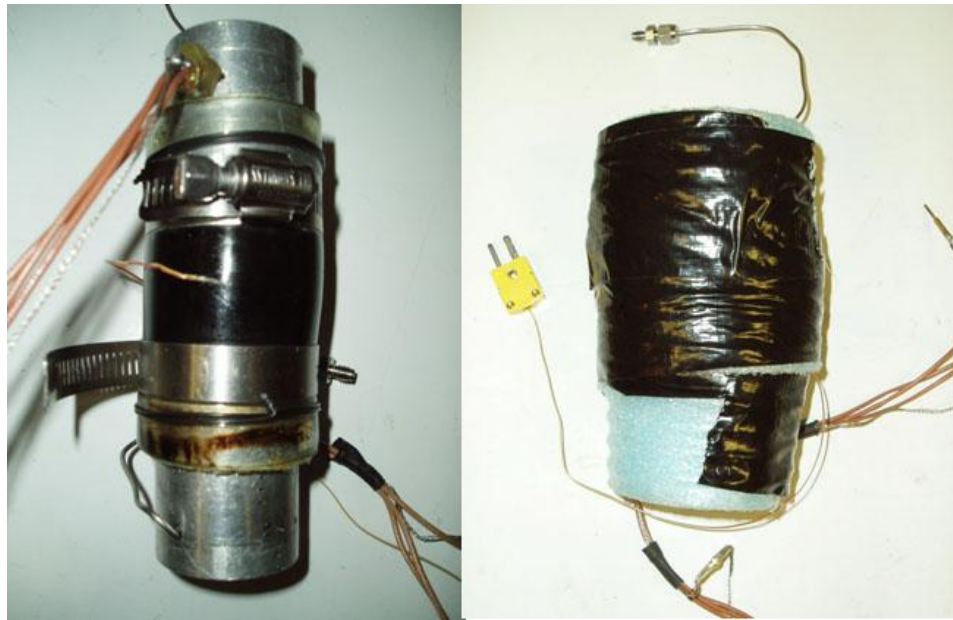
Figure 3.1: System set-up for bitumen measurements. Left: jacketed bitumen sample and aluminum transducers. Right: insulated assembly to allow for uniform temperature increase.

Figure 3.3 shows the shear-wave velocity as a function of temperature. Unfortunately during the time of the experiment, impedance-matched transducers were not available. The aluminum transducers used for these measurements have a high impedance contrast with the oil. This leads to a very noisy signal containing contamination from converted P-waves. In addition, the bitumen viscosity decreases dramatically as it is heated, which limits the ability of a shear-wave to propagate through the oil. In fact, the shear-wave amplitude reduces to background noise levels

once the temperature reaches 5°C. These two factors combined make it very difficult to pick the first arrival of the shear-wave with high confidence.
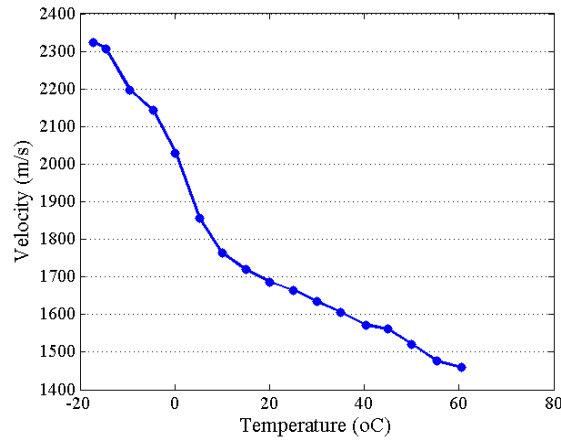
Figure 3.2: P-wave velocity as a function of temperature in the bitumen sample. The steeper slope at lower temperatures (<0°C) is thought to be due to the presence of ice in the sample.
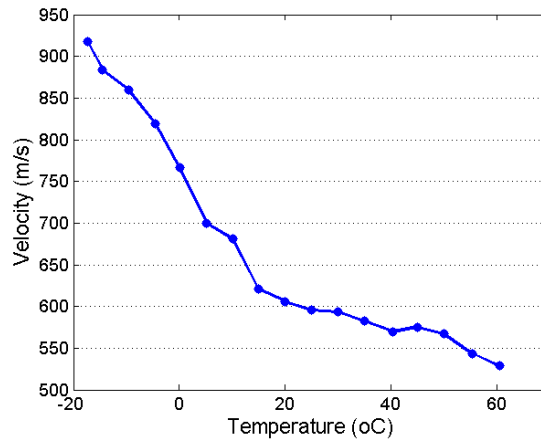
Figure 3.3: S-wave velocity as a function of temperature in the bitumen sample. The steeper slope at lower temperatures is thought to be due to the presence of frozen water in the sample.

Figure 3.4 shows the V_P/V_S ratio as a function of temperature. At low temperatures, the V_P/V_S ratio is 2.53, and as the temperature is increased, the V_P/V_S ratio increases to 2.76. This is expected because the bitumen becomes less viscous as the temperature increases, so the V_P/V_S ratio should increase. This lends some credibility to the first arrival picks of the shear waves. Comparing the data collected in this experiment with previous measurements of heavy oil (Batzle et al., 2004) also supports the validity of

the data collected. Figure 3.5a shows the calculated bulk and shear moduli from this experiment, and Figure 3.5b shows the data from Batzle et al. (2004) for comparison. The most striking difference between the two plots is again the change of slope at lower temperatures, but this is attributed to the presence of frozen water within the sample. A second major difference is the magnitude of the moduli observed at each temperature. The moduli presented by Batzle et al. (2004) were measured from heavier oil than was used in this experiment, and as a result, should have a higher modulus because the oil was denser and more viscous. The encouraging result from comparing these two plots comes from the fact that the slopes of the lines are approximately the same at temperatures above 0°C.
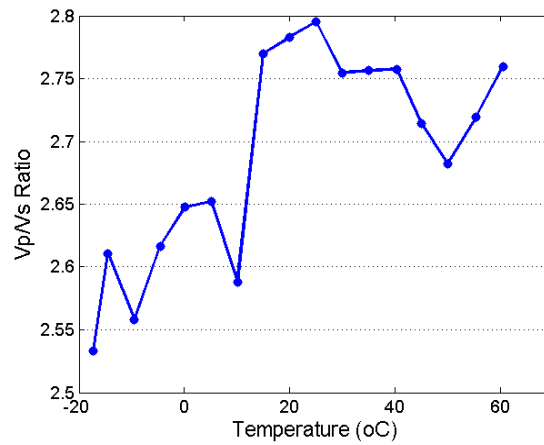
Figure 3.4: V_P / V_S ratio as a function of temperature for the bitumen sample. At low temperatures (<10°C) the V_P / V_S ratio is low, and it increases with temperature, indicating that the sample becomes more fluid.
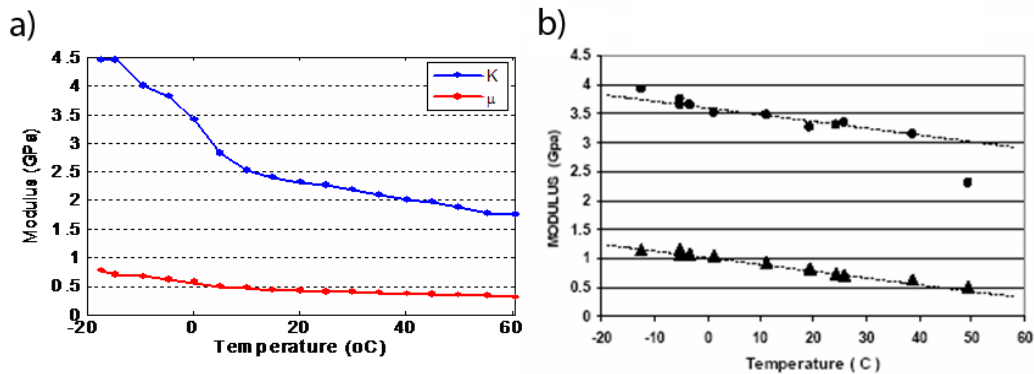
Figure 3.5: a) Bulk and shear modulus as a function of temperature for the bitumen sample from this experiment, b) bulk and shear modulus of a heavier oil measured by Batzle et al. (2004).

3.3.2 Bitumen Core Plug Measurements

Two core plugs from a bitumen reservoir in Canada were tested. The samples come from the same reservoir where the emulsion sample was obtained. The core plugs were both fine-to-medium-grained consolidated sand. Both samples consist of >90% quartz, with minor amounts of feldspar, and trace amounts of clay, mica, volcanic and metamorphic lithics, pyrite and carbonaceous material. The samples contain volumetrically insignificant amounts of cement. The total porosity of the samples is 39.5%, and the bitumen saturation is approximately 87% from core plug measurements made on like samples.

Sample preparation consisted of cutting the frozen core to a desired length, and placing it between two epoxy transducers. The samples were surrounded by two layers of filter paper and a fine metal screen to prevent sand from leaving the sample. This was then sealed within two layers of Teflon shrink wrap (Figure 3.6). The assembly was first frozen to a temperature of $-21^{\circ}C$, the hydraulic oil was cooled in the freezer to $-21^{\circ}C$, and the pressure vessel was cooled as much as possible by surrounding it with dry ice. The length change of the sample was monitored by a resistor mounted to the transducers, and the temperature was monitored by a thermistor that was attached to the outside of the Teflon shrink wrap.

For P- and S-wave measurements, the pulse transmission technique was used. The experimental set-up consisted of a pressure vessel with confining pressure maintained and adjusted by the addition/removal of hydraulic oil. Pore pressure was controlled by the addition/removal of a 10,000 ppm NaCl solution. The epoxy transducers used for this experiment have lower impedance values than the aluminum transducers used. Thus, the impedance contrast between the core plugs and the transducers is much smaller than in the previous experiment. Consequently, less noise was recorded in the waveforms for this experiment.

Once the sample was in the pressure vessel, measurements at each temperature step were made at effective pressures of 2.07, 5.52, 8.27, 6.89, 5.52, 4.14, 3.45, and 2.07 MPa. Measurements were made without the addition of pore fluid up to a temperature of $\sim 0^{\circ}C$, at which time the NaCl solution was added and pressurized to

2.07 MPa. This was done in order to avoid freezing the pore fluid within the pore fluid tubing at sub-zero temperatures. Once the pore fluid was injected into the sample, the filter paper became water wet, and this condition prevented the bitumen from leaving the sample.

Figure 3.6: Sample preparation for the core sample from a bitumen reservoir. The sample is mounted between two impedance matched transducers, and covered by filter paper, a fine metal screen, and two layers of Teflon shrink wrap.

Core Plug Results

The results from the two cores that were tested are very similar. Therefore, only the results for one of the cores will be shown, even though the results and conclusions hold for both. Figure 3.7 shows the compressional-wave velocity as a function of pressure and temperature. Each colored line corresponds to measurements made at a different temperature, as indicated in the legend. This figure shows that as the temperature increases, the compressional velocity of the bitumen-sand mixture decreases. It can also be seen that as the effective pressure increases, the P-wave velocity of the sample increases. The sensitivity of the velocity to pressure appears to be fairly uniform over the temperature range investigated, indicated by the approximately equal slope of each temperature line. Also, there appears to be little to no hysteresis effect on the sample; the increasing and decreasing pressure trends tend to follow the same path. One deviation from this can be observed for the blue curve corresponding to ~0°C and a pore pressure of 0 MPa. For this curve, the initial velocity measurement at 2.07 MPa is 2982 m/s. After the sample has been pressurized and brought back to 2.07 MPa, the velocity is 2355 m/s. The endpoints of this curve differ by approximately 600m/s for the same effective pressure. It is important to

consider, however, that the temperature rose from -1.5 to 1.1^{o}C over the time span in which the measurements were made. The reason for the velocity difference is attributed to ice within the sample thawing between the two measurements. In addition, it is observed that the subsequent two measurements, again at ~0°C, and then at ~10°C have a higher P-wave velocity than the first measurement made at ~0°C and 2.07 MPa. This is attributed to the pore fluid that was injected once the sample was above freezing temperatures. The injected pore fluid fills the empty pore space in the sample and increases the P-wave velocity. Comparing this to Figure 3.8 further supports this hypothesis.
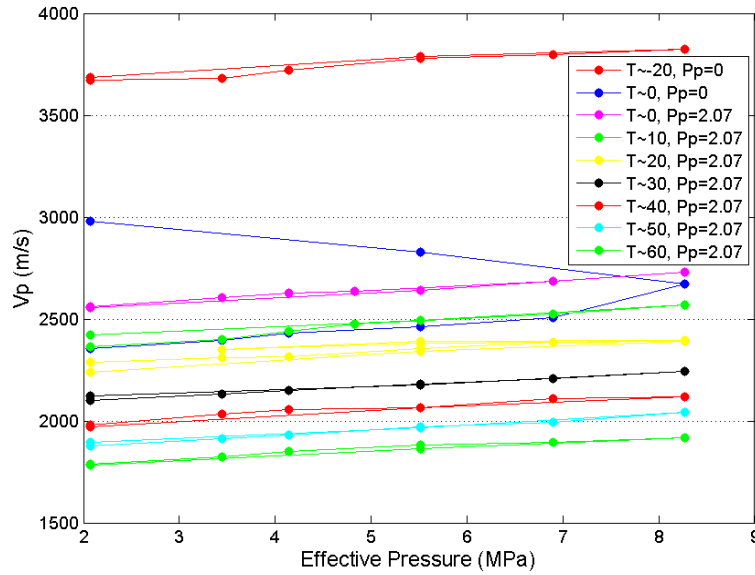
Figure 3.7: P-wave velocity as a function of temperature and pressure for one bitumen sand sample. Note the jump in V_P (pink curve) as the pore-fluid pressure is increased due to the addition of water to the sample.

Figure 3.8 shows the S-wave velocity as a function of pressure and temperature. It can be seen that the addition of the pore fluid has no effect on the S-wave velocities, since the shear wave velocity in water is zero. As the temperature increases, the overall effect is the lowering of the shear-wave velocity. There appears to be little to no hysteresis effect displayed in the shear-wave data, except where the samples undergo thawing. At this stage the rigidity of the sample decreases as the ice turns to water. It can also be seen that the shear-wave velocity is more sensitive to pressure

changes at higher temperatures than it is at low temperatures. This is indicated by the steeper slopes observed at higher temperatures. For temperatures greater than 20°C, increasing the effective pressure from 2.07 to 8.27 MPa increases V_P by ~200 m/s. However, at low temperatures the pressure increase results in a change in V_P of ~100 m/s.
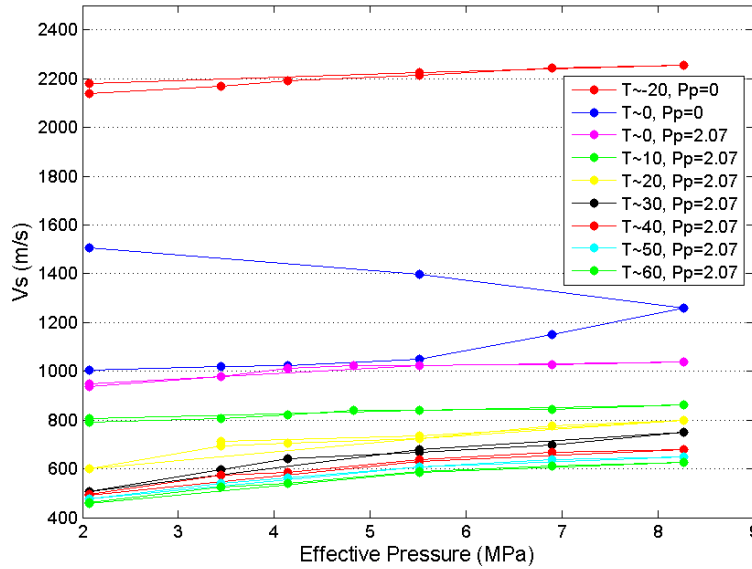
Figure 3.8: S-wave velocity as a function of temperature and pressure for one bitumen sand sample. Note that the addition of pore fluid has no effect on the shear-wave velocity.

Though these measurements did provide us with some data points, the most valuable learning from them was to understand the difficulty of making measurements in these types of materials. The measurements made here were extremely limited in their temperature range, and the quality of the signals, particularly when using the aluminum transducers, was very suspect. After performing these measurements, we were aware of the need for a system that could effectively measure the properties of bitumen sands, and we designed and built the system described in the previous chapter.

3.4 Stanford Bitumen Sand Measurements

There were 8 different samples tested on the newly designed and built ultrasonic system at Stanford. Shell provided these samples, which displayed extreme heterogeneity, even though they were all retrieved from the same well drilled into a

bitumen reservoir in Canada. The majority of samples were tested over a range of effective pressures ranging from 2 to 8 MPa, and temperatures from 4 to 150°C, with two of the samples being measured at a maximum temperature of 180°C.

The samples were been stored in a -80°C freezer to preserve the core and ensure that they remain in a condition as close to in-situ as possible. To prepare samples for testing, we cut them to a length of just over 1 inch (typically ~1.1") while still frozen. We then measured the length, diameter and weight of the samples, loaded them into the core holder, and jacketed them with Viton rubber tubing.

The core holder was then placed into the pressure vessel, which was initially pressurized to 4 MPa, at which time the pore fluid was introduced into the system. The pore fluid, water in this case, was introduced from only one end of the sample, at a pressure of 2 MPa. The other end of the sample remained closed, and the pore pressure was monitored at both ends of the sample. The pressure at the open end of the sample was maintained at 2 MPa so that the pore fluid would have to flow through and saturate the sample fully to equilibrate the pressure at both ends of the sample. The sample was left overnight to allow the pore pressure to equilibrate, and for most samples this happened relatively quickly. For a few samples, the permeability was such pressures did not equilibrate overnight; in these samples, the pore fluid was injected from both ends after the initial overnight period. During testing, the pore pressure was maintained at 2 MPa by keeping both ends of the samples in direct communication with the pore fluid pump. This was done so that fluid could be added and removed from both ends of the sample to maintain the 2 MPa pore pressure. By having both ends of the sample open, we ensure that we are not flushing pore fluid through the sample and decreasing the bitumen saturation of the sample accidentally.

While the sample was sitting overnight, we also raised the confining fluid pressure to 10MPa, the maximum pressure at which we take any measurements. This ensured that any damage, i.e. fractures, which the samples had suffered had a chance to re-compact and not adversely affect our measurements. In addition, the sample was cooled overnight to a temperature of 4°C, which was our first experimental temperature step.

After the samples sat overnight at constant pressure and temperature, we dropped the confining pressure to 4 MPa to make our first measurements. Measurements were made over a pressure range increasing from 2 to 8 MPa effective pressure, and then cycling back. After the pressure cycle at a given temperature was completed, we raised the temperature to the next step and allowed the temperature of the sample to equilibrate. Temperature steps varied from 10 to 35°C, and the temperature of the sample took about 5-7 hours to equilibrate on average, depending on the size of the temperature step and the sample itself.

At each pressure and temperature step, measurements of the sample length and the travel time of P and S waves were recorded so that we could obtain P and S wave velocity estimates over a wide range of pressure and temperature conditions.

3.4.1 Sample Descriptions

As stated earlier, the samples provided to us by Shell are extremely heterogeneous. However, if one were to classify the samples based solely on porosity measurements, then the samples may be falsely interpreted as being fairly similar to each other. Figure 3.9 illustrates the porosity measurements made for each sample utilizing 4 different techniques. The digital porosity is estimated from CT scans of the core samples, which were provided by Ingrain Inc., Houston, Texas. The log porosity was provided by Shell, and the density porosity and helium porosity were measured by Corelab. Based on porosity alone, the samples appear fairly similar, since they all have porosities within the range of 20 to 25%. However, closer inspection of the samples reveals that they are very distinct from one another and display vastly different characteristics and properties. As an example we will take a closer look at 2 samples, samples S2 and S6, which represent the two end members of the sample characteristics displayed by our samples.
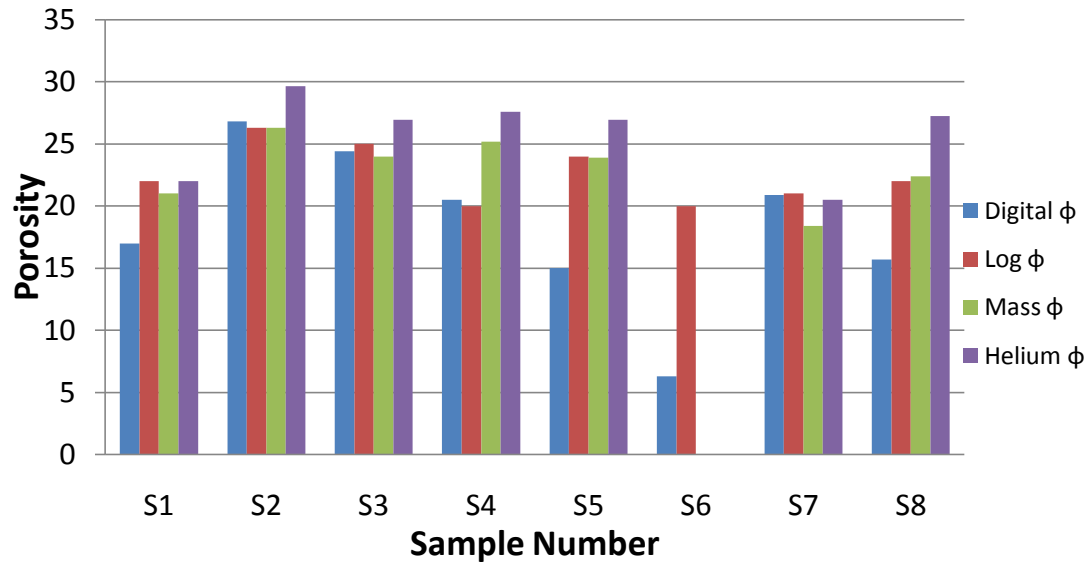
Figure 3.9: Porosity measurements of the 8 samples provided. For each sample we have porosity estimates from digital CT scans (blue), log measured porosity (red), mass or density porosity from core measurements (green), and helium porosity (purple).

Sample S2, which is a 1.5" diameter core plug (Figure 3.10, left) is what we will refer to as ―clean‖ bitumen sand. We call it such because it most closely represents the typical idea of what most think of when imagining bitumen sand. This typical idea consists of a bimodal system where the sample consists of merely sand and bitumen mixed together, exhibiting either a fluid-supported or grain-supported framework. Sample S2 consists of medium-grained quartz and chert-rich unconsolidated sand with a very dark oil stain. It is well sorted and is composed of angular to sub-rounded grains. The nature of the sample is even more apparent if we look at CT scan images of the sample (Figure 3.10). Here we can see a picture of the sub-sample that was scanned (upper middle), a low resolution image of the sample (lower middle) and a high resolution CT scan of the pore space (right). The high resolution image shows that the sample is composed mainly of large grains. Also, the sample is grain supported in nature and does not contain a large amount of fine grained material within it.
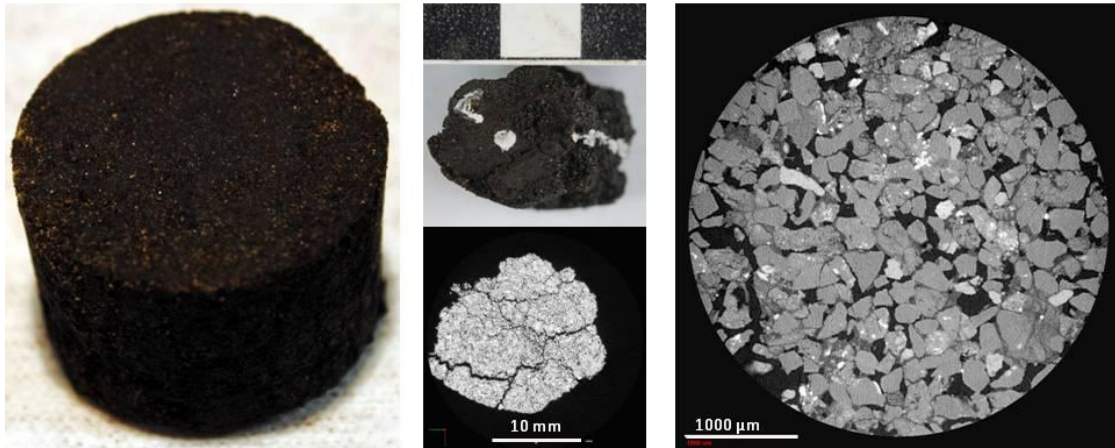
Figure 3.10: Photograph of 1.5" diameter "clean" bitumen sand core plug sample S2 (left). Sub-sample used for CT imaging (upper middle). Low resolution scan of S2 sub-sample (lower middle) and high-resolution image of S2 sub-sample (right).

At the other end of the spectrum we have sample S6, which consists mainly of cryptocrystalline lime mud, which is commonly referred to as a shale within the reservoir from which it was taken. Figure 3.11 shows a photograph of the 1.5" core plug S6, along with the sub-sample of S6 used for CT-scan imaging. From the images it is clear to see that the samples are extremely different from one another. In addition to the vastly different grain size and internal structure, sample S6 shows no oil stain and exhibits very poor reservoir quality when compared with sample S2.
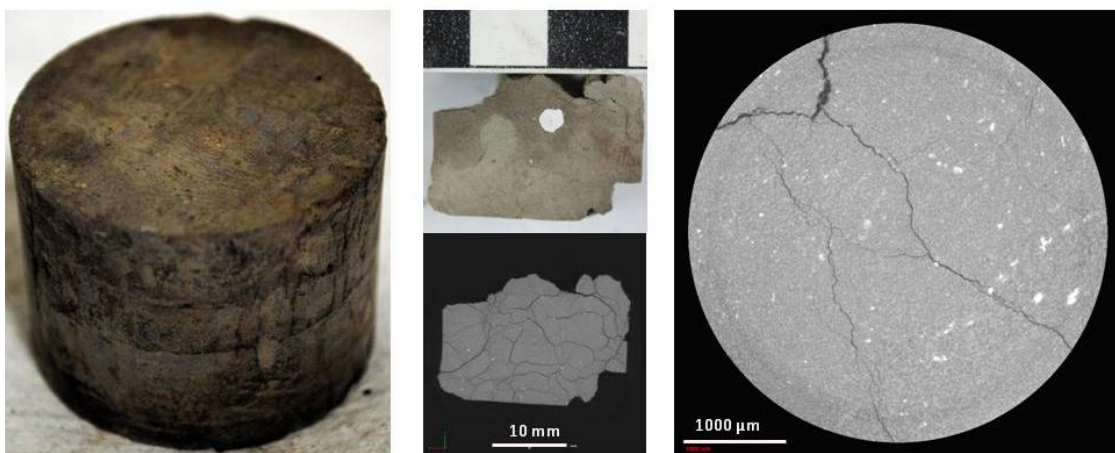
Figure 3.11: Photograph of 1.5" diameter lime mud core plug sample S6 (left). Sub-sample used for CT imaging (upper middle). Low resolution scan of S6 sub-sample (lower middle) and high-resolution image of S6 sub-sample (right).

Samples S2 and S6 represent the two end-members of our samples in terms of the ―clean‖ bitumen sand and lime mud or shale facies, but the 8 samples that were tested span the full spectrum of characteristics between these two extremes (Figure 3.12). The heterogeneity exhibited by the samples is readily apparent in photos of the core plugs. Almost every sample has a unique amount and distribution of clean bitumen and lime mud dispersed throughout the sample. Also note that in Figure 3.12 we have indicated sample S5 and S5_2, these are two samples that were cut from one larger core sample and were immediately adjacent to one another in-situ. Even though these two ―identical‖ samples were cut from the same core, they still exhibit heterogeneity at the core plug scale.

Figure 3.12: Pictures of each of the eight 1.5‖ diameter samples tested. Note that sample S5 has been cut into two individual samples identified as S5 and S5_2.

We have shown the heterogeneity that exists within the samples in terms of the amount of clean bitumen sand and lime mud present, but the heterogeneity does not end there. The samples also have varying amounts of pyrite, coal, shells, shell

fragments and dolomite crystals. Sample S3 contains large amounts of pyrite (Figure 3.13), both disseminated and contained in large clasts. CT scan images show that all of the samples have some amount of pyrite in them in one form or another.
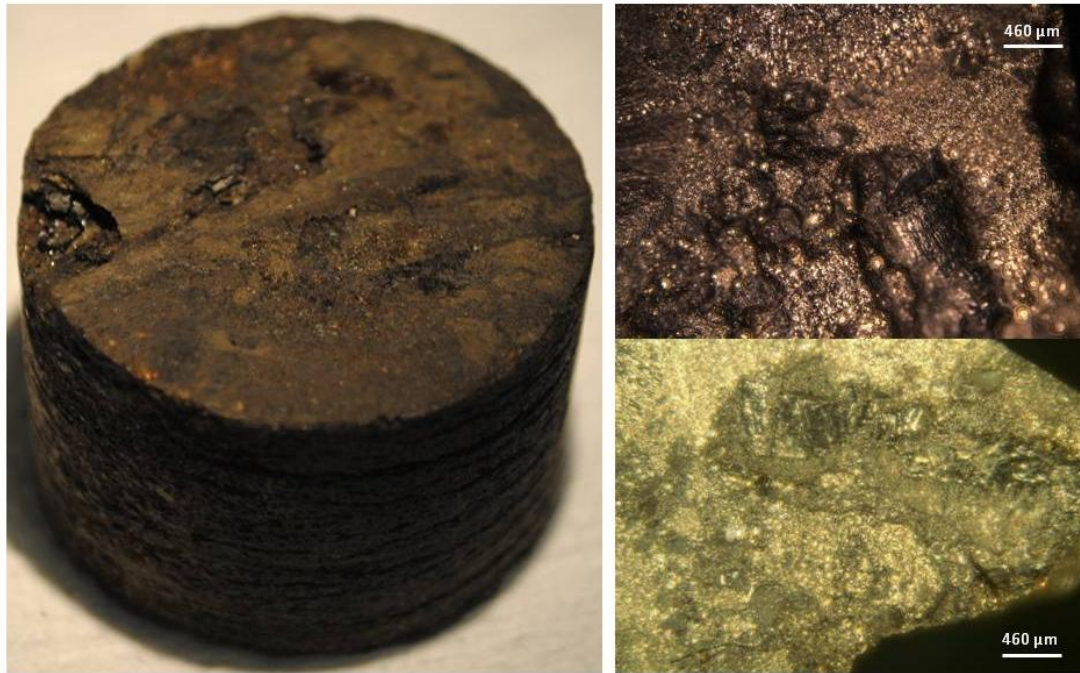
Figure 3.13: Picture of 1.5" diameter core plug S3 (left) showing large pyrite clasts at the top of the sample. Note that a fragment has been broken off the left side and is imaged with a microscope under two different lighting conditions on the right.

In addition, sample S3 also has continuous layers of coal running across the sample as can be seen in Figure 3.14. The pieces of coal exhibit characteristic conchoidal fracture and are very brittle. The presence of both the pyrite and coal within the samples will affect the overall properties of the bitumen-sand core plugs. Pyrite has bulk and shear moduli of 150 and 131 GPa respectively (LePage and Rogers, 2005), which is substantially higher than that of other minerals you would commonly expect to find in bitumen sands. Also the presence of coal further complicates matters as the elastic moduli of coal are dependent on the rank of the coal and pressure (Morcote-Rios et al, 2005) and might possibly be temperature dependent.

Figure 3.12 shows the variability of the samples with respect to one another, but even in a single sample there is a wide range of variability in the properties and

composition. Even at the scale of a single 1.5" diameter core plug, the amount of heterogeneity present makes the modeling of bitumen sands very complex. Figure 3.14 shows 6 slices through the CT scan image of a subsample of S5. The heterogeneity between different samples was previously shown by looking at samples S2 and S6, but the same clean bitumen sand and lime mud facies can be seen within a single sample—for instance Figures 3.14b and e. The transition between the two facies can also be seen (Figure 3.14d). A number of other features can also be seen. The yellow boxes in Figure 3.14 indicate areas where the core has been fractured. These fractures are likely the result of core damage sustained during either core retrieval from the well or subsequent transport and are not thought to be present in in-situ conditions. Also shown is a green box encircling what looks like a very high porosity channel. Again, this feature is not thought to be present in in-situ conditions, but is thought to be core damage associated with gas coming out of solution. As the pore pressure is dropped while removing the core from the well, or during subsequent heating, the bitumen in the pore space may cross the bubble point, and gas may start to come out of solution. This gas pressure will gradually increase and start to migrate through the core, possibly leaving behind the feature we have highlighted in green. There are also numerous bright spots in the CT scan images, some of which we highlighted with blue boxes. There spots are more examples of pyrite clasts scattered throughout the sample. Finally, the last features we have highlighted in Figure 3.14, in orange, are what are thought to be pieces of coal disseminated throughout the sample. These features are a darker grey and hence lower density, and they can be quite elongated in shap,e leading us to believe that they are coal fragments.

In addition to the CT scan images of the cores, we also have SEM images of selected cores. Figure 3.15 shows SEM images collected from sample S3. The left image shows the presence of well formed dolomite crystals contained within the sample, and the right image shows the presence of pyrite in its framboidal form.
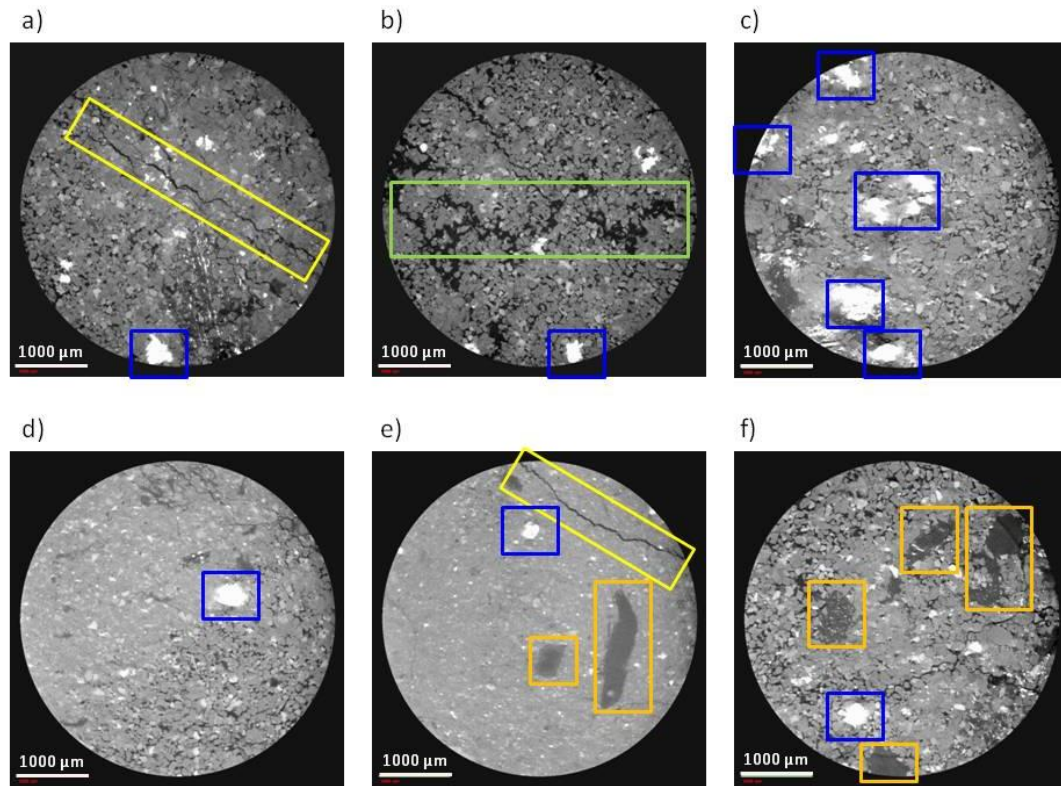
Figure 3.14: Various slices through CT scan image of sample S5, showing the presence of both clean bitumen sand (b) and lime mud (e) facies. Yellow boxes highlight fractures resulting from core damage, the green box highlights damage from gas bubbling out of solution, blue boxes highlight pyrite clasts, and orange boxes highlight coal fragments.
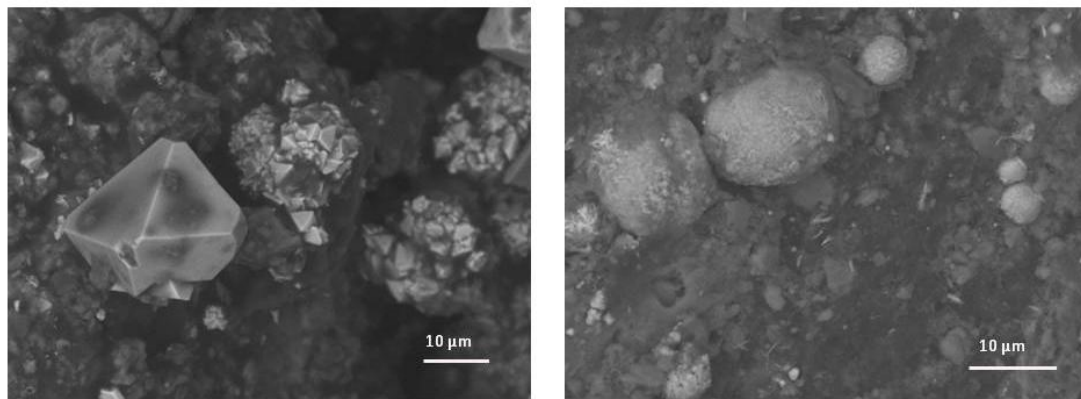
Figure 3.15: SEM images of sample S3 showing the presence of dolomite crystals (left) and framboidal pyrite (right).

The preceding examples show the vast amount of heterogeneity present within these samples, not only from sample to sample, but also on the scale of each individual sample itself. This heterogeneity will make modeling of these samples very complex.

Not only is there an extreme variation in regards to the mineralogy present in the samples, but the nature of grain contacts, supporting frame and pore filling material is greatly varied throughout the samples. To properly model the samples and all the variation present within them, future modeling will need to incorporate much more complexity than current modeling, which largely assumes that bitumen sand is a two-phase composite made up of solely quartz sand and bitumen.

3.4.2 Measured Data

As mentioned previously, samples were measured under many different pressure and temperature conditions. This created a very large dataset that will not be shown in its entirety here. Instead, we will focus on selected measurements to highlight certain characteristics of these reservoir sands brought to light by our measurements. In addition, we were unable to obtain reliable measurements of P- and S-wave velocities for sample S4, and samples S1 and S8 have no S-wave velocity measurements because steel plates on the transducers interfered with signal quality.

One phenomenon our measurements revealed was that not all the samples exhibit the same strain response when exposed to elevated temperatures. We measured the length of the samples at every pressure and temperature stage, and observed that whereas some samples compacted when heated, others expanded. Figure 3.16 displays the length-change behavior of two different samples when exposed to heat. Figure 3.16a shows that sample S5_2 compacts as it is heated. In contrast, Figure 3.16b shows that sample S6 does the opposite; it expands when it is heated. The difference in these two behaviors is most likely due to the different microstructure of the samples and how fluid moves through the sample as it is heated. Any fluid that might be contained within these samples, be it bitumen, water or gas, will expand in volume it is heated. Sample S5_2 is one of the cleaner sand samples, in which pore pressure equilibrated through the sample overnight. This indicates that the permeability of the sample is non-negligible and will allow the expanding fluid to flow through and eventually out of the sample to maintain pore pressure. As the bitumen in the pore space is being heated and expanding, it also loses its ability to support the framework of grains in the sample, and they will tend to rearrange under the applied pressure.

This fluid movement and grain re-arrangement is the likely mechanism leading to the overall sample compaction. On the other hand, we have sample S6, which is the lime mud. This sample did not allow the pore pressure to equilibrate overnight, and must have a very low permeability. This means that pore fluid within the sample is not free to migrate through the pore space. When heated, the expanding pore fluid will be trapped within the pore space, resulting in an overall expansion of the sample.
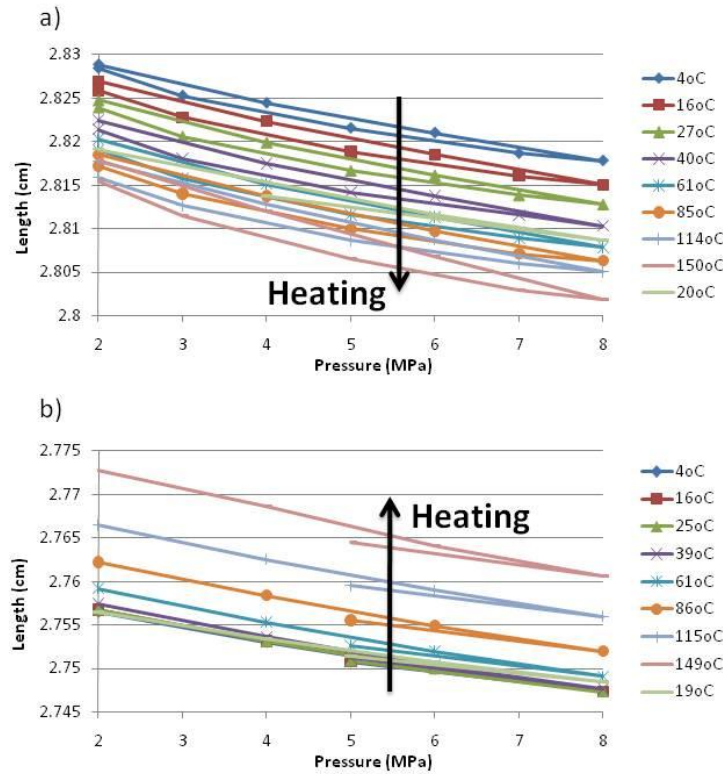
Figure 3.16: Samples S5_2 (a) and S6 (b) which show different strain behavior when heated. The differences in compaction and expansion are most likely due to microstructure and permeability differences.

Figure 3.16 also shows evidence that the compaction of the sample may not be reversible, but that the expansion of the sample is. For both the samples shown in Figure 3.16, the final temperature measurement was made back at room temperature after heating the sample to 150°C. Note that for the compacting sample that some of the compaction is reversible, but not all of it. For the expanding sample, we can see that the swelling is completely reversible and the sample length returns to its original length at room temperature after cooling. This suggests that grain rearrangements that

occur when compacting the sample are not reversible, and will cause some hysteresis in the sample. Conversely, any swelling of the sample due to pore fluid expansion seems to be totally reversible upon cooling of the pore fluid.

Switching the focus to the velocity measurements of the samples, I will present selected measurements of V_P and V_S. Because of the volume of data collected I will focus on measurements made at the highest and lowest pressures measured, 8 and 2 MPa, over the entire temperature range. Data at these two pressures show the upper (high pressure) and lower (low pressure) limits on velocities, and we can extrapolate the results between them. The remaining data at intermediate pressures shows the same trend.

Figure 3.17 shows measurements of V_P made at 8 MPa for all samples with reliable signals. The high pressure helps couple the sample with the transducers and results in good signal quality, giving us high confidence in our measurements. In general, most data display the same trend with respect to temperature. There is an overall decrease in P-wave velocity with increasing temperature, with a slightly higher rate of decrease in approximately the first 50°C. This is likely where the liquid point of the bitumen is located, and we expect to see a shift in the rate of change of velocity once the shear modulus of the bitumen is no longer acting to stiffen the overall rock. The surprising result here is that the change in slope for most samples is very slight, and in some cases not visible at all.

Also note that for the majority of samples, there is one data point at approximately 20°C that is disconnected from the rest of the data points for the sample. The connected data points follow the experimental heating trends, and the disconnected data point is the final measurement made after the sample has cooled back to room temperature. It is somewhat counterintuitive that for every sample the final velocity is higher than the initial room-temperature velocity.
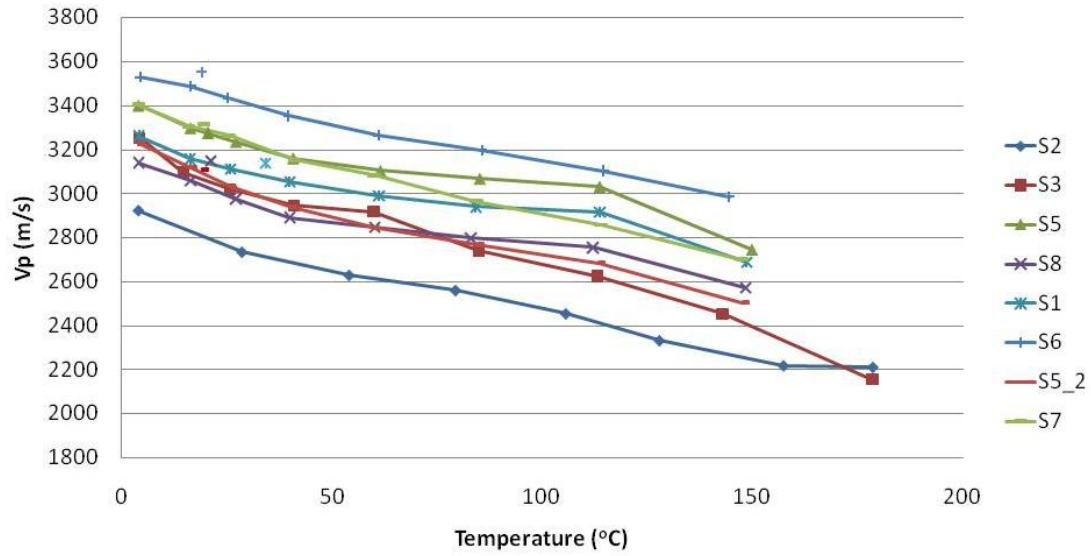
Figure 3.17: High-effective-pressure (8 MPa) measurements of P-wave velocity for bitumen reservoir samples.

The reason that this is counterintuitive is because the most likely changes occurring during sample testing is that heated and expanding bitumen is being pushed out of the pore space, and since we are maintaining pore pressure with water as our medium, once the sample is cooled and the pore fluid contracts we would expect water to be pushed into the pore space in place of the bitumen that was forced out. In fact the majority of samples left some amount of bitumen within fluid reservoirs of the pore fluid system, indicating that some bitumen has been removed from the pore space of the sample. Since bitumen acts to stiffen the overall properties of the bitumen sand, we would expect that the removal of bitumen should result in a lower measured velocity at the same temperature. We observe the exact opposite. This suggests that some sort of grain rearrangement is occurring within the sample as it is heated. A possible explanation for this is that as the samples are heated the bitumen becomes less viscous and will not bond grains together as effectively. This allows for the grains to rearrange slightly, create more grain to grain contacts, and stiffen the overall properties of the frame. One additional oddity is that we see the same behavior with the lime mud sample S6. This sample does not contain significant amounts of bitumen, and yet it still exhibits a higher velocity after it has been heated and cooled. This sample expands when heated, as was shown in Figure 3.16b, and we hypothesize that upon

cooling the reducing pore water volume allows for the grains to rearrange somewhat, which can account for the higher velocity despite the lack of compaction overall.

Figure 3.18 shows measurements made on the same samples at an effective pressure of 2 MPa for comparison with the high pressure data. The most glaring differences are seen for samples S8 and S1. These samples show an increasing velocity trend at temperatures above ~85°C. However, we think these data points are in error, because these two samples were measured with steel plates attached to the transducer faces. Aat low pressures coupling is weaker between the transducers and our samples, and the additional interference caused by the presence of the steel plates makes the arrival of the P-wave difficult to pick. Therefore, we omit these data points from our analysis. For the remaining data, we see that the observed trends at 2 MPa are very similar to those seen at 8 MPa. This indicates that the temperature dependence of V_P has very little pressure sensitivity. This is likely because these specific samples are not crossing the bubble point of the bitumen at any time. If this were not the case, we would expect pronounced changes in the P-wave velocity of the samples as the gas phase begins to form within the samples.
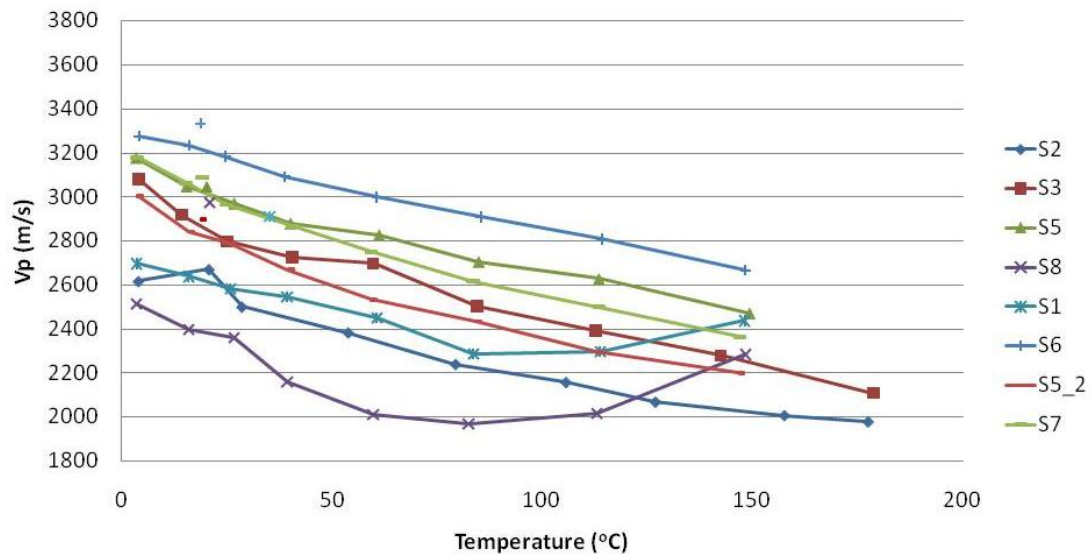
Figure 3.18: Low-effective-pressure (2 MPa) measurements of P-wave velocity for bitumen reservoir samples.

The shear-wave data collected at 8 MPa is shown in Figure 3.19. Note that samples S8 and S1 have been removed from the plots, because even at 8MPa the data collected is unreliable because of the steel plates.
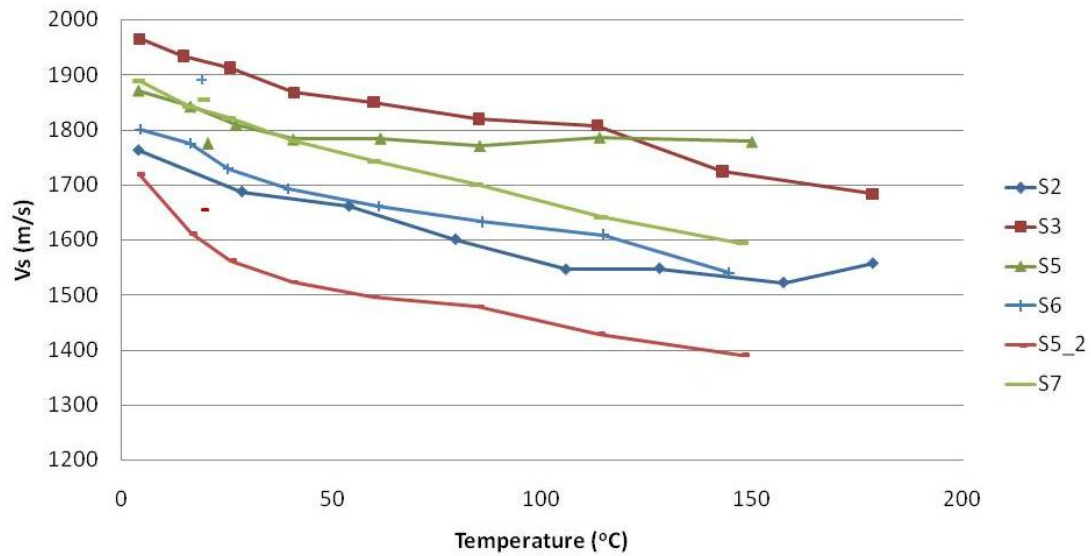
Figure 3.19: High-effective-pressure (8 MPa) measurements of S-wave velocity for bitumen reservoir samples.

The measured shear-wave velocities of these samples again shows that there is a change in the rate of velocity decline at approximately 50°C for the samples. Again, this is likely the point at which the shear modulus of the bitumen approaches zero and it loses the ability to propagate shear waves. The unexpected result here is that beyond this point the shear velocity of the samples continues to decline. This is surprising, because there should be no change in the shear properties of the bitumen above its liquid point. One possible explanation for the continued decrease in shear velocity is that as the bitumen is heated and expands it may alter the grain contacts in a way which results in the observed decrease in velocity. However, note that upon cooling to room temperature we again see an increase in velocity relative to the heating curve as we did for the P waves. To summarize, this means that while heating we have grain rearrangements which result in a velocity *decrease*, whereas during cooling we have grain rearrangements which result in a velocity *increase*. These two somewhat opposed mechanisms can simply be the result of fluid expansion during heating, and compaction during cooling; meaning that grains are pushed apart as the fluid increases in volume while heating, and then are packed back together as the fluid cools and contracts.

Figure 3.20 shows the same data as in Figure 3.19, except that only two samples, S5 and S5_2, are shown. These are the two sub-samples that were cut from one larger core plug. The comparison is interesting because we can compare the effect that the steel plates have on measured data since we can assume that the two samples are fairly similar in nature since they were directly adjacent to one another in the reservoir.
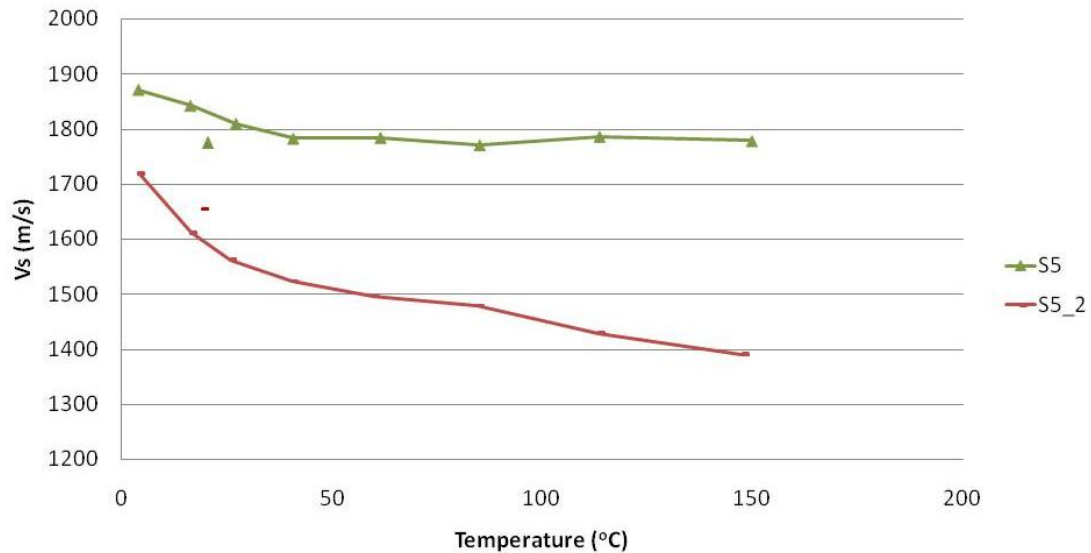
Figure 3.20: High-effective-pressure (8 MPa) measurements of S-wave velocity for bitumen reservoir samples S5, measured with steel plates, and S5_2, measured without steel plates.

Sample S5_2 was tested without the steel plates attached to the transducers and had a very clean reliable shear-wave signal (see Figure 2.27); as a result the measured velocities are accurate. Contrary to this, sample S5 was measured with the steel plates, which resulted in very noisy waveforms; S5 also was one of the first samples, measured before a clear trend in the data was identified. Because of this noisy data, we believe that our picks were biased by our preconceived notions of what bitumen sand behavior should be. As a result, we picked the arrivals such that the velocity decreased to the liquid point of the bitumen, and then remained constant upon subsequent heating. This is clearly not the case for sample S5_2, as well as the other samples shown in Figure 3.19. This demonstrates the pitfalls that may be associated with picking arrival times from poor quality waveforms. When the arrivals are not clear, we

may unknowingly reinforce our preconceived notions simply because we believe we see what we expect to see in the data.

We now compare the 2 MPa shear-wave velocity measurements in Figure 3.21 with the 8 MPa velocities in Figure 3.19. In Figure 3.21 we see the same trends for low effective pressure as for high effective pressure, with a little more scatter in the data, since the waveforms are slightly degraded due to poorer coupling. This shows that the pressure sensitivity of the V_S–temperature relationship is minimal, and again supports the notion that the pressure sensitivity of the velocity–temperature relationship is minimal with these reservoir materials.
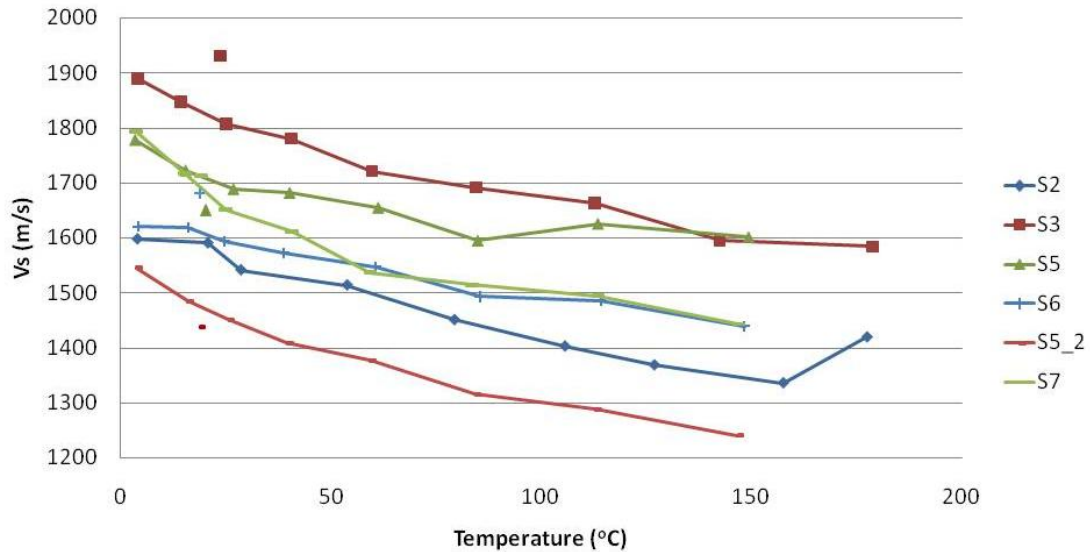
Figure 3.21: Low-effective-pressure (2 MPa) measurements of S-wave velocity for bitumen reservoir samples.

Given that both V_P and V_S measurements are available, it makes sense to see if there are any trends in V_P/V_S ratio that may be instructive or useful. In Figure 3.22 we show the measurements of V_P/V_S ratio for sample S6. The data shows that the V_P/V_S ratio is largely unaffected by pressure and also remains constant for the sample until the temperature reaches approximately 84°C. Above this temperature the V_P/V_S ratio begins to decrease until the upper temperature limit of the experiment is reached.
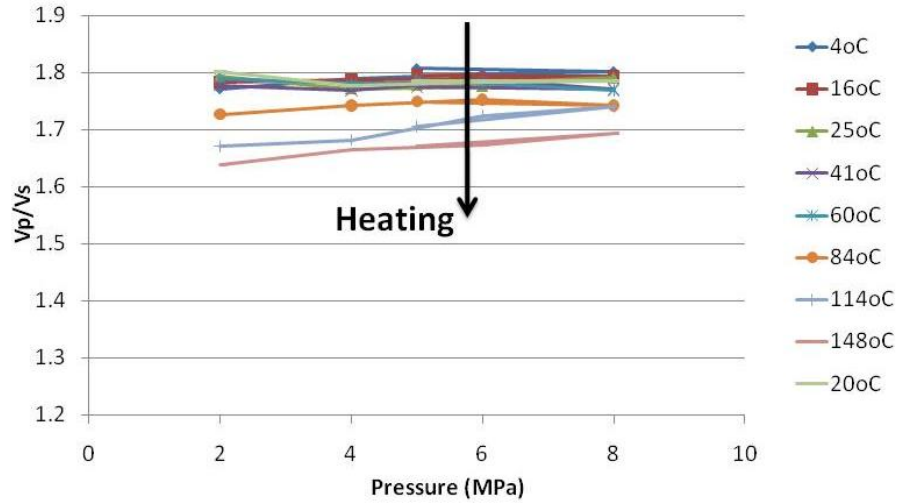
Figure 3.22: V_P/V_S ratio as a function of both temperature and pressure for sample S6.

Figure 3.23 shows that this general trend holds for all of the samples. In this figure, we plot the V_P/V_S ratios for all samples at an effective pressure of 8 MPa. All samples show a relatively constant V_P/V_S ratio at lower temperatures, which begins to decrease as temperature increases. There is some scatter in the data, and of particular note is the sample (S3) that has a V_P/V_S ratio that approaches 1.3 at 185°C. This V_P/V_S ratio corresponds to a sample with a negative Poisson's ratio, which is likely not realistic for these reservoir materials. However, these measurements were made at 185°C on the sample containing a large pyrite piece (Fig. 2.24). This temperature is where the damage to the original transducers occurred, so this data point should not be trusted.
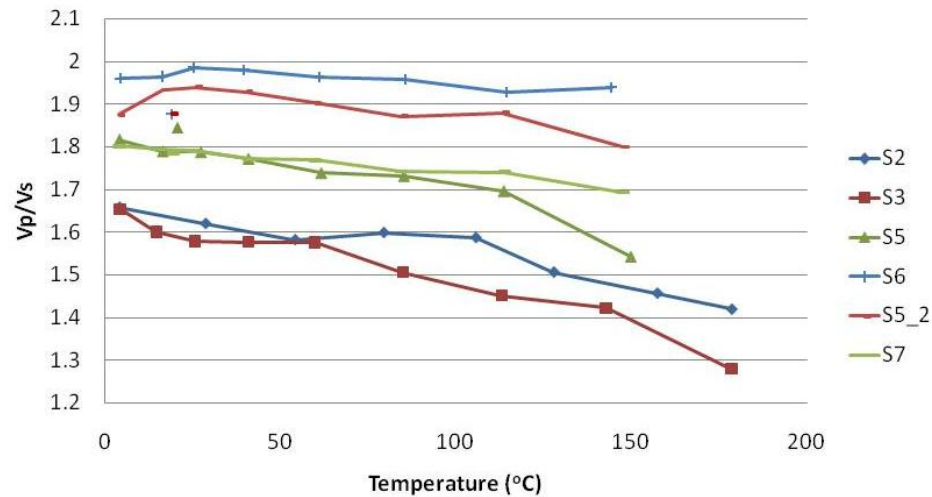
Figure 3.23: V_P/V_S ratio at 8 MPa effective pressure as a function of temperature for all samples.

One of the typical rock-physics crossplots used to analyze data is velocity versus porosity. In Figure 3.24 we show these crossplots for all our measured samples at a temperature of 4°C and effective pressure of 8 MPa. We chose these conditions because they should be fairly representative to in-situ reservoir conditions. We estimated the overburden pressure from a well log density curve for the well from which our samples were taken, and assuming a hydrostatic pressure gradient we calculated the effective pressure within the reservoir to vary between 7 and 8 MPa. Also, given that the average temperature of reservoirs in this area is close to 4°C, the conditions should be fairly representative of initial reservoir conditions.
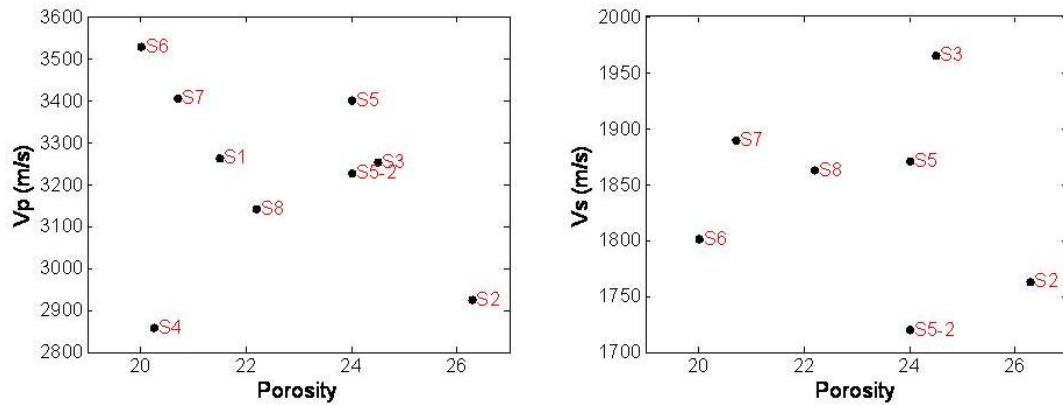
Figure 3.24: Crossplots of measured V_P (left) and V_S (right) versus porosity at 4°C and 8MPa effective pressure. These conditions are representative of in-situ reservoir conditions.

Usually these types of crossplots are very instructive, and we can plot numerous models to help constrain and explain the data we see. However, in this case, given the extreme heterogeneity of the samples, we can draw only minimal conclusions without a much more quantitative analysis of the sample composition and framework. This is evident in the lack of a clear pattern in velocity-porosity space.

Despite this lack of conclusiveness, we can compare the measured V_P in the well with our data. This is not a completely valid comparison, given that the frequency differs between the two methods and that the sampling size is also quite different. However we can at least determine whether our lab measurments reflect the same trend as is observed in the well-log data. Figure 3.25 shows the P-wave velocity

measured in the well as a function of depth in black. Note that the measurements below 613 m are erroneous. Our laboratory measurements at 4°C are plotted as colored dots. Blue and red dots represent measurements made at 6 and 8 MPa effective pressure, respectively. Both pressures are plotted for comparison, given that the effective pressure in the reservoir is assumed to be between 7 and 8 MPa.
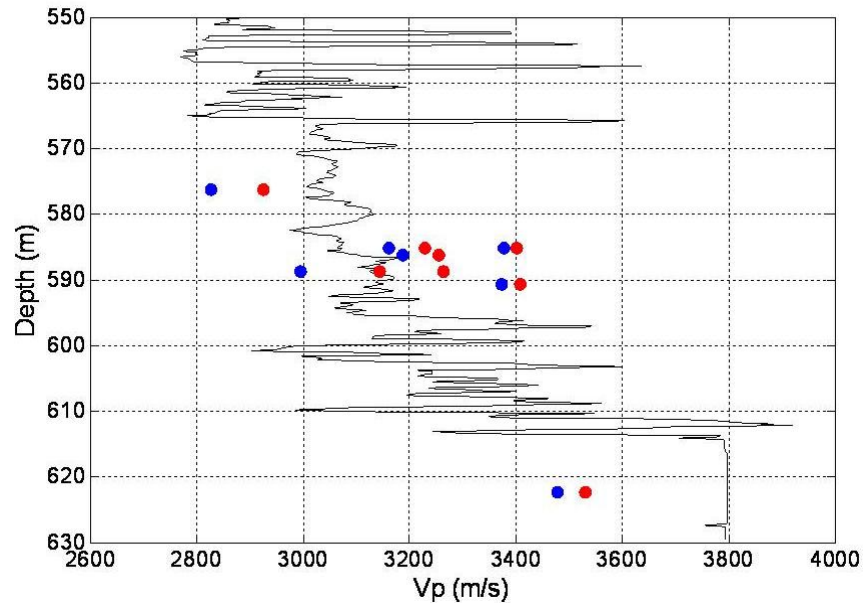
Figure 3.25: Comparison of p-wave velocity measured in the well as a function of depth (black) with laboratory measurements made at 4°C. Data from two pressures is shown – 6MPa in blue and 8MPa in red.

We see that the trend of our data matches that recorded in the well fairly closely. There is a general increase in P-wave velocity between the depths of 570 and 590 meters, which is also reflected in our data. We also see that as the reservoir ends and we reach the lime-mud facies (610 to 613 m), there is a large increase in velocity, which also corresponds well with the increase we see for the lime-mud sample we measured (retrieved from a depth of 622.27 m).

3.5 Conclusions

Our preliminary measurements of bitumen and bitumen-sand reservoir samples were very instructive for pointing out the difficulties in making measurements on these types of samples. They allowed us to better understand the challenges we face and to design a better system to for acquiring velocity measurements of heavy oil reservoirs in the laboratory.

The samples we measured with our new system displayed both P- and S-wave velocities that decreased over the entire experimental temperature range. The velocity changes occurred faster in the range of 4 to 50°C, but the rates of change of both V_P and V_S at temperatures above this range were much greater than we initially anticipated. The pressure sensitivity of the velocity–temperature relationships for both P- and S-waves was negligible, and this is attributed to a lack of gas coming out of solution in our samples. The V_P/V_S ratio for our measured samples remained essentially constant with changes in pressure and heating at low temperature ranges; however, with heating to higher temperatures, the V_P/V_S ratio in all samples began to decrease.

There was also a systematic change in the velocity of both P- and S-wave velocities before and after heating the samples. All samples showed an increase in velocity after being heated and then cooled to room temperature as compared to the initial measurements made at room temperature. Because replacing bitumen in the pore space with water would have had the opposite effect on both P- and S-wave velocities, there must be some sort of grain rearrangement that affects the strength of the sand framework.

These observations point out the shortcomings of a simple or idealized model of bitumen sands, where it is assumed that bitumen sands are comprised mainly of quartz sand and bitumen. First, the heterogeneity and complexity of these reservoirs has been demonstrated, and to model these reservoirs properly the heterogeneity must be taken into account. Second, idealized models typically assume that the mineral framework remains the same under all conditions, and that the observed velocity changes are due solely to changes in the fluids contained within the pore space. This is not the case, as

evidenced by our observed velocity changes, which must be due to grain rearrangements. Future modeling of these types of reservoirs will need to take all of these factors into account to properly characterize and/or predict the properties of these reservoirs and how they will be affected by various reservoir temperature and pressure conditions.

Chapter 4
Modeling approaches for bitumen-saturated sands

"[Those] who have an excessive faith in their theories or in their ideas are not only poorly disposed to make discoveries, but they also make very poor observations."

~Claude Bernard

4.1 Abstract

The viability of several methods for modeling bitumen and bitumen-saturated sand are investigated to determine which model is the most robust for predicting bitumen and bitumen sand acoustic and elastic properties. We consider two conceptual models of the structure of bitumen sand: grain-supported and fluid-supported. Based on the limited data available to us at this time, it is difficult to make definite conclusions. We tested the viability of several methods and again conclude that traditional Gassmann fluid substitution will not work for bitumen sands at low temperatures. However, solid Gassmann substitution, as proposed by Ciz and Shapiro (2007), may overcome the

limitations encountered in traditional Gassmann fluid substitution. We also propose a new model, which employs the cemented-sand model at low temperatures and transitions to traditional Gassmann fluid substitution at elevated temperatures. This model may provide a robust method for predicting the properties of bitumen sands, and it has the advantage that it can be applied over the entire range of temperatures commonly encountered in steam-assisted production methods used in bitumen and heavy oil reservoirs. However, the model is not sensitive to pressure at low temperatures, so it cannot span the range of velocities encountered at low temperatures in bitumen sand. To formulate a hypothesis as to which model is most suitable, we need a greater number of robust laboratory measurements in bitumen sands. Nevertheless, we find that both the solid-Gassmann and newly proposed model appear to fit the measured properties of bitumen sands reasonably well.

4.2 Introduction

The recent increase in production of heavy-oil and bitumen reservoirs has stimulated research into how to effectively and efficiently remove these fluids from the ground. A key factor for better characterization and monitoring of bitumen reservoirs is the development of a robust rock-physics model or transform for translating measured seismic properties to in-situ characteristics of the reservoir. However, the lack of a large, robust, published dataset with the properties of bitumen and bitumen sands over a wide range of temperatures and pressures makes the development of a model of this type challenging.

We explore the plausibility of several models to explain the behavior of bitumen sands under various temperature and pressure conditions from preliminary measurements. This is possible because we have measurements of actual bitumen fluid properties, as well as a set of fairly homogeneous samples consisting mainly of bitumen and sand. Unfortunately, before we can model the dataset collected in our lab, we must more fully characterize the mineral constituents in our samples and improve our understanding of bitumen fluid properties.

Before forging ahead with modeling to explain the behavior of poorly characterized samples, we use this opportunity to explore several methods for modeling bitumen and bitumen sands in order to determine which may be the most applicable to future modeling of these materials.

4.3 Modeling of Preliminary Measurements

4.3.1 Bitumen Modeling

One of the most recent models for predicting the shear modulus of bitumen as a function of API gravity and frequency was presented by Han et al. (2007). This model incorporates the idea of a glass point and liquid point for heavy-oils, and utilizes API gravity and the frequency of measurements to predict the shear modulus for heavy-oil. Figure 4.1 illustrates the conceptual phases of the model.
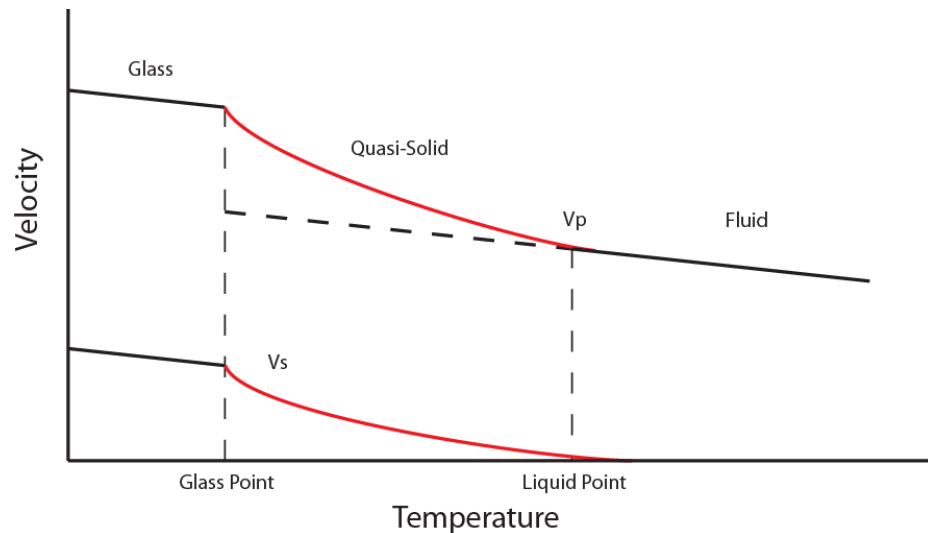
Figure 4.1: Phase changes of heavy oil as a function of temperature (adapted from Han et al, 2007).

Han‟s model is based upon a dataset that was created by first using the DeGhetto model (DeGhetto et al., 1995) to predict the viscosity η of the heavy-oil as a function of API and temperature. The shear velocity at the glass point is then estimated, as well as the viscosity of the oil over a range of temperatures. The relaxation time for each viscosity, τ_i, is then calculated as:

$$\tau_i = \frac{\eta_i}{\mu_g}$$

where η_i is the viscosity at each temperature and μ_g is the shear modulus at the glass point. The normalized shear modulus at each viscosity is then calculated by:

$$G_i = \frac{\mu_i}{\mu_g}$$

where μ_i is the shear modulus for each viscosity. By analyzing several datasets, Han determined that the shear moduli of several different heavy-oils can then be calculated as a function of relaxation time and frequency based upon the Havriliak-Negami (1967) model. We applied this modeling methodology to predict the measured shear modulus from our preliminary measurements of pure bitumen, first reported in Wolf and Mavko (2005). We used the relations developed by Batzle and Wang (1992) to predict the bulk modulus of a heavy-oil sample. The results are illustrated in Figure 4.2.
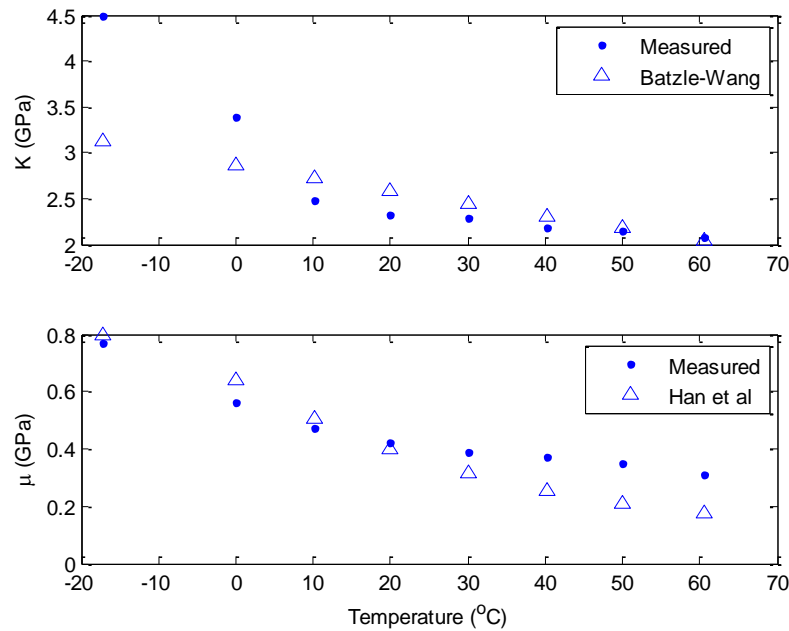
Figure 4.2: Preliminary measurements of pure bitumen and modeled bulk (top) and shear modulus (bottom) for a bitumen sample with an API of 8.5°.

Figure 4.2 shows that the Batzle-Wang (BW) model drastically underestimates the measured bulk modulus for the bitumen sample at low temperatures. The BW model is

based on empirical data and was not developed for use with heavy oils. These results show that the BW model is not valid for this bitumen sample at low temperatures. The lower panel of Figure 4.2 shows that the shear modulus is well predicted by the Han et al. (2007) model up to a temperature of 20 degrees C. Above this temperature there is a mismatch between the measured data and model results.

Several factors may contribute to the discrepancies between the measured properties from our preliminary measurements, and model predictions for both the bulk and shear moduli. The first is that there may be some water contaminating the bitumen sample. The sample was obtained from a wellhead emulsion, and although efforts were made to remove all the water from the sample, some still remained. The freezing of this water at low temperatures could partially explain some of the misfit with the bulk modulus at low temperatures. The misfit in the shear modulus could be partly due to the viscosity modeling. It has been shown that there is not a good correlation between API gravity and oil viscosity (Hinkle and Batzle, 2008; Al-Mamaari et al., 2006). The Han model uses API gravity-viscosity relationships to predict the oil viscosity, which may not be applicable for the oil measured. Another possible reason for this discrepancy could be inaccurate measurement of these samples. The measurements were made in an oven, with limited control over the temperature, and it was difficult to keep the transducer faces parallel as the sample was heated. In addition, the endcaps used were not ideally suited to measure heavy-oil, as they were not properly impedance matched. They were made from aluminum, which resulted in much of the signal being reflected from the surface of the sample instead of being passed through the sample. This resulted in a weak signal, which reduced the accuracy of the first-arrival picks.

The previous modeling of the bitumen bulk and shear moduli does not explain the available data well under all conditions. Although the models do an adequate job within certain temperature ranges, it is clear that a more robust dataset is needed in order to properly evaluate the utility of these models for predicting heavy-oil and bitumen properties under all conditions.

4.3.2 Bitumen Sand Modeling

The preliminary bitumen sands measured by Wolf and Mavko (2005) contain the same bitumen that was measured and modeled in the previous section. Since the properties of the bitumen itself is known, it allows the exploration of various ways of distributing the bitumen in the pore space to predict the overall properties and behavior of the bitumen-sand samples under variable temperature and pressure conditions.

In order to model the properties of the bitumen sand plugs, we also need to know the properties of the sand pack without the bitumen in the pore space. Unfortunately, it is impossible to measure the ultrasonic velocities of the sand pack itself without destroying the structure of the sand that we are interested in. Fortunately, a suitable proxy is provided by the measurements made by Zimmer (2003). Though not identical to the sands in our samples, the sands measured by Zimmer have essentially the same mineralogy, and his data allow us to extract the properties of sand with the same porosity values as our measured cores. Therefore, we have used the ultrasonic velocities measured by Zimmer as the dry-frame properties for our sands.

Armed with both the frame and fluid properties, we are free to explore various ways of including the bitumen within the pore space. For these measurements we investigate the properties predicted by three different models, Gassmann fluid substitution (Gassmann, 1951), the bound-averaging method (Marion, 1990), and the self-consistent approximation (Berryman, 1980).

Gassmann fluid substitution allows substitution of any fluid into the pore space of a dry frame. However, the theory assumes that all fluid shear moduli are zero, and all composite moduli remain unchanged upon the introduction of a fluid into the pore space. For bitumen sands this is not the case, because the fluid itself has a finite shear modulus at low temperatures and will act to reinforce the grain contacts and consequently affect the shear modulus of the pack.

The *bound-averaging method* (BAM) (Marion, 1990) uses a heuristic method based on theoretical bounds to estimate the velocity change when introducing a new pore fluid into the pore space. The Hashin-Shtrikman (1963) bounds limit the range of

elastic moduli, and hence velocities, for a given volumetric mix of two materials. For any proportion of these two materials, the effective modulus will fall between these bounds, with its precise value depending on the geometric arrangement of the two constituents. To apply BAM, we measure the relative positions of the moduli between the upper and lower bounds for a given rock-fluid mixture, then recalculate those bounds for a different mixture, placing the new effective moduli at the same relative distances from the new bounds. For our bitumen sand example, we calculate the bounds using a mixture of sand and air to determine the moduli"s relative positions between the bounds, trecalculate the bounds using the sand and bitumen properties for a given temperature, and assign the effective properties to the mixture by assuming the same relative position between the new bounds.

For the *self-consistent approximation* (Berryman, 1980), we first had to reproduce the pressure sensitivity of the sand pack that was observed by Zimmer. In our self consistent modeling we assumed spherical quartz grains and introduced a distribution of air-filled cracks of various aspect ratios that close under pressure to match the model stiffness with that of the measured data. Once this was accomplished, the distribution of the air-filled cracks was maintained, while the properties associated with those cracks were substituted for the properties of bitumen.

Figure 4.3 shows the measured P-wave velocities (Vp Measured), as well as the modeled P-wave velocities for the three methods outlined above (Vp Gassmann, Vp BAM and Vp Self Consistent). The upper left panel shows the measured behavior of the P-wave velocity as a function of both pressure and temperature. Each colored line on the plot corresponds to measurements made at a given temperature, and the trend of decreasing velocity with increasing temperature is indicated by the arrow labeled "Heating." It can also be seen that the P-wave velocity increases slightly as pressure is increased for each temperature step. The upper right panel, which shows the results of Gassmann fluid substitution of the bitumen properties (Figure 4.2) into Zimmer"s dry frame, shows that the predicted velocities match the measured velocities fairly well at higher temperatures, but at lower temperatures the velocities are drastically underestimated. This is largely due to the assumptions that 1) the shear modulus of the

pore fluid is zero and 2) the composite modulus remains unchanged upon the introduction of a new fluid. This assumption is invalid for bitumen sand at low temperature, where the shear modulus of the bitumen is non-zero. Hence, the low-temperature measured P- and S-wave velocities of bitumen sand are larger than the Gassmann predictions. However, at high temperatures, the shear modulus of the bitumen approaches zero; the assumptions of the Gassmann fluid substitution methodology is no longer violated, and the velocities are predicted reasonably well. The results of BAM (lower left) are more encouraging, as they provide higher estimates of velocity at low temperatures. However, BAM still underestimates the velocities at low temperatures, and does not exactly reproduce the measured data. The self-consistent approximation (lower right) overestimates the P-wave velocities for all but the lowest temperature measurement. At higher temperatures, the velocities are drastically overestimated. This method treats pores as if they are isolated from one another with respect to flow, giving no opportunity for induced pore pressures to equilibrate through the pore space. Hence, the self consistent model predicts higher velocities than we observe in the measured data. Also note that the self-consistent approximation cannot reproduce the pressure dependence observed for any given temperature in the measured data.

Figure 4.4 shows the same information as was presented in Figure 4.3, but for S-wave velocities. We see similar results in all cases as was described for the previous figure, with a glaring exception. Figure 4.4 shows that the Gassmann-predicted shear-wave velocity does not depend on temperature at all. Again, this is because the method does not incorporate any changes in the shear stiffness of the frame when the fluid is changed, which is clearly not the case. Note that we assume a non temperature dependent bitumen density, since we do not have fluid density measurements, which would have a small effect on shear velocities if included.
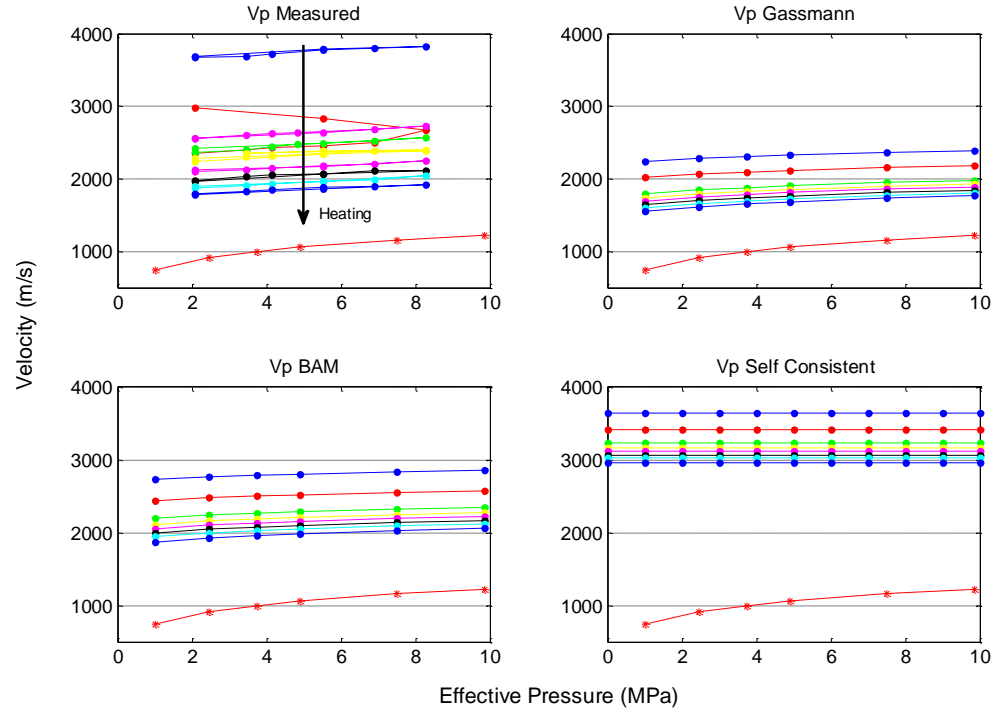
Figure 4.3: Measured P-wave velocity of bitumen sand as a function of pressure and temperature (upper left), modeled velocities using Gassmann fluid substitution (upper right), BAM (lower left) and the self consistent model (lower right).
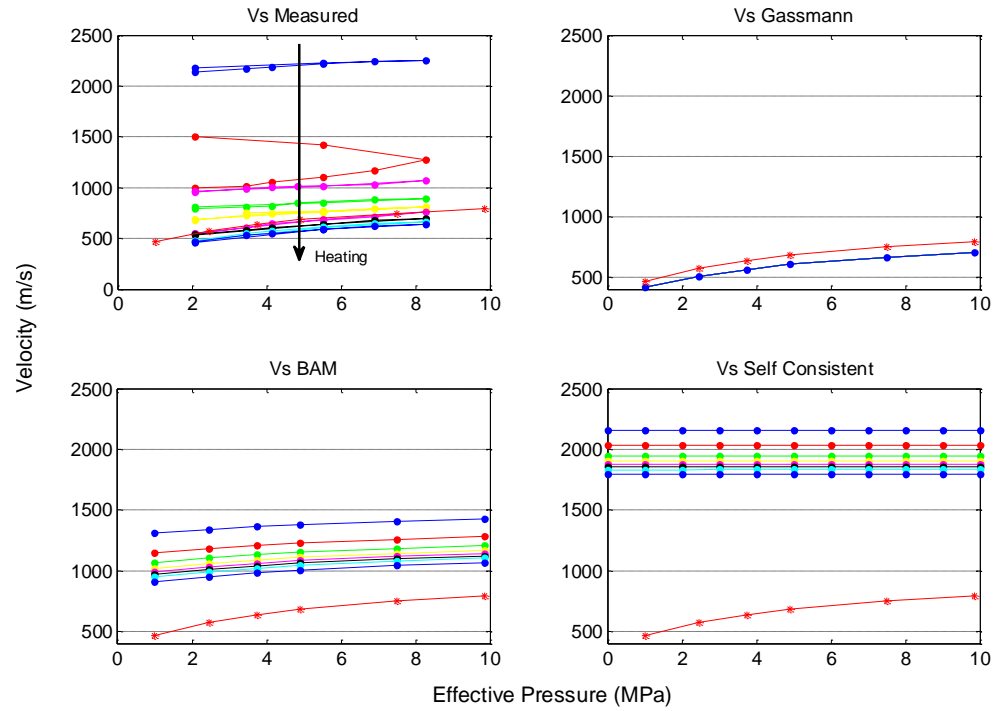
Figure 4.4: Measured S-wave velocity of bitumen sand as a function of pressure and temperature (upper left), modeled velocities using Gassmann fluid substitution (upper right), BAM (lower left) and the self consistent model (lower right).

Of the four models explored above, the most promising appears to be the bound averaging method, as it can model a reasonable spread in the P- and S-wave velocities with varying temperature. It cannot reproduce the amount of variability observed in the measured data, but is the most viable option of the four methods considered above for modeling this dataset. However, given the model"s inability to reproduce the highest velocities at low temperatures, we will continue to explore various methods to better model these kinds of reservoirs.

4.4 Alternative Bitumen Sand Models

At this time the limited data available, and the extremely variable makeup and poor characterization of the samples that have been measured do not generally allow for an in-depth analysis of the most applicable rock-physics models and transforms to use for bitumen sands. However, we will use this opportunity to explore the utility of various rock-physics models as they apply to bitumen sands, and hypothesize which models will best reproduce the properties of these materials.

The structure of bitumen sands may change as they are heated. At low temperatures, the rock may be grain-supported, or possibly even fluid-supported due to the very viscous nature of bitumen. At elevated temperatures, the bitumen in the pore space will expand, which may cause grain-supported sands to become fluid-supported. However, due to the reduced viscosity of the bitumen at high temperatures, the excess oil may be free to escape the pore space, again causing the sands to become grain-supported. At this point it is not clear whether one of these mechanisms will dominate the structure of most bitumen sands, or if the choice of model will change depending on the nature of the sands being tested. Therefore, we will explore the properties of bitumen sands with the conceptual examples illustrated in Figure 4.5, which include both grain- and fluid-supported sand-bitumen mixtures.

The conceptual examples show bitumen sand in three states: grain-supported, a suspension of grains in bitumen, and a representation of a suspension of grains formed by successively smaller shells of bitumen and sand, used to illustrate the concept of

Hashin-Shtrikman bounds. The methods used for modeling these conceptual examples of the structure of bitumen sands are given in Table 4.1. We can always use either Reuss and Voigt averages, or Hashin-Shtrikman bounds to get bounds on the properties of the bitumen sands, without specifying the geometric details of how the bitumen and sand are combined. This means that these bounds apply to both the grain- or fluid-supported bitumen sands. In addition, we know that the Hashin-Shtrikman upper bound will always be lower than the Voigt average, so we will neglect the Voigt average in our modeling.

The grain-supported sands can be modeled in a couple of different ways; however, the properties of the dry frame must first be determined. We do this by using both the soft-sand model (Dvorkin, 1996) and the measurements made by Zimmer (2003) on a dry sand pack. We can then saturate the dry frame by using either Gassmann fluid substitution (Gassmann, 1951) or the modified version of Gassmann"s equations for porous media saturated by solid material (Ciz and Shapiro, 2007), referred to as Solid-Gassmann for the remainder of this paper. One caveat of using the Solid-Gassmann model, as was pointed out by the original authors, is that some of the approximations made may not be applicable if the contrasts in substituted elastic moduli are greater than 40%. For bitumen sands the contrasts are larger than this; however, the results show that violating this limit on the contrast level may not have a large adverse effect on the model"s predicted properties.
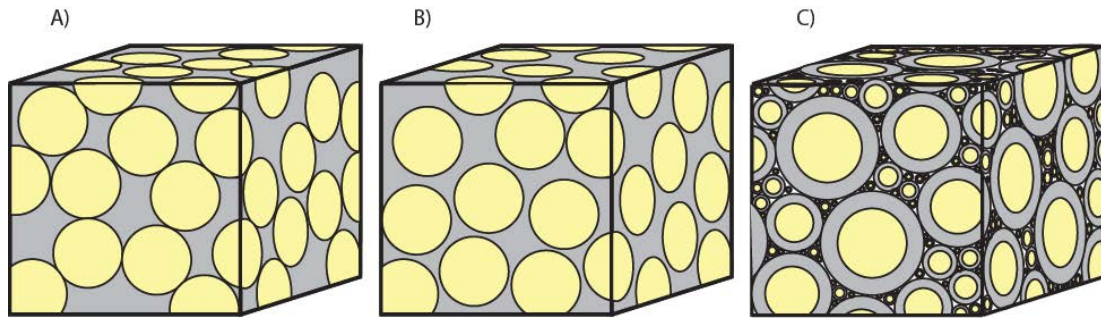
Figure 4.5: Conceptual examples of bitumen sand structure. A) Grain-supported sand, B) fluid-supported sand, and C) Hashin-Shtrikman representation of fluid-supported sand.

Table 4.1: Different models and data used in order to model bitumen sand as grain-supported and fluid-supported systems.

Grain-Supported		Fluid-Supported	
Bounds: Reuss average, HS-, MHS+		Bounds: Reuss average, HS-, HS+	
Dry Frame Modulus	Fluid Substitution	„Dry" Frame Modulus	Fluid Substitution
Soft-Sand (Hertz-Mindlin)	Gassmann	Reuss average of quartz and air	Gassmann
	Solid-Gassmann		Solid-Gassmann
Zimmer Dry Sand Data	Gassmann		
	Solid-Gassmann		

On the other hand, if we are modeling bitumen sands as a fluid-supported system we can directly model the properties of these sands using either the Reuss average or the Hashin-Shtrikman bounds (Mavko et al., 1998). We can also model these sands in a fashion similar to the one we used for the grain-supported sands, however in this case there is no dry frame modulus to use, because there is no dry frame to speak of. We can overcome this problem by calculating the properties of an air-supported „frame" using the Reuss average for air and quartz, and then using either Gassmann or Solid-Gassmann to fluid substitute bitumen into the air-filled pore space.

We will show modeling results for four different possible scenarios: 1) a grain-supported bitumen sand saturated with cold bitumen (Fig. 4.6), 2) a fluid-supported sand saturated by cold bitumen (Fig. 4.7), 3) a grain-supported sand saturated with hot bitumen (Fig. 4.8), and 4) a fluid-supported sand saturated by hot bitumen (Fig. 4.9). Note that Zimmer"s dry-sand data can only be applied to grain-supported models, as no measurements were made on sand suspensions.

In Figures 4.6 and 4.7, we can see that in all cases the Gassmann predicted velocities for these sands fall below the Reuss and Hashin-Shtrikman lower bounds. This means that Gassmann fluid substitution cannot be used for cold bitumen sands regardless of whether they are grain-supported or fluid-supported. On the other hand, the Solid-Gassmann fluid-substituted models all lie at or above the Reuss average. This means that the Solid-Gassmann fluid substitution method is much more suited to modeling cold bitumen sand than traditional Gassmann fluid substitution is. This is

because the Solid-Gassmann fluid substitution method takes the non-negligible shear modulus of the cold bitumen into account. However, even though it falls within the bounds of a bitumen-sand mixture, it may not reproduce the exact properties of bitumen sand at low temperatures.

Comparing Figures 4.8 and 4.9, we see that the Reuss and Hashin-Shtrikman models both predict the same lower bound for the hot bitumen sands. This is because the heated bitumen, like a traditional pore fluid, has zero shear modulus. Similarly, the Gassmann and Solid-Gassmann fluid-substitution methods both predict the same velocity for hot bitumen sands. Again, since the shear modulus of the heated bitumen is zero, the two fluid substitution methods are identical. Since both methods predict properties that fall within the acceptable bounds, both Gassmann and Solid-Gassmann fluid substitution seem to be viable models for predicting the properties of heated bitumen sands. However, this does not show whether the Gassmann or Solid Gassmann models will predict the absolute velocities for heated bitumen sands.
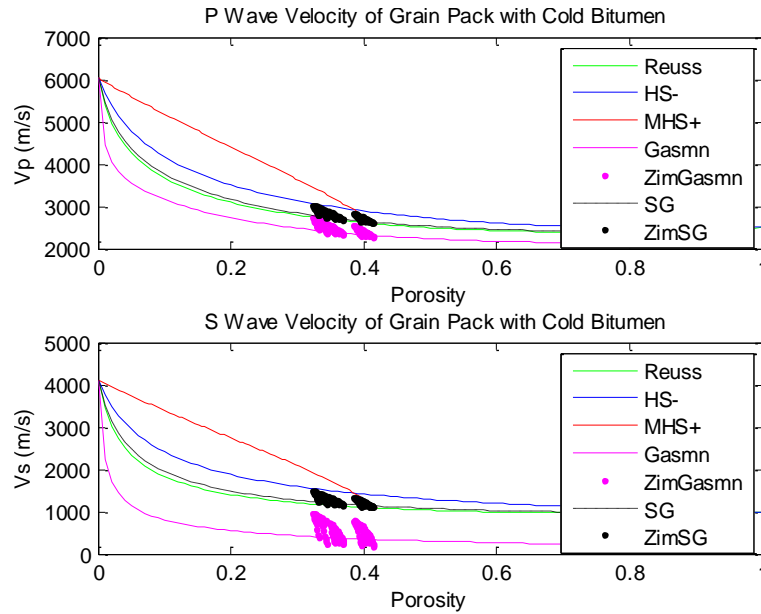
Figure 4.6: Vp (top) and Vs (bottom) modeling results for a grain-supported sand saturated with cold bitumen. Models shown are the Reuss average (green), Hashin-Shtrikman lower and modified upper bounds (blue and red), Gassmann fluid-substituted soft sand (pink) and Zimmer's dry sand data (pink dots), and Solid-Gassmann fluid-substituted soft sand (dashed black) and Zimmer's dry sand data (black dots). The soft-sand model utilizes a pressure of 0.1 MPa, which is the lower pressure limit for Zimmer's dry sand data.
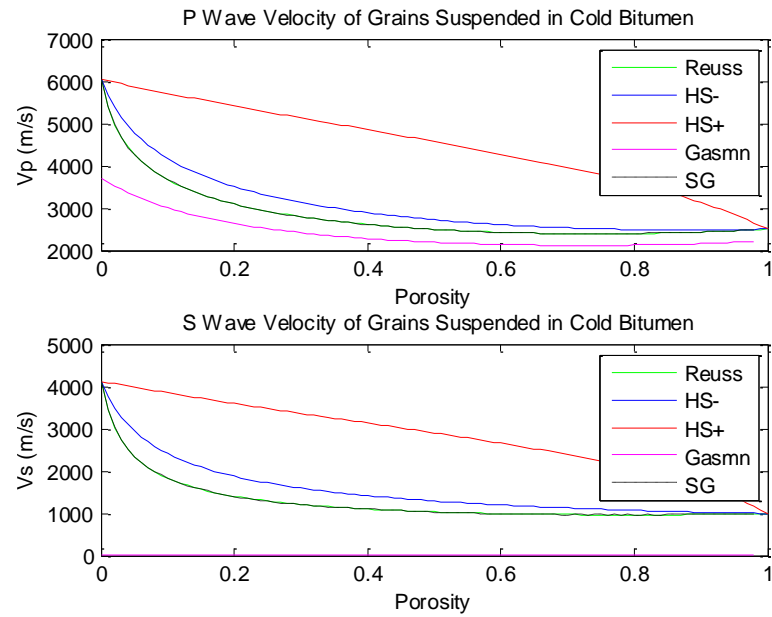
Figure 4.7: Vp (top) and Vs (bottom) modeling results for a fluid-supported sand saturated with cold bitumen. Models shown are the Reuss average (green), Hashin-Shtrikman lower and upper bounds (blue and red), Gassmann fluid substituted soft sand (pink) and Solid Gassmann fluid substituted soft sand (dashed black).
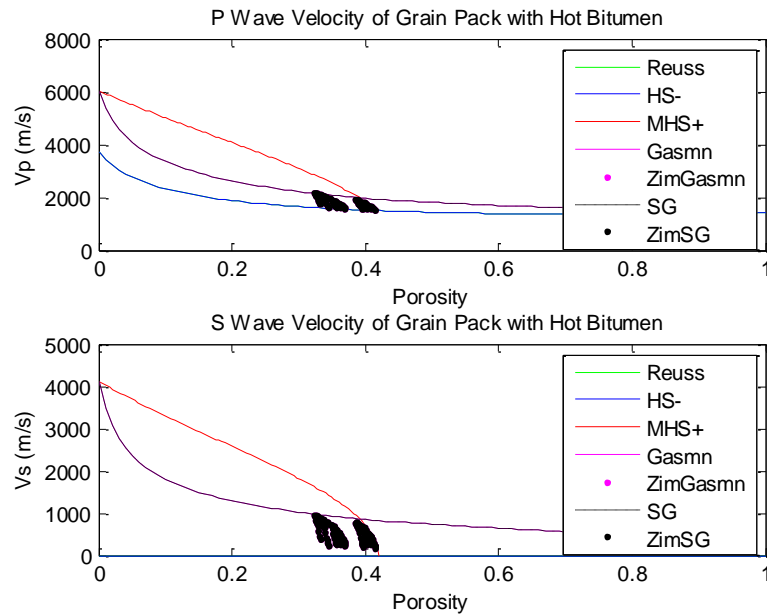
Figure 4.8: Vp (top) and Vs (bottom) modeling results for a grain-supported sand saturated with hot bitumen. Models shown are the Reuss average (green), Hashin-Shtrikman lower and modified upper bounds (blue and red), Gassmann fluid-substituted air-suspended sand (pink) and Zimmer"s dry sand data (pink dots), and Solid-Gassmann fluid-substituted soft sand (dashed black) and Zimmer"s dry sand data (black dots). The soft-sand model utilizes a pressure of 20 MPa, which is the upper pressure limit for Zimmer"s dry sand data.
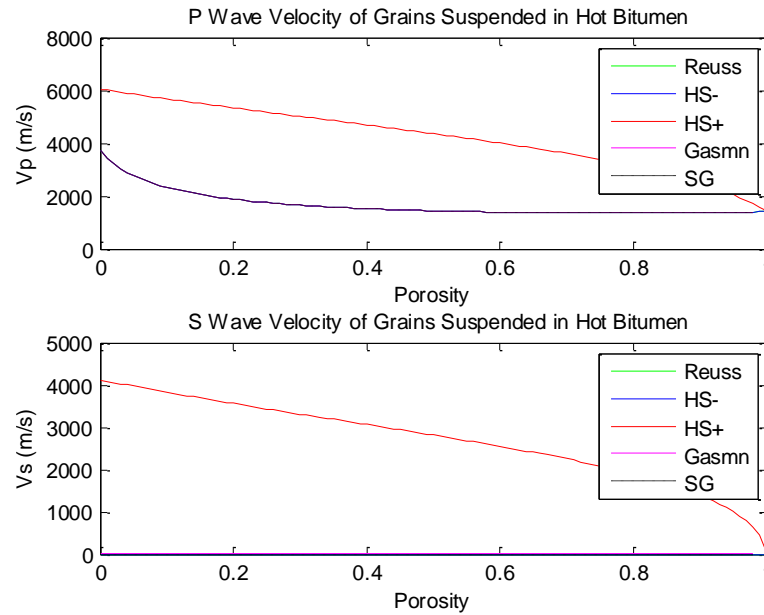
Figure 4.9: Vp (top) and Vs (bottom) modeling results for a fluid-supported sand saturated with hot bitumen. Models shown are the Reuss average (green), Hashin-Shtrikman lower and upper bounds (blue and red), Gassmann fluid-substituted air-suspended sand (pink) and Solid-Gassmann fluid-substituted soft sand (dashed black).

Figures 4.10 and 4.11 show a closer view of Zimmer's measured dry sand data with cold bitumen (Fig. 4.10) and hot bitumen (Fig. 4.11) substituted into the pore space using Gassmann (open circles, dashed lines) and Solid-Gassmann (filled circles, solid lines). The data are also color-coded by effective pressure. Again we see that Solid-Gassmann predicts a higher velocity than traditional Gassmann when the bitumen is cold and has a finite shear modulus; at high temperatures when the shear modulus is zero, the models are the same. These plots also show that both Solid-Gassmann and Gassmann fluid substitution can account for differences in the effective pressure applied to bitumen sands. However, it should be noted that these plots again only show modeling results, and give no indication as to the ability of the models to accurately predict measured bitumen sand velocities over a given temperature range.

In order to determine how well these models predict the properties of bitumen sands over a range of temperatures, we compare them with preliminary ultrasonic velocity measurements of a bitumen sand core plug from a reservoir in Canada (Wolf and Mavko, 2005) (Fig. 4.12). Here we use estimated bulk and shear moduli for pure

bitumen based upon measurements made on a de-watered wellhead emulsion sample from the same reservoir. Figure 4.12 shows that Gassmann fluid substitution drastically underestimates the P- and S-wave velocities of bitumen sand at low temperatures. This is not unexpected, since we have already seen that Gassmann fluid substitution violates the lower bound for bitumen sands at low temperatures. At high temperatures, once the shear modulus of bitumen approaches zero, Gassmann fluid substitution reasonably predicts the measured properties of the bitumen sand. This is because at these temperatures the bitumen is at or above the liquid point and behaves more like a traditional pore fluid.
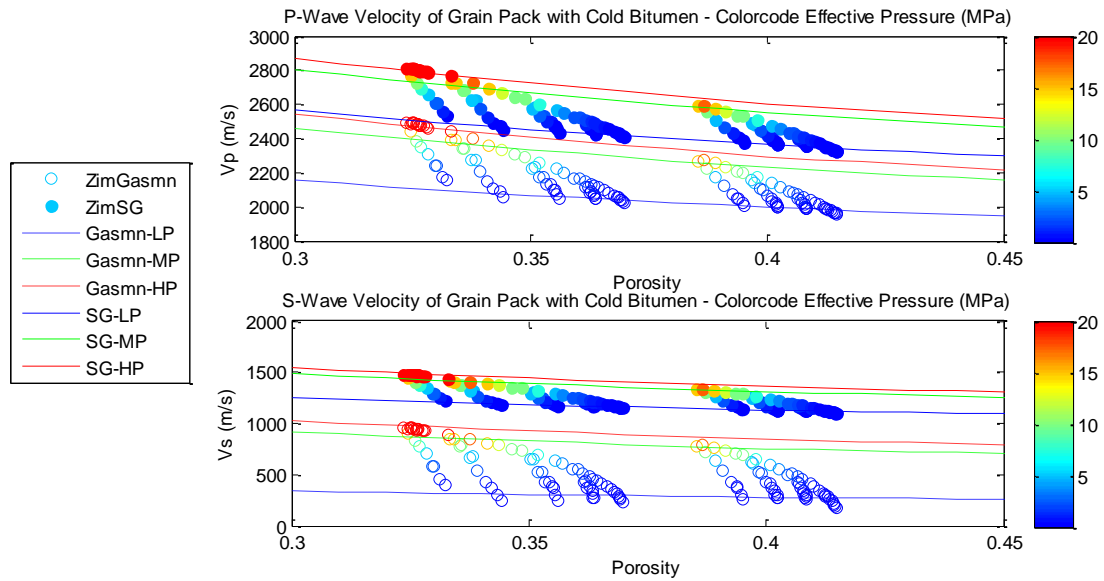
Figure 4.10: Closer view of Zimmer's dry sand measurements with cold bitumen in the pore space, fluid-substituted by Gassmann (open circles) and Solid-Gassmann (filled circles), color-coded by effective pressure. Also shown are the modeling results using the soft-sand model with Gassmann fluid substitution (dashed lines) and Solid-Gassmann fluid substitution (solid lines), with various effective pressures indicated by color.
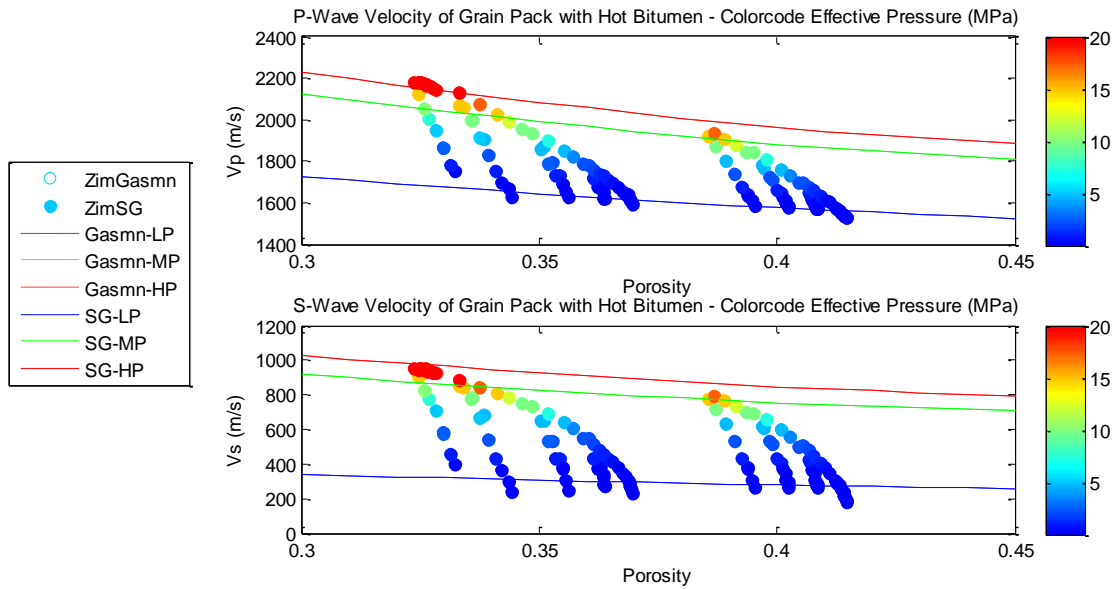
Figure 4.11: Closer view of Zimmer's dry sand measurements with hot bitumen in the pore space, fluid-substituted by Gassmann (open circles) and Solid-Gassmann (filled circles), color-coded by effective pressure. Also shown are the modeling results using the soft-sand model with Gassmann fluid substitution (dashed lines) and Solid-Gassmann fluid substitution (solid lines), with various effective pressures indicated by color.
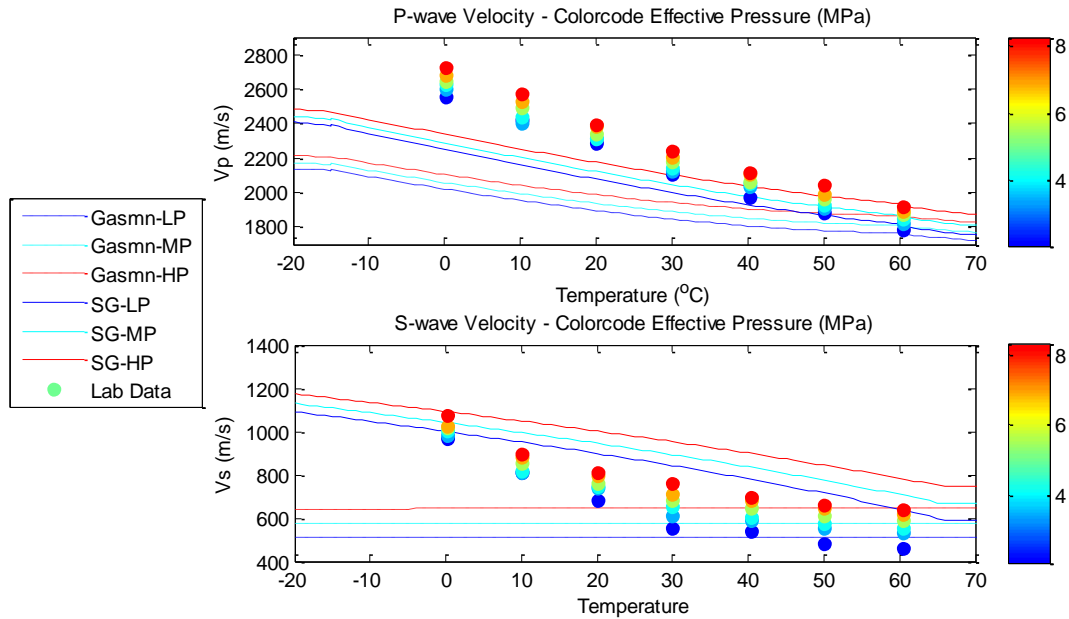
Figure 4.12: Predicted Vp (top) and Vs (bottom) from the soft-sand model with Gassmann fluid substitution (dashed lines) and Solid-Gassmann fluid substitution (solid lines). Also shown are measured ultrasonic velocities of a bitumen sand from Canada (dots). The different colors correspond to different pressures ranging from approximately 2 to 8 MPa (blue to red).

The predicted P- and S-wave velocities of bitumen sand using Solid-Gassmann fluid substitution are better than the prediction of traditional Gassmann, however the measured velocities are still not reproduced. At low temperatures, the P-wave velocity is still underestimated, and though the model matches the S-wave velocity at the lowest temperature, it does not do a good job representing the change in velocity over the entire temperature range. One cause for this may be improper estimates of the bitumen moduli; however, we used the best estimate of properties that we have at this time. At elevated temperatures, we again see that the Solid-Gassmann and traditional Gassmann predictions converge.

4.4.1 Proposed Model for Bitumen Sands

Given that neither traditional Gassmann nor Solid-Gassmann fluid-substitution methods predict bitumen sand velocities across a wide temperature range, we propose a new heuristic model to predict bitumen sand velocities. Given the phase transitions that heavy-oil and bitumen undergo during heating, we attempt to include these properties in our model. Below the glass-point, bitumen can be thought of as a solid. We can effectively model this mixture of solid bitumen and sand as unconsolidated sand cemented by bitumen. The bitumen cement can be added to the pore space using the cemented sand model (Dvorkin, 1996). Similarly, above its liquid point bitumen acts very similar to a conventional hydrocarbon fluid, and Gassmann fluid substitution can be used to add the bitumen into the pore space. This then leaves only the zone where the bitumen is acting as a quasi-solid without a sufficient model to predict the behavior of the bitumen sand. Provided that the glass- and liquid-point temperatures are known, we propose calculating the velocity by means of a weighted average between these two points as follows:

$$V_P = (1-w)V_{P_C} + wV_{P_G} \tag{1}$$

$$V_S = (1-w)V_{S_C} + wV_{S_G} \tag{2}$$

$$w = \frac{T - T_{Glass}}{T_{Liquid} - T_{Glass}} \tag{3}$$

where V_{P_C} is the cemented sand velocity, V_{P_G} is the Gassmann fluid substituted velocity, and *w* is the weighting factor that varies from zero to one as we move from the glass-point temperature to the liquid-point temperature.

Figure 4.13 shows the results of the proposed model. At low temperatures, the model underpredicts the P-wave velocity, while at the same time, it overpredicts the S-wave velocity. Again, this may be related to improper estimates of the bulk and shear moduli of bitumen at low temperatures. However, the model does a decent job of reproducing the measured velocities, and for P-wave velocities it maintains a good prediction as the temperature is increased. One downfall of the model is that the pressure sensitivity of the model is lost as the temperature is decreased. This is because the cemented sand model is not affected by pressure, and as a result, as the weighting for the cemented sand model increases, the pressure sensitivity decreases. Despite this fact, the proposed model does show some promise for predicting the measured velocities of the bitumen sand samples over a wide range of temperatures, and with some modifications may prove to be useful.
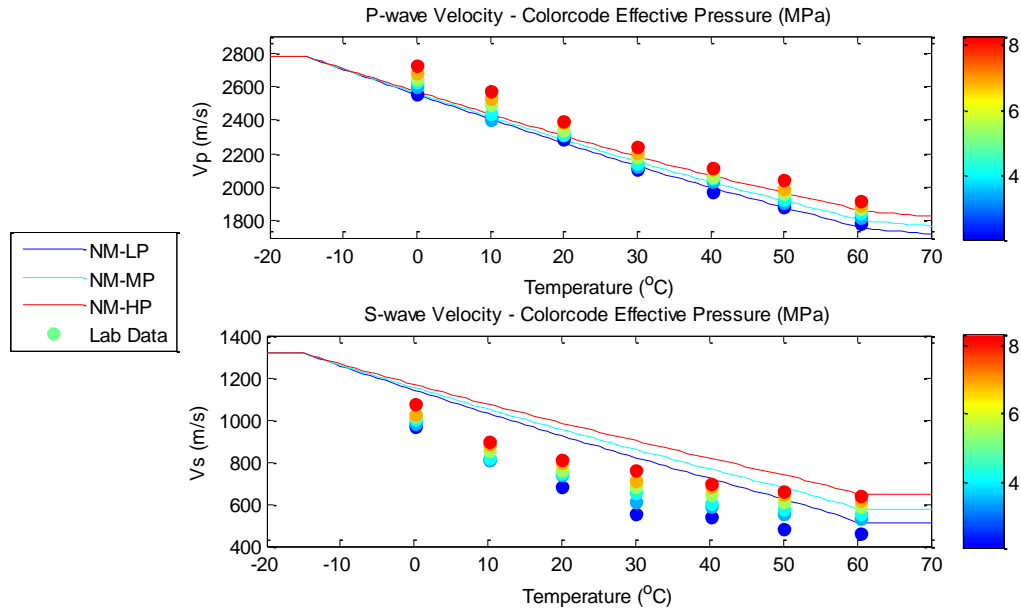
Figure 4.13: Predicted Vp (top) and Vs (bottom) from the proposed heuristic model for bitumen sands. Also shown are measured ultrasonic velocities of a bitumen sand from Canada (dots). The different colors correspond to different pressures ranging approximately from 2 to 8 MPa (blue to red).

4.5 Discussion

Though the dataset available for calibrating bitumen and bitumen sand models is quite small and insufficient in detail, comparing these data with the aforementioned models provides insights into the validity of modeling approaches when first trying to develop a robust method for linking bitumen sand properties to seismic properties. BAM, Solid-Gassmann and the newly proposed model applied to bitumen sands show some promise in providing this crucial link. None of the methods flawlessly predicts both the P- and S-wave velocities. However, with a more robust dataset including better-defined fluid properties over a wide range of temperature and pressure, we will be able to further test our hypothesis based on these models. This will allow us to determine which method provides the best estimates of bitumen sand properties given the mineralogy, fluid properties and distribution of fluids in the pore space. Also, with more data we will be able to determine whether any of the models can do a satisfactory job, or if we must develop a whole new modeling methodology.

Chapter 5
Modeling attenuation and velocity dispersion in bitumen-saturated sand

"Science is the century-old endeavor to bring together
by means of systematic thought the perceptible
phenomena of this world into as thorough-going an
association as possible."
~Albert Einstein

5.1 Abstract

Attenuation and velocity dispersion can be attributed to several different mechanisms in saturated rocks. These include, but may not be limited to, interactions between the fluid and rock matrix, as well as inelastic properties of the saturating fluids themselves. One of the major controls on the effect of these mechanisms is the

viscosity of the saturating fluid. This is especially true when considering heavy-oil or bitumen reservoirs. This paper investigates the predicted effects of various attenuation mechanisms at frequencies ranging from seismic to ultrasonic and the impact that viscosity has on them. From this analysis we find that with highly viscous fluids, any observed attenuation over the entire frequency band should be attributed to inelastic properties of the pore fluid. For highly viscous fluids, velocity dispersion from the squirt mechanism will always be present. If the viscosity if lowered sufficiently, the Biot mechanism will begin to affect velocity and attenuation measured at ultrasonic frequencies. Similarly, if the viscosity is lowered sufficiently, the squirt mechanism will begin to affect velocity and attenuation measurements at both seismic and sonic frequencies. With decreasing viscosity, it also appears that velocity dispersion and attenuation will increase due to the inelastic properties of the pore fluid; however, additional measurements are needed in order to determine the magnitude of this effect.

5.2 Introduction

There has been much research done in the past regarding velocity dispersion and attenuation in rocks. Two results of this work are the Biot and Squirt models, which are used to estimate the amount of velocity dispersion and attenuation expected due to interactions between rock and pore fluid (Biot, 1956; Dvorkin et al., 1995; Mavko and Nur, 1975). However, these models differ in how they predict the effects of viscosity, a fact that is very important to consider when dealing with bitumen reservoirs. Biot's theory states that dimensionless attenuation is proportional to frequency and the inverse of viscosity, whereas the squirt mechanism is proportional to the product of frequency and viscosity. This is important for seismic and ultrasonic measurements of bitumen sands, because the pore fluid can have viscosities in excess of 10^6 cP. Obviously this needs to be taken into consideration if attenuation and dispersion estimates are to be made. In addition to the effects from fluid-rock interaction, the fluid itself, i.e. bitumen, can also contribute to attenuation and dispersion without the presence of the rock frame. Previous measurements (Batzle et al., 2004) have

indicated that as the bitumen's viscosity decreases, its capacity to propagate shear waves is severely impeded, and the velocity of the waves is also reduced.

These effects and their relationships with viscosity are important to consider, because reservoir managers commonly use thermal methods to reduce bitumen viscosity as an aid in production. The aim of this study is to model the attenuation and velocity dispersion of bitumen sands for a variety of fluid viscosities over a frequency range spanning seismic to ultrasonic frequencies.

5.3 Bitumen Modeling

Bitumen is mainly comprised of asphaltenes and maltenes. The structure-based model of Lesueur et al. (1996) represents bitumen as a colloidal dispersion of a temperature-dependent solid in a liquid phase. The solid phase is an asphaltene core, which is covered by a maltene solvation shell, the variable thickness of which depends on temperature. The liquid phase is the remainder of the maltene fraction that is not in solid form (Figure 5.1).
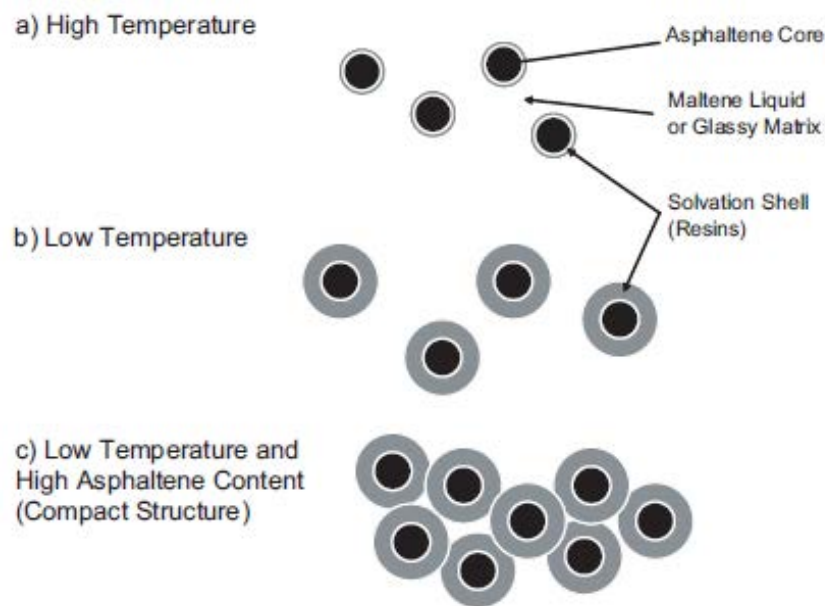
Figure 5.1: Structural model depicting the colloidal nature of bitumen. The asphaltene core is surrounded by a maltene shell, the thickness of which is determined by the temperature (a, b). For high-asphaltene content, the colloidal particles form a compact structure at temperatures above the glass point of the liquid fraction (c). Modified from (Lesueur et al., 1996).

Based on this structure, a bimodal model for shear properties of bitumen is proposed that describes bitumen as a Newtonian viscous fluid at high temperatures, and as a viscoelastic material at low temperatures. The bulk modulus is assumed to be elastic over the entire temperature range. This model is supported by observations made in previous bitumen measurements (Wolf and Mavko, 2005), where bitumen supported the propagation of an ultrasonic shear wave at low temperatures, indicating an instantaneous elastic material response. However, as the temperature was raised, and hence the viscosity decreased, the ability to propagate a shear wave was severely impeded. This suggests that at lower viscosities bitumen acts as a viscous fluid.

There are a number of viscoelastic models that could be used to model the shear properties of bitumen at low temperatures. At this time we believe using a Maxwell viscoelastic model (Christensen, 2003) to represent the shear modulus is a good approximation. This model predicts that with decreasing viscosity the shear modulus will decrease and attenuation will increase (Figure 5.2); both of which were observed in ultrasonic shear-wave pulse transmission experiments in bitumen (Wolf and Mavko, 2005). In addition, the Maxwell solid behaves as a viscous fluid in the low-frequency limit, which is also thought to be true of bitumen.
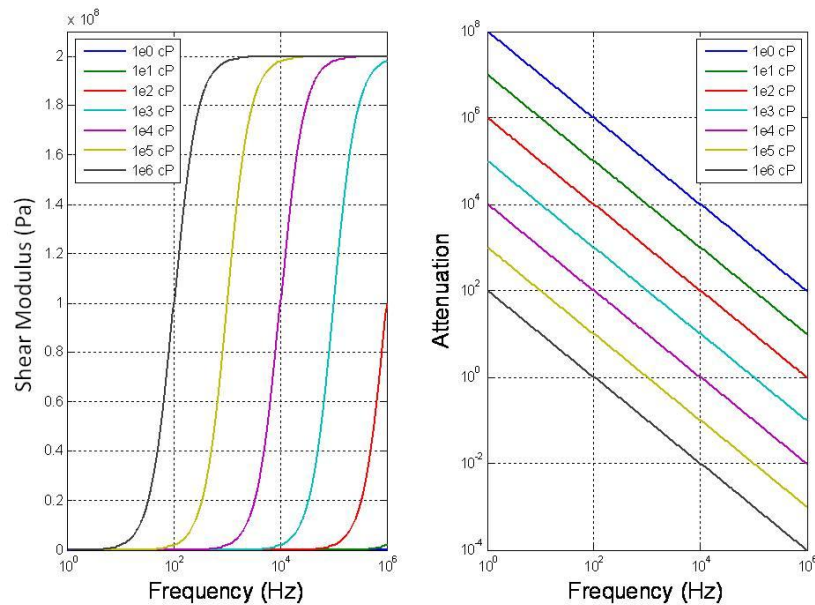
Figure 5.2: Shear modulus (left) and attenuation (right) versus frequency from a Maxwell Solid viscoelastic model. Elastic modulus input as 0.1 GPa, and viscosity range shown in legend.

5.4 Fluid-Rock Interaction

In order to determine which dispersion mechanisms will be dominant at certain frequencies, it is important to understand where the critical frequency for each particular mechanism lies. For squirt phenomena, the characteristic frequency (f_c) is approximated by the relation

$$f_{c_{squirt}} \cong \frac{K_0 \alpha^3}{\eta}$$

where K_0 is the mineral bulk modulus, α is the pore aspect ratio, and η is the viscosity of the pore fluid (Mavko et al., 1998). Similarly, the characteristic frequency of the Biot mechanism is approximated by

$$f_{c_{biot}} \cong \frac{\varphi \eta}{2\pi \rho_{fl} \kappa}$$

where φ is the porosity, ρ_{fl} is the pore fluid density, and κ is the permeability. From these formulas it is obvious that increasing viscosity will have an opposite effect on the characteristic frequency of the two dispersion mechanisms. The characteristic frequencies for both mechanisms were calculated using parameters that span a broad range of reservoir properties for heavy-oil and bitumen sands (Table 5.1).

Table 5.1: List of properties and typical values or ranges used for characteristic frequency modeling.

Property	Value/Range
φ	$0.2 - 0.4$
ρ_{fl}	1080 kg/m^3
κ	$0.1 - 5 \text{ D}$
K_0	36.6 GPa
η	$1 - 10^6 \text{ cp}$

The results of the characteristic frequency modeling are shown in Figure 5.3. Examining the figure reveals that the characteristic frequency for squirt phenomena will always be below the megahertz frequency range used in the laboratory for the

given reservoir parameters. This means that for all measurements in the laboratory, the squirt mechanism will contribute to velocity dispersion, but not to any observed attenuation. The modeling also shows that the Biot mechanism may contribute to both velocity dispersion and attenuation for ultrasonic laboratory measurements. If the permeability of the sample is sufficiently high and the viscosity of the fluid is low, then the characteristic frequency of the Biot mechanism is ultrasonic.
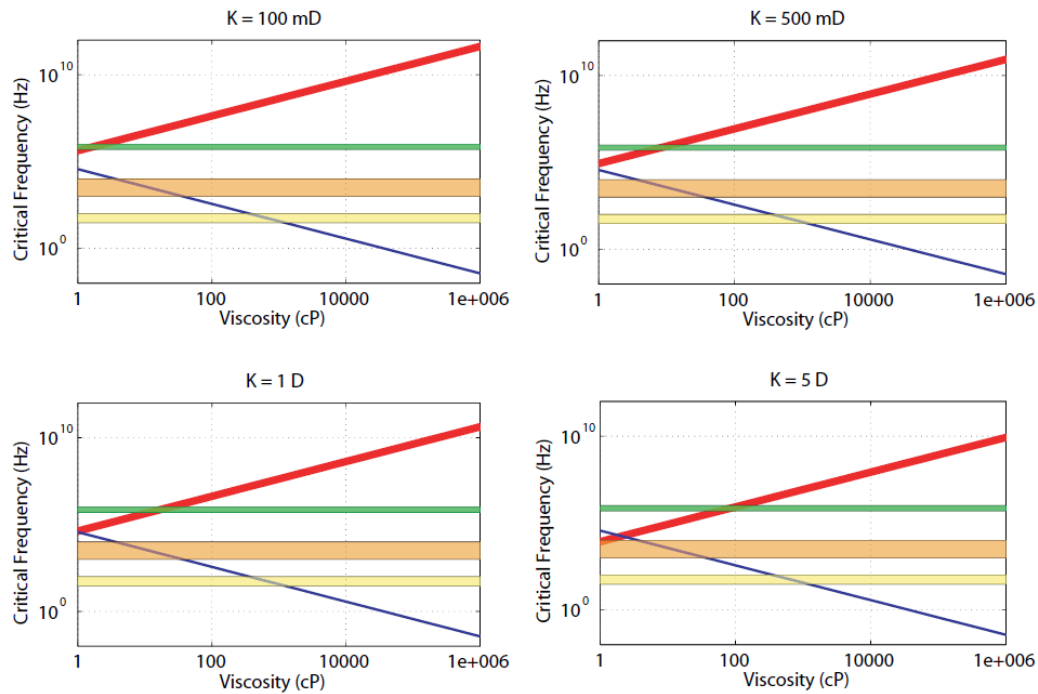
Figure 5.3: Critical frequencies for the Biot (red) and squirt (blue) mechanisms. Highlighted on each plot are the seismic frequency range (yellow), well-log frequency range (orange) and ultrasonic frequency range (green). Each plot corresponds to a different permeability, listed above the plot.

Though a permeability of 5 Darcys is unrealistically high for conventional oil or gas reservoirs, this may not be the case for bitumen reservoirs. Heavy-oil and bitumen reservoirs are typically unconsolidated sand reservoirs, and their permeabilities can be quite high; measured values of permeability from core samples can be 5 Darcys or higher. However, this is likely due to gas exsolution and core disturbance during sample retrieval, and in-situ permeabilities are likely closer to 1 Darcy (Dusseault, 1980). Examining the plot corresponding to 1 Darcy permeability in Figure 5.3 shows

that even with this high permeability, fluid viscosities must still be within the range of 10-30 cp for the characteristic frequency to move into the ultrasonic range. Based on viscosity-temperature relationships for heavy and extra-heavy oils (Beggs and Robinson, 1975; DeGhetto et al., 1995), the temperature required to obtain a bitumen viscosity within this range is extremely high, and it may not be feasible in the lab. However, if the sample has significant water saturation, these low viscosities may be reached at lower temperatures.

The analysis of characteristic frequencies for the squirt mechanism shows that it will always contribute to velocity dispersion for samples saturated with very viscous fluids at ultrasonic frequencies (Figure 5.3). However, attenuation effects from the squirt mechanism should be minimal, because the characteristic frequency is much lower than the ultrasonic regime. On the other hand, at logging and seismic frequencies the effect of the squirt mechanism will greatly depend on the saturating-fluid viscosity. If the viscosity is ~800 cP then the attenuation at seismic frequencies due to squirt should be at a maximum, and dispersion effects will begin to be seen. For the same to occur at logging frequencies, the viscosity of the fluid must be further reduced to ~20 cP. The Biot modeling demonstrates that in order for this mechanism to contribute to velocity dispersion and attenuation, the samples must have a high permeability and the saturating fluid a low viscosity. However, even if these conditions are satisfied, the Biot mechanism will only affect measurements performed at ultrasonic frequencies.

The previous analysis indicates that the Biot and squirt mechanisms can have various effects on measurements made at different frequencies on samples with varying viscosities. Thus, it is worthwhile to examine the influences of these mechanisms under certain conditions. This will be of particular importance when trying to extend measurements made at ultrasonic frequencies in the laboratory to either seismic or logging frequencies in the field. In order to model the squirt mechanism over a wide range of frequencies, we used the method proposed by Mavko and Jizba (1991) to calculate the modified dry frame modulus. The dry frame was then saturated with fluid using Gassmann fluid substitution (Gassmann, 1951). The Biot

mechanism was modeled using the method proposed by Biot (1956). For further details on the methods the reader is referred to either the aforementioned papers or Mavko et al. (1998). Both models are Gassmann-consistent in the low frequency range, and as such, they both give the same velocity for the relaxed state; however, individually they do not give an accurate representation of the total dispersion and attenuation over all frequencies. Because velocity dispersion is a cumulative effect, in order to obtain the total velocity dispersion, the unrelaxed modulus from the squirt model can be used as input into the Biot model. This combined result will allow us to estimate the total dispersion for the entire frequency range.

Whether heating a bitumen reservoir in the field to aid production or a core sample in the lab to simulate this effect, the factor that we change most drastically is the viscosity of the pore fluid. To examine the role of changing viscosity in the Biot and squirt mechanisms, we modeled a wide range of viscosities, from water (1 cP) to extremely viscous bitumen (10^6 cP). The combined results of modeling both the P- and S-wave attenuation and velocity dispersion with the Biot and squirt models are shown in Figures 5.4a through d. The modeling was performed with bitumen sand consisting entirely of quartz, with a permeability of 1 Darcy, porosity of 40%, and varying bitumen viscosity. The Biot model contributes velocity dispersion and attenuation at higher frequencies than the squirt model, as expected from the characteristic frequency analysis. The peak attenuation from the squirt (magenta) and Biot (black) mechanisms converge towards one another as the viscosity decreases, until they are nearly coincident as the viscosity drops to 1 cp. In addition, the figure demonstrates that depending on the fluid viscosity, the amount of attenuation expected at a given frequency can be drastically different. At high viscosities, one would expect no attenuation due to either the Biot or squirt mechanism at ultrasonic frequencies; however, if the bitumen were heated enough to drop the fluid viscosity to 1 cP, or if the pore fluid were replaced by water, the attenuation should be expected to increase substantially.
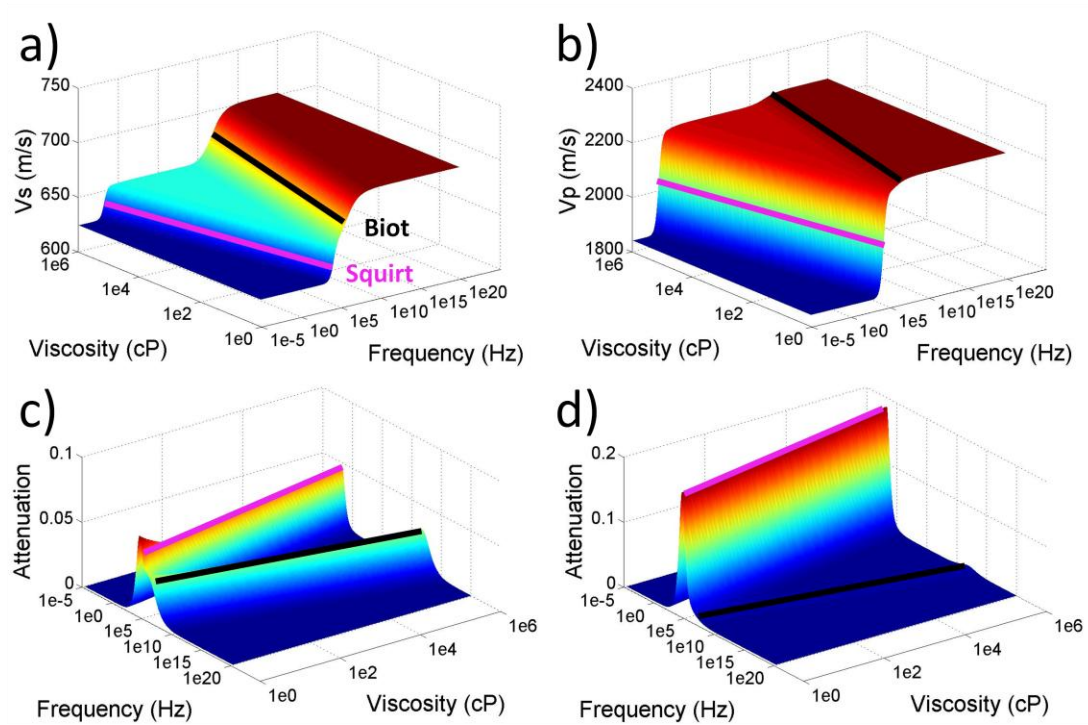
Figure 5.4: a) Velocity dispersion for S-waves, b) velocity dispersion for P-waves, c) attenuation for S-waves and d) attenuation for P-waves for varying fluid viscosity and frequency. The characteristic frequency is shown for squirt flow attenuation in magenta, and for Biot in black.

5.5 Conclusions

In samples with low permeability and very high-viscosity fluid, attenuation due to either the squirt or Biot mechanisms is negligible at all frequencies of interest, but attenuation from the pure viscoelastic fluid may be important, as seen in Figure 5.2. In addition, under these conditions the only fluid-rock mechanism that will contribute to velocity dispersion is squirt. However, if measurements are made on heated samples with high permeability, the Biot mechanism may begin to affect measurements made at ultrasonic frequencies, and the squirt mechanism may no longer have an effect on the measurements at either seismic or sonic frequencies.

At this time, modeling bitumen as a Maxwell solid at low temperatures and a Newtonian viscous fluid at elevated temperatures appears to be the best option for modeling the attenuation and dispersion due to the fluid alone. However, for this hypothesis to be verified, more experimental results are needed for both bitumen itself and bitumen-saturated sands. By measuring bitumen properties over a wide temperature range at high frequencies in the laboratory we hope to quantify the effects that are due to changes in the bitumen itself, and not to fluid-rock interactions. Carrying out these experiments at high frequencies should ensure that measured effects are due solely to bitumen property changes. A further challenge in future studies will be how to separate the fluid-rock interaction effects from the pure fluid effects under conditions where both mechanisms are actively influencing measurements. We hope that by measuring the changing ultrasonic properties of the fluid and the fluid-rock systems individually, a way to separate the two effects will become evident.

Chapter 6
P-to-S converted-wave elastic impedance for heavy-oil reservoir characterization and monitoring

The important thing in science is not so much to obtain new facts as to discover new ways of thinking about them.

~Sir William Bragg

6.1 Abstract

We present a methodology to characterize and monitor the state of a heavy-oil reservoir undergoing thermal production. Several synthetic examples are presented in order to establish trends for shear-wave velocity and density changes in cross-plots of P-to-S converted-wave elastic impedance (PSEI) calculated at various angles. If large-angle data are available, then there is a separation between the velocity and density trends, and this can be used to investigate the fluid content and state of a reservoir.

Modeling indicates that PSEI can be effectively utilized to discriminate between hot and cold regions of the reservoir, as well as to delineate areas of steam chamber formation.

Converted-wave seismic data is used to invert for PSEI for several synthetic cases. The synthetic cases are intended to mimic the processes of thermal production within heavy-oil or bitumen reservoirs and capture the rock properties of the reservoirs using rock-physics models. These properties are then used to synthesize converted-wave seismic data at near and far offsets. These data are then inverted for PSEI values at specific angles of incidence. The results show that the methodology can reveal heated zones within the reservoir as well as areas where steam chambers have formed.

The synthetic results suggest that it is possible to gain insight into the temperature and state of the reservoir remotely by inverting converted-wave seismic data collected from a reservoir that is undergoing thermal production. This knowledge can greatly aid in efficiently producing the reservoir fluids and maximizing recovery, as well as helping to guide any infill drilling that may be required in order to fully sweep the reservoir.

6.2 Introduction

In certain cases pertaining to reservoir characterization and monitoring, traditional P-to-P reflection seismic data does not provide adequate information on the elastic rock properties to allow accurate characterization of a reservoir and its fluids. In these cases, converted P-to-S waves have been proposed as a way to gather more valuable information to help constrain reservoir properties. Various successful applications of converted waves, summarized by Stewart *et al.* (2003), include imaging improvements, characterizing fluids and lithology, and reservoir monitoring. There have been various ways of using converted-wave information, but for our purposes we will focus on P-to-S converted-wave elastic impedance (PSEI), which was first derived by Gonzalez et al. (2003). After deriving the formulation for PSEI, Gonzalez (2006) uses it to help identify lithology and partial gas saturation in reservoirs. In this work, we use PSEI to gain insight into the temperature of the reservoir, as well as fluid saturations, including

the formation of steam chambers during steam-assisted production of bitumen or heavy oil.

Bitumen sand reservoirs differ from conventional hydrocarbon reservoirs in both their physical characteristics and how they are commonly produced. Unlike conventional reservoir fluids, bitumen is extremely viscous—even solid-like—at low temperatures, while at elevated temperatures it is less viscous, and its shear modulus approaches zero (Batzle et al., 2006, Han et al., 2006). The temperature-dependent characteristics of bitumen enable it to support the propagation of shear waves at low temperatures and also make thermally-enhanced recovery a valuable production method in bitumen reservoirs.

The ability of bitumen to support shear waves also has an effect on the properties of bitumen-saturated sand. Previous velocity measurements and modeling have shown that cold bitumen sand can be modeled as sand cemented by bitumen (Wolf and Mavko, 2005). The bitumen 'cement' acts to stiffen the sand at low temperatures, which results in higher shear-wave velocities than in sand saturated with water, heated bitumen, or lighter oil. This shear-wave velocity dependence on fluid properties makes the use of converted P-to-S (PS) waves a viable option for characterizing bitumen reservoirs. With this approach it should be possible to find both areas where bitumen saturation is low and areas of relatively low bitumen viscosity within the reservoir.

Previous measurements also show that the velocity of shear waves in bitumen sand is highly temperature-dependent (Wolf and Mavko, 2005, Han et al, 2006). Since bitumen reservoirs are often produced by thermal means to reduce the viscosity of bitumen in the reservoir, monitoring of the heated zones within the reservoir is important. Since the shear modulus of bitumen changes so drastically from a solid-like to a fluid-like state as temperature increases, PS waves may provide a way of monitoring the temperature of the reservoir remotely. In addition, the formation of steam chambers within the reservoir will result in changes in reservoir densities. These density changes in the reservoir may also be detected by converted waves, as was shown by Gonzalez et al. (2003) for a case where density changes were associated with small gas saturations. The drastic changes in shear-wave velocity and density

suggest that P-to-S converted-wave elastic impedance, or PSEI, will be an effective way to characterize and monitor heavy-oil reservoirs being produced by thermal means.

PSEI was defined by Gonzalez *et al.* (2003) as follows:

$$PSEI(\theta_P) = \rho^c V_S^d ,$$ (1)

where

$$c = \frac{K \sin \theta_P}{\sqrt{\frac{1}{K^2} - \sin^2 \theta_P}} \left(2 \sin^2 \theta_P - \frac{1}{K^2} - 2 \cos \theta_P \sqrt{\frac{1}{K^2} - \sin^2 \theta_P} \right) ,$$ (2)

$$d = \frac{4K \sin \theta_P}{\sqrt{\frac{1}{K^2} - \sin^2 \theta_P}} \left(\sin^2 \theta_P - \cos \theta_P \sqrt{\frac{1}{K^2} - \sin^2 \theta_P} \right) .$$ (3)

Here K is the average V_S/V_P, θ_P is the incident P-wave angle at the conversion point, ρ is the density and V_S is the shear-wave velocity.

They also showed that the incidence angle at which PSEI gives a direct estimate of density is given by:

$$\theta_{PD} = \arctan\left(\frac{1}{K} \right),$$ (4)

$$PSEI(\theta_{PD}) = \rho .$$ (5)

This direct estimate of density is due to the behavior of the exponents c and d. Figure 2.2 (from Gonzalez, 2006) shows the values of c and d over a range of incidence angles and at two different values of K. We observe that at large angles the density and velocity exponents decouple from each other. This leads to the value of

PSEI being due mainly to the density term at large offsets; at $\theta_P = \theta_{PD}$ the value of PSEI is an exact estimate of density, since the value of $c = 1$ and $d = 0$.

At smaller angles, less than -10°, the exponents are roughly equal, so both terms contribute to the obtained PSEI value. It is at these smaller angles where information about the shear velocity of the reservoir, and therefore, the temperature of the reservoir is contained. Though the value of PSEI at these smaller angles does not give a direct estimate of shear-wave velocity, the following analysis will demonstrate its utility in discriminating between various shear-wave velocities.
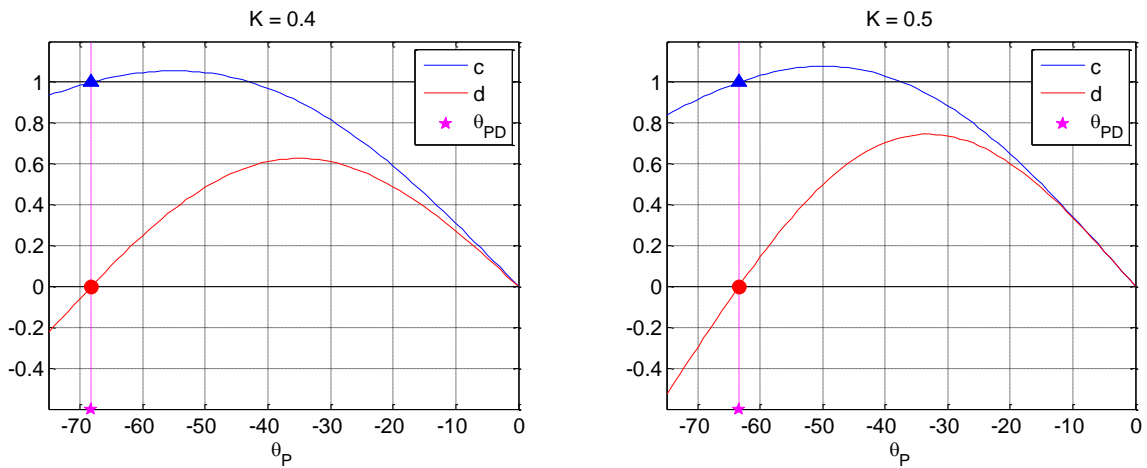
Figure 6.1: Plots of the value of exponents c and d versus angle for two different values of K.

To explore the behavior of PSEI with shear-wave velocity (V_S), we calculate the values of PSEI at various angles while varying V_S between 500 and 2100 m/s and holding density constant. Figure 6.2 shows cross-plots of these PSEI values at near angles (-10°) versus the density-indicator (θ_{PD}), far (-50°) and mid-range (-30°) angles. The top row shows PSEI(-10°) vs. PSEI(θ_{PD}), the middle row shows PSEI(-10°) vs. PSEI(-50°) and the bottom row shows PSEI(-10°) vs. PSEI(-30°). The left column is color-coded by density, and the right column is color-coded by shear-wave velocity. These cross-plots show that if PSEI data can be collected at exactly θ_{PD}, the change in velocity is revealed by movement along the PSEI(-10°) axis. However, obtaining data at an angle this accurate is not feasible for real-world applications. The remaining four plots show that even though it is not possible to obtain data at θ_{PD}, it is still possible to
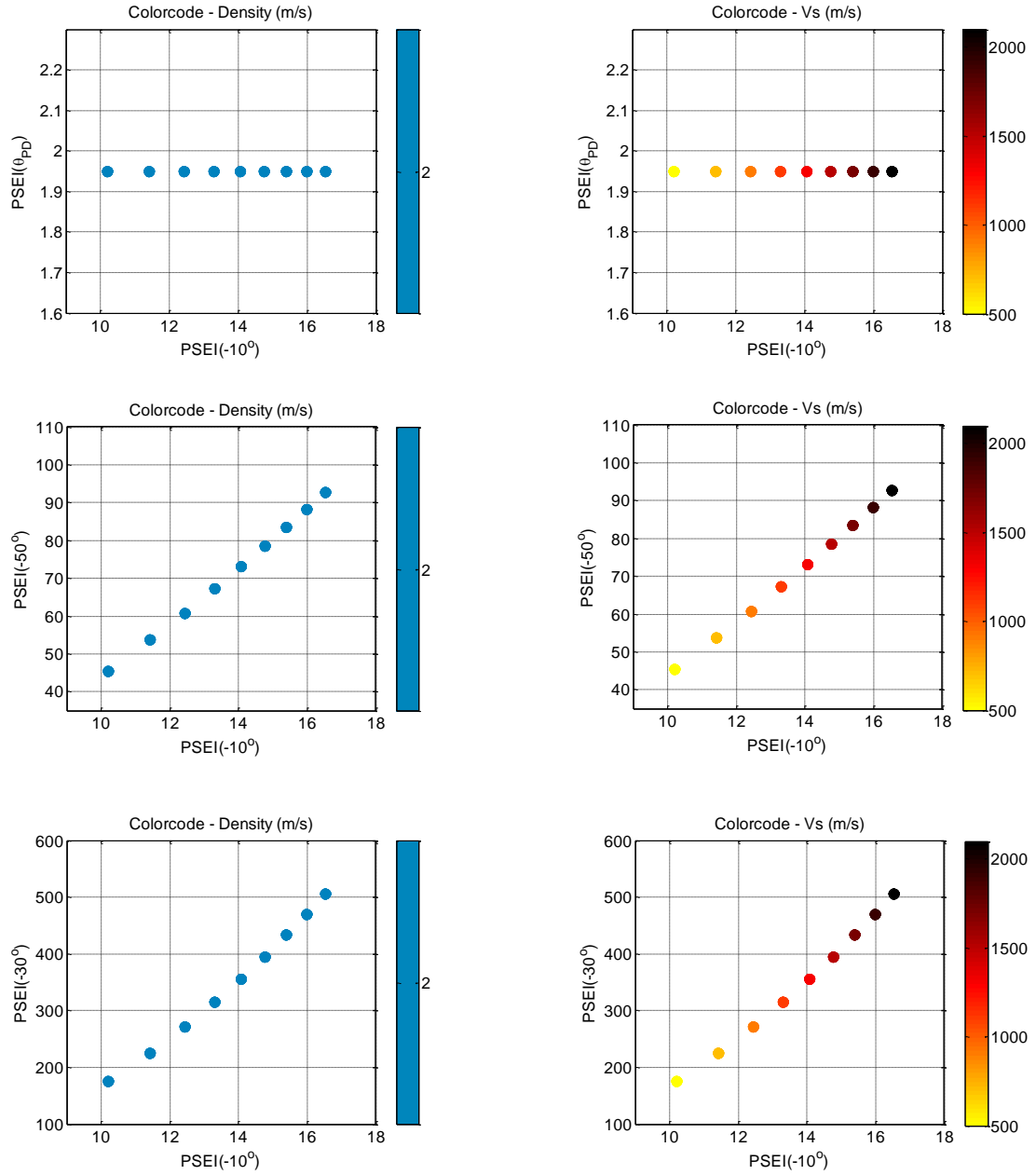
Figure 6.2: Cross plots of near angle PSEI versus PSEI at angles varying from the density-indicator angle to -10° for velocities ranging from 500 to 2100 m/s and constant density of 2.5 g/cc.
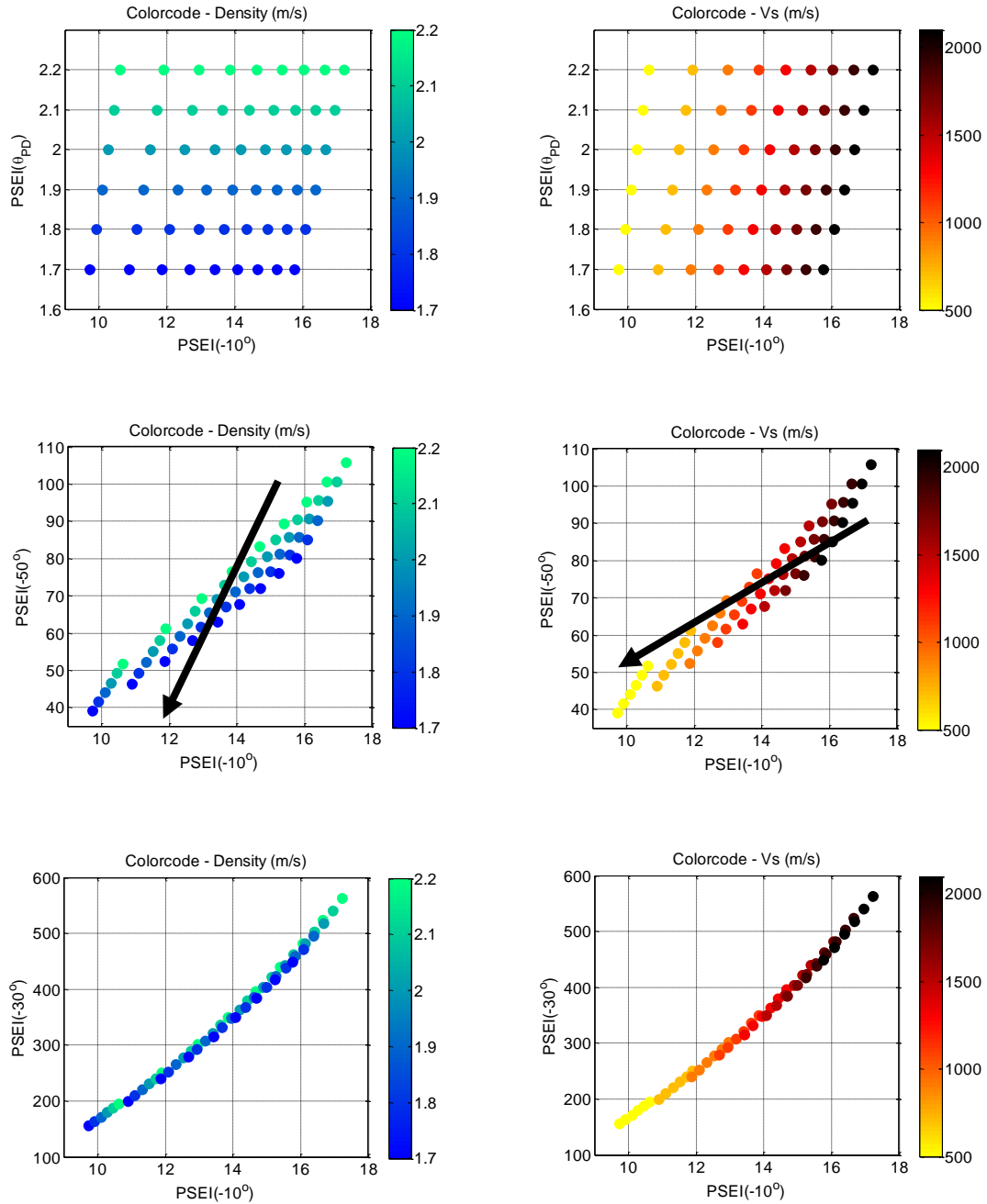
Figure 6.3: Cross plots of near angle PSEI versus PSEI at angles varying from the density-indicator angle to -10° for velocities ranging from 500 to 2100 m/s and densities of 2 to 3g/cc. Black arrows indicate the trends for decreasing density and velocity on respective plots.

observe shear-wave velocity changes on PSEI cross-plots. However, in this case the velocity changes are represented by movement along both axes, not just along the PSEI(-10°) axis.

As mentioned previously, at near angles the value of PSEI has contributions from both the density and velocity terms. Figure 6.3 explores the relationship between PSEI and simultaneously changing density and shear-wave velocity values. The same cross-plots are shown as in Figure 6.2, but the density is now varied from 2 to 3 g/cc in addition to varying the shear-wave velocity.

Figure 6.3 highlights the fact that if PSEI at θ_{PD} is known, velocity changes are revealed by movement solely along the PSEI(-10°) axis. However, here we can see that there is also density-change information contained along the PSEI(-10°) axis, as should be expected, since both exponents, c and d, are non zero. A more practical cross-plot to examine is between the values of PSEI at near (-10°) and far (-50°) angles, since it is unlikely that PSEI at the exact angle θ_{PD} can be determined accurately. This cross-plot illustrates specific identifiable trends that represent both relative density and velocity changes. These are indicated by arrows on the respective plots. If far-offset data are unavailable and only mid-range angles are on hand (e.g. -30°), this ability to discriminate between the shear velocity trend and the density trend is lost. Examining the last row in Figure 6.3 shows that the PSEI data collapse toward a single curve when comparing PSEI values at near (-10°) and mid (-30°) angles. With only a single curve, it is impossible to differentiate between the two effects.

As a more practical example, Figure 6.4 shows a cross-plot of PSEI at near angles vs. far angles from a well log located in a bitumen reservoir in Canada. The original well-log data is shown in black. Also shown are the same data with V_S reduced in 10% decrements to 50% of the original value, (indicated by colors ranging from red to yellow) and with ρ reduced in 5% decrements to 75% of the original value (indicated by colors ranging from green to blue). Here we can again see the two distinct trends for velocity and density changes. Ideally, the far angle should be as close to the value of θ_{PD} as possible, as this will result in the maximum decoupling, or separation, between the two trends.

Provided that the converted-wave data can be collected at large angles of incidence in order to decouple the density from the shear-wave velocity, it should be possible to use a cross-plot of PSEI(far) vs. PSEI(near) to differentiate between density and shear-wave velocity changes upon heating of a bitumen reservoir. Heating a reservoir will decrease the ability of the bitumen to support shear waves and will also result in a weakening of the bitumen 'cement' surrounding grains. This causes a decrease in the shear velocity of the reservoir. Another phenomenon that commonly occurs when heating reservoirs with steam is the development of a steam chamber. Replacing the fluid in the reservoir with steam will reduce the density of the reservoir. Both the velocity and density changes within the reservoir should be seen by cross-plotting PSEI at near and far angles, which suggests that PSEI analysis can be an effective way of monitoring steam-heated bitumen reservoirs.
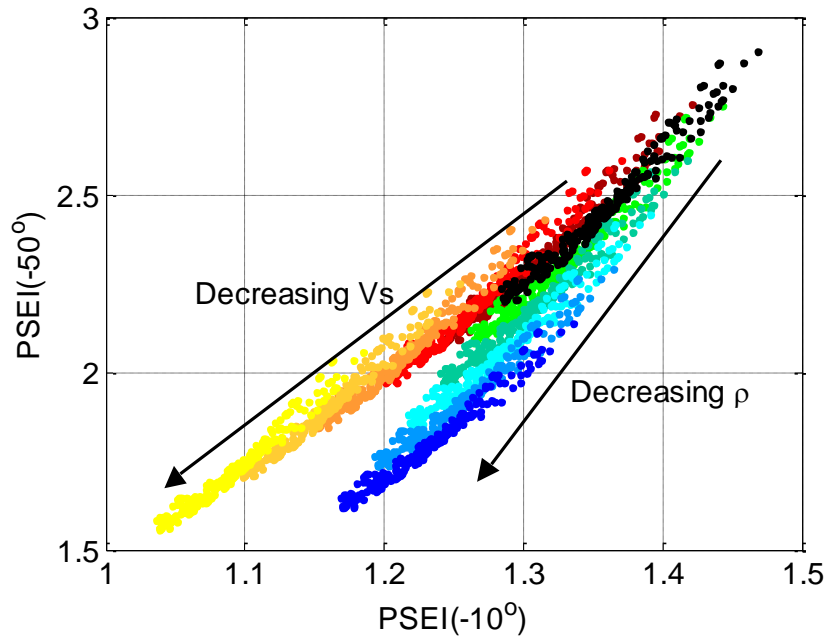
Figure 6.4: Cross-plot of near-angle PSEI (-10°) versus far-angle PSEI (-50°) for a well log from a bitumen reservoir. The original well-log data are shown in black. The warm colors represent changing shear velocity measurements by decrements of 10% to a minimum of 50% of their original value. The cool colors represent changing density measurements by decrements of 5% to a minimum of 75% of their original value.

6.3 PSEI trends for heavy-oil reservoirs

In this section we show the results of applying PSEI analysis to two separate data sets. The first data set consists of various simulated reservoir states that are encountered during production with methods involving steam injection. The second dataset is laboratory-measured data from bitumen sand reservoir core samples, first reported in Wolf and Mavko (2005).

6.3.1 Simulated Reservoir States

In order to determine the utility of PSEI in reservoir characterization and monitoring of steam-assisted production, we first decided to determine whether PSEI could differentiate between six distinct reservoir states of a quartz-sand reservoir with 30% porosity. Multiple rock-physics models along with some previous measurements of bitumen properties (Wolf and Mavko, 2005; Batzle et al, 2006) were used to estimate the properties of these reservoir states. For more information on the rock-physics models used, refer to Mavko *et al.* (1998). Those reservoir states, as well the rock-physics models used to calculate their properties of interest, are listed in Table 6.1. If a single fluid is listed, the reservoir is assumed to be 100% saturated by that fluid, and if two fluids are listed, each is assumed to make up 50% of the pore-filling fluid. The properties of interest for the calculated reservoir states as are shown in Figure 6.5.

Table 6.1: Table of reservoir states and how their properties were calculated.

Reservoir States Modeled		
Reservoir State	Fluid Property Calculation	Model(s) Used
10°C Water Sand	Batzle-Wang	Soft-sand with Gassmann
10°C Bitumen Sand	Lab Measurements	Cemented-sand
10°C 50% Bitumen/50% Water Sand	Batzle-Wang and Lab Measurements	Cemented-sand with Gassmann
300°C Steam Sand	Hot water/Steam Tables	Soft-sand with Gassmann
60°C Bitumen Sand	Lab Measurements	Soft-sand with Gassmann
60°C 50% Bitumen/50% Water Sand	Reuss Avg. of Batzle-Wang & Lab Measurements	Soft-sand with Gassmann

Figure 6.5 shows that the densities of the various reservoir states are virtually identical, except for when the pore-filling fluid is steam. However, there is more variability in the shear-wave velocity of the different reservoir states. The cold bitumen and cold bitumen/water reservoirs have relatively higher velocities than the other reservoir states, because the cold bitumen acts as a cementing agent for the sand grains. The steam-saturated reservoir also has a higher shear-wave velocity because of the density effect of the steam. Last, the cold water, hot bitumen and hot bitumen/water sands all have very similar velocities. This is because at elevated temperatures the bitumen has become more fluid-like, and behaves more like a conventional pore fluid than one that can support shear waves and/or cement grains together.

Given these reservoir properties, the average value for K was computed by dividing the average V_S by the average V_P. Performing the calculation for K in this manner ensures that the result is not biased by using the exact value of K for each reservoir state we are analyzing. Faced with real data the exact value of K, and it's variation throughout the reservoir would not be known. Using this average value of K, we can then calculate θ_{PD}, which in this case is 61.92°.
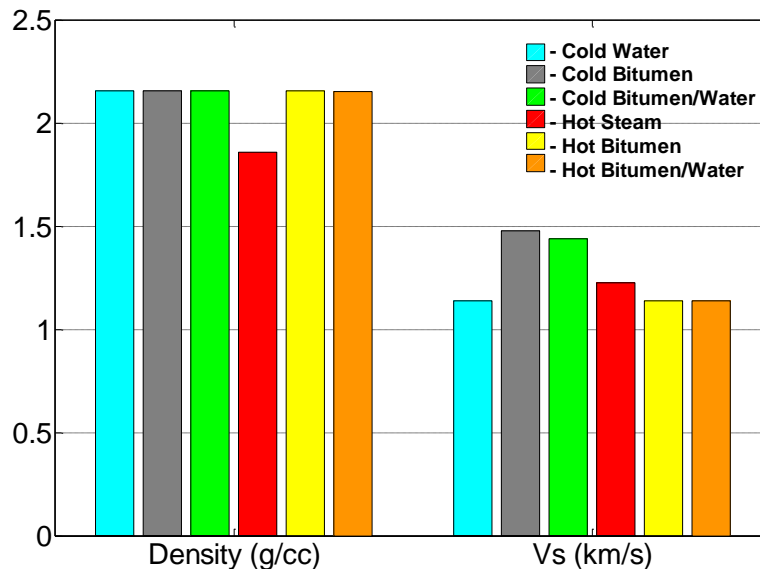
Figure 6.5: Calculated reservoir density and shear-wave velocity for various reservoir states; blue – 10°C water sand, grey – 10°C bitumen sand, green – 10°C bitumen/water sand, red – 300°C steam sand, yellow – 60°C bitumen sand, orange – 60°C bitumen/water sand.

As previously stated, to effectively separate velocity and density trends, the far angle used to calculate PSEI values should be close to the value of θ_{PD}. Figure 6.6 shows cross-plots of near angle PSEI (-10°) versus PSEI values calculated at angles varying from -20 to -60° in 10° decrements, and at θ_{PD}.

As the vertical axis changes from near to far angles, the separation of the velocity and density trends become more pronounced. In the extreme case where we have PSEI values calculated at θ_{PD}, the velocity information is contained solely along the horizontal axis, and the density along the vertical axis. Obtaining PSEI at that specific an angle is not feasible for real-world applications, so for the remainder of the analysis of this data set we will use -60° as the far angle, since it is close to θ_{PD} and will help to maximize the separation of density and velocity trends while remaining plausible for real data situations.

Another observation from Figure 6.6 is that certain reservoir states plot in the same area as others. This result is discouraging, because it means that PSEI cannot effectively discriminate between these reservoir states. The cold water, hot bitumen and hot bitumen/water points all plot almost directly on top of one another. However, this should not be surprising, since heated bitumen becomes more fluid-like in its characteristics, with lower viscosity and limited ability to support shear waves or cement grains together. Even though the reservoir states look essentially the same with PSEI, the possibility to differentiate between them exists based upon the way the reservoir is characterized and monitored. When a baseline reservoir characterization is performed, the entire reservoir is at in-situ cold temperature. Therefore, any data points that plot in the area where you expect to see an overlap of points must be due solely to the presence of cold-water saturation in the reservoir, since there are no heated zones present. On the other hand, if the purpose of the analysis is to monitor a reservoir after or during steam injection, then provided that an initial characterization was done, it should still be possible to differentiate between heated and cold zones in the reservoir. In the monitoring cross-plot, any points that have migrated to the zone of overlap from elsewhere in the cross-plot must be due to the presence of heated bitumen or a mixture of heated bitumen and water. In this case, the operator will know

that these points correspond to a heated section of the reservoir. This provides some reassurance, because it should be possible to differentiate between coinciding reservoir states in PSEI space, provided that an initial PSEI analysis was performed to characterize the cold reservoir.
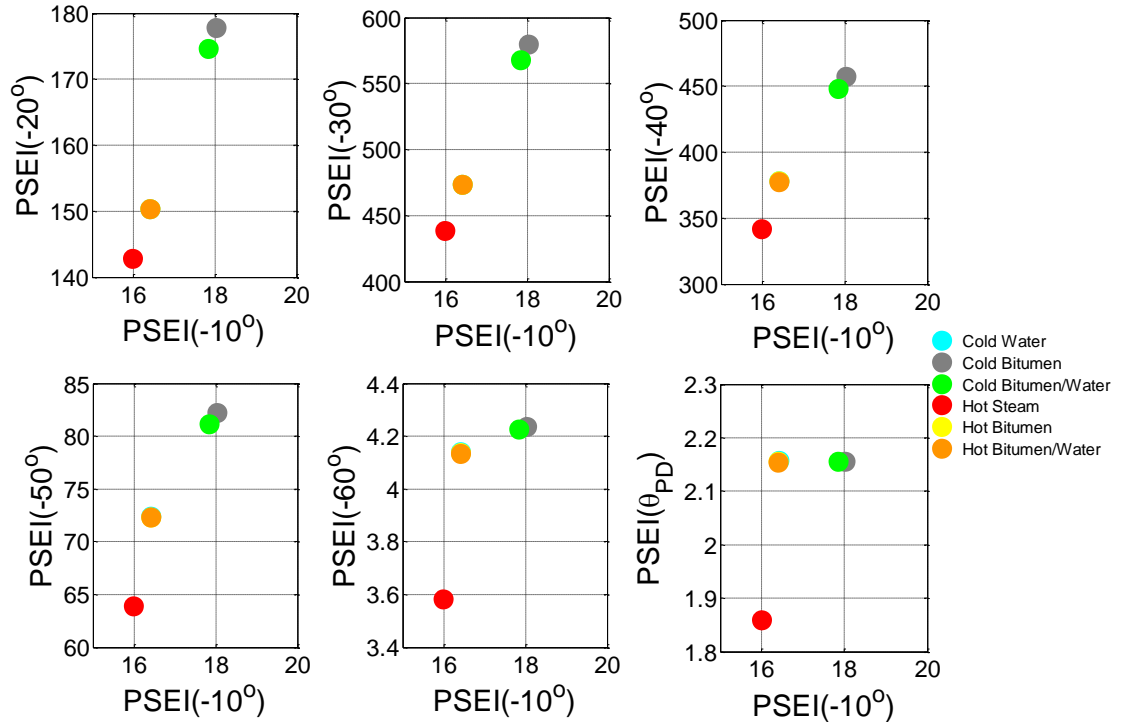
Figure 6.6: Cross-plots of PSEI calculated at -10° versus PSEI at angles from -20 to θ_{PD} where θ_{PD} is -62.92°. Notice that as the angle on the vertical axis increases the separation between the density and velocity trends also increases. Although it appears that the cold water and hot bitumen points are missing from the plot, they are actually present; however they are obscured behind the hot bitumen/water point.

Given that we have PSEI data at angles of -10° and -60°, we now analyze the usefulness of cross-plotting the data corresponding to certain reservoir conditions in order to characterize and monitor a hypothetical bitumen reservoir. The first cross-plot, shown in Figure 6.7, represents the scenario where PSEI analysis is being applied to a cold reservoir for its initial characterization. In this case, the only fluids present within the reservoir are cold bitumen and cold water, mixed in various proportions. Figure 6.7 illustrates a 100% cold-bitumen saturated reservoir, a 100% cold water saturated reservoir, and various saturations in between. We see that there is a trend that

separates the bitumen-saturated reservoir from the water-saturated reservoir, but the saturation does not monotonically increase between the two endpoints. Bitumen saturations above 60% all plot very close to one another, and it will be hard to differentiate among them. However, there is a clear difference between very low bitumen saturation and higher bitumen saturations that is easily discernable.

The next step was to investigate what reservoir states should be identifiable in monitoring surveys in a heated reservoir that had an initial cold reservoir characterization performed. The four cross-plots shown in Figure 6.8 represent various monitoring scenarios; monitoring a reservoir zone with an initial 100% cold bitumen saturation (top left), a reservoir zone with an initial 100% cold water saturation (top right), a reservoir zone with an initial 50% bitumen-50% water saturation (bottom left), and a repeat monitoring survey scenario where the reservoir zone is hot initially (bottom right).
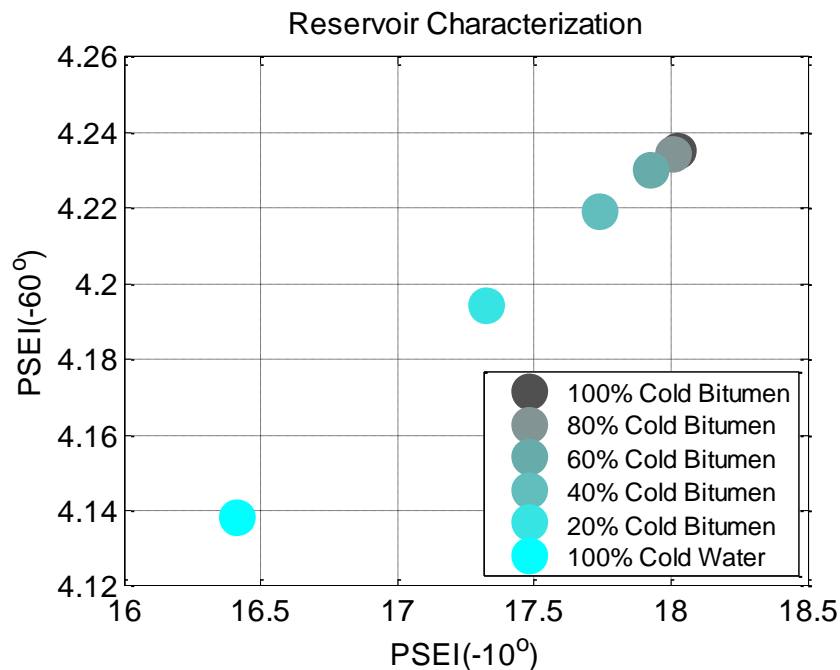
Figure 6.7: PSEI analysis as applied to a cold reservoir for initial characterization.

In Figure 6.8, we can easily differentiate between points that are unheated and those that have been heated. The heated points of the reservoir, regardless of whether the bitumen saturation remains at 100%, will migrate down and to the left in PSEI

space. Tracking the movement of these points from the initial survey in subsequent surveys should allow for easy identification of heated zones in the reservoir. The water zone cross-plot shows a different response. Here it is not possible to tell if the reservoir in this area has been heated; however, heating of water zones is typically avoided because it is a waste of energy. However, if a steam chamber forms in a water-saturated zone, it can be identified by a large shift in PSEI space once the reservoir becomes saturated with steam. The third scenario, consisting of an initial cold bitumen and water saturation, reveals that we should be able to resolve two things by tracking the movement of points in PSEI space: whether the reservoir zone has been heated, and whether a steam chamber has formed. Both these reservoir state alterations are represented by large shifts in PSEI space that should be easily identifiable. The fourth scenario deals with a repeat monitor survey, where a zone in the reservoir has already been heated. In this case PSEI analysis will not reveal whether the bitumen saturation is being depleted due to production; however, it is possible to monitor the formation of a steam chamber due to a large shift in the location of reservoir data points in PSEI space once they become steam saturated.

The preceding modeling of various reservoir states and their spatial relationships with one another in PSEI space reveals that PSEI should be an effective tool for bitumen reservoir characterization and monitoring. For initial reservoir characterization, there is an identifiable trend between zones of high and low bitumen saturation in the reservoir. Additionally, when PSEI analysis is used in monitoring applications, it is effective at delineating cold bitumen zones from hot bitumen zones, as well as identifying areas of steam chamber formation. These results are encouraging, but need to be applied to real data in order to confirm their validity in real situations.
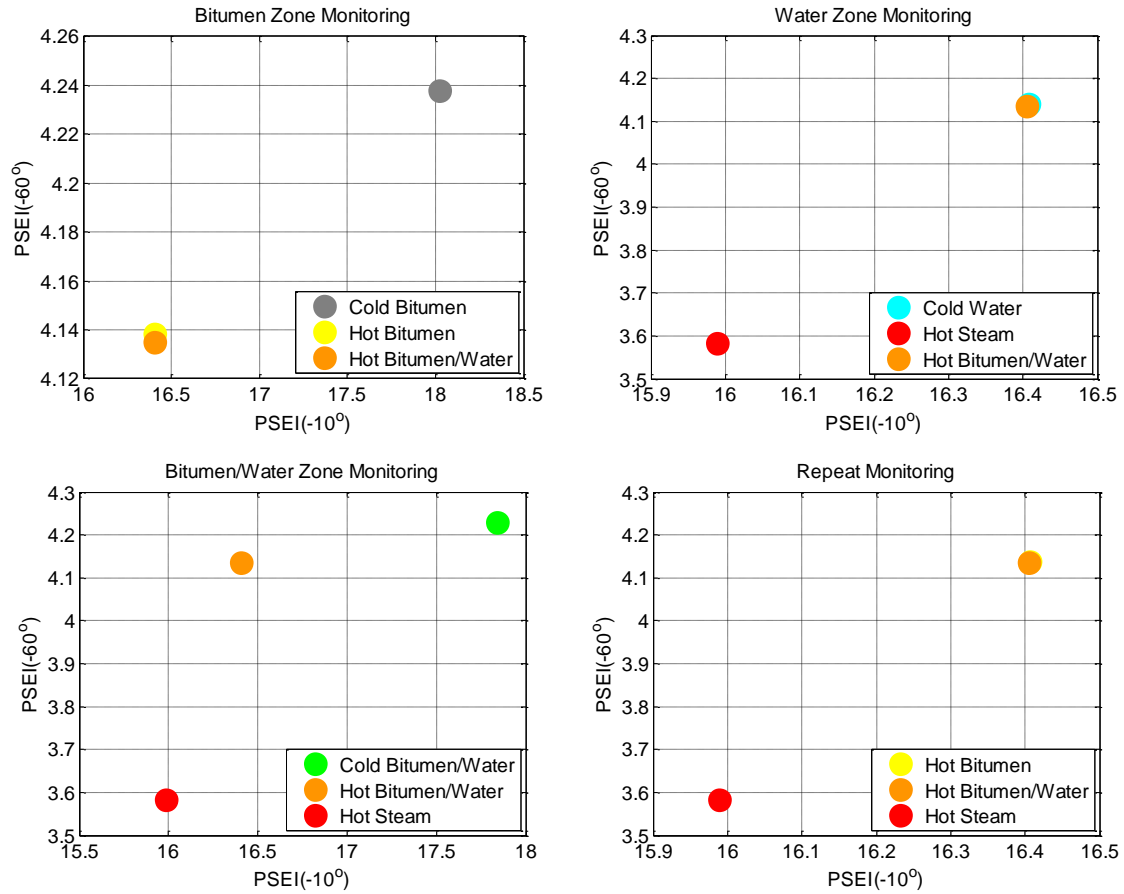
Figure 6.8: PSEI analysis as applied to reservoir states for monitoring heated zones and steam chambers.

6.3.2 Laboratory-Measured Data

Since the preceding analysis was performed solely upon simulated reservoir states, this section explores the application of PSEI analysis to laboratory-measured data from two bitumen reservoir core samples. The measurements were first reported in Wolf and Mavko (2005). In both samples, the porosity is ~40%; the matrix is over 90% quartz with minor amounts of feldspar; and bitumen saturation is ~85% with the remaining pore space filled with water. Measurements were made over a temperature range of -20°C to 70°C and effective pressures of 2 to 8.3 MPa. At each temperature step, measurements were made as the effective pressure was cycled from low to high pressure, and then back down. During testing, the densities of the samples were

between 1.8 and 1.95 g/cc. However, a reliable measurement of the density at all times during the test was not available. Since the actual density of the sample at all times during testing is unknown, a random density between 1.8 and 1.95 g/cc has been assigned to each measurement point for viewing purposes. If this is not done, and a constant density is assigned to each point, then all points in PSEI space lie along a single curve and viewing the data becomes difficult. This does little to the horizontal position of the data points, but does create some spread in the vertical direction to improve viewing of the data.

The average compressional-wave velocity for all measurements was 2492 m/s, and the average shear-wave velocity was 1003 m/s. This leads to a value of 0.4024 for K and -68.08° for θ_{PD}. The far angle used for the calculation of PSEI was -65°. Figure 6.9 shows the near and far values of PSEI cross-plotted against one another, color-coded by density (upper left), shear-wave velocity (upper right), temperature (lower left) and effective pressure (lower right).

The two upper plots show the same trends observed in the previously modeled data for the density and shear-wave velocity. More interesting effects are seen in the two lower plots. The bottom left plot shows that the temperature trend follows roughly that of the shear-wave velocity; this is not unexpected. As temperature is increased the ability of bitumen to cement grains and support shear waves is decreased, both of which will act to slow the shear-wave velocity in the sample. However, there are some points that are obviously out of sequence with the rest. There are several examples of data points that lie further along the decreasing velocity trend that are at a lower temperature than surrounding points. This is counter-intuitive, because shear-wave velocities in bitumen sands are typically higher at lower temperatures. This anomalous behavior is because the measurements were made at a variable effective pressure. The commonly observed phenomenon of increasing velocity with increasing pressure was observed during the testing of these samples. The effect of pressure on velocity was so pronounced in these samples that it overcame the effect of temperature on velocity. In other words, a sample at higher temperature, and therefore with lower expected velocity, could have a faster velocity than a colder sample at lower pressure. This can

explain the out-of-sequence points that are observed. However, examining the plot color-coded by effective pressure reveals no more insight, because there are no identifiable pressure trends seen in the cross-plotted data.
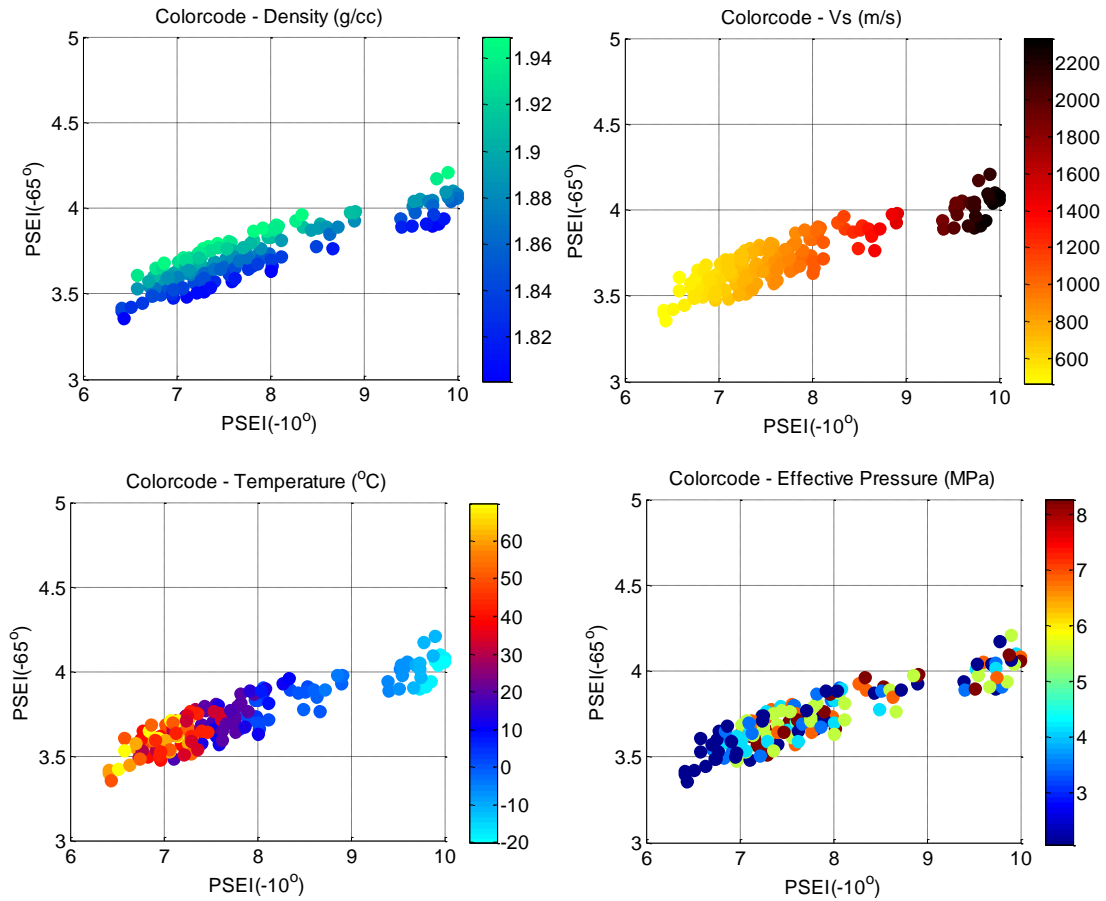
Figure 6.9: PSEI analysis as applied to laboratory-measured data from two bitumen core plugs color-coded by density (upper left), shear-wave velocity (upper right), temperature (lower left) and effective pressure (lower right).

We can learn more by altering one of the axes in the plot. Since this was a controlled experiment, the temperature of each measured data point is known, and the dependent axis can be changed from far-angle PSEI to temperature. We can then re-plot the data in this new domain and color-code it by effective pressure. This is shown in Figure 6.10.
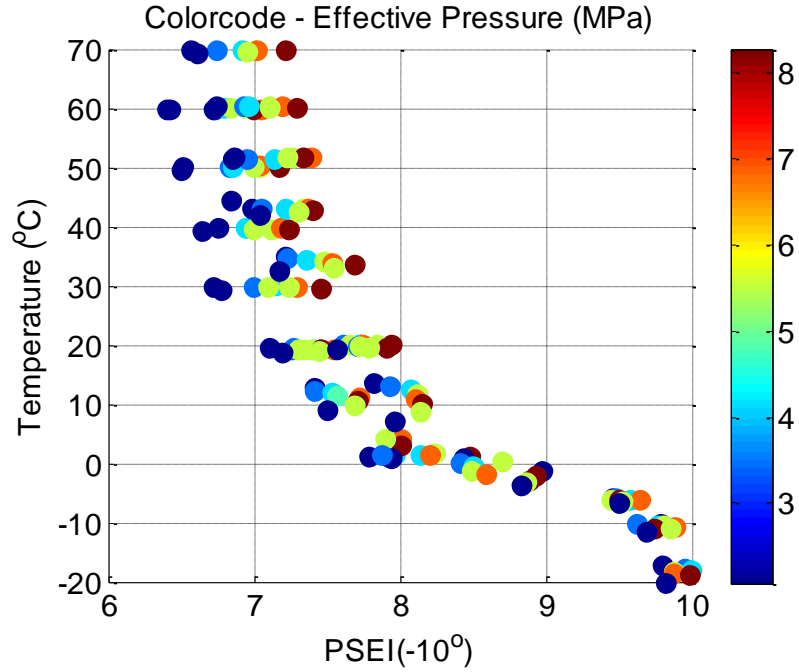
Figure 6.10: Cross-plot of near-angle PSEI versus temperature color-coded by effective pressure for lab-measured bitumen sand core plugs.

Figure 6.10 shows that there is a clear relationship between PSEI(-10°) and effective pressure at a given temperature. This is because as effective pressure is increased, the shear-wave velocity of the sample increases, which increases the value of PSEI through the term V_S^d. However, we can see this effect clearly only if the shear velocity of the reservoir is changing solely due to pressure changes, or if the temperature of the measurement is known, as is the case here. This is an encouraging result nonetheless, because it shows that PSEI has the capability to discern pressure changes within a reservoir if pressure is the lone factor affecting shear-wave velocity, or if other factors contributing to V_S changes can be measured.

Applying PSEI analysis to laboratory-measured data has revealed the same observed trends for density and shear-wave velocity as were seen with the synthetic results. In addition, since the temperature and pressure at which the measurements were made are known, it allowed the establishment of a link between temperature, pressure and the value of PSEI at near and far angles.

6.4 Synthetic case for simple reservoir model

6.4.1 Synthetic earth model

The properties of the synthetic earth models used in this exercise are representative of a typical bitumen reservoir undergoing steam injection to stimulate production. We simplify the models by having a uniform shale layer overlying the reservoir and a uniform limestone layer beneath it. The reservoir itself is 30 m thick, spanning a depth from 470 to 500 m. We proceed to model the reservoir in three different states. The first state represents an untouched reservoir at a uniform temperature of 4°C in the subsurface (Fig. 6.11A). The second state has a heated zone in the reservoir that is 15 m wide and 15 m thick at its widest and thickest points (Fig. 6.11B). This is representative of a heated zone that would result from steam injection into the reservoir. The maximum temperature of the heated zone is 60°C, and it cools slightly towards the edges. The third state has the same temperature profile as the second, but a density variation has been added in the lower central portion of the reservoir, representing the formation of a steam chamber at the point of steam injection (Fig. 6.11C). This density anomaly is 6 m wide and 6 m thick at its widest and thickest parts. The seismic velocities of the reservoir are taken from measurements made on a bitumen sand sample over a temperature range of 4 to 60°C, and Gassmann fluid substitution was used to substitute steam into the pore space to calculate the properties of the steam chamber. Figure 6.11 shows the properties of the three reservoir states, along with the overlying shale and underlying limestone.

6.4.2 PSEI inversion methodology

These three earth models were imported into Hampson-Russell, and converted-wave synthetic seismic was shot through each model. The converted-wave seismic was simulated using the AVO module of Hampson-Russell, employing the Elastic Wave Method and recording the P-S wave response. This included modeling down-going P-waves and up-going S-waves. The recorded data is representative of the total particle motion recorded at the receivers. The wavelet used for the modeling was a

zero phase, 125 Hz Ricker wavelet. Offsets were extracted at 166 m, 543 m, 790 m, and 1120 m, which correspond to incidence angles that are approximately 10°, 30°, 40°, and 50° at the top of the reservoir. This allows us to analyze the results of the inversion over a set of different angles. The synthetic seismic sections are shown in Figure 6.12 for the cold reservoir model, in Figure 6.13 for the heated reservoir model, and in Figure 6.14 for the heated reservoir with steam chamber. In each figure, panels A, B, C, and D refer to offsets of 10°, 30°, 40°, and 50° respectively.

One thing that should be noted in the seismic data is that as the angle of incidence increases from 40° to 50° there is a drastic change in the character of the reflection due to the limestone basement. This is because the critical angle at the interface between the reservoir and the limestone is exceeded. As a result, the reflection from the top of the limestone disappears. This leads to much higher apparent amplitudes at the top of the reservoir, but this is due to the scaling, and is not a direct result of the physics of the problem.

Once the synthetic seismic data was simulated, it was then exported to the STRATA module in Hampson-Russell to perform the seismic inversion. The model-based inversion algorithm was used, which required the creation of starting models for the inversion of each set of seismic data. In order to create the initial models for the inversion, three 'wells' were used as inputs. These 'wells' were located at cross-line locations 1, 23 and 46. These locations correspond to the two extreme ends of the earth models and a single well at the center of the heated zone, or steam chamber, in the reservoir. Before we can use these wells to create an initial model that will correspond to the converted-wave seismic data at various angles, we must first convert them from regular well logs to pseudo-well logs, as originally described by Gonzalez (2006). He proposed the generation of pseudo-velocity (pseudo-v) and pseudo-density (pseudo-ρ) logs from which to construct the initial model, which is basically equivalent to the principle used by Connolly (1999) to invert PP data for elastic
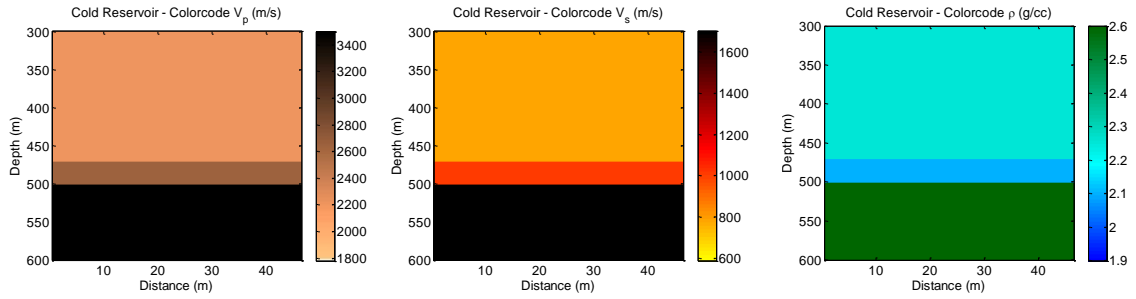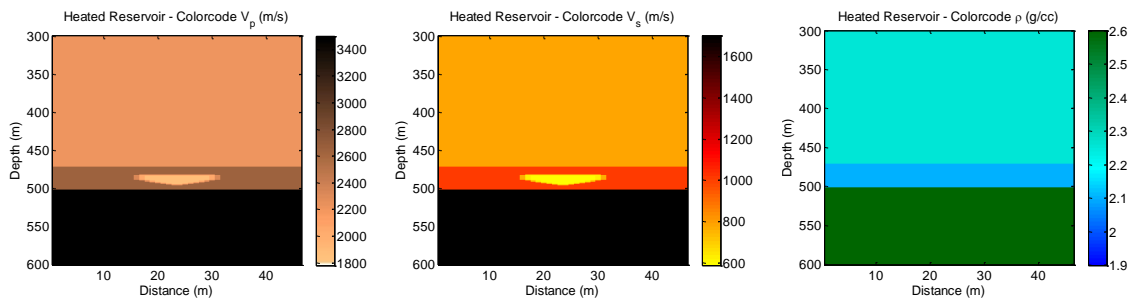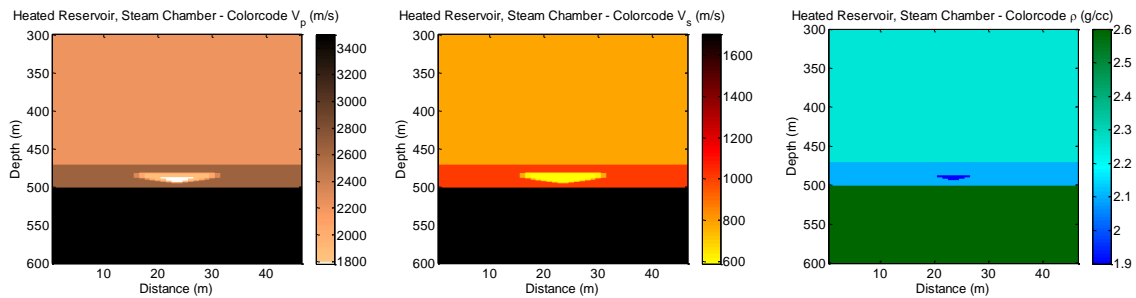
Figure 6.11: Synthetic earth models for A) the cold reservoir, B) the heated reservoir, and C) the heated reservoir with a steam chamber. The shale overburden and limestone basement rock are the same in all cases, and the reservoir spans the depth from 470 to 500 m. The P-wave velocity is shown in the first column, S-wave velocity in the middle column, and density in the right column.

A)

B)

C)

D)
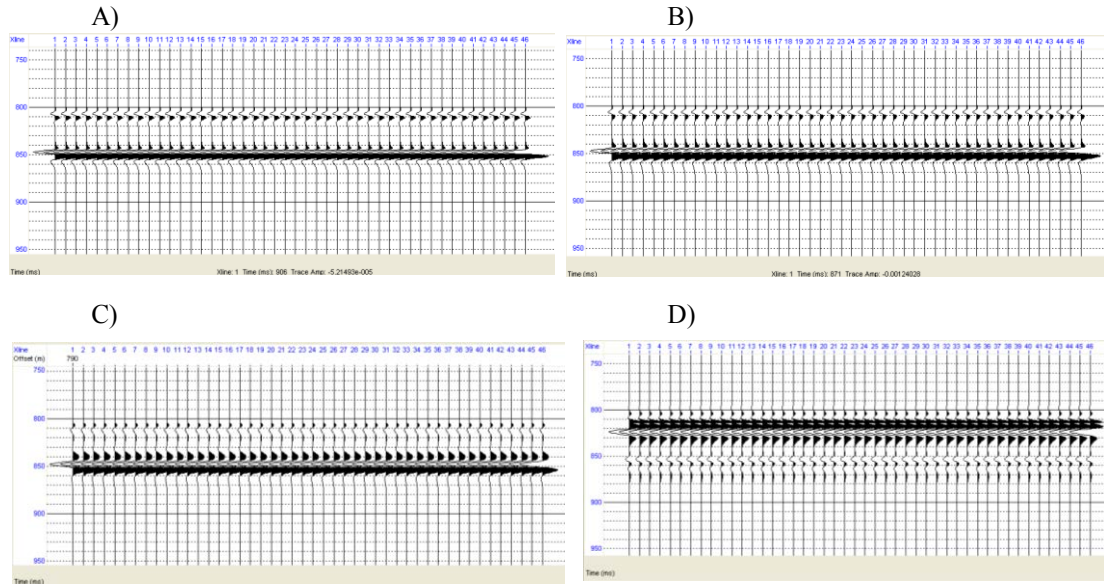
Figure 6.12: Synthetic converted-wave seismic sections of the cold-reservoir model. A) 10 degree offset, B) 30 degree offset, C) 40 degree offset, and D) 50 degree offset.

A)

B)

C)

D)
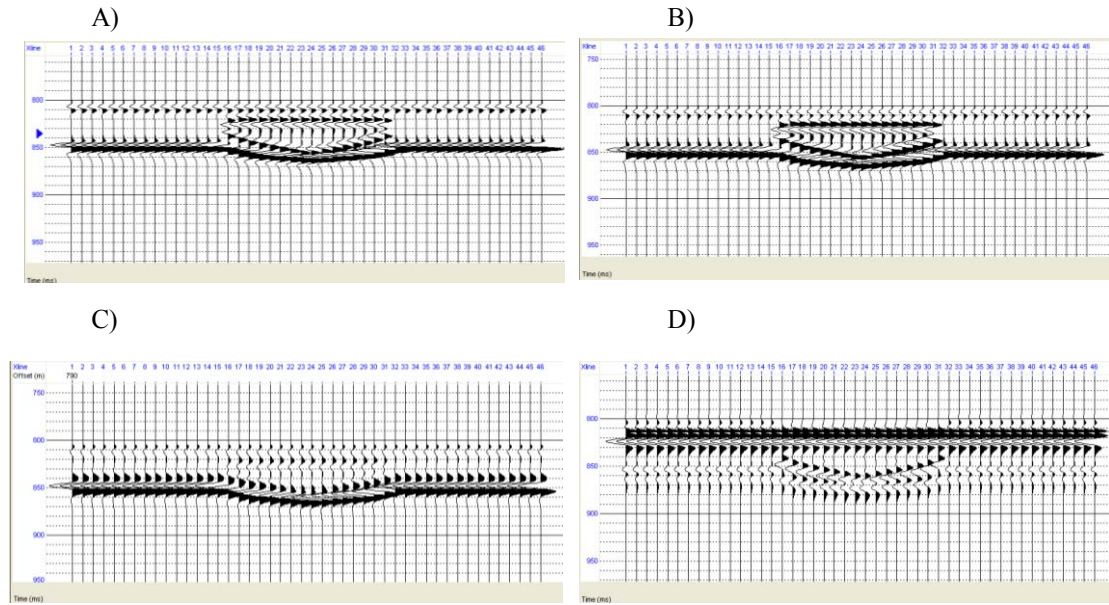
Figure 6.13: Synthetic converted-wave seismic sections of the heated-reservoir model. A) 10 degree offset, B) 30 degree offset, C) 40 degree offset, and D) 50 degree offset.
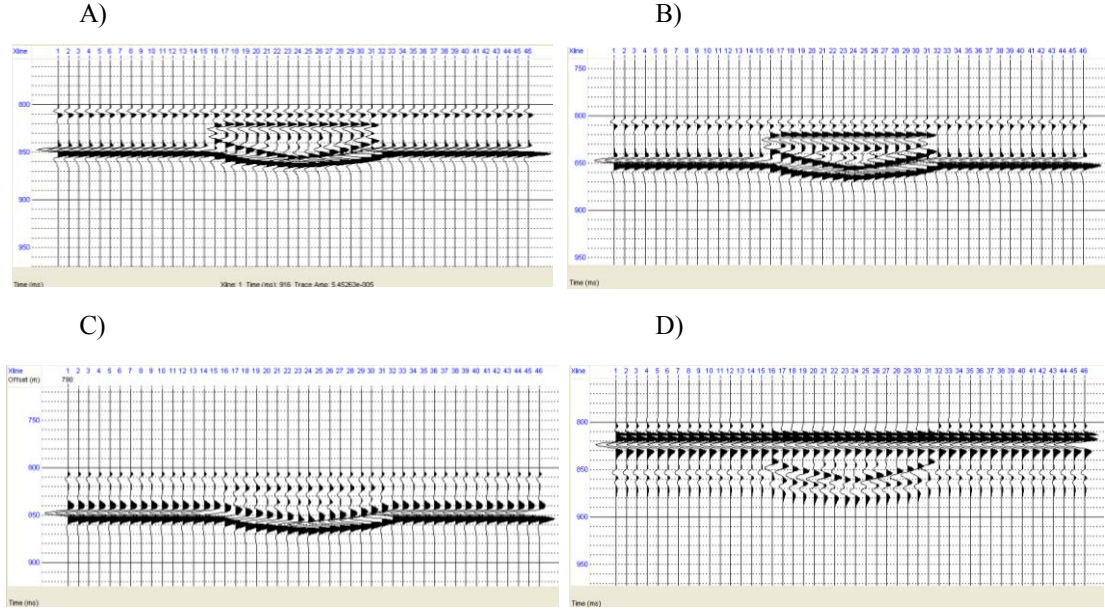
Figure 6.14: Synthetic converted-wave seismic sections of the heated -reservoir model with steam chamber. A) 10 degree offset, B) 30 degree offset, C) 40 degree offset, and D) 50 degree offset.

impedance. Constructing these logs and sampling them in pseudo-depth (pseudo-z) allows the inversion software to attain consistency in the time-to-depth conversion between log PSEI values and the synthetic converted-wave data. To calculate the values of these logs, the following formulas are used:

$$pseudo\_v = V_s^d \qquad (4)$$

$$pseudo\_\rho = \rho^c \qquad (5)$$

$$pseudo\_z = \frac{z}{2}\left(\frac{1}{V_p} + \frac{1}{V_s}\right) pseudo\_v \qquad (6)$$

where the exponents c and d are a function of incidence angle as previously given.

Using the set of three pseudo-well logs at 1, 23 and 46 m, calculated at incidence angles of 10°, 30°, 40°, and 50°, the three initial earth models were created. This was done by interpolating between the wells along horizons at the top and bottom of the reservoir, as picked from the corresponding angle synthetic seismic data. Figure 6.15

shows the initial models created for the cold reservoir earth model, Figure 6.16 shows the heated reservoir earth model, and Figure 6.17 shows the heated earth model with steam chamber. In each figure, panels A, B, C, and D correspond to the model for 10, 30, 40, and 50 degrees respectively. We can see that the initial models of the heated reservoir and the reservoir with the steam chamber show a zone of lower PSEI values roughly correlated with the position of the heated reservoir zone. However, it is important to notice that the initial model does not directly correspond to the actual distribution of properties in the reservoir, which ensures that if the inversion result matches the earth model, it is because of the inversion and not simply because the initial model is the actual earth model.

A)

B)

C)

D)
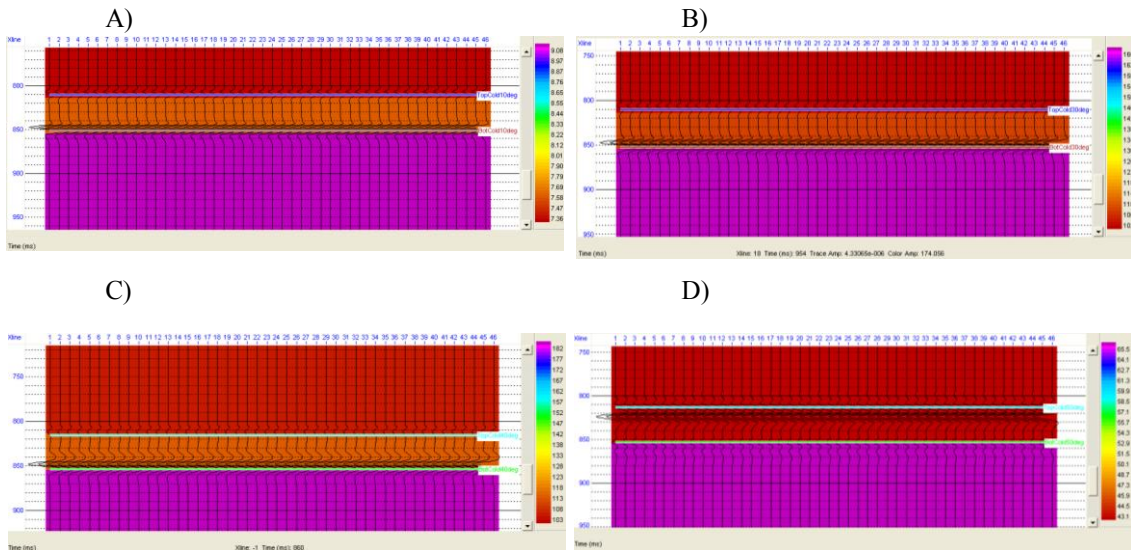
Figure 6.15: Initial models of PSEI values created for the inversion of the cold reservoir earth model using three pseudo-wells; one at each side of the section, and in the center of the reservoir. A) 10 degree offset, B) 30 degree offset, C) 40 degree offset, and D) 50 degree offset.

A)

B)

C)

D)
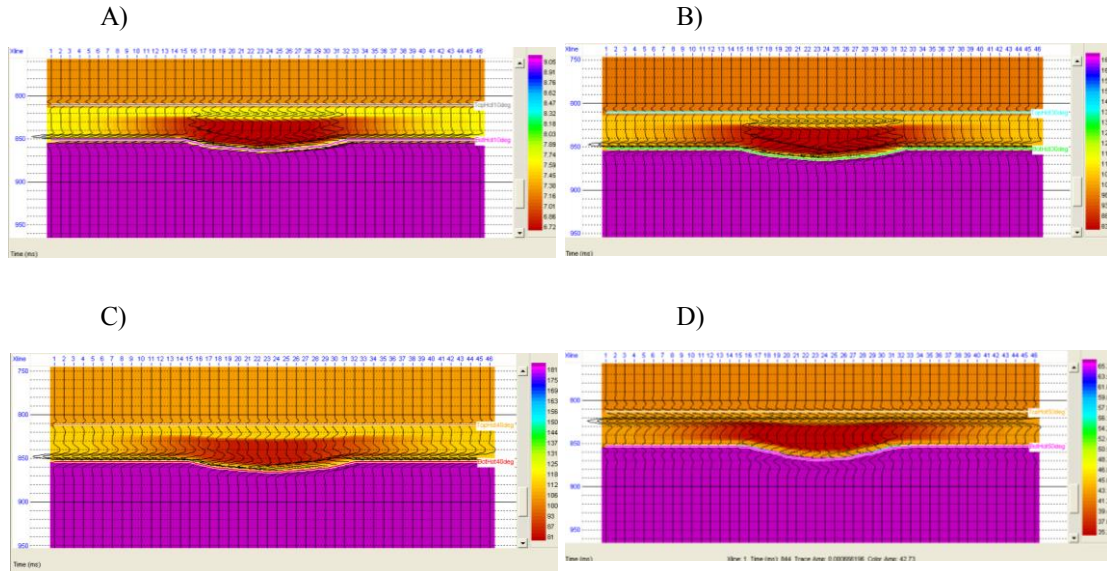
Figure 6.16: Initial models of PSEI values created for the inversion of the heated reservoir earth model using three pseudo-wells; one at each side of the section, and in the center of the reservoir. A) 10 degree offset, B) 30 degree offset, C) 40 degree offset, and D) 50 degree offset.

A)

B)

C)

D)
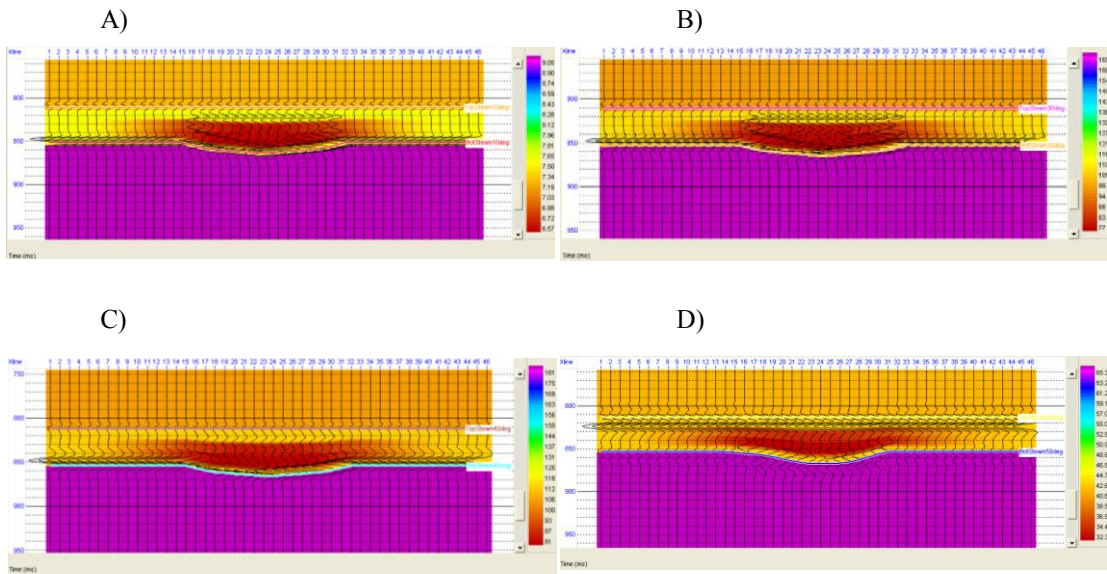
Figure 6.17: Initial models of PSEI values created for the inversion of the heated reservoir earth model with steam chamber using three pseudo-wells; one at each side of the section, and in the center of the reservoir. A) 10 degree offset, B) 30 degree offset, C) 40 degree offset, and D) 50 degree offset.

The inversion process used was the model-based inversion algorithm provided in the Hampson-Russell STRATA software package. The inversion was set up to run as a

typical P-impedance inversion, however PS seismic data were used along with the initial model created from the corresponding pseudo-wells. The inversion was run with a heavy weight placed upon the seismic data, and minimal weight placed upon the initial model itself (model parameter of 0.001). A 1 ms block size was used for the inversion, which is sufficiently larger than the 0.5 ms sample rate of the seismic data. The results of the cold-reservoir earth model inversions are shown in Figure 6.18, the heated-reservoir earth model inversions in Figure 6.19, and the heated-reservoir earth model with steam chamber inversions in Figure 6.20. In each figure, panels A, B, C, and D correspond to inversions performed at 10°, 30°, 40°, and 50° respectively.

Examining the results from the cold-reservoir inversion (Fig. 6.18) we can see that as the angle is increased the bottom of the reservoir is less clearly resolved. This is due to the character of the seismic data at the reservoir-limestone interface. As was previously mentioned, the incident angle becomes post-critical as it is increased from 40° to 50°. The resulting low amplitudes are not sufficient for the inversion to clearly resolve the boundary between the reservoir and the limestone basement. However, the interface can be clearly seen on the near-angle inversion, which can be used to define the geometry and extent of the reservoir.

A)

B)

C)

D)-
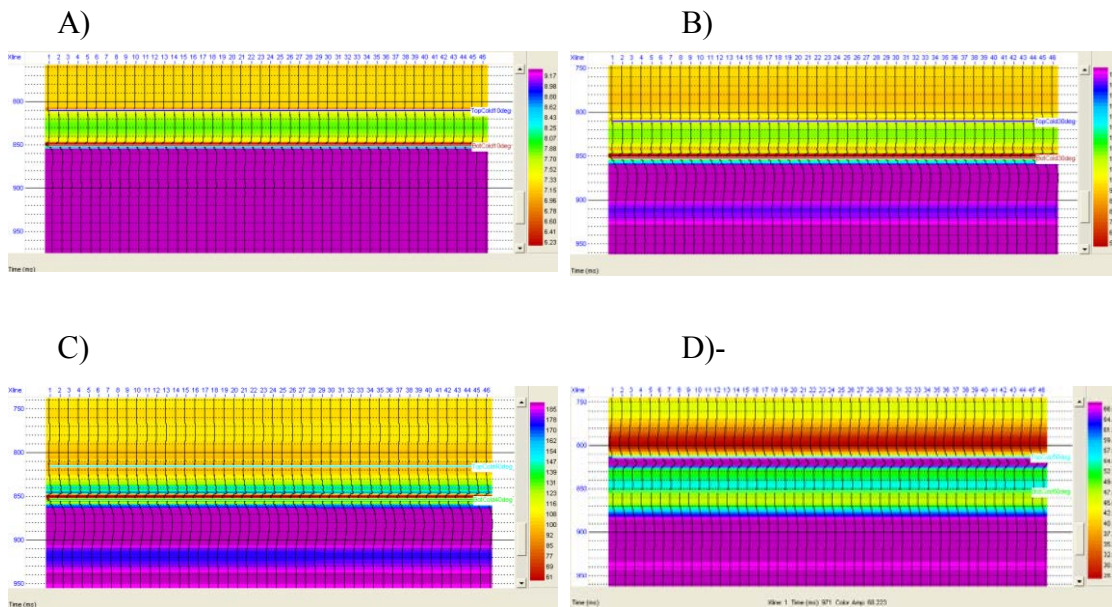
Figure 6.18: Inversion results for the cold-reservoir earth model at A) 10 degree offset, B) 30 degree offset, C) 40 degree offset, and D) 50 degree offset.

A)

B)

C)

D)
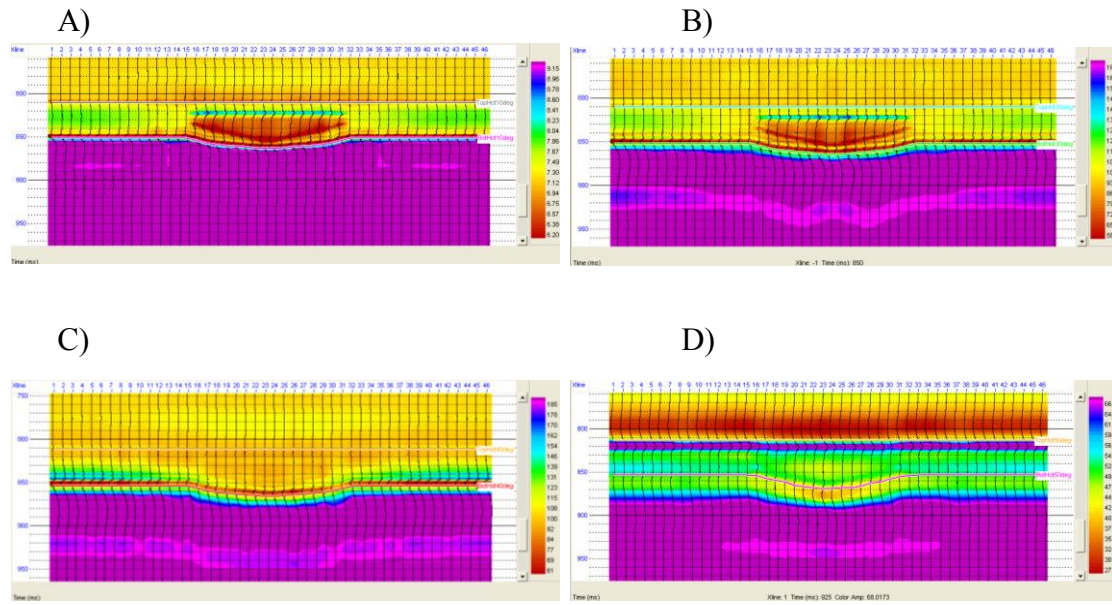
Figure 6.19: Inversion results for the heated-reservoir earth model at A) 10 degree offset, B) 30 degree offset, C) 40 degree offset, and D) 50 degree offset.

A)

B)

C)

D)
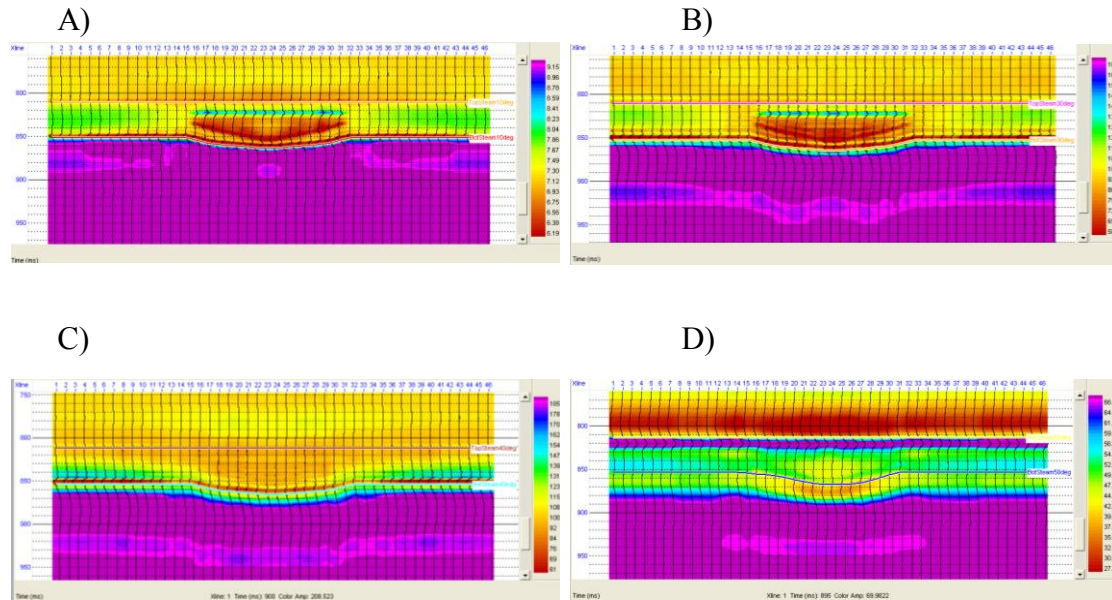
Figure 6.20: Inversion results for the heated-reservoir earth model with steam chamber at A) 10 degree offset, B) 30 degree offset, C) 40 degree offset, and D) 50 degree offset.

We see similar patterns with regard to incident angle when we look at the inversion results from the heated reservoir (Fig. 6.19). We again see that the far-angle

data (panel D) do not adequately define the base of the reservoir. However, if we look on the near -angle data (panel A), not only can we see the base of the reservoir, but also the heated zone is clearly visible within the inversion result and corresponds to the location in the original heated reservoir earth model. As the incidence angle is increased, we lose this ability to see the heated zone in the reservoir, but this is not unexpected. As the angle is increased, the PSEI value becomes less sensitive to changes in shear-wave velocity and more sensitive to density. Since the heated reservoir contains contrasts only in the shear-wave velocity, we expect the reservoir to appear homogeneous at far offsets. Figure 6.20 shows the same patterns at the base of the heated reservoir (including the steam chamber) with increasing angle because the critical angle is surpassed. Also, in the 10° inversion result (panel A) we see the heated zone clearly defined. However, in the 50° inversion result (panel D) we can also see a lower impedance zone in the center of the heated zone which corresponds to the location of the steam chamber. These results are very encouraging and demonstrate that the proposed methodology can provide a robust method for tracking heated zones within a bitumen reservoir as well as the formation of steam chambers, provided that high-quality converted-wave seismic data is available.

However, there are also some artifacts in the inversion that must be taken into account when interpreting the results. One example is the high-impedance zone directly overlying the heated reservoir at angles of 10° and 30°. This high-impedance zone is likely a result of wavelet effects and tuning. Also, with real seismic data, there will be a lower signal-to-noise ratio than in our idealized synthetic case, which will likely have an effect on the quality of the inversion that cannot be ignored when interpreting the results.

6.4.3 Discussion

The results of the near- and far-angle inversions for PSEI values appear promising. However, to get a better idea of the utility of this methodology it is necessary to plot the inverted data in PSEI space, or as cross-plots between PSEI values obtained at various angles. The PSEI values obtained from the inversions are shown plotted in

PSEI space in Figure 6.21. In the figure the rows (from top to bottom) correspond to the cold reservoir model, heated reservoir model, and heated reservoir model with steam chamber respectively; the columns correspond to cross-plots of the 10° PSEI values with 30°, 40°, and 50° respectively.
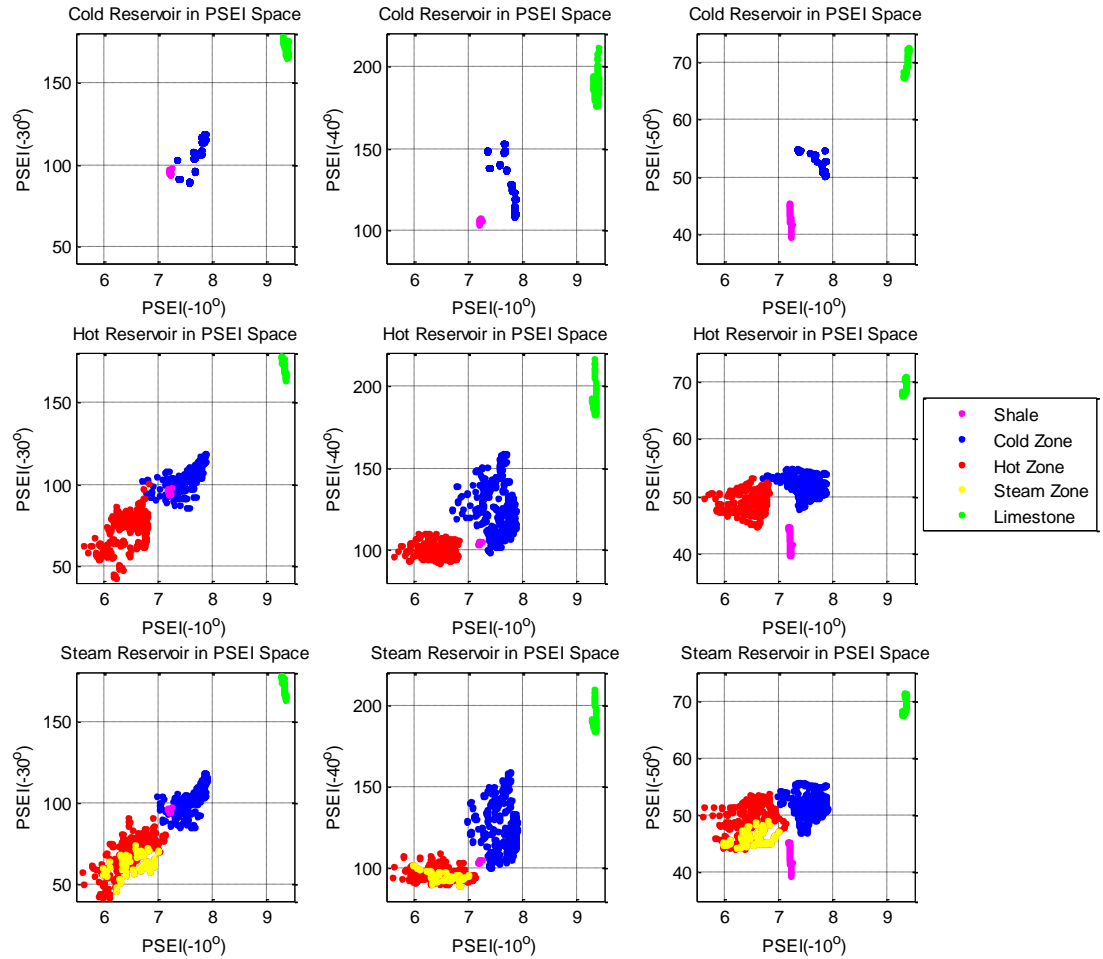
Figure 6.21: PSEI-space representation of inverted data from the three earth models. The top row shows the cold reservoir, the middle row shows the heated reservoir, and the bottom row shows the heated reservoir with steam chamber. The three columns correspond to plots of the data in PSEI space with increasing angle on the ordinate axis; 30, 40 and 50 degrees respectively. The shale overburden is shown in magenta, cold reservoir zones in blue, heated reservoir zones in red, steam chamber areas in yellow, and the limestone basement in green.

Examining the columns in Figure 6.21 it is apparent that in order for the density trend to separate from the velocity trend the PSEI values plotted along the ordinate axis must be calculated at a large angle, as originally described in Wolf and Mavko

(2007). However, caution must be used when cross-plotting the data, since we already saw that the base of the reservoir is not well defined in the far-offset data. This is not a concern for this synthetic example; however, it does illustrate that when designing a survey for monitoring a reservoir, care must be taken to ensure that the features of interest will be visible within the data. Therefore, we suggest that forward modeling be performed in order to help plan the seismic survey design. Doing this will help to ensure that the survey is designed to optimally capture the features of interest.

Knowing that the far-angle data will have the best separation between shear velocity and density trends, we examine the cold, heated and steam-filled reservoirs in PSEI space with a near-angle of 10° and far-angle of 50° in Figures 6.22, 6.23 and 6.24. A realistic way of looking at these data is to imagine them as snapshots of a reservoir at different times during production. The cold reservoir (Fig. 6.22) is representative of the untouched reservoir. Here we can see a clear separation in data points that correspond to the overlying shale (magenta), underlying limestone (green), and the reservoir interval we are interested in (blue). The next snapshot (Fig. 6.23) corresponds to the reservoir after steam has been injected to heat the reservoir and stimulate production. Heating the reservoir reduces the viscosity of the bitumen, which in turn lowers the shear-wave velocity in the heated zone. As expected, the location of the heated-reservoir points (red) shift to the left in PSEI space. Note that some of the blue data points also have migrated in the same direction, but this is because the lateral smoothing of the seismic inversion.

The next snapshot (Fig. 6.24) occurs later, when there is the formation of a steam chamber around the injection point. The effect of this is to lower the density of the reservoir in the steam chamber zone and to decrease the P-wave velocity. As density decreases, we expect data points to migrate downwards in PSEI space. Looking at the distribution of points corresponding to the steam chamber in Figure 6.23 (yellow), we can see that these points generally plot below the heated-zone data points (red). This is encouraging; however, if we compare the location of the yellow points in Figure 6.24 with the location of heated data points in Figure 6.23, we can see that these points do have some overlap. This suggests that the formation of a steam chamber may not be

sufficient to delineate a clear separation of data points corresponding to heated-reservoir zones versus steam-filled-reservoir zones. However, the relative distribution of the points corresponding to the heated and steam filled zones does make it possible to discriminate which data points, and hence which reservoir zones, may be more likely to be saturated with steam. Also, if the size of the steam chamber grows larger in dimension than is presented in this example, the effect of smearing the boundaries in the inversion will be less pronounced, which may allow for a clear distinction between heated and steam-saturated sections of the reservoir.
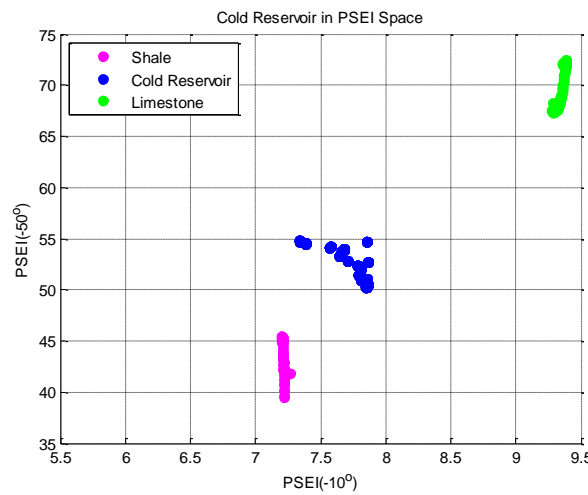
Figure 6.22: Results of the cold-reservoir earth model plotted in PSEI space. The shale overburden is shown in magenta, cold reservoir in blue, and the limestone basement in green.
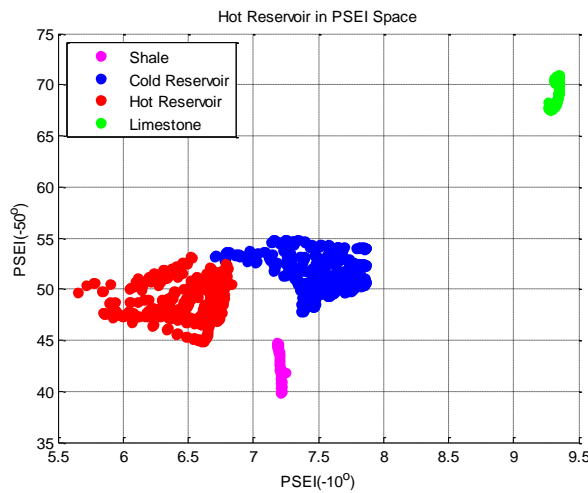
Figure 6.23: Results of the heated-reservoir earth model plotted in PSEI space. The shale overburden is shown in magenta, cold reservoir in blue, heated reservoir zones in red, and the limestone basement in green.
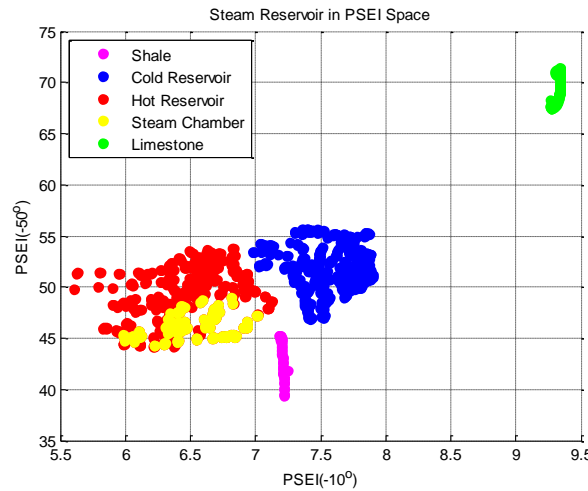
Figure 6.24: Results of the heated-reservoir earth model with steam chamber plotted in PSEI space. The shale overburden is shown in magenta, cold reservoir in blue, heated reservoir zones in red, steam saturated zones in yellow, and the limestone basement in green.

6.4.4 Conclusions

The preceding modeling was carried out as an exercise to illustrate the utility of inverting converted-wave seismic data for PSEI attributes. These attributes were obtained using commercial inversion software, and can be used to monitor the state of a bitumen reservoir being produced by thermal means. We've shown that the inverted results, when plotted in PSEI space, show a clear distinction between cold and heated sections of the reservoir. In addition, the inversion also contains information regarding the presence and location of steam-chamber formation within the reservoir. Though this example does not result in a definitive separation of data corresponding to heated zones and steam-filled zones when plotted in PSEI space, it does show that PSEI analysis can be used to delineate which are areas of the reservoir are most likely to contain steam. Comparing these areas with known locations of steam injector wells will greatly aid in determining whether the area is likely to contain steam, or if it may simply be a heated area of the reservoir. It is also important that preliminary modeling be carried out in order to aid with the design of the seismic survey. This will ensure that the desired information is contained and can be extracted from the seismic data that is acquired.

By inverting converted-wave seismic sections for PSEI attributes there is much that can be inferred in regards to the state of the reservoir in the subsurface. Incorporating this knowledge into the production strategy of the reservoir will greatly aid in making decisions that maximize the efficiency and production from bitumen and heavy-oil reservoirs.

6.5 Synthetic case for reservoir simulation results

6.5.1 Synthetic reservoir model

The synthetic reservoir model used in this case study is the unfractured 3D reservoir model used by Chen et al. (2008) to simulate the results of a steam-assisted gravity drainage process in a heterogeneous reservoir. The reservoir is representative of a generic formation in the Alberta oil sands in Western Canada. The model was originally created for the purposes of a reservoir simulation, and as such, certain properties of the reservoir that are of great importance to this study, such as mineralogy, were not explicitly stated. The properties given for the simulation are listed in Table 6.2.

Table 6.2: Reservoir properties used for the SAGD reservoir simulation.

Reservoir depth	300 m
Reservoir thickness	20 m
Porosity	0.32
Horizontal permeability	3,000 mD
Vertical permeability	1,800 mD
Oil viscosity (RC)	1,000,000 cp
Reference depth	315 m
Initial pressure	2,896 kPa
Initial temperature	50 $^{\circ}$F
Initial oil saturation	0.80
Initial water saturation	0.20
Oil density (RC)	8.8 $^{\circ}$API

The reservoir model was created such that it contained a 'clean sand' facies and a 'shaley sand' facies, the latter containing laterally oriented thin shales. Sequential indicator simulation, a geostatistical method, was used to determine the distribution of these facies throughout the reservoir. In the reservoir model, different vertical permeabilities were used to differentiate between the two facies. From the distribution of vertical permeability, it was possible to assign a mineralogical makeup to these specific clean and shaley sand lithologies. The mineralogy of the shaley sand unit was set to 60% quartz and 40 % clay, whereas the clean sand unit was set to 95% quartz and 5% clay. Figure 6.25 shows the distribution of clean sand (yellow) and shaley sand (brown) throughout the reservoir unit.
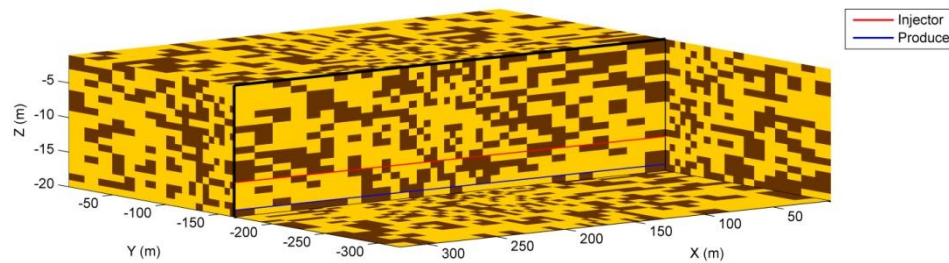
Figure 6.25: Distribution of clean sand (yellow) and shaley sand (brown) throughout the reservoir. Also shown are the injection well (red) and production well (blue) used in the SAGD simulation.

The simulation was performed using CMG STARS thermal and compositional simulator. In the simulation, electrical preheating was performed for 90 days, followed by 95% quality steam injected at 3000 kPa. During the simulation, the production wells were operated such that they avoid excessive steam production, and the state of the reservoir was output after 3 and 6 years of injection.

Figure 6.26 shows the temperature and gas saturation of the reservoir after a) 3 years and b) 6 years of SAGD production. The temperature profile of the reservoir is shown by isosurfaces of different temperatures, and the gas saturation is shown by the isosurface corresponding to 10% gas saturation. The temperature and gas saturation are important properties for us to consider in our study, since they relate to the heating of the reservoir and formation of the steam chamber, and hence to shear-wave velocity

and density changes, which will have a direct effect on the PSEI values obtained from the inversion.

a)   b)
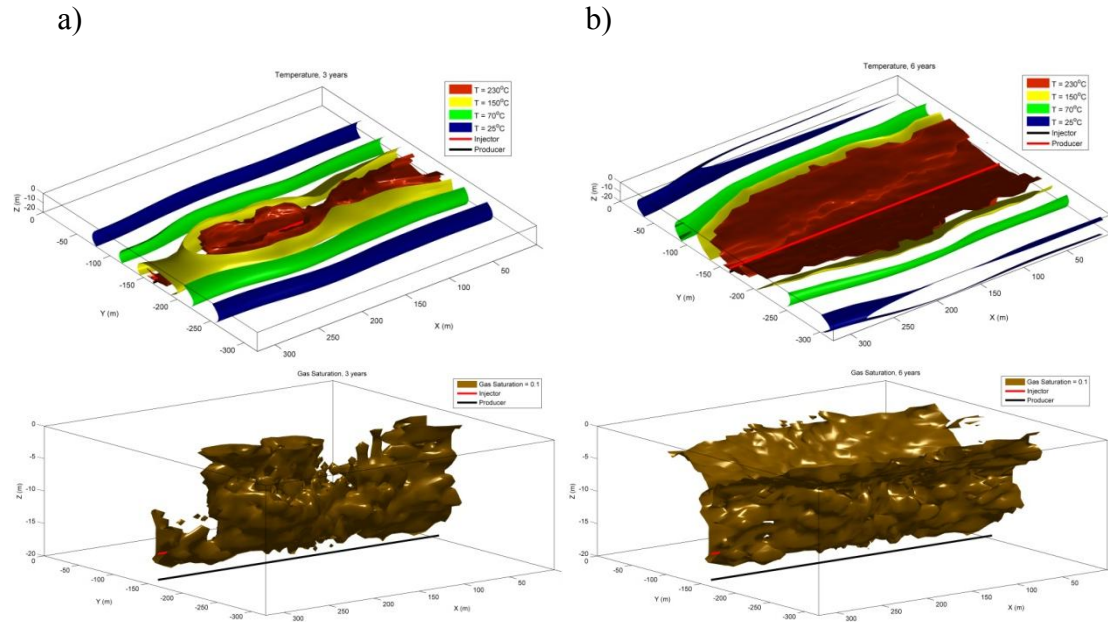
Figure 6.26: Temperature and gas saturation from reservoir simulation after a) 3 and b) 6 years of SAGD production. The upper row shows temperature isosurfaces of 230, 150, 70 and 25°C in hot to cool colors. The bottom row shows the 10% gas saturation isosurface.

6.5.2 Rock-physics modeling

Rock-physics models for bitumen and bitumen sands are currently not well developed. A large robust set of bitumen and bitumen sand measurements for rock-physics model calibration is not currently available. In order to translate the physical properties of the reservoir into elastic properties, rock-physics models and empirical relationships were employed that are thought to be the most appropriate for bitumen sands. First, the dry-frame modulus of the reservoir was calculated using the soft-sand model (Dvorkin and Nur, 1996). The fluid properties were calculated by two different methods; the bulk moduli and densities of the heavy oil, water and gas were calculated using the Batzle-Wang relationships (Batzle and Wang, 1992), and the shear modulus of the heavy oil as a function of temperature was calculated using an empirical relationship based on previous measurements made by Batzle et al. (2006) and Wolf and Mavko (2005) (Figure 6.27). Once the individual fluid component properties were

calculated, the overall fluid properties were calculated using a Voigt average. This average was used because the saturation is assumed to be patchy.

a)   b)
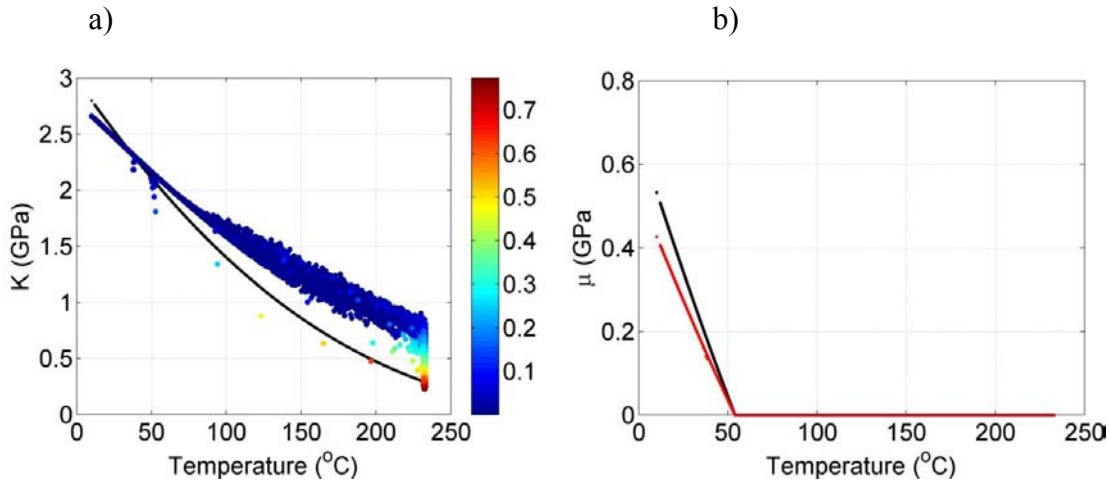
Figure 6.27: a) Bulk modulus as a function of temperature. The black line is for the heavy oil alone, and the colored points are for the variable fluid mixtures in the reservoir (oil, water and gas) over time color-coded as a function of gas saturation. b) Shear modulus as a function of temperature. The black line is for the heavy oil, and the red line is for the variable fluid mixtures throughout the reservoir over time.

The solid Gassmann model of Ciz and Shapiro (2007) was then used to saturate the dry frame to obtain the overall elastic properties of the reservoir (Figure 6.28). This model was used because at low temperatures the saturating fluid has a significant non-zero shear modulus, and upon heating the shear modulus decreases to zero. The solid Gassmann model has the advantage of being able to handle both scenarios, and is equivalent to traditional Gassmann fluid substitution when the fluid has zero shear modulus.
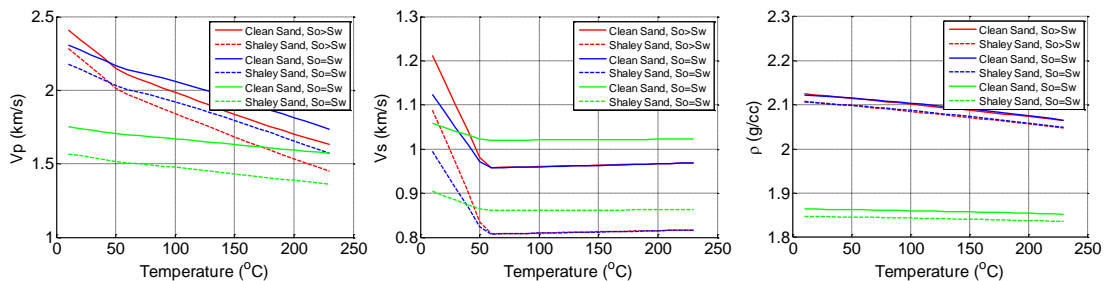
Figure 6.28: Vp, Vs and density of the reservoir as a function of temperature. Solid lines are for clean sand reservoir intervals and dashed lines are for shaley sand intervals. Red lines correspond to a fluid saturation of 80% heavy oil and 20% water, blue lines are 50% heavy oil and 50% water, and green lines are 10% heavy oil, 10% water and 80% gas saturation.

To complete the synthetic earth model, the reservoir was overlain by a uniform shale cap rock, and underlain by a limestone unit with properties similar to heavy-oil reservoirs in Canada. These reservoir and rock properties were then imported into Hampson-Russell, where converted-wave seismic sections were synthesized. The converted-wave seismic was simulated using the AVO module of Hampson-Russell, employing the Elastic Wave Method and recording the P-S wave response. This included modeling down-going P-waves and up-going S-waves. The recorded data are representative of the total particle motion recorded at the receivers. The wavelet used for the modeling was a zero-phase, 125 Hz Ricker wavelet. Offsets were extracted at 71 m and 441 m, which correspond to incidence angles of 10° and 50° at the top of the reservoir.

The inversion performed was a model-based inversion using Hampson-Russell STRATA software. The initial model was created from nine pseudo-wells equally spaced throughout the model; one at each corner, one halfway along each edge of the model, and one located in the center of the model. The pseudo-wells are sampled at pseudo-depths such that they correspond to the PS travel times of the synthetic seismic data. This is accomplished using the following formulas originally proposed by Gonzalez (2006):

$$pseudo\_v = V_s^d \, , \tag{6}$$

$$pseudo\_\rho = \rho^c \, , \tag{7}$$

$$pseudo\_z = \frac{z}{2}\left(\frac{1}{V_p} + \frac{1}{V_s}\right) pseudo\_v \tag{8}$$

6.5.3 'True' PSEI from reservoir model

Since this is a purely synthetic case, we have the actual reservoir properties of interest available to us. As a result, we can directly calculate what the value of PSEI is in the reservoir for a given angle. This allows us to directly compare how much of the information available from PSEI is lost when inverting for PSEI values from seismic data. Obviously the inverted result will have much lower resolution than the 'true'

PSEI calculated from the reservoir model, but it provides a means of evaluating the amount of information lost by the lower resolution of the seismic as well as in the inversion process itself.

Figure 6.29 shows the 'true' PSEI values calculated at 10° and 50° after 3 years of steam injection. From the calculated values of PSEI at 10 degrees we can see that the isosurface plots as roughly vertical planes located at approximately -100m and -230m along the y-axis. If we compare this to the temperature isosurface plot in Figure 6.26a, we see that this corresponds to roughly 50°C. This is in good agreement with our rock-physics model, which has the shear-wave velocity fairly constant after a temperature of roughly 60°C is reached. For the PSEI values calculated at 50°, we see a much different isosurface shape. At an angle of 50° PSEI is more sensitive to density changes within the reservoir. If we compare the PSEI isosurface in Figure 6.29b with the gas saturation isosurface in Figure 6.26a, we see that the two isosurfaces share the same shape. This demonstrates the potential for using PSEI to differentiate between heated zones and steam-saturated zones. Figure 6.30 shows the 'true' PSEI values calculated after 6 years of steam injection.

Comparing Figure 6.30a with the temperature isosurfaces in Figure 6.26b we can again see that the PSEI isosurface at an angle of 10° corresponds with a temperature of roughly 50°C, showing that near angle PSEI can indicate reservoir temperature from changes in shear-wave velocity. Also, if we compare Figure 6.30b with the gas saturation isosurface is Figure 6.26b the shapes are again very similar, indicating that the far angle values of PSEI can indicate the areas where there has been the formation of a steam chamber.

a)
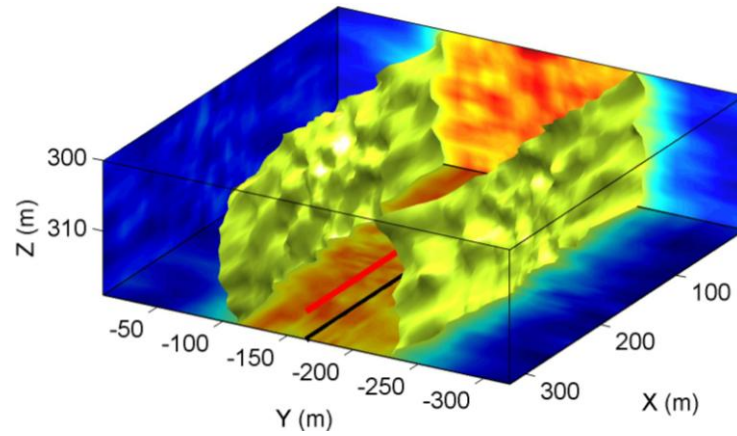
b)
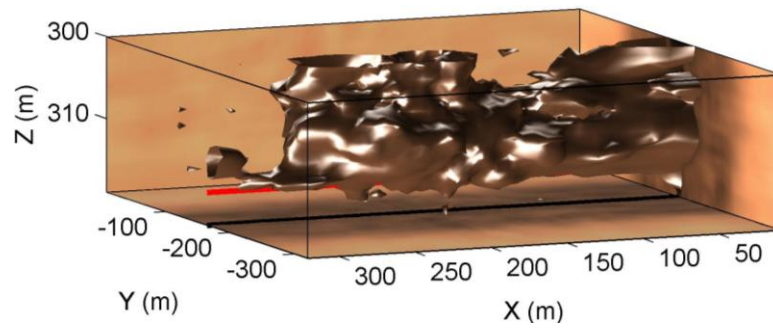
Figure 6.29: PSEI isosurfaces calculated from true reservoir properties after three years of steam injection at a) 10° incident P-wave angle and b) 50° incident P-wave angle.

a)

b)

Figure 6.30: PSEI isosurfaces calculated from true reservoir properties after six years of steam injection at a) 10° incident P-wave angle and b) 50° incident P-wave angle.

6.5.4 PSEI from inversion results

In order to directly compare the inverted results to those of the calculated PSEI values and the reservoir temperature and gas saturation, it was first necessary to convert the inverted sections from time to depth. This results in some errors in depth due to interpolation as is apparent in the results. In addition, given the finite bandwidth of the seismic and inversion processes, the result is also lower in resolution than the calculated PSEI result and actual reservoir properties. Nevertheless, examining the results of the inversion shows that the inversion does provide insight into the state of the reservoir.

Figures 6.31a) and b) show PSEI isosurfaces of the inversion results after 3 years of steaming for incident P-wave angles of 10° and 50° respectively. There are some definite dissimilarities between the results of the inversion and the calculated PSEI

values. The first difference is that there is a distinct top and bottom to the isosurface that are not located at the true locations of the reservoir top and bottom. This is due to both the finite bandwidth and depth conversion of the inversion. Also, the surfaces display less fine detail than the actual calculated PSEI surfaces. This is again due to the finite bandwidth, but also because the inversion results were smoothed.

Despite these differences, there are still characteristics common between the calculated and inverted results. Figure 6.31a displays vertical walls in the isosurface at approximately 100 m and 225 m. These correlate well in the horizontal dimensions with the vertical surfaces in the calculated result. In Figure 6.31b) there is an oblong shaped isosurface that displays similar characteristics to that seen in the calculated 50° PSEI isosurface. It does not contain as much detail, but correlates fairly well with the horizontal extent of the calculated isosurface. It does not extend along the x-axis to the origin as the calculated result does, but we can see that near the origin the extent of the calculated isosurface is much smaller. This smaller gas area cannot be resolved in detail due to bandwidth limitations and smoothing.

Figure 6.32 shows isosurfaces of the PSEI inversion results after six years of steam injection for a) 10° incident P-wave angle and b) 50° incident P-wave angle. The results after six years display problems that are similar to those seen in Figure 6.31 and again are due to bandwith limitations, time-to-depth conversion and smoothing. It is apparent though that after six years the isosurfaces have spread in the lateral direction, along the y-axis specifically, and despite the limitations of the process display a character similar to the calculated PSEI isosurfaces.

a)
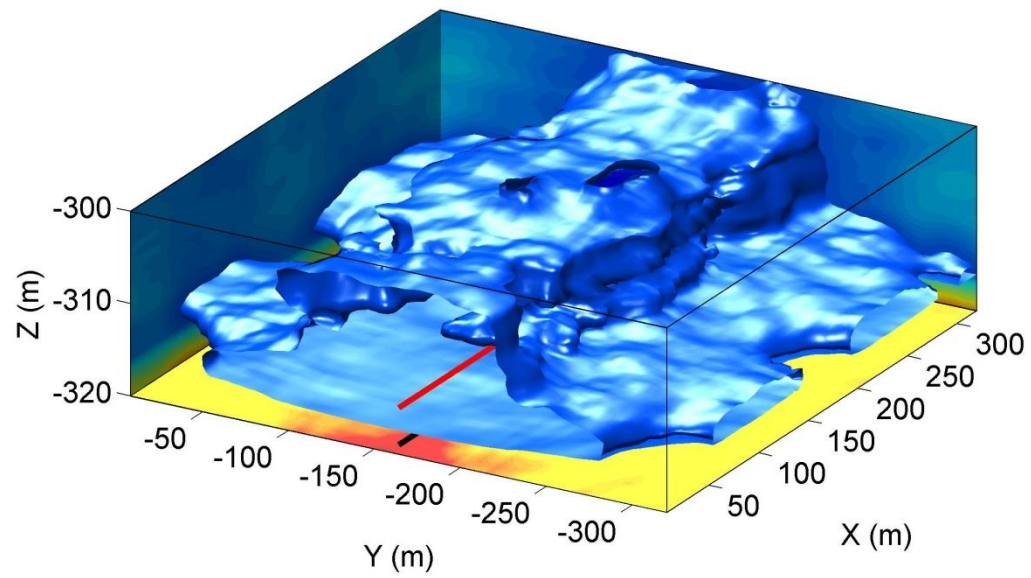
b)
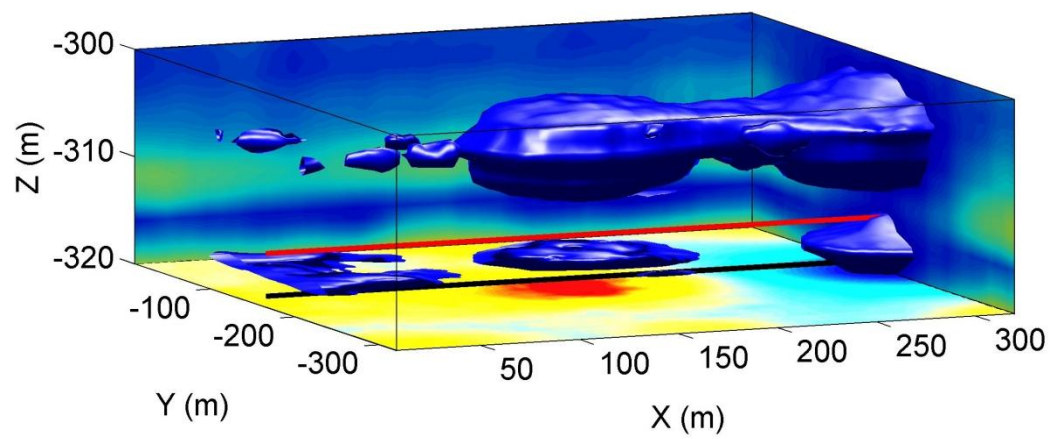
Figure 6.31: PSEI isosurfaces from the inversion after 3 years of steam injection at a) 10° incident P-wave angle and b) 50° incident P-wave angle.

a)
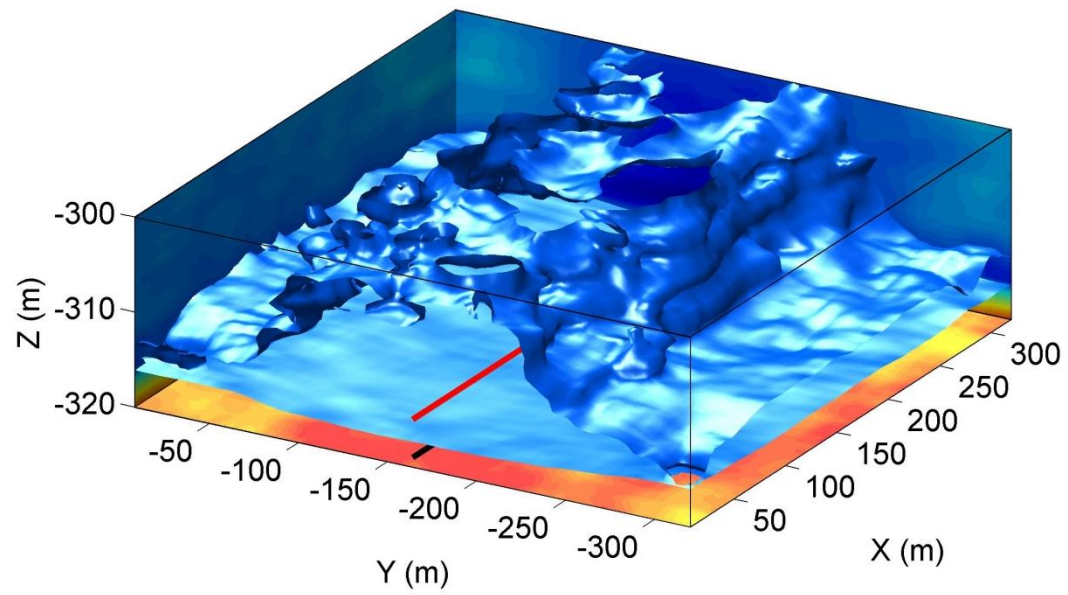
b)
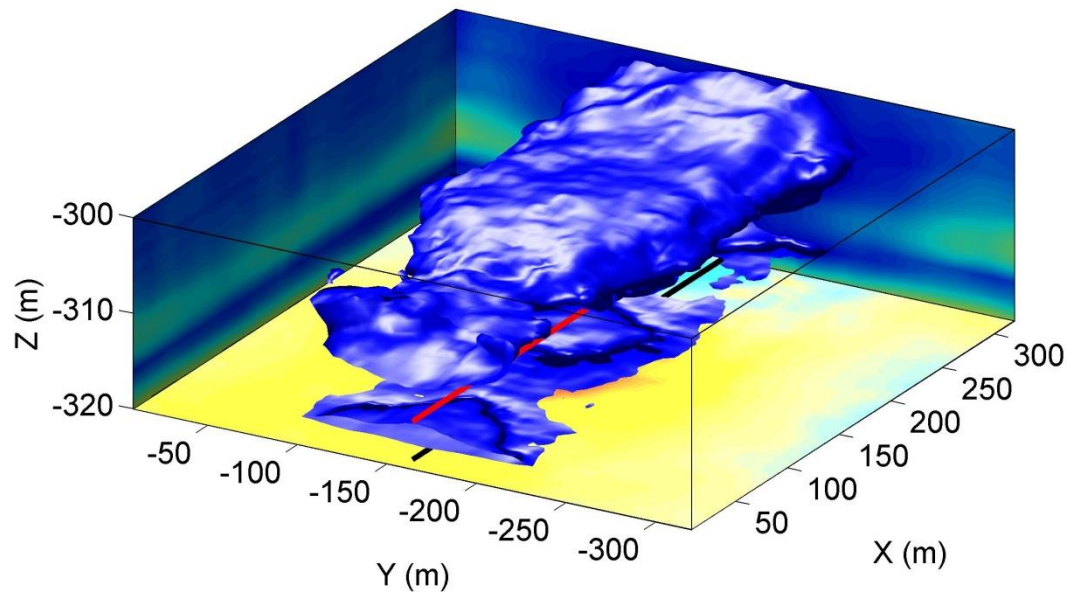
Figure 6.32: PSEI isosurfaces from the inversion after 6 years of steam injection at a) 10° incident P-wave angle and b) 50° incident P-wave angle.

6.5.5 Discussion

The preceding synthetic example and inversion results demonstrate that the inversion of converted-wave seismic data for PSEI attributes is a viable way to monitor the status of a heavy-oil reservoir produced by thermal means, or more specifically SAGD in this case. However, before this methodology is applied to a reservoir it is worth noting that a preliminary study should be carried out to assess the chances of a successful outcome.

The near-angle inversion will typically not be a problem; however, depending on the specific reservoir setting, the far-angle data may pose a problem. The angle at which the density and shear-wave velocity information begin to separate from one another may be large enough that it may not be feasible to collect that data, depending on the depth of the reservoir, the properties of the overlying rock, and the properties of the reservoir itself. To determine the far angle required, it is advisable to create a plot similar to that shown in Figure 6.33. This plot shows the value of the exponents c and d as a function of angle. To create this plot all that is needed is the average V_S/V_P ratio, or K as given in formulas (2) and (3). With this information and the depth of the reservoir, it is possible to determine the feasibility of acquiring the needed far-offset data.

In addition to determining the offsets required for a successful implementation of this methodology, it is also advisable to determine the reflectivity of the converted waves for the given reservoir scenario. This is shown in Figure 6.34 for this case study. For this example we can see that the initial reservoir properties provide a much higher reflectivity, and it decreases dramatically as the reservoir is heated and the steam chamber forms. This may also lead to the somewhat poorly defined top of the reservoir in our inversion results, as there is not a strong reflector for the inversion to key on at the top of the reservoir. In other cases the reservoir and cap rock properties can lead to this effect being more or less pronounced, which could further obfuscate results or lead to better ones depending on the specific situation.
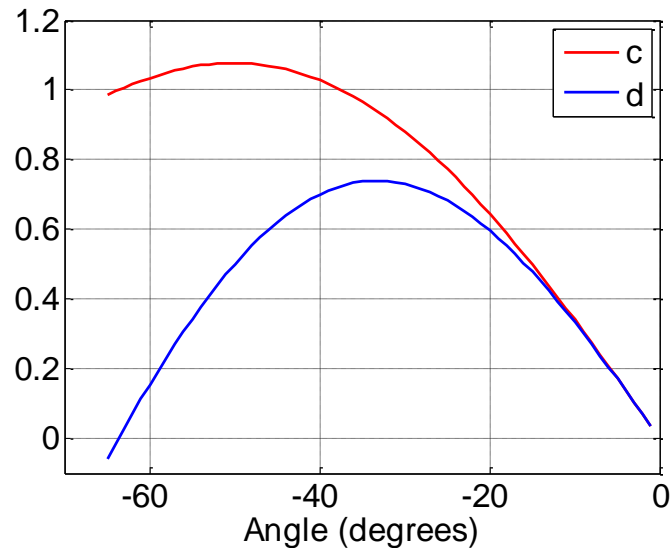
Figure 6.33: PSEI exponents *c* and *d* as a function of incident P-wave angle for this synthetic case.
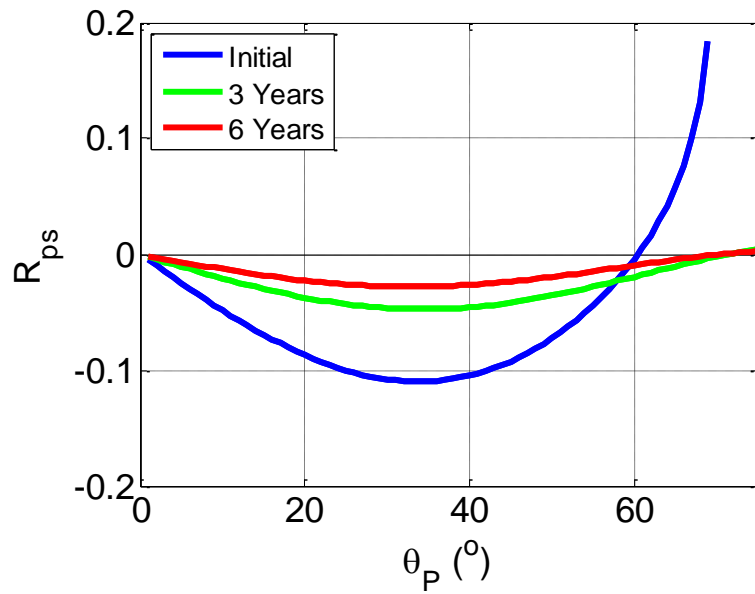
Figure 6.34: Converted-wave reflectivity at the top of the reservoir as a function of angle for constant overlying shale and average reservoir properties; initial (blue), after three years (green) and six years (red) of steam injection.

6.6 Discussion and conclusions

Applying PSEI analysis to investigate the state of bitumen reservoirs appears promising. Applying the method to synthetic data examples has revealed separate trends that indicate both velocity and density changes. In addition, modeling of specific reservoir states encountered during steam-assisted production of bitumen has shown that PSEI should be an effective tool for characterizing the reservoir as well as monitoring heated zones and the formation of steam chambers. PSEI analysis of laboratory measured data supported the previous modeling results, as well as provided further insight into how PSEI analysis can be used to monitor temperature and pressure in the reservoir given the proper conditions.

The preceding synthetic examples were carried out as an exercise to illustrate the utility of inverting converted-wave seismic data for PSEI attributes. The inverted attributes were obtained using commercial inversion software, and can be used to monitor the state of a bitumen reservoir being produced by thermal means. The inverted results, when plotted in PSEI space, show a clear distinction between cold and heated sections of the reservoir. In addition, the inversion also contains information regarding the presence and location of steam-chamber formation within the reservoir. Though this example does not result in a definitive separation of data corresponding to heated zones and steam filled zones when plotted in PSEI space, it does show that PSEI analysis can be used to delineate which areas of the reservoir are most likely to contain steam. Comparing these areas with known locations of steam injector wells will greatly aid in determining whether the area is likely to contain steam, or if it may simply be a heated area of the reservoir. It is also important that preliminary modeling be carried out in order to aid with the design of the seismic survey. This will ensure that the desired information is contained and can be extracted from the seismic data that is acquired.

The synthetic SAGD example demonstrates the usefulness of using PSEI inversion of converted-wave seismic data to monitor the status of a reservoir undergoing thermal production. If the seismic data has sufficient offset to ensure the separation of shear-wave velocity and density information at far offsets, this methodology should provide

a means of locating heated zones of the reservoir and areas where a steam chamber has formed. Of course, the success of the results will depend on the properties of the overlying and underlying rocks, as well as the variability of the reservoir properties themselves. For example, if the unit overlying or underlying the reservoir has very similar properties to the reservoir itself, there may not be sufficient contrast for the inversion to resolve anything. Similarly, if the reservoir is very stiff and the shear-wave velocity does not vary much upon heating, it may not be possible to differentiate heated zones from cold ones. Fortunately, the majority of Canadian heavy-oil reservoirs produced by thermal means should be fairly similar to the example presented here, and so this methodology should provide decent results in most situations for Canadian heavy-oil reservoirs as well as those in other parts of the world with similar properties.

Inverting converted-wave seismic sections for PSEI attributes can reveal much about the state of the reservoir in the subsurface. Incorporating this knowledge into the production strategy of the reservoir will greatly aid in making decisions that maximize efficiency and production from bitumen and heavy-oil reservoirs.

Chapter 7
Comparing PSEI inversion with acoustic and elastic impedance inversion

7.1 Abstract

The previous chapter introduced a methodology to monitor the state of a heavy-oil reservoir undergoing thermal production. Converted-wave seismic data was used to invert for P-to-S converted-wave elastic impedance (PSEI) in a reservoir simulation. The simulation mimicked the process of steam-assisted gravity drainage (SAGD) in a heterogeneous reservoir. The results of the simulation were fed into various rock-physics models to convert the reservoir properties to elastic properties. These

properties were then used to synthesize converted-wave seismic data at near and far offsets. The results showed that PSEI inversion can reveal heated zones within the reservoir as well as areas where steam chambers have formed.

We now compare those results with results from other inversion methodologies that do not require converted-wave seismic data as an input, to see if the added expense of acquiring converted-wave data is justified. If similar results can be obtained using compressional-wave data, then there may be no added benefit to acquiring and processing the converted-wave data for characterizing and monitoring heavy-oil reservoirs undergoing thermal production methods.

We compare acoustic impedance inversion and elastic impedance inversion in order to see which provides the best results. For this specific simulated case, acoustic impedance inversion provides a better image of the heated and steam filled portions of the reservoir than elastic impedance inversion. In addition, acoustic inversion is also cheaper computationally. However, we conclude that the PSEI inversion technique provides the most accurate location of heated zones and steam chamber formation within the reservoir. For this reason, the added cost and effort involved in PSEI inversion is justified in cases where a detailed picture of heated zones and steam is needed. Where less detail is needed, traditional acoustic-impedance inversion may suffice.

7.2 Introduction

Using PSEI inversion to characterize and monitor thermal production of heavy-oil reservoirs can be useful in determining areas of the reservoir that have been heated, as well as indicating where steam chambers have formed (Wolf and Mavko, 2009). However, it is rational to compare these results with more traditional inversion methods such as acoustic impedance inversion and elastic impedance inversion in order to better understand the benefits and drawbacks of using PSEI inversion.

The traditional approach is to use post-stack seismic data to invert for acoustic impedance. However, since the introduction of elastic impedance by Connolly (1999), we can also use pre-stack data to estimate elastic impedance, and gain further insight

into the reservoir. Both of these methods utilize compressional-wave seismic data in one form or another to investigate the properties of the reservoir in question.

In contrast, PSEI inversion requires converted-wave seismic data, making it essential to know whether the benefits of PSEI inversion can justify the extra cost of acquiring converted-wave data. To this end, the synthetic SAGD case study used in the previous chapter is used again to see how much can be learned about the reservoir state using only compressional-wave seismic data.

Acoustic impedance inversion has become a common practice in reservoir characterization and is part of numerous commercial software packages. Elastic impedance is a pseudo-impedance attribute (Connolly, 1998, Mukerji *et al..*, 1998) that is a far-offset equivalent of acoustic impedance. Information regarding the V_P/V_S ratio is contained within it, and can be useful for gaining further insight into the state of the reservoir while still being fairly straightforward and inexpensive.

7.3 Synthetic reservoir model

The synthetic model used in this study is the unfractured 3D reservoir model used by Chen et al (2008) to simulate a steam-assisted gravity drainage process in a heterogeneous reservoir. The reservoir is representative of a generic formation in the Alberta oil sands in Western Canada. The model was originally created for reservoir simulation, so certain properties of the reservoir which are of great importance to this study, such as mineralogy, were not explicitly stated. The properties given for the simulation are listed in Table 7.1.

The reservoir was created such that it contained a „clean sand‟ facies and a „shaley sand‟ facies, the latter containing laterally oriented thin shales. Sequential indicator simulation, a geostatistical method, was used to distribute these facies throughout the reservoir. In the reservoir model, different vertical permeabilities were used to differentiate between the two facies. From the distribution of vertical permeability, it was possible to assign plausible mineralogies to these specific clean and shaley sand lithologies. The mineralogy of the shaley sand unit was set to 60% quartz and 40 % clay, whereas the clean sand unit was set to 95% quartz and 5% clay. Figure 7.1 shows

the simulated distribution of clean sand (yellow) and shaley sand (brown) throughout the reservoir unit.

Table 7.1: Reservoir properties used for the SAGD reservoir simulation.

Reservoir depth	300 m
Reservoir thickness	20 m
Porosity	0.32
Horizontal permeability	3,000 mD
Vertical permeability	1,800 mD
Oil viscosity (RC)	1,000,000 cp
Reference depth	315 m
Initial pressure	2,896 kPa
Initial temperature	50 °F
Initial oil saturation	0.80
Initial water saturation	0.20
Oil density (RC)	8.8 °API
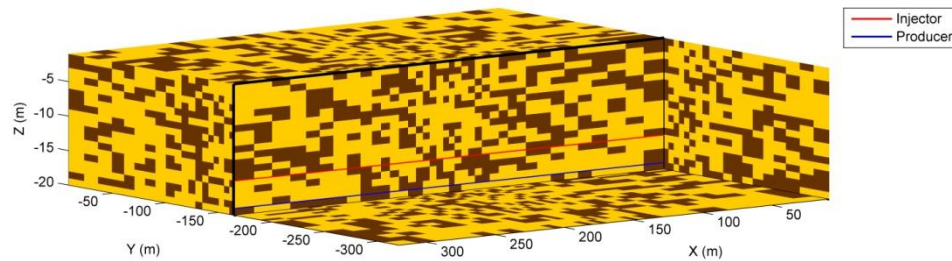
Figure 7.1: Distribution of clean sand (yellow) and shaley sand (brown) throughout the reservoir. Also shown are the injection well (red) and production well (blue) used in the SAGD simulation.

The flow simulation was performed using CMG STARS thermal and compositional simulator. In the simulation, electrical preheating was performed for 90 days, followed by 95% quality steam injected at 3000 kPa. During the simulation the production wells were operated such that they avoid excessive steam production, and the state of the reservoir was output after three and six years of injection.

Figure 7.2 shows the temperature and gas saturation of the reservoir after a) three years and b) six years of SAGD production. The temperature profile of the reservoir is shown by isosurfaces of different temperatures, and the gas saturation is shown by the isosurface corresponding to 10% gas saturation. The temperature and gas saturation are important properties for us to consider in our study, because they relate to the heating of the reservoir and formation of the steam chamber. Hence, they relate to shear-wave velocity and density changes which will have a direct effect on the PSEI values obtained from the inversion.

a)   b)
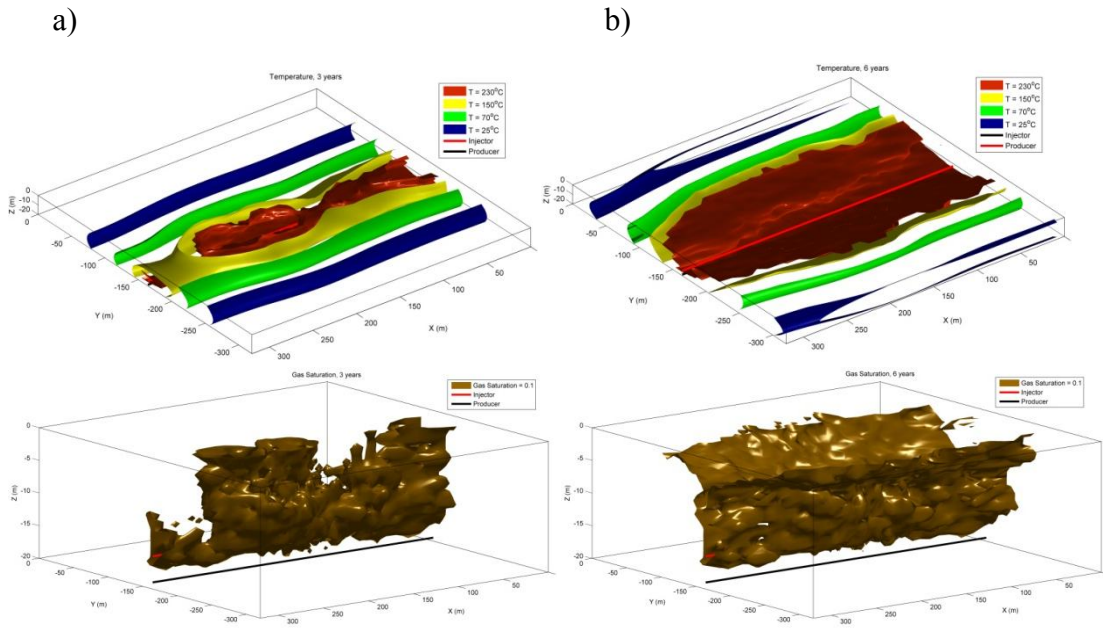
Figure 7.2: Temperature and gas saturation from reservoir simulation after a) three and b) six years of SAGD production. The upper row shows temperature isosurfaces of 230, 150, 70 and 25°C in hot to cool colors. The bottom row shows the 10% gas saturation isosurface.

7.4 Reservoir properties of interest

Rock-physics models for bitumen and bitumen sands are currently not well developed. This is because a large, robust set of bitumen and bitumen sand measurements for rock-physics model calibration is not currently available. The system outlined in Chapter 2 and the measurements reported in Chapter 3 begin to

address the lack of data, and insights gained from the measurements reported were used to guide our rock property modeling. To translate the physical properties of the reservoir simulation into elastic properties, we used rock-physics models and empirical relationships that we thought most appropriate for bitumen sands. First, the dry-frame modulus of the reservoir was calculated using the soft-sand model (Dvorkin and Nur, 1996). The fluid properties were calculated by two different methods. The bulk moduli and densities of the heavy oil, water and gas were calculated using the Batzle-Wang relationships. To calculate the shear modulus of the heavy oil as a function of temperature, an empirical relationship based on previous measurements made by Batzle et al (2004) and Wolf and Mavko (2005) was used. Once the individual fluid component properties were calculated, the overall fluid properties were calculated using a Voigt average (Mavko *et al*., 1998). This average was used because the saturation is assumed to be patchy.

The solid Gassmann model of Ciz and Shapiro (2007) was then used to approximately saturate the dry frame to obtain the overall elastic properties of the reservoir. This model was used, because at low temperatures the saturating fluid has a significant non-zero shear modulus; and upon heating the shear modulus decreases to zero. The solid Gassmann model has the advantage of being able to handle both scenarios, and is equivalent to traditional Gassmann fluid substitution when the fluid has zero shear modulus.

To complete the synthetic earth model, the reservoir was overlain by a uniform shale cap rock, and underlain by a limestone unit with properties similar to heavy-oil reservoirs in Canada. These reservoir and rock properties were then imported into the Hampson-Russell AVO module where seismic sections were synthesized.

In order to efficiently produce heavy-oil reservoirs by thermal recovery methods, it is important to know the state of the reservoir, and how it is changing during production. Therefore, it is important to understand how those properties will be reflected in the measurable seismic parameters, namely V_P, V_S and density. The properties of greatest interest for heavy-oil reservoir production by steam-assisted or

thermal means are the temperature of the reservoir and the formation of steam chambers.

The main goal of thermal production is to heat the heavy oil, so that it becomes less viscous and is able to flow in the reservoir. This means that as we heat the reservoir, the shear modulus of the oil will change from a finite value to zero, and this will in turn affect the P- and S-wave velocities in the reservoir. Several cross-plots of reservoir properties have been constructed which show the reservoir simulation data at original in-situ conditions, as well as after three and six years of production. Figure 7.3 shows a cross-plot of the S-wave velocity as a function of temperature, with data points color-coded by the fluid shear modulus. It is apparent that the shear velocity of the reservoir decreases as the temperature increases, up to about 60°C. Above 60°C, the shear modulus of the reservoir fluid has reached zero; thus the velocity levels off. It is apparent that the shear velocity of the reservoir will give us an indication of the reservoir temperature up to about 60°C, beyond which it is not important to know, since at that point the reservoir fluids are already able to flow.
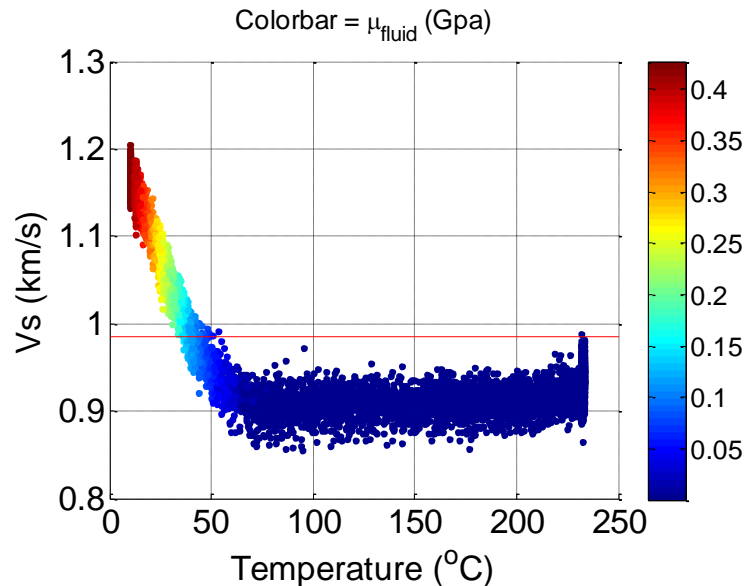
Figure 7.3: Cross-plot of S-wave velocity vs. temperature for the reservoir, color-coded by fluid shear modulus.

Figure 7.4 shows a cross-plot of the P-wave velocity as a function of temperature, with data points again color-coded by the fluid shear modulus. The plot shows that the

P-wave velocity decreases as a function of temperature over the entire temperature range, unlike the S-wave velocity. However, there is a slight bend in the P-wave velocity versus temperature trend at about 60°C. These trends show that we can still extract information on the temperature of the reservoir from the P-wave velocity of the reservoir; however we can expect the velocity to change over the entire temperature range given, instead of only where the fluid shear modulus is decreasing.
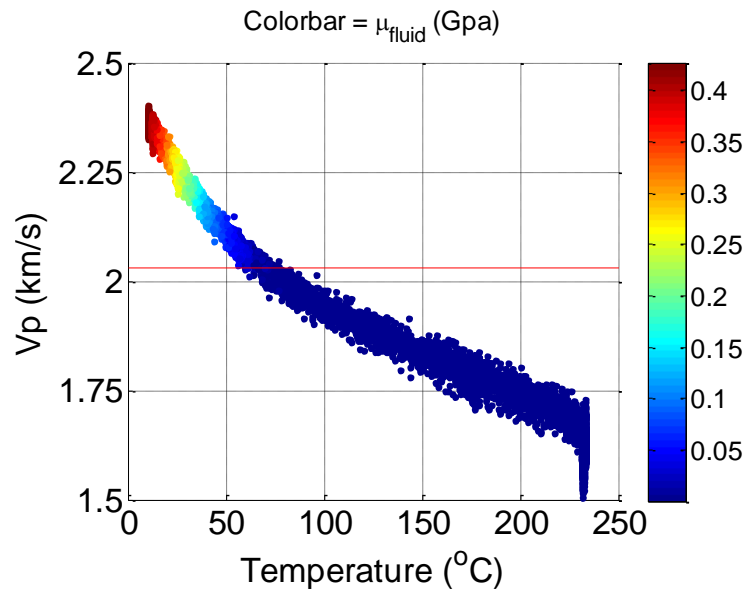
Figure 7.4: Cross-plot of P-wave velocity vs. temperature for the reservoir, color-coded by fluid shear modulus.

As was mentioned earlier, another valuable piece of information for heavy-oil reservoirs undergoing thermal production is to know when and where steam chambers are forming. When steam and/or gas replaces the fluids originally saturating the reservoir, whether they be heavy oil or water, there will be a decrease in the overall bulk density in that location, due to the density differences between the steam/gas and the oil or water. Figure 7.5 shows a cross-plot of density versus temperature for the entire reservoir simulation lifetime, color-coded by the gas saturation. As expected, the higher the gas saturation the lower the bulk density. This illustrates that if we can get an estimate of density from our seismic data, we should be able to identify areas of the reservoir likely to be saturated by steam and gas.
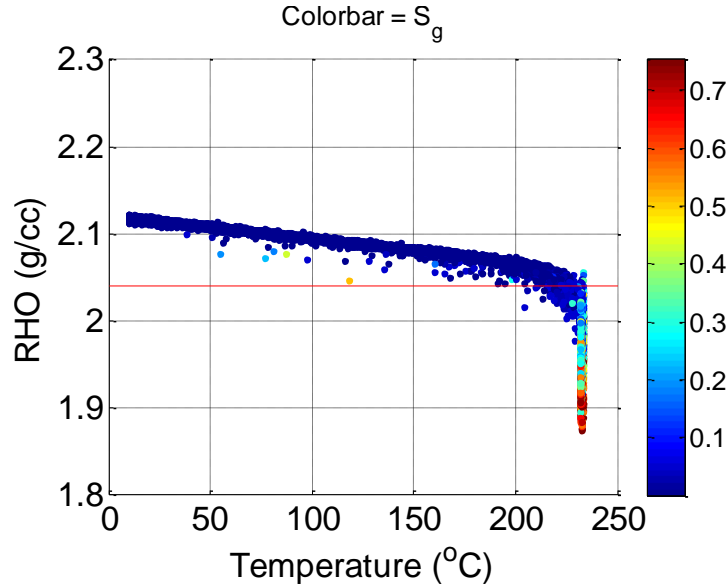
Figure 7.5: Cross-plot of density vs. temperature for the reservoir color-coded by gas saturation. The red horizontal line corresponds to a threshold of 2.04 g/cc, which will be used as an isosurface threshold in later analysis.

Figure 7.6 shows a plot of acoustic impedance versus temperature, color-coded by a) fluid shear modulus and b) gas saturation. Acoustic impedance is the product of P-wave velocity and density. We can see the two trends that we observed earlier in the plots of P-wave velocity (Figure 7.4) and density (Figure 7.5) now reflected in the acoustic impedance.

The presence of these trends allows us to set thresholds on the data in order to help highlight properties of the reservoir that are of interest. First, examining Figure 7.6a, we can see that by setting a threshold of 4300 m/s*g/cc, we can separate the reservoir areas where the fluid modulus has not been reduced to zero from the areas where the fluid has been heated further and will be able to flow easily. Similarly, if we examine Figure 7.6b, we can see that by setting a threshold of 3375 m/s*g/cc, we can separate the areas of the reservoir that have a significant gas saturation from the rest of the reservoir, and get an indication of where a steam chamber has formed.

Examining the cross-plots of shear impedance and temperature, we can see features similar to those in the acoustic impedance case. Figure 7.7a shows the data color-coded by fluid shear modulus. There is a clear threshold at 1970 m/s*g/cc where the heated areas of the reservoir, which are able to flow, can be separated from the rest

of the reservoir. However, Figure 7.7b shows that, unlike in the acoustic case, there is no effective threshold to separate the areas of the reservoir with high gas saturation from the rest. In an attempt to do so, a threshold of 1825 m/s*g/cc has been plotted, but it is not very effective.
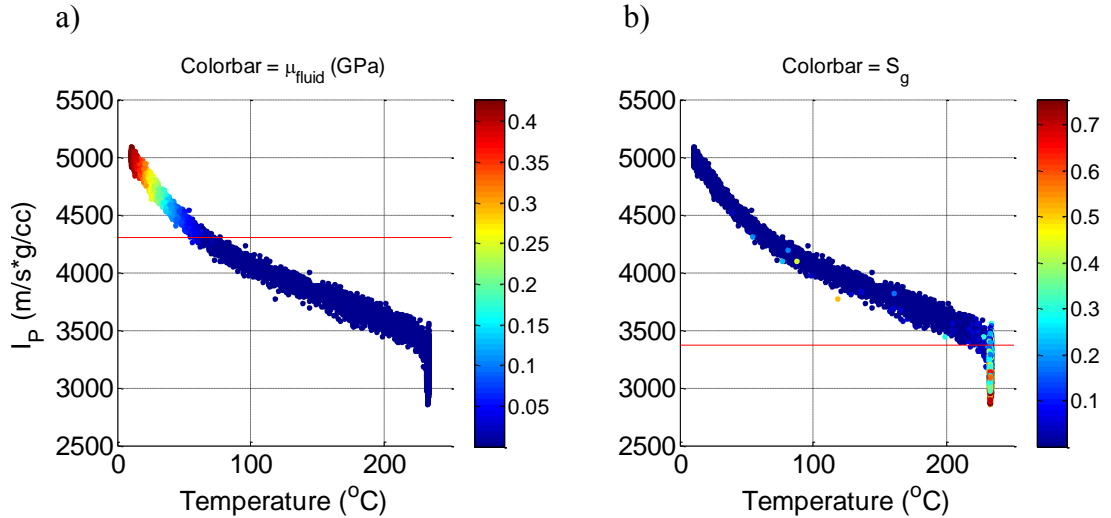
Figure 7.6: Cross-plot of P-wave impedance vs. temperature for the reservoir, color-coded by a) fluid shear modulus and b) gas saturation. The red horizontal lines in a) and b) correspond to the thresholds chosen for the following isosurface plots of P-wave impedance.

By taking the thresholds selected and applying them to the data volume from the synthetic reservoir simulation we can see the expression and location of heat and steam chamber features within the reservoir at different times during the production of the reservoir. Figure 7.8a shows the reservoir P-wave impedance after three years of steam injection using the threshold of 4300 m/s*g/cc (from Figure 7.6a) to create an isosurface. From this image we can see that the heated zone of the reservoir can be identified by using the acoustic impedance. Similarly, if we look at Figure 7.8b, using the threshold of 3375 m/s*g/cc (from Figure 7.6b) reveals the location of the steam chamber. Comparing these isosurfaces with the actual temperature and gas saturation isosurface plots shown in Figure 7.2, we see good agreement, indicating that the thresholds applied to the acoustic impedance are providing the information we need about the heat distribution in the reservoir, as well as the distribution of steam.

a)   b)
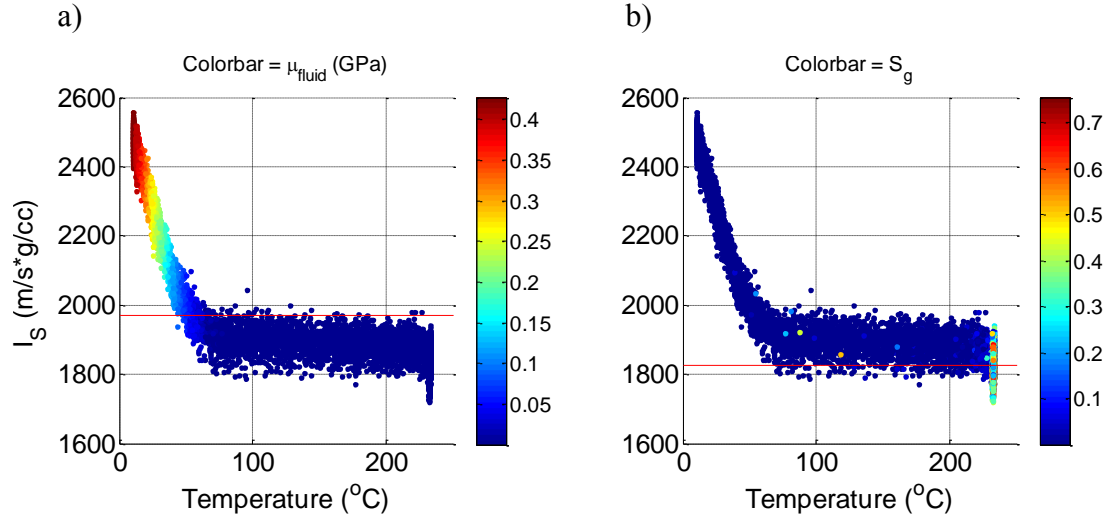
Figure 7.7: Cross-plot of S-wave impedance vs. temperature for the reservoir, color-coded by a) fluid shear modulus and b) gas saturation. The red horizontal lines in a) and b) correspond to the thresholds chosen for the following isosurface plots of S-wave impedance.

a)   b)
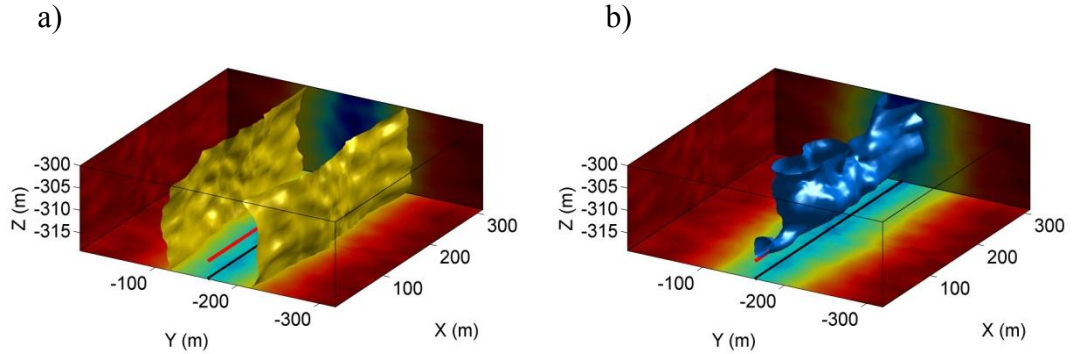
Figure 7.8: Isosurface plots of P-wave impedance after three years of steam injection with a) threshold taken from Figure 7.6a, and b) threshold taken from 7.6b. Red and black lines are the injector and producer wells respectively.

Figures 7.9a and b show the upper and lower thresholds applied to the acoustic impedance volumes of the reservoir simulation after six years of steam injection. Again we see that these thresholds provide isosurfaces that match well with the corresponding temperature and gas saturation plots in Figure 7.2.

This illustrates that the information required to properly monitor and efficiently produce heavy-oil reservoirs undergoing steam-assisted production can be found in the acoustic impedance. To determine where the heated zones of the reservoir are, a relatively high threshold for acoustic impedance, in this case 4300 m/s*g/cc, must be chosen. To image the area of steam-chamber formation, a relatively low threshold

must be set for acoustic impedance. In this case it is 3375 m/s*g/cc. The thresholds chosen to reveal the heated and steam zones will not be universal, and will be highly dependent on the reservoir properties for each specific reservoir. However, this investigation does demonstrate that given the correct reservoir properties it may be possible to use acoustic impedance to delineate heated and steam zones within a heavy-oil reservoir undergoing steam-assisted production.
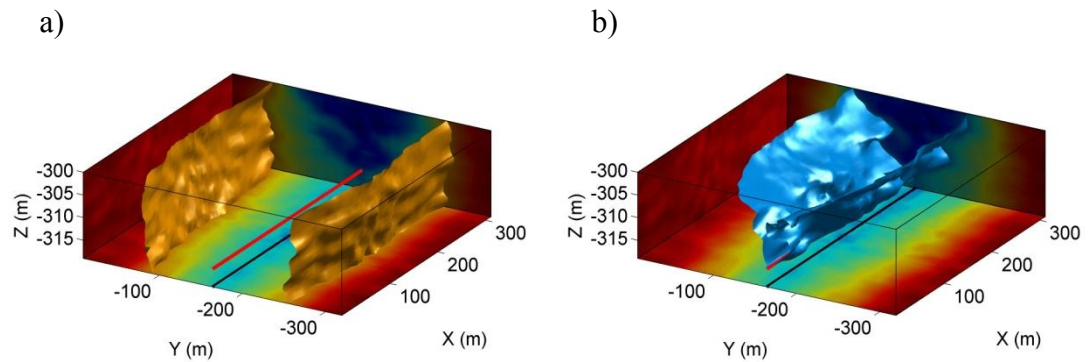
Figure 7.9: Isosurface plots of P-wave impedance after six years of steam injection with a) threshold taken from Figure 7.6a, and b) threshold taken from 7.6b. Red and black lines are the injector and producer wells respectively.

The same approach can be taken with the shear impedance volumes from the reservoir simulation to see what information pertaining to the heat and steam distribution within the reservoir can be revealed. Not surprisingly, when the upper threshold of 1970 m/s*g/cc (from Figure 7.7a) is used to create isosurfaces in the shear impedance volume as shown in Figure 7.10a, the heated zone in the reservoir is well defined, and compares well with the temperature isosurface plots in the previous chapter.

However, we are not as successful in defining the areas of the reservoir that contain steam by using the lower threshold of 1825m/s*g/cc (from Figure 7.7b). This is because of the relatively small effect of density on the shear impedance. When density decreases due to fluid substitution and the shear modulus of the rock remains the same, as is the case when steam replaces heated bitumen, the result is a very small change in the shear wave impedance. This is because the shear impedance changes proportional to the square root of the change in density. This results in the inability of

the shear impedance to adequately define the steam chamber in the reservoir as can be seen in Figure 7.10b.

a)   b)
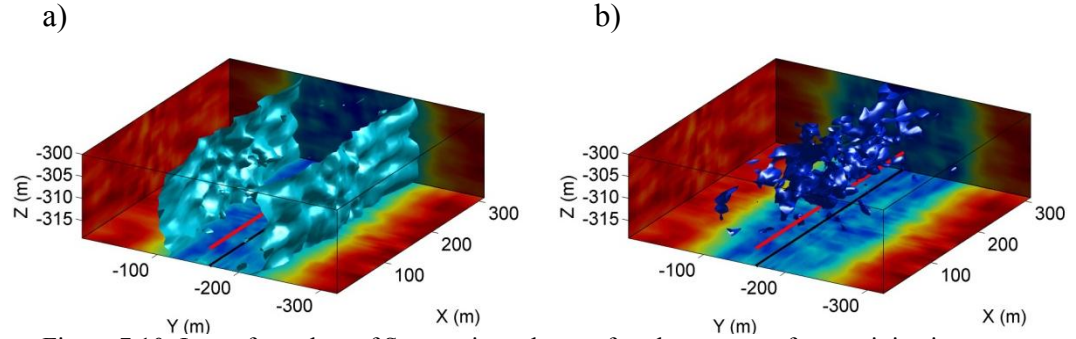
Figure 7.10: Isosurface plots of S-wave impedance after three years of steam injection with a) threshold taken from Figure 7.7a, and b) threshold taken from 7.7b. Red and black lines are the injector and producer wells respectively.

Figures 7.11a and b show the upper and lower thresholds applied to the shear impedance volumes of the reservoir simulation after six years of steam injection. Again we see that the upper threshold isosurface (Figure 7.11a) matches well with the corresponding temperature isosurface plot in the previous chapter, but the lower threshold isosurface does not indicate where the steam chamber is located within the reservoir.

a)   b)
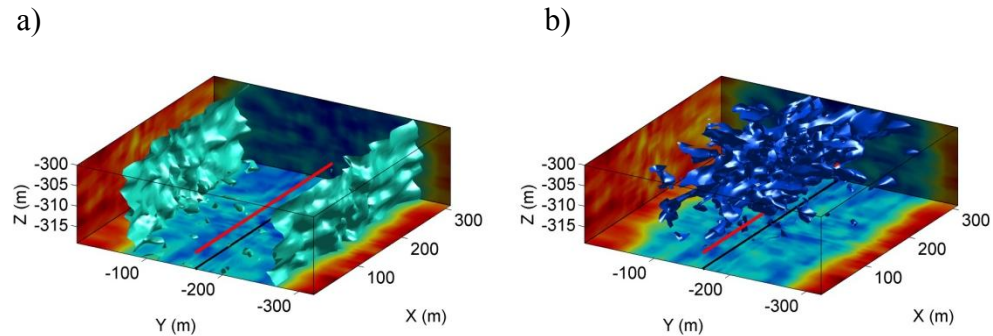
Figure 7.11: Isosurface plots of S-wave impedance after six years of steam injection with a) threshold taken from Figure 7.7a, and b) threshold taken from 7.7b. Red and black lines are the injector and producer wells respectively.

7.5 Acoustic impedance inversion

The preceding analysis demonstrates that the acoustic impedance values within the reservoir contain information that can help to delineate heated zones and areas of steam chamber formation. However, an investigation into the effectiveness of the inversion process for these types of reservoirs is yet to be completed. To this end, compressive wave seismic data was synthetically generated from the properties obtained through the reservoir simulation with the AVO module of Hampson Russell, and the acoustic impedance was inverted for using the STRATA module of the same commercial software package.

In AVO, the seismic data was synthesized using a zero-phase, 120Hz Ricker wavelet, with offsets every 50 m ranging from 0 to 500 m. To perform the acoustic inversion, only the zero-offset data were used. The inversion algorithm used was the model-based inversion algorithm in STRATA. To create the initial model, 9 equally spaced "wells" were used from the reservoir simulation output; one well at each corner of the model, one at the center of each edge, and one in the very center of the model. For the actual inversion, the initial model was given minimal weight (model parameter of 0.001) to ensure that the inversion result was driven by the seismic data and not the initial model.

Examining the results of the inversion of the seismic data after three years of steam injection, as shown in Figure 7.12, reveals some interesting features. If the inversion result is first plotted as an isosurface with a threshold of 4300 m/s*g.cc (Figure 7.12a), it roughly corresponds with the extent of the heated zone in the reservoir. This is not unexpected, since the threshold of 4300 m/s*g/cc was established to highlight the heated zones. There are some slight differences in the inversion result with the threshold and the true location of the heated zones in the reservoir, but overall the method does a good job of highlighting the correct areas. Similarly, if the inversion result is plotted as an isosurface with a threshold of 3375 m/s*g/cc (Figure 7.12b) it roughly corresponds to the location of the steam chamber within the reservoir. Again, this isn‟t unexpected since the lower threshold is designed to highlight the location of steam within the reservoir. The correlation between this isosurface and the

actual steam chamber location is not as high as for the result for the heated zones, but it still does a fairly good job of predicting the areas where a steam chamber is most likely.
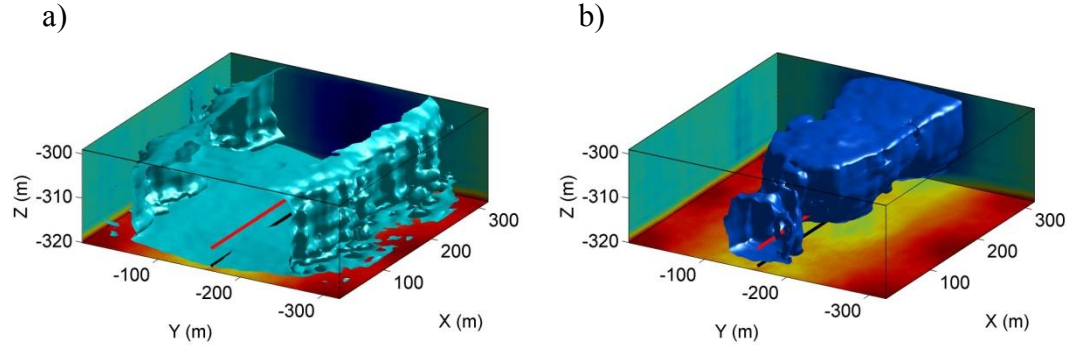
Figure 7.12: Isosurface plot of the acoustic impedance inversion result after three years of steam injection. Red and black lines are the injector and producer wells respectively. The threshold used for the isosurface plot in a) is 4300 m/s*g/cc, and in b) is 3375 m/s*g/cc. These are the same thresholds illustrated in Figure 7.6.

If the results of the inversion after six years of steam injection are plotted in the same way, we see similar results (Figure 7.13). First, in Figure 7.13a, we see the higher threshold of 4300 m/s*g/cc applied to the inverted data. Again, this result corresponds well with region within the reservoir that has been heated to the point where the fluid shear modulus is zero. Second, if the lower threshold of 3375 m/s*g/cc is applied to the inversion result, we get an isosurface that mimics the distribution of gas within the reservoir.

Comparing the results shown in Figures 7.12 and 7.13 reveals that the acoustic impedance inversion tends to perform better at revealing heated zones within the reservoir than it does identifying gas saturated zones. The results of the inversion with the lower threshold applied tend to overestimate the size of the steam chamber when compared to the actual steam chamber that develops during the reservoir simulation. This is most likely due to the limited bandwidth of the seismic data and the inversion process, both temporally and spatially. Comparing the acoustic impedance inversion results plotted in Figures 7.12b and 7.13b with the actual acoustic impedance in plots 7.8b and 7.9b, it is apparent that the thinner the gas saturated zone, the harder it is for the inversion to narrow down the location of the steam chamber. This is particularly evident in the end of the reservoir near X = 0 m after three years, and lower in the

reservoir (Z = −320 m) after six years of steam injection. In both of these areas the acoustic impedance inversion greatly amplifies the size of the steam chamber. This is likely due to the inversion seeing a change in the reservoir, but the limited nature of the seismic bandwidth makes it difficult for the inversion to focus the results on the small area that is contributing to the acoustic response.
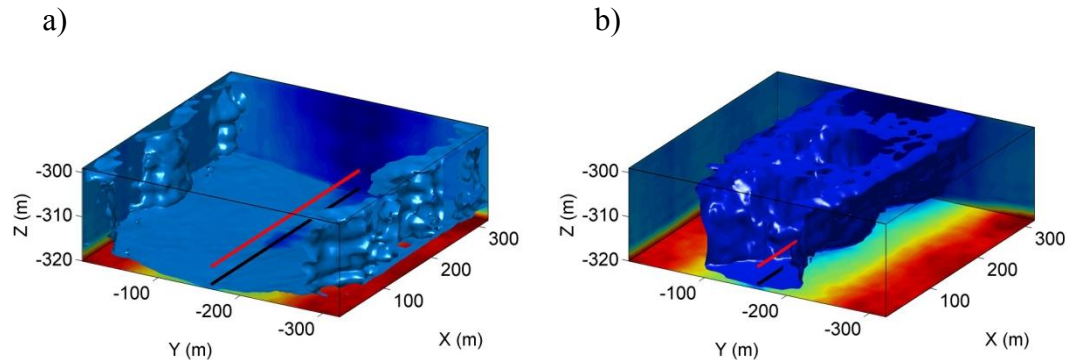
Figure 7.13: Isosurface plot of acoustic impedance inversion result after six years of steam injection. Red and black lines are the injector and producer wells respectively. The threshold used for the isosurface plot in a) is 4300 m/s*g/cc, and in b) is 3375 m/s*g/cc. These are the same thresholds illustrated in Figure 7.6.

However, keeping this in mind, the acoustic impedance still does a decent job at revealing the areas where the reservoir has been heated and where steam chambers have formed in the reservoir. Both of these pieces of information are important when producing heavy-oil reservoirs by steam assisted methods, and using traditional converted-wave zero-offset or stacked data and inverting it for acoustic inversion could prove valuable.

7.6 Elastic impedance inversion

Elastic impedance is a pseudo-impedance attribute (Connolly, 1998, Mukerji *et al.*., 1998) that is a far-offset equivalent of acoustic impedance. Information regarding the V_P/V_S ratio is contained within it, and as such it can be a useful way of gaining further insight into the state of the reservoir while still being fairly straightforward to obtain and not too expensive computationally. For this example, we invert for elastic impedance at near, mid and far angles. This allows us to investigate multiple angles of elastic impedance and determine whether any of them aid in determining the extent of

heated zones in the reservoir, or if they indicate the location of steam chambers within the reservoir.

The elastic impedance inversion was performed using the Hampson Russell software package. First, seismic data that was previously simulated was stacked according to angle. Range-limited stacks were created to give three angle ranges to be inverted; these were near angle (0-20°), mid angle (20-40°) and far angle (40-60°). Using the Strata package within Hampson Russell, an initial model for each range-limited stack was created by using the same 9 wells as were used for the acoustic impedance initial model. However, to create an initial model that corresponded to the elastic impedance, the well logs were filtered so that they were consistent with the elastic impedance at the mean values of the angle stacks, 10°, 30° and 50° respectively. For each of the angles, the inversion itself was performed as a model-based inversion, using a wavelet extracted from the reservoir portion of each angle stack. Minimal weighting was used for the initial model to ensure that the result of the inversion was data driven, and not model driven.

Figures 7.14 through 7.16 show the results of the near-, mid- and far-angle inversions, respectively, after three years of steam injection. Each figure consists of two isosurface plots with a different threshold used in each case in order to attempt to highlight the steam chamber and heated zones within the reservoir. One challenge in using elastic impedance to monitor a reservoir over time is that the units and dimensions of elastic impedance are unusual and vary with angle. Because of this, a trial-and-error approach to setting thresholds was used in this case, rather than a deterministic method of selecting thresholds based on data or a model, as is the case for acoustic impedance.

Figure 7.14 shows the inverted near-angle (0-20°) elastic impedance after three years of steam injection. Thresholds of a) 3050 and b) 3250 were chosen to attempt to highlight the extent of steam chamber formation and heating respectively. The near angle elastic impedance seems to pick up more of the character of the steam chamber than of the heated zone. Despite this, it still does a poor job of defining the extent of the steam chamber. It does give a decent indication of where steam may be in the

reservoir laterally (Figure 7.14a), but the vertical resolution of the inversion result is very poor. Even when the isosurface threshold is changed to highlight the heated zones of the reservoir, the sides show much more relief than the actual sides of the heated area do in the reservoir simulation, and still seem to reflect the shape of the steam chamber.

a)   b)
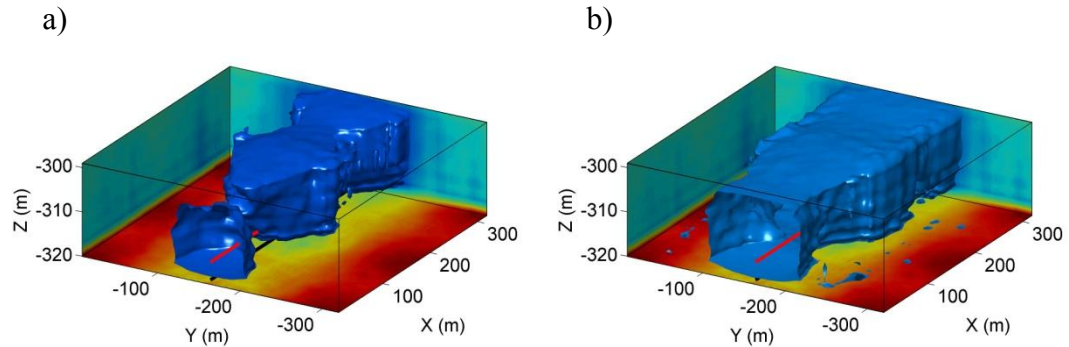
Figure 7.14: Isosurface plot of near-angle elastic impedance after three years of steam injection. Isosurface thresholds of a) 3050 and b) 3250 were used in order to attempt to highlight the steam chamber and heated zones respectively. Red and black lines are the injector and producer wells respectively.

Examining the results of the mid-angle (20-40°) elastic impedance inversion it is apparent that the inversion does a slightly better job of imaging the heated zone than it did in the near-angle case. Figure 7.15a reveals the extent of the steam chamber, although there again is an issue with the vertical resolution of the result. Changing the threshold of the isosurface plot to highlight the heated zone (Figure 7.15b) shows that, compared to the near-angle elastic inversion, the mid-angle seems to be less influenced by the steam-chamber location. This gives a more accurate representation of the extent of the reservoir that has been heated.

In contrast to the near- and mid-angle elastic inversion results, the far-angle (40-60°) elastic impedance inversion does not give a very accurate representation of either the location of the steam chamber within the reservoir or the extent of heating. These results can be seen in Figure 7.16. This figure shows that the definition of both areas has been greatly compromised as compared to the inversions at lesser angles.

a)   b)
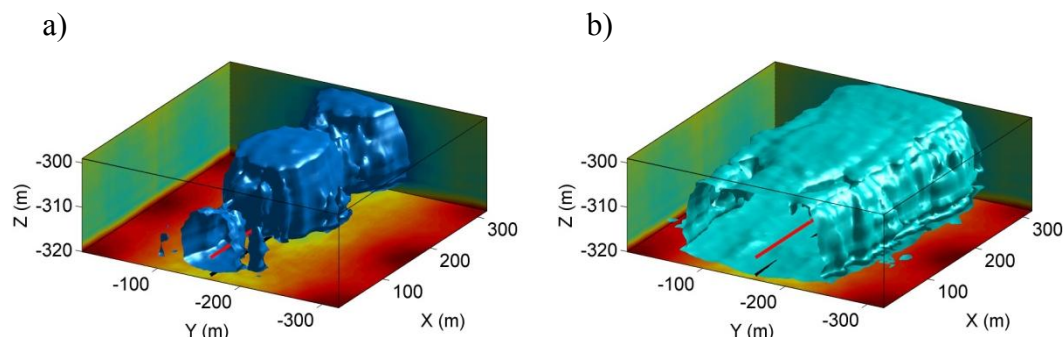
Figure 7.15: Isosurface plot of mid-angle elastic impedance after three years of steam injection. Isosurface thresholds of a) 600 and b) 700 were used in order to attempt to highlight the steam chamber and heated zones respectively. Red and black lines are the injector and producer wells respectively.

a)   b)
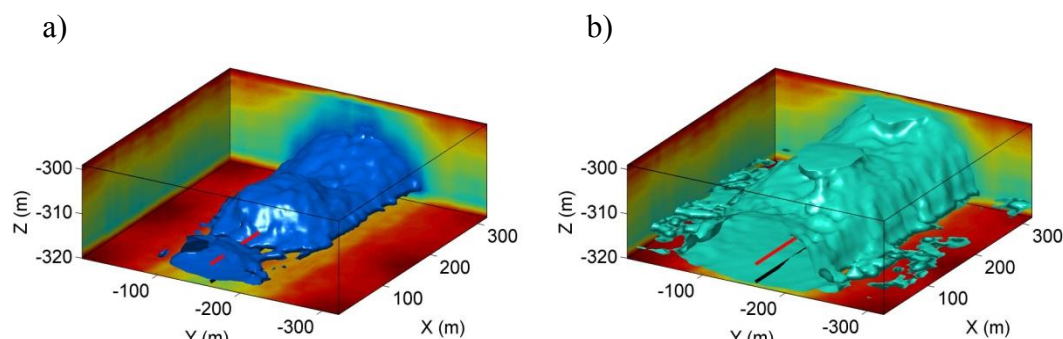
Figure 7.16: Isosurface plot of far-angle elastic impedance after three years of steam injection. Isosurface thresholds of a) 39 and b) 52 were used in order to attempt to highlight the steam chamber and heated zones respectively. Red and black lines are the injector and producer wells respectively.

Figures 7.17 through 7.19 show the results of the near-, mid- and far-angle inversions respectively after six years of steam injection. The results here, not unexpectedly, show features similar to those in the inversions carried out after three years. Again, it is apparent that the near- and mid-angle inversions (Figures 7.17 and 7.18) do a decent job of revealing the location of heated and steam filled zones, but there are some limitations in the resolution and accuracy of the results. The far-angle inversion (Figure 7.19) again fails to provide much insight into either the extent of heating or steam-chamber formation within the reservoir.

a)   b)
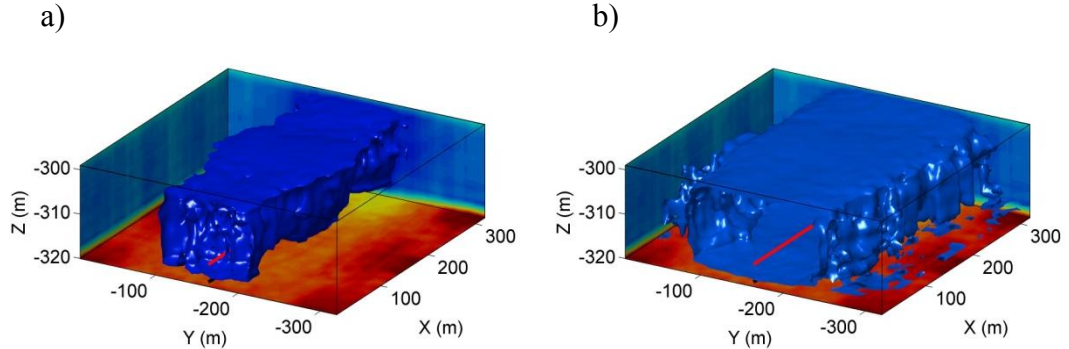
Figure 7.17: Isosurface plot of near-angle elastic impedance after six years of steam injection. Isosurface thresholds of a) 2200 and b) 2600 were used in order to attempt to highlight the steam chamber and heated zones respectively. Red and black lines are the injector and producer wells respectively.

a)   b)
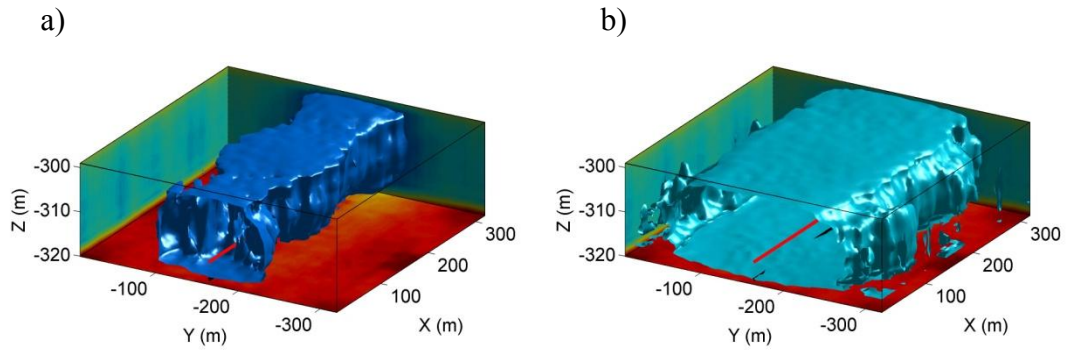
Figure 7.18: Isosurface plot of mid-angle elastic impedance after six years of steam injection. Isosurface thresholds of a) 525 and b) 625 were used in order to attempt to highlight the steam chamber and heated zones respectively. Red and black lines are the injector and producer wells respectively.

The results of the elastic impedance inversion are mixed. The method as applied here does not particularly excel in illuminating either of the steam chamber features or the heated zones. Some insight can be gained by applying varying thresholds to the near- and mid-angle elastic inversion results; however, the results are not as compelling as they are from either the PSEI or acoustic inversion cases. In addition, it is harder to ascertain where the threshold should be set in order to reveal heated or steam filled zones, because the nature of elastic impedance and its variable units with angle can further obscure the relevance of results. In this synthetic case, since the distribution of heat and steam is known, it is much easier to say what threshold is most accurate, but in a field study this would not be the case. It is true that further modeling could be carried out to model the properties of interest at various angles and predict which the thresholds could be most informative, but this would further add to the cost

of running the inversion. Adding this to the limited resolution of the obtained inversions and the uncompelling results in general does not make this method very appealing.

a)   b)
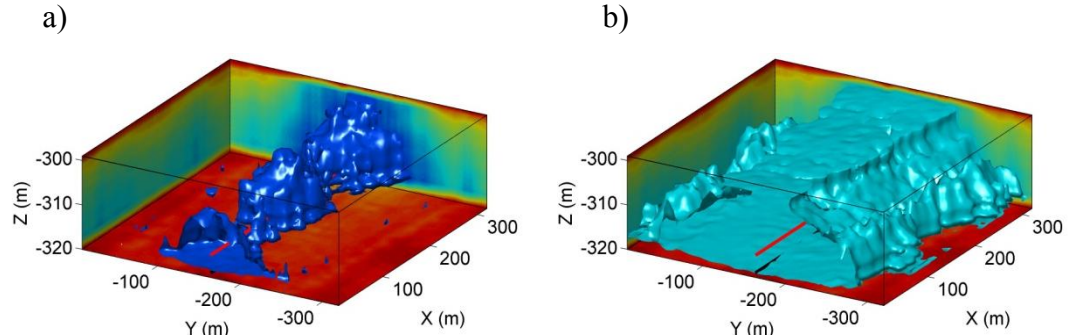
Figure 7.19: Isosurface plot of far-angle elastic impedance after six years of steam injection. Isosurface thresholds of a) 39 and b) 52 were used in order to attempt to highlight the steam chamber and heated zones respectively. Red and black lines are the injector and producer wells respectively.

7.7 Discussion and conclusions

One further consideration when it comes to the inversion processes examined is the computational cost associated with each. The cheapest inversion method is acoustic impedance inversion, and there are many commercial software packages available that can easily handle this type of inversion. This is followed by elastic impedance inversion, which requires some additional computational time because of the extra stacking and sorting of the data, as well as filtering the well logs to correspond with the elastic impedance at a given angle.

After examining the results from the acoustic and elastic inversions and taking the computational costs into consideration, it is clear that the acoustic impedance inversion provides better results, for lower cost than does elastic impedence inversion. As such, the acoustic impedance inversion results will be compared with the PSEI inversion results.

Figure 7.20 shows the actual heat and steam distribution in the reservoir after three years of steam injection. For comparison, Figure 7.21 shows the inversion results from the PSEI inversion (upper row) and the acoustic inversion (lower row) after three

years. In the figure, column a) has a threshold applied which highlights the heated zones of the reservoir, whereas column b) has a threshold applied which highlights the steam chamber in the reservoir. In the predicted heated zones of the reservoir, there is one obvious difference between the two models, which appears at the base of the reservoir. In the PSEI inversion, there is a distinct area at the base of the reservoir that would seem to be a heated zone; however, this is not the case as is shown by Figure 7.20a. This artifact is due to the presence of a large impedance contrast that exists at the base of the reservoir. The relatively soft bitumen reservoir is underlain by a limestone basement (as is often the case for bitumen reservoirs in Canada). This large impedance contrast is smoothed vertically by the band-limited nature of the seismic data and inversion process. In fact, this upscaling effect of the seismic data and inversion process can be seen throughout all the inverted datasets. Both the vertical and lateral resolution are diminished in the inversion results compared with the original models.

a)   b)
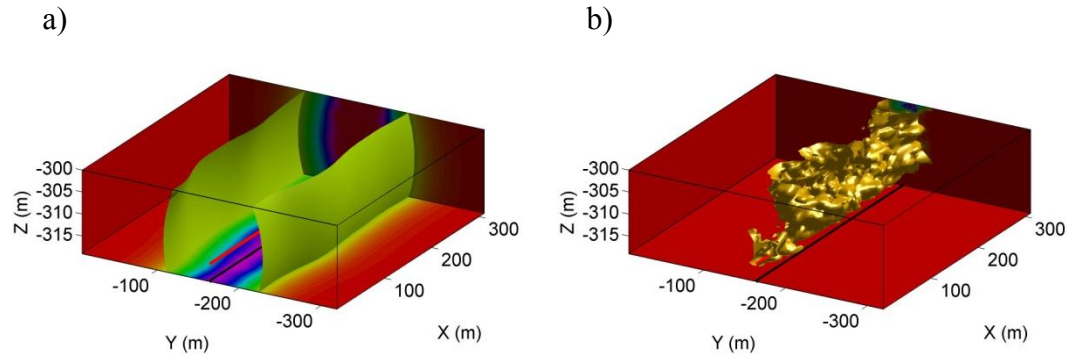
Figure 7.20: Isosurface plots of reservoir properties after three years of steam injection. The isosurface corresponding to a temperature of 60°C is shown in a), and b) shows the 10% gas saturation isosurface in the reservoir.

Despite the artifact at the base of the reservoir, the vertical walls of the heated zone in the PSEI inversion result are still well defined and accurately located within the upper portion of the reservoir. In the acoustic inversion result, the walls of the heated zone are again well defined, but they indicate that the heated zone extends further towards the edge of the simulation than is actually the case. The results highlighting the steam chamber within the reservoir show some similar results. Again, the acoustic impedance inversion would suggest that the extent of steam chamber

formation within the reservoir is greater than is actually the case. The PSEI inversion does not suffer this deficiency, however it does slightly underestimate the extent of the steam chamber and does not provide the exact shape of the steam body in the reservoir.
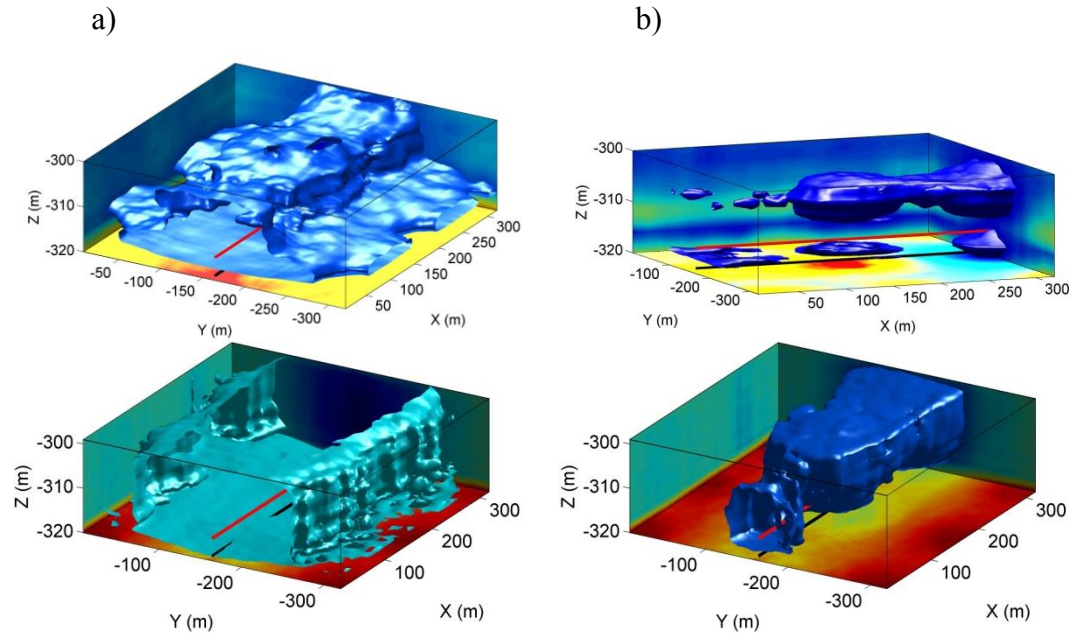
Figure 7.21: Isosurface plots of inverted data after three years of steam injection. The upper row shows the PSEI inversion, and the bottom row shows the acoustic inversion with a threshold to reveal a) the heated zones, and b) the steam chamber location in the reservoir.

Figure 7.22 shows the actual distribution of a) heat and b) steam distribution in the reservoir after six years of steam injection. Figure 7.23 shows the inversion results from PSEI and acoustic impedance inversion after six years with thresholds applied to highlight the heat and steam distributions within the reservoir for comparison. Much like the results after three years, the PSEI results here show a fairly accurate representation of both the heat distribution (aside from the base of the reservoir) and steam distribution within the reservoir. The acoustic impedance inversion also does a decent job revealing these features; however, it tends to overestimate the extent of heating and the size of the steam chamber.

a)   b)
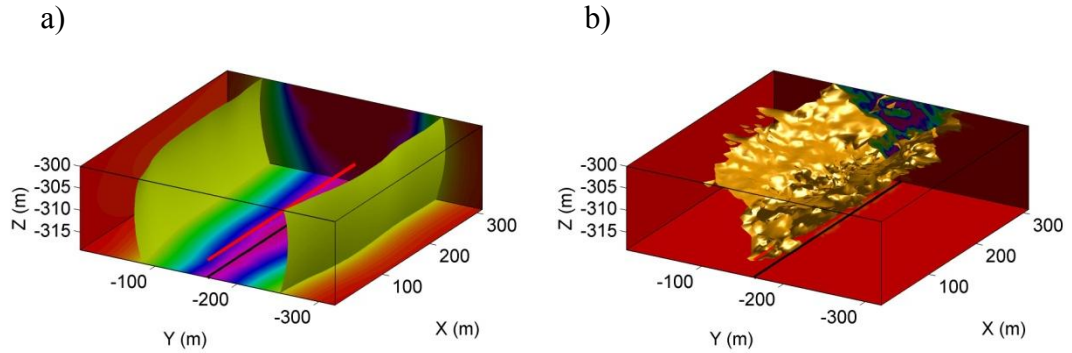
Figure 7.22: Isosurface plots of reservoir properties after six years of steam injection. The isosurface corresponding to a temperature of 60°C is shown in a), and b) shows the 10% gas saturation isosurface in the reservoir.

a)   b)
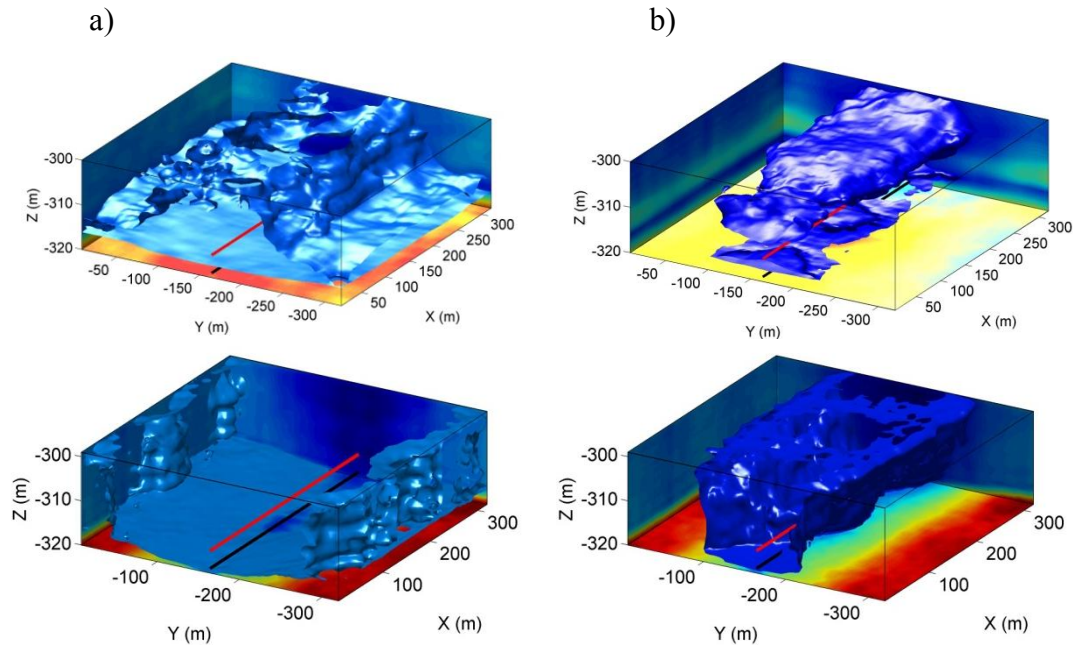
Figure 7.23: Isosurface plots of inverted data after three years of steam injection. The upper row shows the PSEI inversion, and the bottom row shows the acoustic inversion with a threshold to reveal a) the heated zones, and b) the steam chamber location in the reservoir.

These results show that if converted-wave data is available, then the PSEI inversion will provide the most accurate picture of the distribution of heat and steam throughout the reservoir. However, if no converted-wave data is available, or if computational simplicity and cost efficiency are of the utmost importance, then an acoustic impedance inversion may suffice. However, when interpreting acoustic

impedance inversion results, it is important to be aware that they may overestimate the extent of heat and steam within the reservoir.

Appendix
Bitumen sand data

Table A.1: Data from bitumen sand sample S1.

Temperature (°C)	Effective Pressure (Mpa)	Vp (m/s)	Vs (m/s)	Length (cm)
3.6	2	2697	1442	2.6590
3.8	4	2984	1095	2.6518
3.9	6	3143	1243	2.6470
4.1	8	3263	1261	2.6431
4.0	7	3201	1259	2.6444
3.9	5	3075	1215	2.6477
3.7	3	2880	1083	2.6531
3.7	2	2719	1065	2.6584
15.9	2	2639	926	2.6580
16.1	4	2896	1068	2.6501
16.2	6	3050	1212	2.6451
16.3	8	3158	1471	2.6411
16.3	7	3104	1228	2.6423
16.1	5	2985	1189	2.6458
16.0	3	2786	1070	2.6513
15.9	2	2645	1060	2.6568
25.9	2	2582	1041	2.6566
25.9	4	2846	1055	2.6485

26.0	6	3016	1224	2.6434
25.9	8	3111	1500	2.6394
25.8	7	3076	1179	2.6407
25.6	5	2960	1176	2.6440
25.4	3	2749	1042	2.6498
25.4	2	2578	1032	2.6553
39.4	2	2546	919	2.6547
39.6	4	2793	943	2.6466
39.8	6	2962	991	2.6415
40.0	8	3055	1022	2.6375
40.0	7	3032	1008	2.6388
39.9	5	2899	972	2.6422
39.8	3	2673	920	2.6477
39.9	2	2550	911	2.6535
60.8	2	2451	922	2.6534
60.9	4	2703	836	2.6451
61.0	6	2881	966	2.6399
61.2	8	2990	1003	2.6359
61.2	7	2951	981	2.6370
61.1	5	2837	954	2.6404
61.0	3	2559	921	2.6461
61.0	2	2432	921	2.6515
83.7	2	2287	923	2.6526
83.9	4	2635	942	2.6442
84.2	6	2844	1126	2.6390
84.3	8	2941	1246	2.6349
84.2	7	2894	1231	2.6361
84.1	5	2784	1167	2.6394
84.0	3	2519	676	2.6451
84.1	2	2342	615	2.6507
113.8	2	2297	566	2.6530
113.8	4	2702	1143	2.6449
113.8	6	2803	1165	2.6393
113.8	8	2916	1188	2.6347
113.7	7	2875	1180	2.6357
113.8	5	2764	1153	2.6387
114.1	3	2562	902	2.6443
114.5	2	2347	678	2.6497

148.2	2	2438	718	2.6537
148.5	4	2511	748	2.6470
148.6	6	2634	1145	2.6380
148.6	8	2690	1166	2.6318
148.3	7	2676	1169	2.6328
148.0	5	2651	925	2.6355
147.9	3	2553	923	2.6402
148.1	2	2477	832	2.6436
35.2	2	2911	1154	2.6460
34.7	4	3057	1191	2.6414
34.4	6	3105	1216	2.6374
34.3	8	3138	1430	2.6341

Table A.2: Data from bitumen sand sample S2.

Temperature	Effective Pressure	Vp	Vs	Length
(°C)	(Mpa)	(m/s)	(m/s)	(cm)
4.1	2	2618	1598	2.6531
4.2	6	2827	1728	2.6275
4.1	8	2924	1763	2.6187
3.9	7	2890	1745	2.6199
3.8	5	2852	1717	2.6228
3.7	4	2836	1705	2.6247
3.8	3	2773	1669	2.6272
3.7	2	2725	1630	2.6310
28.7	2	2502	1542	2.6303
28.7	6	2692	1641	2.6201
28.7	8	2735	1688	2.6157
28.5	7	2725	1664	2.6168
28.2	5	2677	1626	2.6197
27.9	4	2623	1610	2.6216
27.9	3	2579	1579	2.6240
27.7	2	2530	1556	2.6279
53.9	2	2385	1514	2.6282
54.2	6	2559	1625	2.6179
54.2	8	2629	1661	2.6139
54.0	7	2625	1645	2.6151
53.9	5	2554	1604	2.6179
53.8	4	2518	1589	2.6197

54.0	3	2457	1547	2.6222
53.9	2	2393	1507	2.6260
79.4	2	2241	1451	2.6273
79.3	6	2477	1563	2.6171
79.5	8	2561	1601	2.6134
79.6	7	2520	1581	2.6144
79.8	5	2459	1546	2.6172
80.0	4	2409	1526	2.6191
80.2	3	2332	1501	2.6216
80.3	2	2232	1448	2.6255
105.7	2	2159	1403	2.6287
105.8	6	2379	1507	2.6176
105.7	8	2455	1546	2.6133
105.5	7	2424	1529	2.6146
105.3	5	2355	1503	2.6177
105.2	4	2308	1475	2.6197
105.0	3	2232	1436	2.6225
104.4	2	2174	1386	2.6264
126.9	2	2069	1369	2.6299
127.4	6	2269	1500	2.6177
128.0	8	2333	1548	2.6130
128.1	7	2299	1532	2.6145
128.3	5	2228	1468	2.6180
128.4	4	2171	1433	2.6202
128.7	3	2114	1399	2.6232
128.9	2	2044	1366	2.6276
157.6	2	2008	1336	2.6315
157.6	6	2171	1512	2.6193
157.5	8	2218	1522	2.6141
157.3	7	2206	1505	2.6155
157.3	5	2165	1473	2.6190
157.4	4	2143	1450	2.6213
157.4	3	2079	1436	2.6241
157.4	2	2009	1374	2.6281
177.5	2	1979	1420	2.6344
178.4	6	2176	1507	2.6209
178.7	8	2211	1558	2.6147
178.5	7	2199	1535	2.6159

178.6	5	2175	1498	2.6196
178.6	4	2131	1470	2.6219
178.5	3	2087	1423	2.6248
178.5	2	2032	1410	2.6288
20.8	2	2672	1591	2.6184

Table A.3: Data from bitumen sand sample S3.

Temperature (°C)	Effective Pressure (Mpa)	Vp (m/s)	Vs (m/s)	Length (cm)
4.1	2	3080	1890	2.6213
4.3	6	3186	1940	2.6126
4.3	8	3254	1966	2.6093
4.2	7	3227	1943	2.6107
3.9	5	3180	1930	2.6140
3.9	4	3171	1916	2.6160
3.8	3	3094	1903	2.6181
3.8	2	3057	1897	2.6205
14.4	2	2918	1848	2.6202
14.6	6	3048	1899	2.6116
14.7	8	3098	1935	2.6083
14.6	7	3085	1920	2.6097
14.3	5	3046	1893	2.6130
14.3	4	3002	1865	2.6150
14.2	3	2981	1866	2.6170
14.1	2	2937	1854	2.6194
25.1	2	2798	1808	2.6192
25.5	6	2940	1879	2.6105
25.8	8	3021	1913	2.6071
25.8	7	2995	1900	2.6085
25.6	5	2948	1880	2.6118
25.6	4	2901	1852	2.6139
25.6	3	2875	1847	2.6160
25.7	2	2801	1835	2.6185
40.6	2	2727	1781	2.6186
40.8	6	2889	1835	2.6094
40.9	8	2947	1868	2.6060
40.7	7	2929	1855	2.6074
40.6	5	2859	1829	2.6107

40.5	4	2830	1817	2.6127
40.4	3	2787	1811	2.6149
40.4	2	2737	1767	2.6174
59.8	2	2697	1722	2.6178
60.0	6	2846	1825	2.6083
59.9	8	2918	1851	2.6045
59.8	7	2875	1830	2.6060
59.6	5	2810	1805	2.6093
59.5	4	2779	1774	2.6114
59.6	3	2735	1756	2.6137
59.6	2	2682	1727	2.6165
84.6	2	2504	1692	2.6184
84.9	6	2690	1770	2.6078
84.9	8	2742	1821	2.6036
84.8	7	2712	1800	2.6051
84.6	5	2652	1764	2.6088
84.6	4	2609	1731	2.6111
84.6	3	2558	1721	2.6136
84.6	2	2490	1697	2.6164
112.7	2	2392	1664	2.6197
113.0	6	2552	1765	2.6083
113.1	8	2625	1809	2.6041
113.0	7	2593	1783	2.6057
113.0	5	2529	1747	2.6098
113.0	4	2512	1736	2.6122
113.1	3	2460	1702	2.6149
113.2	2	2400	1669	2.6179
142.6	2	2280	1595	2.6234
142.8	6	2418	1687	2.6110
142.9	8	2454	1725	2.6056
142.7	7	2451	1702	2.6074
142.6	5	2403	1681	2.6117
142.5	4	2377	1654	2.6142
142.7	3	2337	1639	2.6170
142.5	2	2303	1609	2.6204
178.8	2	2108	1584	2.5967
178.4	6	2198	1677	2.5787
178.6	8	2156	1684	2.5700

178.6	7	2137	1678	2.5703
178.5	5	2148	1646	2.5740
178.2	4	2062	1630	2.5761
177.9	3	2053	1604	2.5786
177.8	2	1998	1554	2.5818
178.3	2	2000	1535	2.5821
23.7	2	2551	1932	2.5621

Table A.4: Data from bitumen sand sample S4.

Temperature (°C)	Effective Pressure (Mpa)	Vp (m/s)	Vs (m/s)	Length (cm)
3.6	2	1567	812	1.9638
3.7	4	2324	838	1.9567
3.9	6	2654	873	1.9522
4.1	8	2859	894	1.9485
4.1	7	2827	882	1.9495
3.9	5	2595	868	1.9525
3.7	3	2179	818	1.9578
3.7	2	1919	804	1.9630
15.2	2	1589	784	1.9665
15.5	4	2140	818	1.9587
15.7	6	2550	860	1.9540
15.9	8	2742	872	1.9501
15.9	7	2680	863	1.9511
15.8	5	2436	854	1.9543
15.6	3	2055	810	1.9597
15.6	2	1598	781	1.9652
25.0	2	1580	776	1.9682
25.2	4	2097	806	1.9600
25.4	6	2415	843	1.9552
25.6	8	2685	861	1.9513
25.6	7	2590	857	1.9523
25.4	5	2365	841	1.9554
25.3	3	2015	796	1.9607
25.2	2	1586	769	1.9664
41.1	2	1505	763	1.9706
41.2	4	2091	795	1.9626
41.4	6	2389	818	1.9578

41.5	8	2628	819	1.9538
41.4	7	2550	838	1.9548
41.3	5	2275	821	1.9576
41.1	3	1545	781	1.9631
41.1	2	1491	764	1.9687
59.5	2	1258	751	1.9741
59.8	4	2059	763	1.9663
60.1	6	2389	876	1.9614
60.4	8	2606	786	1.9576
60.5	7	2482	768	1.9585
60.3	5	2176	775	1.9614
60.2	3	1491	762	1.9666
60.2	2	1256	752	1.9722
84.2	2	1285	782	1.9796
84.5	4	1653	746	1.9721
84.7	6	2415	846	1.9668
84.9	8	2665	796	1.9626
84.8	7	2836	777	1.9635
84.7	5	2417	739	1.9664
84.5	3	2394	725	1.9715
84.6	2	1865	710	1.9773
114.1	2	1732	725	1.9872
114.4	4	2202	699	1.9798
114.3	6	2727	1202	1.9742
114.1	8	2846	1281	1.9703
113.6	7	2804	950	1.9709
113.3	5	2681	933	1.9734
113.0	3	2565	915	1.9779
113.1	2	2500	883	1.9828
147.7	2	2658	716	1.9958
148.0	4	2723	738	1.9895
148.3	6	2758	759	1.9838
148.5	8	2760	775	1.9788
148.5	7	2734	768	1.9797
148.5	5	2698	754	1.9828
148.5	3	2679	742	1.9877
148.5	2	2677	733	1.9921
19.8	2	2961	1269	1.9602

19.9	4	3108	1338	1.9545
20.0	6	3147	1382	1.9506
20.1	8	3194	1438	1.9474

Table A.5: Data from bitumen sand sample S5.

| Temperature | Effective Pressure | Vp | Vs | Length |
(°C)	(Mpa)	(m/s)	(m/s)	(cm)
3.6	2	3176	1779	2.8289
3.8	4	3282	1808	2.8244
3.9	6	3377	1856	2.8210
4.1	8	3401	1871	2.8178
4.0	7	3382	1858	2.8186
3.9	5	3341	1832	2.8216
3.7	3	3245	1799	2.8253
3.7	2	3185	1769	2.8284
15.6	2	3048	1723	2.8269
15.9	4	3155	1764	2.8224
16.1	6	3261	1804	2.8185
16.4	8	3299	1843	2.8150
16.4	7	3278	1824	2.8161
16.3	5	3202	1787	2.8188
16.3	3	3135	1743	2.8228
16.1	2	3047	1715	2.8259
26.9	2	2970	1689	2.8248
27.0	4	3116	1717	2.8199
27.2	6	3211	1762	2.8162
27.3	8	3237	1810	2.8128
27.1	7	3223	1797	2.8139
27.0	5	3175	1757	2.8167
26.8	3	3059	1714	2.8206
26.7	2	2981	1682	2.8240
40.3	2	2880	1682	2.8225
40.5	4	3020	1695	2.8175
40.8	6	3110	1742	2.8138
40.9	8	3162	1783	2.8104
40.8	7	3131	1762	2.8116
40.7	5	3086	1745	2.8142
40.6	3	2966	1694	2.8181

40.6	2	2873	1663	2.8214
61.3	2	2827	1656	2.8203
61.5	4	2940	1686	2.8152
61.6	6	3055	1741	2.8114
61.6	8	3105	1785	2.8079
61.5	7	3092	1765	2.8089
61.3	5	3018	1732	2.8116
61.2	3	2907	1684	2.8158
61.1	2	2792	1642	2.8191
85.0	2	2706	1595	2.8185
85.1	4	2867	1670	2.8138
85.2	6	2981	1741	2.8097
85.2	8	3069	1772	2.8063
85.1	7	3033	1757	2.8071
84.9	5	2953	1718	2.8100
84.8	3	2815	1646	2.8140
84.8	2	2723	1601	2.8172
113.5	2	2628	1626	2.8177
113.7	4	2811	1693	2.8128
113.7	6	2942	1758	2.8087
113.7	8	3033	1787	2.8051
113.5	7	2988	1773	2.8060
113.4	5	2895	1728	2.8087
113.2	3	2738	1676	2.8127
113.2	2	2623	1618	2.8160
149.3	2	2473	1602	2.8179
149.5	4	2589	1682	2.8120
149.7	6	2695	1735	2.8068
149.9	8	2747	1779	2.8019
150.0	7	2716	1747	2.8030
150.2	5	2659	1720	2.8066
150.4	3	2574	1666	2.8115
150.7	2	2511	1609	2.8155
20.6	2	3047	1651	2.8192
20.7	6	3231	1744	2.8116
20.8	8	3276	1776	2.8087
20.6	4	3157	1702	2.8137

Table A.6: Data from bitumen sand sample S5_2.

Temperature (°C)	Effective Pressure (Mpa)	Vp (m/s)	Vs (m/s)	Length (cm)
3.7	2	3005	1546	2.1330
3.7	4	3093	1612	2.1277
3.9	6	3161	1676	2.1235
4.0	8	3227	1720	2.1197
3.9	5	3138	1653	2.1240
15.9	2	2843	1485	2.1359
16.1	4	2970	1513	2.1302
16.3	6	3062	1566	2.1255
16.4	8	3119	1613	2.1215
16.2	5	3027	1550	2.1257
25.7	2	2788	1451	2.1370
25.9	4	2886	1490	2.1313
26.0	6	2977	1532	2.1270
26.0	8	3031	1563	2.1230
25.8	5	2948	1512	2.1272
39.6	2	2670	1409	2.1396
39.9	4	2781	1470	2.1339
40.2	6	2877	1502	2.1297
40.5	8	2940	1524	2.1257
40.4	5	2836	1500	2.1299
59.4	2	2534	1378	2.1447
59.7	4	2673	1428	2.1389
59.9	6	2778	1473	2.1345
60.0	8	2847	1496	2.1304
59.8	5	2736	1461	2.1346
84.4	2	2435	1315	2.1517
84.5	4	2575	1384	2.1458
84.7	6	2696	1439	2.1413
84.7	8	2770	1480	2.1370
84.4	5	2652	1426	2.1413
112.9	2	2295	1288	2.1609
113.2	4	2482	1344	2.1550
113.4	6	2584	1401	2.1503
113.5	8	2686	1429	2.1460
113.2	5	2550	1391	2.1503
146.8	2	2201	1241	2.1729

147.3	4	2343	1307	2.1666
147.5	6	2423	1353	2.1612
147.7	8	2505	1391	2.1560
147.6	5	2394	1328	2.1612
18.8	2	2897	1439	2.1260
18.9	4	2992	1539	2.1209
19.1	6	3061	1606	2.1172
19.2	8	3110	1655	2.1139
19.1	5	3027	1579	2.1178

Table A.7: Data from bitumen sand sample S6.

Temperature (°C)	Effective Pressure (Mpa)	Vp (m/s)	Vs (m/s)	Length (cm)
4.2	2	3277	1621	2.7565
4.2	4	3402	1701	2.7530
4.3	6	3476	1762	2.7500
4.4	8	3530	1801	2.7474
4.2	5	3442	1741	2.7508
16.0	2	3233	1619	2.7568
16.2	4	3347	1675	2.7532
16.3	6	3422	1728	2.7500
16.4	8	3489	1775	2.7474
16.2	5	3390	1710	2.7508
24.8	2	3183	1594	2.7568
25.0	4	3286	1651	2.7532
25.2	6	3358	1694	2.7500
25.4	8	3435	1729	2.7473
25.2	5	3335	1681	2.7509
38.9	2	3093	1573	2.7575
39.2	4	3208	1625	2.7537
39.5	6	3289	1656	2.7504
39.7	8	3354	1693	2.7477
39.6	5	3255	1647	2.7512
60.7	2	2999	1548	2.7592
60.8	4	3103	1594	2.7553
61.0	6	3186	1619	2.7520
61.1	8	3266	1662	2.7491
60.8	5	3164	1611	2.7526

85.4	2	2909	1493	2.7622
85.5	4	3007	1528	2.7584
85.6	6	3112	1584	2.7549
85.7	8	3199	1633	2.7520
85.5	5	3081	1572	2.7556
114.2	2	2808	1487	2.7665
114.3	4	2902	1509	2.7626
114.5	6	2996	1560	2.7590
114.6	8	3104	1609	2.7560
114.4	5	2974	1550	2.7595
148.4	2	2667	1439	2.7727
147.0	4	2756	1473	2.7687
145.0	6	2856	1509	2.7641
144.5	8	2987	1540	2.7606
143.7	5	2865	1488	2.7645
18.8	2	3334	1681	2.7566
18.8	4	3417	1775	2.7534
19.0	6	3488	1835	2.7508
19.1	8	3552	1892	2.7485
18.9	5	3471	1826	2.7514

Table A.8: Data from bitumen sand sample S7.

Temperature (°C)	Effective Pressure (Mpa)	Vp (m/s)	Vs (m/s)	Length (cm)
3.7	2	3179	1794	2.4408
3.8	4	3297	1843	2.4356
4.0	6	3373	1876	2.4312
4.2	8	3406	1890	2.4276
3.9	5	3346	1851	2.4321
15.3	2	3064	1717	2.4431
15.5	4	3184	1781	2.4376
15.8	6	3268	1826	2.4331
15.9	8	3308	1843	2.4294
15.8	5	3235	1801	2.4339
25.0	2	2964	1651	2.4448
25.3	4	3081	1738	2.4390
25.5	6	3175	1787	2.4344
25.6	8	3264	1822	2.4306

25.4	5	3148	1770	2.4352
40.7	2	2868	1612	2.4475
40.9	4	2987	1689	2.4417
41.0	6	3095	1731	2.4370
41.1	8	3154	1780	2.4330
40.9	5	3065	1727	2.4375
59.5	2	2751	1537	2.4508
59.8	4	2895	1625	2.4449
60.0	6	2999	1684	2.4402
60.1	8	3085	1744	2.4361
60.0	5	2960	1655	2.4406
83.6	2	2617	1515	2.4559
84.0	4	2767	1588	2.4498
84.2	6	2903	1656	2.4449
84.4	8	2965	1701	2.4408
84.3	5	2859	1634	2.4450
113.6	2	2499	1495	2.4631
113.8	4	2641	1570	2.4572
113.9	6	2792	1618	2.4522
114.0	8	2859	1642	2.4479
113.7	5	2735	1603	2.4521
147.1	2	2364	1443	2.4721
147.3	4	2505	1504	2.4660
147.5	6	2608	1559	2.4605
147.6	8	2700	1594	2.4553
147.5	5	2575	1540	2.4602
19.2	2	3090	1714	2.4373
19.3	4	3177	1787	2.4326
19.4	6	3257	1826	2.4288
19.5	8	3315	1856	2.4256
19.3	5	3227	1806	2.4295

Table A.9: Data from bitumen sand sample S8.

Temperature	Effective Pressure	Vp	Vs	Length
(°C)	(Mpa)	(m/s)	(m/s)	(cm)
3.6	2	2515	1773	2.5706
3.8	4	2827	1799	2.5651
3.9	6	2995	1816	2.5609

4.1	8	3142	1863	2.5575
4.0	7	3101	1791	2.5585
3.9	5	2967	1745	2.5614
3.7	3	2747	1473	2.5659
3.7	2	2643	1453	2.5697
16.0	2	2400	1420	2.5702
16.2	4	2728	1476	2.5643
16.3	6	2919	2235	2.5600
16.4	8	3058	1830	2.5564
16.3	7	2998	1777	2.5574
16.2	5	2858	1437	2.5603
16.0	3	2583	1230	2.5650
16.0	2	2383	1159	2.5690
26.8	2	2361	1154	2.5691
26.9	4	2651	1229	2.5634
27.1	6	2839	1706	2.5590
27.2	8	2977	1811	2.5555
27.1	7	2923	1776	2.5564
26.9	5	2771	1455	2.5594
26.7	3	2514	1226	2.5640
26.7	2	2337	1177	2.5680
39.4	2	2159	1178	2.5686
39.6	4	2526	1208	2.5625
39.8	6	2718	1716	2.5581
40.0	8	2893	1798	2.5546
39.9	7	2829	1764	2.5553
39.9	5	2690	1450	2.5584
39.8	3	2387	1180	2.5632
39.9	2	2154	1134	2.5671
59.8	2	2011	1152	2.5682
59.9	4	2427	1230	2.5623
60.1	6	2671	1416	2.5577
60.2	8	2847	1476	2.5542
60.1	7	2776	1422	2.5550
59.9	5	2565	1205	2.5580
59.8	3	2266	1195	2.5628
59.8	2	1994	1155	2.5668
82.5	2	1970	1121	2.5686

82.8	4	2454	1387	2.5627
83.0	6	2637	1432	2.5580
83.1	8	2798	1486	2.5545
83.0	7	2733	1466	2.5552
82.8	5	2597	1431	2.5579
82.7	3	2342	1355	2.5628
82.8	2	2018	1321	2.5669
113.1	2	2015	1304	2.5708
113.0	4	2475	1382	2.5654
112.5	6	2615	1453	2.5602
112.1	8	2756	1487	2.5562
111.6	7	2706	1479	2.5570
111.2	5	2566	1427	2.5598
110.9	3	2205	1368	2.5639
111.3	2	2041	1323	2.5679
148.5	2	2285	1312	2.5738
148.6	4	2359	1495	2.5680
148.5	6	2530	1551	2.5620
148.4	8	2571	1558	2.5563
148.5	7	2532	1551	2.5571
148.7	5	2462	1524	2.5605
148.8	3	2354	1485	2.5654
148.9	2	2343	1419	2.5698
21.0	2	2977	1477	2.5638
21.2	6	3097	1582	2.5555
21.3	8	3151	1610	2.5525
21.2	4	3059	1534	2.5575

References

Alboudwarej, H., J. Felix, S. Taylor, R. Badry, C. Bremmer, B. Brough, C. Skeates, et al. 2006. Highlighting Heavy Oil. *Oilfield Review* 18, no. 2: 34-53.

Batzle, M., R Hofmann, and D-H Han. 2006. Heavy oils—seismic properties. *The Leading Edge* 25, no. 6: 750.

Batzle, Michael, and Zhijing Wang. 1992. Seismic properties of pore fluids. *Geophysics* 57, no. 11: 1396.

Beggs, H.D., and J.R. Robinson. 1975. Estimating the Viscosity of Crude Oil Systems. *Journal of Petroleum Technology* 27, no. 9 (9).

Behura, Jyoti, Mike Batzle, Ronny Hofmann, and John Dorgan. 2007. Heavy oils: Their shear story. *Geophysics* 72, no. 5: E175.

Berryman, J.G. 1995. Mixture Theories for Rock Properties. In *Rock Physics and Phase Relations: A Handbook of Physical Constants*, 205-228. American Geophysical Union.

———. 1980. Long-wavelength propagation in composite elastic media II - Ellipsoidal inclusions. *J. Acoust. Soc. Am.* 68, no. 6: 1820-1831.

Biot, M. A. 1956. Theory of Propagation of Elastic Waves in a Fluid-Saturated Porous Solid. I. Low-Frequency Range. *The Journal of the Acoustical Society of America* 28, no. 2 (March 0): 168-178.

Byerley, Grant, Greg Barham, Tim Tomberlin, and Bryan Vandal. 2009. 4D seismic monitoring applied to SAGD operations at Surmont, Alberta, Canada. *SEG Technical Program Expanded Abstracts* 28, no. 1 (January 0): 3959-3963.

Chen, Q, M.G. Gerritsen, and A.R. Kovscek. 2008. Effects of reservoir heterogeneities on the steam-assisted gravity-drainage process. *SPE Reservoir Evaluation & Engineering* 11, no. 5 (October): 921-932.

Christensen, R.M. 2003. *Theory of Viscoelesticity*. 2nd ed. Mineola, N.Y.: Dover Publications.

Ciz, Radim, and Serge A. Shapiro. 2007. Generalization of Gassmann equations for porous media saturated with a solid material. *Geophyics* 72, no. 6 (December): A75-A79.

Connolly, Patrick. 1999. Elastic impedance. *The Leading Edge* 18, no. 4 (4): 438.

Curtis, C., R. Kopper, E. Decoster, A. Guzman-Garcia, C. Huggins, L. Knauer, M. Minner, et al. 2002. Heavy-Oil Reservoirs. *Oilfield Review* 14, no. 3: 30-51.

Das, Agnibha, and Michael Batzle. 2009. A combined effective medium approach for modeling the viscoelastic properties of heavy oil reservoirs. In *SEG Technical Program Expanded Abstracts*, 2110-2114.

DeGhetto, G., Francesco Paone, and Marco Villa. 1995. Pressure-Volume-Temperature Correlations for Heavy and Extra Heavy Oils. In *Proceedings of SPE International Heavy Oil Symposium*. 6.

Desilets, C.S., J.D. Fraser, and G.S. Kino. 1978. The Design of Efficient Broad-Band Piezoelectric Transducers. *Sonics and Ultrasonics, IEEE Transactions on* 25, no. 3: 115-125.

Dumitrescu, Carmen C., and Larry Lines. 2009. Case study of a heavy oil reservoir interpretation using Vp/Vs ratio and other seismic attributes. In *SEG Technical Program Expanded Abstracts*, 1765-1769.

Dusseault, M. 2006. Mechanics of Heavy Oil. Short Course presented at the US Society of Rock Mechanics.

Dusseault, Maurice. 1980. Sample Disturbance In Athabasca Oil Sand. *Journal of Canadian Petroleum Technology*.

Dvorkin, Jack, and Amos Nur. 1996. Elasticity of high-porosity sandstones: Theory for two North Sea data sets. *Geophysics* 61, no. 5: 1363.

Eastwood, John, P. Lebel, and A. Dilay. 1994. Seismic monitoring of steam-based recovery of bitumen. *The Leading Edge* 13, no. 4 (4): 242.

Gassmann, F. 1951. Uber die elastizitat poroser medien. *Verteljahrsscrift der Naturforschenden Gesellschaft* 96: 1.

González, Ezequiel. 2006. Physical and quantitative interpretation of seismic attributes for rocks and fluids identification. Stanford University, June.

González, Ezequiel, Gary Mavko, and Tapan Mukerji. 1999. A practical procedure for P-to-S "elastic" impedance (PSEI) inversion: Well log and synthetic seismic examples for identifying partial gas saturations. *SEG Technical Program Expanded Abstracts* 23, no. 1: 1782.

González, Ezequiel, Tapan Mukerji, and Gary Mavko. 2003. Near and far offset P-to-S elastic impedance for discriminating fizz water from commercial gas. *The Leading Edge* 22, no. 10: 1012.

Haller, Matthew Isaac. 1998. Micromachined Ultrasonic Devices and Materials. Stanford University.

Han, De-Hua, Qiuliang Yao, and Hui-zhu Zhao. 2007a. Complex properties of heavy-oil sand. *SEG Technical Program Expanded Abstracts* 26, no. 1: 1609.

———. 2007b. Complex properties of heavy-oil sand. *SEG Technical Program Expanded Abstracts* 26, no. 1: 1609.

Han, De-hua, Jiajin Liu, and Michael Batzle. 2005. Measurement of shear wave velocity of heavy oil. *SEG Technical Program Expanded Abstracts* 24, no. 1: 1513. doi:

———. 2006. Acoustic property of heavy oil — measured data. *SEG Technical Program Expanded Abstracts* 25, no. 1: 1903.

———. 2009. Viscosity model of heavy oil with calibration of shear velocity data. In *SEG Technical Program Expanded Abstracts*, 2115-2119.

Han, De-hua, Jiajin Liu, and Micheal Batzle. 2007. Shear velocity as the function of frequency in heavy oils. *SEG Technical Program Expanded Abstracts* 26, no. 1: 1716.

———. 2008. Velocity and dispersion of heavy oils. *SEG Technical Program Expanded Abstracts* 27, no. 1: 1690.

Han, De-hua, Jiajin Liu, and Michael Baztle. 2008. Seismic properties of heavy oils—measured data. *The Leading Edge* 27, no. 9: 1108.

Han, De-hua, Hui-zhu Zhao, Qiuliang Yao, and Michael Batzle. 2007. Velocity of heavy-oil sand. *SEG Technical Program Expanded Abstracts* 26, no. 1: 1619.

Hashin, Z., and S. Shtrickman. 1963. A variational approach to the elastic behavior of multiphase materials. *J. Mech. Phys. Solids* 11: 127-140.

Havriliak, S., and S. Negami. 1967. A complex plane representation of dielectric and mechanical relaxation processes in some polymers. *Polymer* 8: 161-210.

Hinkle, A., and M. Batzle. 2008. Relating Chemical and Physical Properties of Heavy Oil. In *AAPG Hedberg Research Conference*. Banff, AB, Canada: AAPG.

Kato, Ayato, Shigenobu Onozuka, and Toru Nakayama. 2008. Elastic property changes in a bitumen reservoir during steam injection. *The Leading Edge* 27, no. 9: 1124.

Kendall, Rob. 2009. Using timelapse seismic to monitor the THAI™ heavy oil production process. In *SEG Technical Program Expanded Abstracts*, 3954-3958.

King, M. S. 1966. Wave velocities in rocks as a function of changes in overburden pressure and pore fluid saturants. *Geophysics* 31, no. 1 (2): 50.

Krimholtz, R., D.A. Leedom, and G.L. Matthaei. 1970. New equivalent circuits for elementary piezoelectric transducers. *Electronics Letters* 6, no. 13: 398-399.

Le Page, Y., and J. Rodgers. 2005. Ab initio elasticity of FeS2 pyrite from 0 to 135 GPa. *Physics and Chemistry of Minerals* 32, no. 8 (December 1): 564-567.

Lesueur, Didier, Jean-Francois Gerard, Pierre Claudy, Jean-Marie Letoffe, Jean-Pascal Planche, and Didier Martin. 1996. A structure-related model to describe asphalt linear viscoelasticity. *Journal of Rheology* 40, no. 5: 813-836.

Li, Guoping, G. Purdue, S. Weber, and R. Couzens. 2001. Effective processing of nonrepeatable 4-D seismic data to monitor heavy oil SAGD steam flood at East Senlac, Saskatchewan, Canada. *The Leading Edge* 20, no. 1 (1): 54.

Makarynska, Dina, Boris Gurevich, Jyoti Behura, and Mike Batzle. 2010. Fluid substitution in rocks saturated with viscoelastic fluids. *Geophysics* 75, no. 2: E115.

Marion, D. 1990. Acoustical, Mechanical and Transport Properties of Sediments and Granular Materials. PhD Dissertation, Stanford University.

Mavko, Gary, and Diane Jizba. 1991. Estimating grain-scale fluid effects on velocity dispersion in rocks. *Geophysics* 56, no. 12 (December 0): 1940-1949.

Mavko, Gary, Tapan Mukerji, and Jack Dvorkin. 1998. *The Rock Physics Handbook: Tools for Seismic Analysis in Porous Media*. Cambridge: Cambridge Univeristy Press.

Morcote-Rios, A., G. Mavko, and M. Prasad. 2005. The elastic properties of coal. *Stanford Rock Physics and Borehole Geophysics Annual Report* 100.

Morton, Susan Lynn. 1999. Ultrasonic Sensor for Photoresist Process Monitoring. Stanford University.

Nakayama, Toru, Akihisa Takahashi, Leigh Skinner, and Ayato Kato. 2008. Monitoring an oil-sands reservoir in northwest Alberta using time-lapse 3D seismic and 3D P-SV converted-wave data. *The Leading Edge* 27, no. 9: 1158.

Nur, Amos, Carol Tosaya, and Dung Vo-Thanh. 1999. Seismic monitoring of thermal enhanced oil recovery processes. *SEG Technical Program Expanded Abstracts* 3, no. 1: 337.

Ramo, Simon, John R. Whinnery, and Theodore Van Duzer. 1994. *Fields and Waves in Communication Electronics*. 3rd ed. Wiley, February 9.

Rojas, Maria Alejandra, John Castagna, Ramanan Krishnamoorti, De-hua Han, and Azra Tutuncu. 2008. Shear thinning behavior of heavy oil samples: Laboratory measurements and modeling. *SEG Technical Program Expanded Abstracts* 27, no. 1: 1714.

Stewart, Robert R., James E. Gaiser, R. James Brown, and Don C. Lawton. 2003. Converted-wave seismic exploration: Applications. *Geophysics* 68, no. 1: 40.

Wang, Zhijing, and Amos Nur. 1990. Wave velocities in hydrocarbon-saturated rocks: Experimental results. *Geophysics* 55, no. 6: 723.

Wolf, K, and G Mavko. 2005. Ultrasonic properties of bitumen and bitumen sands. *Stanford Rock Physics and Borehole Geophysics Annual Report* 100.

Zimmer, Michael. 2003. Seismic Velocities in Unconsolidated Sands: Measurements of Pressure, Sorting, and Compaction Effects. Stanford University.